Dynamic Hydrogels to Dissect the Mechanobiology of Epithelial Ageing

Von der Fakultät für Mathematik und Naturwissenschaften der RWTH Aachen University zur Erlangung des akademischen Grades eines Doktors der Naturwissenschaften genehmigte Dissertation

vorgelegt von

Felix Reul, M. Sc.

aus

Mainz, Deutschland

Berichter: *Priv.-Doz. Dr. rer. nat. Jacopo Di Russo*

Prof. Dr.-Ing. Laura De Laporte

Tag der mündlichen Prüfung: *27.08.2026*

Diese Dissertation ist auf den Internetseiten der Universitätsbibliothek verfügbar.

Table of contents

Table of contents i
Declaration of Authorship/ Eidesstattliche Erklärung iv
Scientific contribution v
Journal article v
Conference contribution v
Acknowledgments vi
Summary vii
Zusammenfassung viii
I. Introduction 1
1. Mechanobiology 1
Balancing forces: tissue level mechanics 1
2. Epithelia in mechanobiology 3
Cytoskeleton, junctions and extracellular matrix elements 4
The retinal pigment epithelium 9
3. Dynamic hydrogel systems for tissue engineering 11
Hydrogels as substrate mimics 11
Microgels in tissue engineering and mechanobiology 16
4. Knowledge gap 19
Substrate-mediated force balance disruption as a model for RPE disease progression 19
Cytoskeleton specific in monolayer force balance disruption 19
II. Aim 20
III. Results 21
1. Synthesis of the photodegradable crosslinker 21
Carbamate-based photodegradable crosslinker 23
2. A photodegradable hydrogel to mimic ECM ageing of the outer retina 27
Synthesis and characterization of the photodegradable hydrogel 27
hiPSC-RPE monolayer formation on the photodegradable hydrogel 34
Distance dependent quantification of morphometric parameters 39
3. Photodegradable microgels as phantom cells 47

Microgel synthesis 47
Integration of photodegradable microgels within epithelial monolayers 52
IV. Discussion 71
1. Photodegradable hydrogel as artificial drusen mimic 71
Artificial drusen characterization 71
Bio-functionalization strategies of the photodegradable hydrogel 71
Impact of topographical defects on the epithelial monolayer 72
2. Photodegradable microgels as phantom cells 74
Microgel synthesis optimization 74
UV degradation and bio-functionalization characterization 74
Embedded phantom cells in Madin-Darby canine kidney epithelium 75
Embedded phantom cells in hiPSC-RPE monolayer 75
V. Conclusion and Outlook 78
1. What is next for the artificial drusen model? 78
2. What is next for the photo-responsive phantom cell? 79
VI. Methods 81
1. Photodegradable crosslinker synthesis 81
2. Carbamate-based photodegradable crosslinker synthesis 86
1st synthesis strategy adapted from Kim et al.[295] 86
2nd synthesis strategy adapted from Kim et al.[295] 86
4-nitrophenyl chloroformate-based hydroxyl activation synthesis adapted from LeValley et al.[187] 87
1,1'-carbonyldiimidazole-based hydroxyl activation synthesis[338,339] 89
Carbamate-based photodegradable crosslinker synthesis 90
3. Photodegradable hydrogel as an artificial drusen mimic 93
Photodegradable hydrogel preparation 93
PDH Characterization 94
Hydrogel bio-functionalization 95
Cell seeding of hiPSC-RPE on PDH 97
Localized on-demand topographical defect induction on hiPSC-RPE monolayer .. 98
Immunofluorescent staining and imaging 98

Analysis of cell morphology: monolayer height, cell area, shape factor, and angle to origin 99
Traction force microscopy of hiPSC-RPE monolayers on PDH 100
4. Photodegradable microgels 101
Microfluidic chip production 101
Microfluidic microgel production 101
Microgel characterization.....104
Microgel functionalization 105
Microgel-cell co-culture.....106
Microgel illumination in co-culture 107
Immunofluorescent staining and imaging of co-culture.....107
Analysis of cell morphology in microgel cell co-culture 108
VII. References 109
VIII. Appendix..... - 1 -
1. List of abbreviations ..... - 1 -
2. List of figures ..... - 3 -
3. List of tables .....- 10 -
4. Code for analysis .....- 11 -
Fiji macro for batch analysis of Shape Factor/Area, Angle to Origin, Monolayer height .....- 11 -

Declaration of Authorship/ Eidesstattliche Erklärung

I, Felix Alexander Wassili Reul

declare that this thesis and the work presented in it are my own and has been generated by me as the result of my own original research.

Hiermit erkläre ich an Eides statt / I do solemnely swear that:

1. This work was done wholly or mainly while in candidature for the doctoral degree at this faculty and university;

2. Where any part of this thesis has previously been submitted for a degree or any other qualification at this university or any other institution, this has been clearly stated;

3. Where I have consulted the published work of others or myself, this is always clearly attributed;

4. Where I have quoted from the work of others or myself, the source is always given. This thesis is entirely my own work, with the exception of such quotations;

5. I have acknowledged all major sources of assistance;

6. Where the thesis is based on work done by myself jointly with others, I have made clear exactly what was done by others and what I have contributed myself;

7. Parts of this work have been published before as:

Reul, Felix; Bergerbit, Cédric; Scarlat, Iulia; Piskova, Teodora; Krishnamurthy, Vasudha Turuvekere; Kozyrina, Aleksandra N; Yam, Stacy Lok Sze; Laporte, Laura de; Di Russo, Jacopo (2026): Photodegradable Hydrogels for On-Demand Modeling of Age-Related Spatiotemporal ECM Deformation. In Small, Article e09246. DOI: 10.1002/smll.202509246.

02.06.2026, Aachen

_____

Felix Reul

Scientific contribution

Journal article

1. ***Reul, Felix**; Bergerbit, Cédric; Scarlat, Iulia; Piskova, Teodora; Krishnamurthy, Vasudha Turuvekere; Kozyrina, Aleksandra N; Yam, Stacy Lok Sze; Laporte, Laura de; Di Russo, Jacopo (2026): Photodegradable Hydrogels for On-Demand Modeling of Age-Related Spatiotemporal ECM Deformation. In Small, Article e09246. DOI: 10.1002/smll.202509246.*

Conference contribution

1. Mechanobiology in Epithelial 3D Tissue Constructs Annual Retreat, Erlangen, Germany, 15-17.04.2026: **Poster**
2. Mechanobiology in Time & Space, MBI 2025 Conference, Singapore, Singapore, 09-12.09.2025: **Poster**
3. Bridging the scales in Mechanobiology: From cytoskeleton to 3D tissues – CYTAC meets ME3T symposium, Göttingen, Germany, 25-27.03.2025: **Talk**
4. Future 3D Additive Manufacturing | The 3DMM2O Conference 2024, Schöntal, Germany, 07-11.04.2024: **Flash talk & Poster**
5. FEBS 2023 Advanced Course on Mechanics in Biology, Glasgow, United Kingdom, 04-09.06.2023: **Flash talk & Poster**
6. Aachen-Dresden-Denkendorf International Textile Conference, Aachen, Germany, 01-02.12.2022: **Poster**

Acknowledgments

Firstly, I want to thank my Doktorvater Jacopo Di Russo. Thank you for your honesty, which has given me so many opportunities to reflect and grow. For the trust you placed in me to overcome the challenges. Above all, thank you for your guidance: for steering me back whenever I got lost in detail or chasing a tangent, for helping me bring focus to my work, and for teaching me how to grow as a scientist. Furthermore, I want to thank Prof. Laura De Laporte for her scientific input, her continued feedback and general support that she provided throughout my PhD. Also, I want to thank Prof. Rudolf Leube, who always engaged in interesting discussions, found solutions for every organizational hurdles, and provided an essential forum for me to learn.

I would have never made it this far without my colleagues from the REMeD group, which I share so many hours in and outside the laboratory. Aleksandra “Sasha” Kozyrina, who was the social glue that welcomed me into the workgroup. I’m still convinced that you made the REMeD spirit that sets this workgroup apart. Many “thank yous” to Teodora Piskova who always had an ear for idle chatting in the office or scientific matters. Seeing your growth as a person and scientist is nothing short of awe inspiring. And to Vasudha Turuvekerev Krishnamurthy, who helped me so much in the lab but also showed me Indian cuisine around the world. I also want to thank all my colleagues in the De Laporte group. Especially Cedric Bergerbit who always had a minute for me on the busiest of his days, helping and inspiring me to keep the proper order in the lab. I also want to thank Matthias Mork and Tom Schneider for helping me with everything microfluidic. Furthermore, I want to thank all my colleagues in MOCA for their pragmatic, scientific and emotional help throughout the years.

This work, and the experience of it, would not have been the same without all the wonderful students I had the chance to supervise. I want to thank you all for your trust and hope you have learned at least as much as you taught me. With this I want to thank: Alexandra Raab, Stacy Lok Sze Yam, Daniel Gutmann, Yuxin Ji, Karla Prediger, Jovana Stevanovikj, Alejandra Sarzosa Salazar, Lena Schildkamp, and Tanishka Watts for their contributions as master students, interns, HiWis, or trainees. I want to thank the Me3t graduate school for their extensive support and enabling me to go to so many conferences near and far, but also providing a place of learning, expression of ideas, and discussion of science.

Finally, I want to thank my family, friends and girlfriend who supported me through the years emotionally and scientifically, especially during the writing process. Thank you to my brother and to both my parents Christine Wassilew and Thomas Reul who inspired me to become a scientist early on and who supported me throughout my studies. And to my grandparents, Manfred, Edith und Helga for supporting me in achieving my goals and for raising me to become the person I am today.

Summary

The emergent field of mechanobiology has begun to elucidate tissue-level mechanical homeostasis and link it to physiological ageing or pathological degeneration. In epithelial tissues there are two key regulators of this homeostasis: basal remodeling of the extracellular matrix (ECM) and the lateral force balance between neighboring cells. An exemplary system of high in vivo relevance is the outer retina, where the ECM develops heterogenous deposits, so called drusen, over the course of its lifecycle. This basal perturbation introduces localized mechanical heterogeneity and ultimately leads to tissue-scale functional decline. In parallel, the postmitotic retinal pigment epithelium (RPE) is subjected to tissue remodeling due to naturally occurring cell loss, resulting in lateral force balance disruption of the monolayer. Since individual susceptibility to the development of a pathological state is mostly restricted to genetic predispositions, a mechanobiological elucidation into the basal or lateral induced force balance disruptions could give valuable new insights.

In this work, I developed a dynamic poly (ethylene glycol) (PEG) based hydrogel with light-tunable mesh density, as a tool to facilitate on-demand mechanical modulation of cellular interfaces. The photo responsiveness of the system was facilitated though the incorporation of an ortho nitro-benzyl (oNB) based moiety into the hydrogel network which undergoes irreversible bond cleavage when illuminated with UV light, giving a high degree of control over the dose, frequency and shape of the affected region. Using this platform, I investigated the on-demand topographical disruption of mature hiPSC-RPE monolayers, mimicking medium and large drusen. I found distinct defect size and distance dependency of the collective monolayer responses by quantification of the morphometric parameters and cellular traction forces. On the other hand, to investigate lateral force-balance disruptions, I integrated photo responsive microgels into the RPE force transmission network through hybrid adherens junctions. On-demand softening of these phantom cells elicited a biphasic tissue-level response expressed by actin cytoskeleton reorganization and nuclei deformation.

Altogether, this work demonstrates the application of a photo-responsive hydrogel platform that allows precise spatial and temporal control over tissue level mechanical properties, like topography and organization, providing a versatile tool for studying mechanobiological aspects of dynamic cell-matrix or cell-cell interactions.

Zusammenfassung

Das aufstrebende Forschungsgebiet der Mechanobiologie hat damit begonnen, die mechanische Homöostase auf Gewebeebene zu erforschen und damit physiologische Alterung oder pathologischer Degeneration aufzuklären. In epithelialen Geweben gibt es zwei zentrale Regulatoren dieser Homöostase: die basale Umstrukturierung der extrazellulären Matrix (EZM) und das laterale Kräftegleichgewicht zwischen benachbarten Zellen. Ein beispielhaftes System von hoher in-vivo-Relevanz ist die Netzhaut, dessen EZM im Laufe ihres Lebenszyklus heterogene Ablagerungen, sogenannte Drusen, entwickelt. Diese basale Störung führt zu lokaler mechanischer Heterogenität und letztlich zu einer Reduktion in Funktionalität auf Gewebeebene. Parallel dazu unterliegt das postmitotische retinale Pigmentepithel (RPE) einem natürlich auftretenden Zellverlust, welcher einen Gewebeumbau zufolge hat und schlussendlich zu einer Störung des lateralen Kräftegleichgewichts in dem einschichtigen Gewebe führt. Da zurzeit die Einschätzung der individuellen Anfälligkeit für die Entwicklung eines pathologischen Zustands überwiegend auf genetische Prädispositionen beschränkt ist, könnte eine mechanobiologische Aufklärung der basal oder lateral induzierten Störungen des Kräftegleichgewichts wertvolle neue Erkenntnisse liefern.

In dieser Arbeit habe ich ein dynamisches Poly (ethylenglycol) (PEG) basiertes Hydrogel entwickelt, welches durch dessen licht-steuerbare Festigkeit und Topografie-Änderungen die Substratänderungen in Zellulären Umgebungen nachahmen kann. Die Lichtempfindlichkeit des Systems wird durch das Einbinden einer ortho Nitrobenzol (oNB) Gruppe im das Hydrogel Netzwerk ermöglicht, welche bei Bestrahlen mit UV-Licht einen irreversiblen Bindungsspaltung unterläuft. Dies ermöglicht einen hohen Grad an Kontrolle über die Dosis, Frequenz und Form der bestrahlten Region. Mit dieser Plattform habe ich die bedarfsgesteuerte topographische Störung ausgereifter einschichtiger hiPSC-RPE zur Nachahmung mittlerer und großer Drusen untersucht. Durch die Quantifizierung morphometrischer Parameter und zellulärer Traktionskräfte konnte ich eine ausgeprägte Abhängigkeit in der kollektiven Reaktion zu Defektgröße und -abstand nachweisen. Zur Untersuchung lateraler Störungen des Kräftegleichgewichts integrierte ich photoresponsive Mikrogele über hybride Adhärenz-Verbindungen in das Kräftenetzwerk der RPE. Die bedarfsgesteuerte Erweichung dieser Phantomzellen löste eine biphasische Reaktion auf Gewebeebene aus, die sich in einer Reorganisation des Aktin-Zytoskeletts und einer Verformung der Zellkerne äußerte.

Insgesamt demonstriert diese Arbeit die Anwendung einer photoresponsiven Hydrogel-Plattform, die eine präzise räumliche und zeitliche Kontrolle über mechanische Eigenschaften auf Gewebeebene, wie zu Beispiel Topografie und Organisation, ermöglicht. Sie stellt damit ein vielseitiges Werkzeug zur Untersuchung mechanobiologischer Aspekte, insbesondere dynamischer Zell-Matrix- oder Zell-Zell-Wechselwirkungen, bereit.

I. Introduction

1. Mechanobiology

At the interface of biology, physics and engineering, the interdisciplinary field of mechanobiology elucidates how mechanical forces shape cellular behavior, tissue architecture and disease progression. However, the field of mechanobiology has gone a step further and formed an amalgamation which investigates how cells sense and transduce mechanical cues deepening our understanding of key processes such as cell migration, differentiation and tissue remodeling. A major contributor of the advancements is the development of versatile engineered biomaterials and biophysical tools that enable precise modulation of cellular environment across length scales ranging from sub-cellular, over single cell to tissue level[1–4].

Balancing forces: tissue level mechanics

Multicellular life unfolds within a mechanically active microenvironment, where adhesion is not a passive anchor but a dynamic, force-dependent process. Intercellular contacts are sites of continuous mechanical negotiation, where tensile forces generated within cells meet resistances imposed by neighboring cells and the extracellular matrix (ECM), producing a dynamic equilibrium that governs cell shape, tissue architecture, and ultimately cell fate. Understanding how this equilibrium is established and maintained has become one of the central questions of modern cell biology and mechanobiology[5,6]. To understand emergent tissue mechanics, it is instructive to first examine the fundamental building block of each tissue. At single cell level Ingber et al. have described the concept of tensional integrity, in short tensegrity, which provides a foundational framework to describe the balance of contractile forces generated by actomyosin filaments with compression-bearing elements such as microtubules and intermediate filaments[7]. Thus, the mechanical equilibrium of a cell is the sum of the forces generated by the cytoskeleton network exerted on and experienced from the surrounding microenvironment through cell-ECM and cell-cell adhesion[7] (**Figure 1** A).

When cells assemble into tissues, tensegrity extends beyond the single-cell level and becomes a collective phenomenon. Forces are transmitted to the surrounding microenvironment through cell-ECM adhesions and propagated between individual cells through cell-cell adhesion sites connecting cells into an active force network (**Figure 1** B). Despite their distinct molecular compositions and localization, both adhesion types share a common architecture, where an extracellular adhesion domain couples to an intracellular mechanosensitive unit that subsequently links the adhesion complex to the cytoskeleton. This arrangement enables a mechanical feedback loop in which contractile forces drive conformational changes in the mechanosensitive units, promoting additional cytoskeletal recruitment and adhesion clustering. The resulting growth of the adhesion site redistributes forces and re-regulates the rate of further conformational changes,

closing the feedback loop that couples cytoskeletal tension to adhesion maturation[8,9]. In this way, adhesion complexes act not merely as a structural linker but as active mechanical transducers, converting mechanical input into biochemical signals that feed back to reinforce or remodel the adhesion sites themselves[9].

Furthermore, each tissue operates within a preferred range of mechanical properties, which it actively establishes during development, maintains in homeostasis and restores in response to perturbation[10]. This concept of mechanical homeostasis reflects the idea that tissues are not passive structural materials but dynamic systems that sense and respond to mechanical cues to preserve their integrity and function[10]. Already during development, cells and tissues generate, transmit and respond to mechanical forces which have emerged as an integral part of morphogenesis with tissue and substrate stiffness and stress patterns providing instructive cues that influence cell fate and tissue architecture[10–12]. Mature epithelia demonstrate how to maintain the homeostatic state by continuous coordination of cell division, extrusion and shape changes. This turnover preserves the internal tissue tension and barrier function despite constant external mechanical challenges[13]. With ageing, the mechanical equilibrium of tissues shifts as external cues like matrix stiffness and porosity change and internal compensatory mechanisms like cytoskeleton organization loses its ability compensate and restore the homeostatic state. This slow but continuous breakdown of the mechanical homeostasis contributes significantly to the functional decline characteristic of aged tissues[14–16]. In disease, the mechanical homeostasis is frequently disrupted before pathology is diagnosed. A prime example is stiffening, which is a hallmark of fibrosis but also a permissive factor in cancer progression. Another example is the loss of epithelial tension, which can act as an indicator of inflammatory or degenerative conditions[17–19].

Dissecting the specific physical parameters through which the ECM exerts these instructive cues has therefore become a central focus of mechanobiology research. A direct parameter to investigate is ECM stiffness[20], where it has been shown that different tissues exhibit characteristic stiffnesses, ranging from brain (~100 Pa) over muscle (~12 kPa) to cartilage (~1-10 MPa)[21–24]. Recapitulating the right tissue environment and initiating correct feedback loops is essential for in vitro cell culture as a substantial body of work has shown that matching the native stiffness of the respective tissue is important for in vivo relevance in either drug response[25], differentiation[26] or general functionality[1]. Advancement in the field of mechanobiology lead to the realization that, beyond elasticity, the contribution of viscous terms to the force balance of tissues is essential as it was shown that a loss of elasticity and the subsequent loss in dynamic force adaptability is a driver in disease progression[1,27,28] Additionally, the ECM curvature influences cellular organization and behavior[29,30], regulating cell morphology, polarity and function as curved surfaces generate anisotropy in the tissue through varying the stress field and inducing changes in membrane tension which invoke a cytoskeleton reorganization response[31,32]. The effect of curvotaxis was reported by Pieuchot et al.

highlighting the importance of the force transmission from FA, over the actin cytoskeleton into the nucleus for cells to sense and respond to curvature[33].

Similarly, efforts to investigate the force transmission through cell-cell junctions in vitro have focused on measuring the tensile forces of singular cadherins and junctions. Through Förster resonance energy transfer (FRET) based tension sensor, Borghi et al. have shown that the cadherin cytoplasmic domain is under 1-2 pN constitutive load on average[34,35]. However, single-molecule experiments demonstrated that a-catenin unfolded the cryptic vinculin-binding site ~5 pN[36,37], highlighting the role of actomyosin force generation on junction stability[35]. Despite these molecular insights, only a limited body of work has attempted to recapitulate cadherin-mediated contacts in engineered environments. In 2D, cadherin extracellular domains have been conjugated on hydrogels to probe cadherin-dependent rigidity sensing and its downstream consequences for cell morphology and cytoskeletal organization[38], while in 3D hydrogels co-presenting the N-cadherin-derived HAVDI motif alongside RGD have revealed that cadherin ligation actively modulates ECM stiffness interpretation and stem cell fate commitment[39,40]. Overall, these examples highlight the significance of adherens junctions for tissue level mechanotransduction and the gap that remains between the current reductionist approaches and recapitulating the complexity of native cell-cell contacts[35,37].

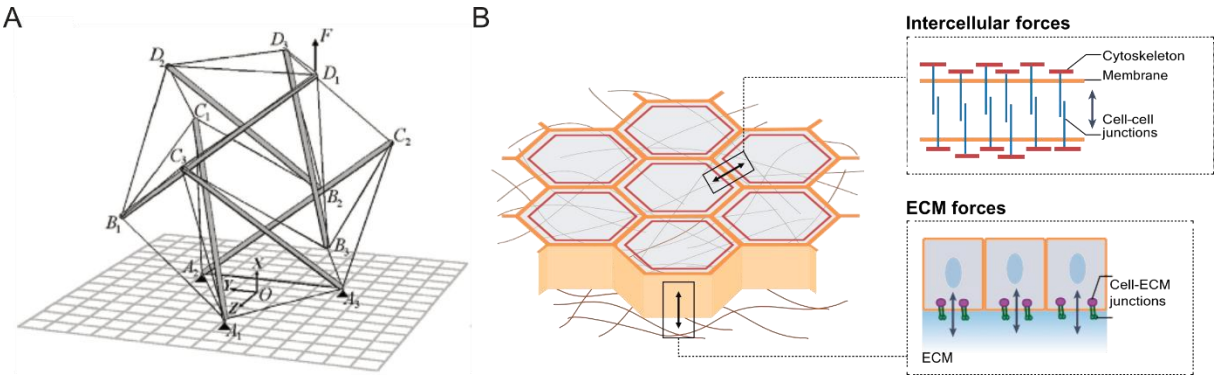


Figure 1: Cellular tensegrity and tissue-scale mechanical homeostasis. *A) Tensegrity model in a round configuration, anchored to the substrate (grey grid) and under applied force at node D_1. Adapted from Ingber et al.[7] B) Tissue-scale mechanical homeostasis is governed through the balance of intercellular and cell-ECM forces. Adapted from Luciano et al.[41]*

2. Epithelia in mechanobiology

Epithelial tissues have emerged as the leading model systems for studying tissue mechanics in vitro, owing to a unique combination of biological versatility and experimental accessibility. In contrast to other tissue types, epithelial tissues exhibit the full repertoire of collective mechanical behavior emerging from cell-ECM and cell-cell junction force transmission, specifically tissue fluidity transition[42], collective migration[43], and active stress generation[44]. Furthermore, these studies are feasible due to the self-organization into coherent, optically accessible tissues under in vitro conditions[45,46], which exhibit polarization, the formation of relevant junctions and

establishment of physiological tension levels[47,48], as well as response to ECM stiffness matching in vivo observations[49].

The extensive research dedicated to epithelial mechanobiology is also highlighted in the suite of well-established methods spanning across the relevant length scale, ranging from FRET-based tension sensors for molecular-scale junction forces[50], over laser ablation for multicellular force inference[51,52], to particle image velocimetry (PIV) for collective flow fields[53], and shape index as a readouts of the solid-fluid tissue state[42]. However, the gold standard for measuring cell-generated forces on a monolayer scale are traction force microscopy (TFM)[54], which assesses the generated forces at the basal interface, and monolayer stress microscopy (MSM), an extension of the previous method, which infers intercellular stresses within a monolayer[55].

As epithelial tissues depend on stable but dynamic adhesive interactions with neighboring cells and the ECM to develop and maintain tissue architecture, a disruption of these interactions can signal onset of pathological development[56,57]. This breakdown of mechanical homeostasis is exemplified in the progression of carcinomas[49,57], inflammatory bowl disease[58], and fibrosis[59] among others, highlighting the relevance in studying disease development and progression with in vitro systems (**Figure 2** A). Overall, in vitro epithelial tissues thus offer a unique window into the mechanics of both physiological tissue homeostasis and disease development and progression.

Cytoskeleton, junctions and extracellular matrix elements

The cytoskeleton serves as the primary determinant of internal order, mechanical integrity and force transmission[60]. The cytoskeleton can be divided into three families of protein filaments, microtubules, intermediate filament and actin filament, each with distinct mechanical properties and biological roles (**Figure 2** B). Although these filament networks form far-reaching, persistent macromolecular structures, their macromolecular components are in a state of constant dynamic flux[61–65].

Through specialized adhesion sites the intercellular cytoskeleton connects to the surrounding microenvironment. The adhesion sites can be characterized by their location into lateral cell-cell and basal cell-ECM junctions. At the lateral cell-cell interface epithelia junctions are arranged in a defined order, with tight junctions forming the most apical seal, followed by force-active adherens junctions, stabilizing desmosomes and finally gap junctions closer to the basal side. At the basal interface actin-linked cell-matrix junctions and hemidesmosomes are found.

The actin cytoskeleton plays a central role in cellular force generation

Actin filaments assemble from globular actin (G-actin) subunits either by passive diffusion or active polymerization through nucleators assembling into a linear double helical filament actin (F-actin). F-actin is not organized as a singular network but appears as multiple architecturally and functionally distinct arrays tailored to specific mechanical tasks[60]. A lateral actin belt runs beneath the plasma membrane and connects to the

cadherin-based cell-cell adherens junctions, providing the structural backbone for epithelial cohesion and lateral force transmission between neighboring cells. The apical and basal actin cortices maintain mechanical homeostasis through cell-cell and cell-ECM adhesion respectively. Furthermore, the apical cortex supports epithelial polarization through the formation of microvilli[66,67], while the basal cortex can form specialized structures to support epithelia organization[68] (**Figure 2** B). The primary role of F-actin is force transmission[69] and generation[70]. Contractile force is produced through the interaction with myosin II, driving ATP-dependent filament sliding. The resulting actomyosin contractility is transmitted into the surrounding environment through cadherin-based cell-cell junction and integrin-mediated cell-ECM adhesion sites. This continuous mechanical linkage through which internally generated forces are transmitted also relay forces inwards connecting to the nucleolus via the linker of nucleoskeleton and cytoskeleton (LINC) complex[71–73].

The keratin cytoskeleton protects the monolayer from external forces

Keratin intermediate filaments are epithelia specific members of the broader intermediate filament family and assemble through spontaneous coil-coil interactions of two heterodimers, one type I and one type II keratin. These dimers bundle into staggered tetramers, which further grow through helical packing into flexible filaments[60]. The keratin network forms a continuous, pan-cytoplasmic scaffold that is spatially organized along a cell-periphery-to-nucleus axis, ending in a cage surrounding the nucleus[74,75]. This spatial organization is tightly coupled to adhesion, with keratin filaments anchored to desmosomes at cell-cell contacts and to hemidesmosomes at the basal cell-ECM interface, integrating the keratin network into a transcellular mechanical continuum that spans the entire epithelial sheet[60,75] (**Figure 2** B). The primary mechanical role of this network is not force generation but rather elastic resilience and resistance to large deformation. It allows epithelial cells to withstand and dissipate large mechanical stresses without suffering permanent deformation[75,76].

Adherens junctions are essential in active intercellular force transmission

Homophilic, calcium dependent cadherins, such as E-, P- and N-cadherin are found in epithelial adherens junctions and confer strong intercellular attachment through extracellular domains[60]. The cytoplasmic domain of cadherins interacts with p120-catenin and β-catenin which in turn recruit α-catenin that binds to F-actin (**Figure 2** C), thereby interconnecting the actin cytoskeleton of neighboring epithelial cells[56,77–79] (**Figure 2** A). In their mature form, adherens junctions are large protein complexes containing hundreds to thousands of cadherin molecules, packed into dense, regular arrays that are linked on the extracellular side by lateral interactions between cadherin domains, while on the cytoplasmic side, a complex network of catenins, actin regulators, and contractile actomyosin bundles cluster the cadherins and link the junction to the actin cytoskeleton[79].

Cadherin complexes act as central mechanotransducers as mechanical tension alters the conformation of key proteins such as α-catenin, which shifts from a folded to an extended state when actomyosin contractility increases, thereby exposing a cryptic vinculin-binding site[36,37,60]. Vinculin recruitment amplifies the recruitment of actin to the junction and reinforces the linkage between cadherins and the cytoskeleton, effectively tuning junction strength and stability in response to mechanical load[80,81]. More recent work shows that cadherins do not merely passively transmit forces but actively regulate junctional fluidity and tissue-scale mechanics, for instance through the formation of ordered nanoclusters that control how cadherins are anchored to actin and how cell–cell contacts remodel under stress[80,82]. Across epithelia, these mechanisms allow cadherin-based junctions to sense, integrate, and adapt to mechanical cues, thereby playing a central role in the maintenance and active regulation of tissue homeostasis, morphogenesis, and emergent tissue-level mechanical properties[80,81].

Desmosomes mediate strong intercellular adhesion

Desmosomes are structurally similar to adherens junctions but are functionally and mechanically distinct. They contain specialized cadherins, which engage in trans-homolytic binding in the intercellular space and connect intracellularly to the intermediate filament network. Mature desmosomes are highly localized and dense structures located equatorial and connect the cellular keratin network into a mechanical continuous network, which provides mechanical strength to the epithelial sheet[60]. Crucially, FRET-based tension sensor measurements of desmoplakin have directly demonstrated that desmosomes are under negligible tension from cell-generated forces under homeostatic conditions[83]. Only when cells are subjected to external stress that threaten tissue integrity desmoplakin becomes mechanically loaded[84].

Cell-ECM interactions regulate tissue function

Tissues are not made up solely of cells but also contain a remarkable complex and intricate network of macromolecules constituting the extracellular matrix. The matrix is composed of many different proteins and polysaccharides that are secreted locally and assembled into organized meshwork in close proximity with the surfaces of the cells that produce them[85,86]. Epithelial tissues anchor to a highly specialized exceedingly thin[87–89] (tens of nanometer to microns), though flexible matrix called the basement membrane (BM), which is primarily composed of laminin, type IV collagen, nidogen and proteoglycans. This specialized ECM is an important regulator of cell polarity, differentiation, apoptosis and functionality and in the absence of the relevant mechanical and biochemical signaling the tissue can form a non-functional phenotype[56,90].

Laminins act as the primary organizer of the sheet-like structure and plays a critical role in the functional signaling cascade that links the ECM to the actin cytoskeleton and cell-surface receptors[91,92]. Laminins comprise a large family of proteins, each composed of three long polypeptide chains (α, β, and γ) held together by disulfide bonds and arranged in the shape of a cross. These heterotrimers can self-assemble in vitro into a

network, largely through interactions between their heads, although interaction with cells is needed to organize the network into an orderly sheet, planar sheet in vivo[92]. Type IV collagen is a second essential component of mature BM and exists in several isoforms, with three long chain proteins twisting together to form a flexible superhelix. Laminin and type IV collagen interact with other BM components forming a highly crosslinked network which serves the tissue specific function. Changes in the composition and organization of the basement membrane accompany tissue morphogenesis, development, and homeostasis, and even in mature tissues the ECM undergoes continuous turnover through controlled degradation and resynthesis to maintain a healthy, mechanically competent microenvironment[56,90,92]. Cells adhere to their BM primarily through integrin-based adhesion complexes that physically couple the ECM to the actin cytoskeleton and mediate bidirectional mechanotransduction[85,86,91]. Integrins cluster at cell–ECM contact sites and recruit a network of adaptors and signaling proteins that regulate focal adhesion formation, stability, and dynamics in response to mechanical cues[92]. Cell–ECM binding is not a static tether but a dynamic, mechanosensitive interface that integrates local matrix properties with intracellular signaling and cytoskeletal organization to control tissue morphogenesis, homeostasis, and mechanical integrity[85,90,92].

Integrin heterodimers containing the β1 subunit are the transcellular domain in FA[93] and bind to the actin cytoskeleton, like almost all integrins[60] (**Figure 2** D). The mechanosensitive Talin-vinculin complex regulates the dynamical coupling between ECM and actomyosin cytoskeleton, a concept described by Mitchison and Kirschner in 1988 as molecular clutch[93,94]. In the absence of integrin-actomyosin connectivity the clutch is disengaged and no forces are transmitted. However, once the clutch is engaged actomyosin contractility is converted into traction forces exerted on the ECM and polymerizing F-actin advances the leading edge of the plasma membrane forward[93]. Furthermore, FA stability is increased under mechanical load through a catch bond character, where an allosteric activation prolongs protein-protein bond lifetime[93,95–97]. The singular exception to the connection to the integrin-actin connectivity are integrin heterodimers containing the β4 subunit forming transcellular hemidesmosomes which are connected to the keratin cytoskeleton via plectin instead[98–100] (**Figure 2** D).

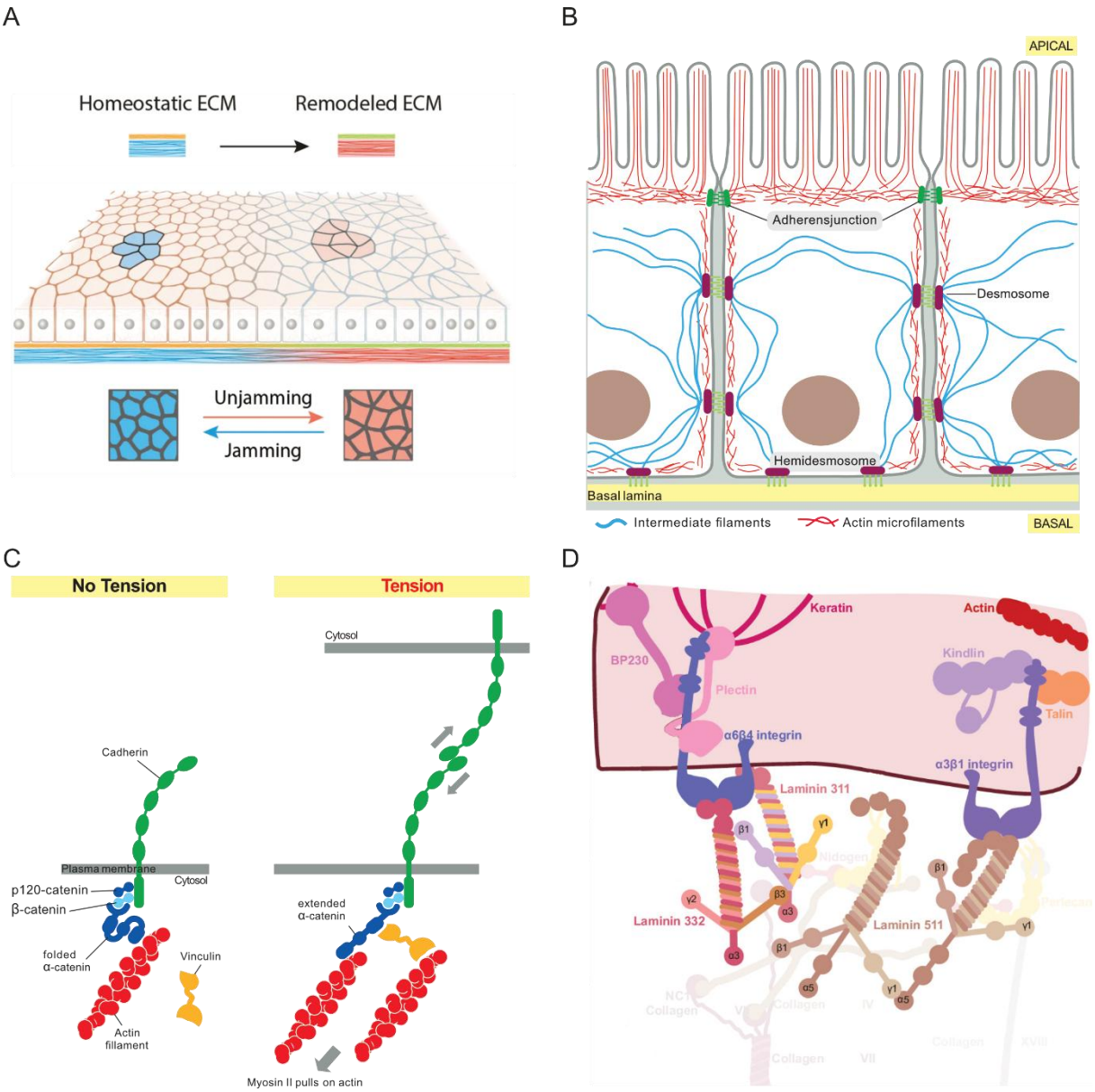


Figure 2: Cellular cytoskeleton and adhesion motives. *A) Simplified rendition of epithelia cytoskeleton, highlighting the actin and keratin networks and their respective cell-cell and cell-ECM junctions. Adapted from Kozyrina et al. [90] B) Adherens junction complex showing the unengaged state and the complex under tension when engaged with cadherin of another cell. B) and C) adapted from Alberts et al.[60] D) Schematic of basal integrin adhesion motives β4 and β1 with their respective ECM laminins and cytoskeletal partners. Adapted from Rousselle et al.[101]*

The retinal pigment epithelium

The retinal pigment epithelium (RPE) is a monolayer of highly specialized, postmitotic cells located between the neural retina and the underlying choroid, forming a critical part of the blood–retinal barrier. RPE cells are typically cuboidal to low columnar in shape, with an apical surface facing the photoreceptor outer segments and a basal surface in close contact with the underlying Bruch's membrane, which in turn separates the RPE from the choroidal vasculature[102]. (**Figure 3** A-B) The cells are polarized and tightly adherent to one another, forming a continuous epithelial sheet that helps maintain the structural integrity of the outer retina and control the vectorial transport of ions, metabolites, and waste products across the retina–choroid interface as well as active photoreceptor outer segment phagocytosis[103,104]. A recent investigation by Piskova et al. has shown that the ability of the RPE to perform phagocytosis is significantly affected when artificially aged, highlighting the importance of the mechanical homeostasis for physiological tissue functionality[105].

The Bruch's membrane (BrM) is a thin, multilayered extracellular matrix located at the basal side of the RPE and is composed of the internal collagenous layer, the central elastic layer, and the external collagenous layer, and its dynamic composition and ultrastructure are tightly regulated throughout life[106] (**Figure 3** A). Immunohistochemical and structural analyses of the human macula reveal that BrM is enriched in type IV collagen and laminin, which are major components of its basement-membrane-like architecture indicating their importance in maintaining the mechanical and adhesive integrity of this interface[107,108]. Furthermore, BrM structure and composition are not uniform but vary systematically along the visual axis, reflecting the distinct mechanical and functional demands of the macular versus peripheral retina[99,106]. Moreover, a study by Kozyrina et al. has elucidated the importance of specific laminin isoforms on the mechanical homeostasis of RPE in vitro and projecting consequences for phagocytotic function and retinal integrity due to progressive BrM remodeling in ageing[99,105].

Ageing of the outer retina

The highly specialized and postmitotic RPE, unlike most epithelia, does not undergo continuous self-renewal[109–111], rendering it vulnerable to a progressive decline in cell density reduction driven by naturally occurring apoptotic events[112]. Nevertheless, the RPE largely maintains a functional state through a series of compensatory mechanisms, both structurally and functionally[112]. With the loss of cell density, the monolayer rearranges and thins, with increased frequency of hypertrophic cells[112] (**Figure 3** C). Furthermore, on a cellular scale the actin cytoskeleton remodels, with the formation of intracellular stress fibers and disruption of the lateral actin belt[113]. Functionally the increased load in metabolic and visual demands is compensated through an increase in double nucleation although it has been shown that a progressive decline in phagocytotic efficiency is unavoidable[114–117].

Along with these cellular changes, the underlying Bruch's membrane undergoes its own age-related deterioration, characterized by thickening, increased lipid and protein deposition, and altered crosslinking of collagen. These drastic changes impair diffusion between the choroid and the RPE and contribute to the development and progression of age-related macular degeneration[102,105,106,108,118] (AMD). A particularly prominent and well documented pathological phenotype of this ageing progress is the appearance of heterogenous lipoprotein deposits between the RPE and Bruch's membrane, so called drusen[106]. While small drusen in early physiological ageing pose little challenge to tissue organization and function, their growth over time progressively disrupts the structural and functional integrity of the RPE[119–121] (**Figure 3** A-C).

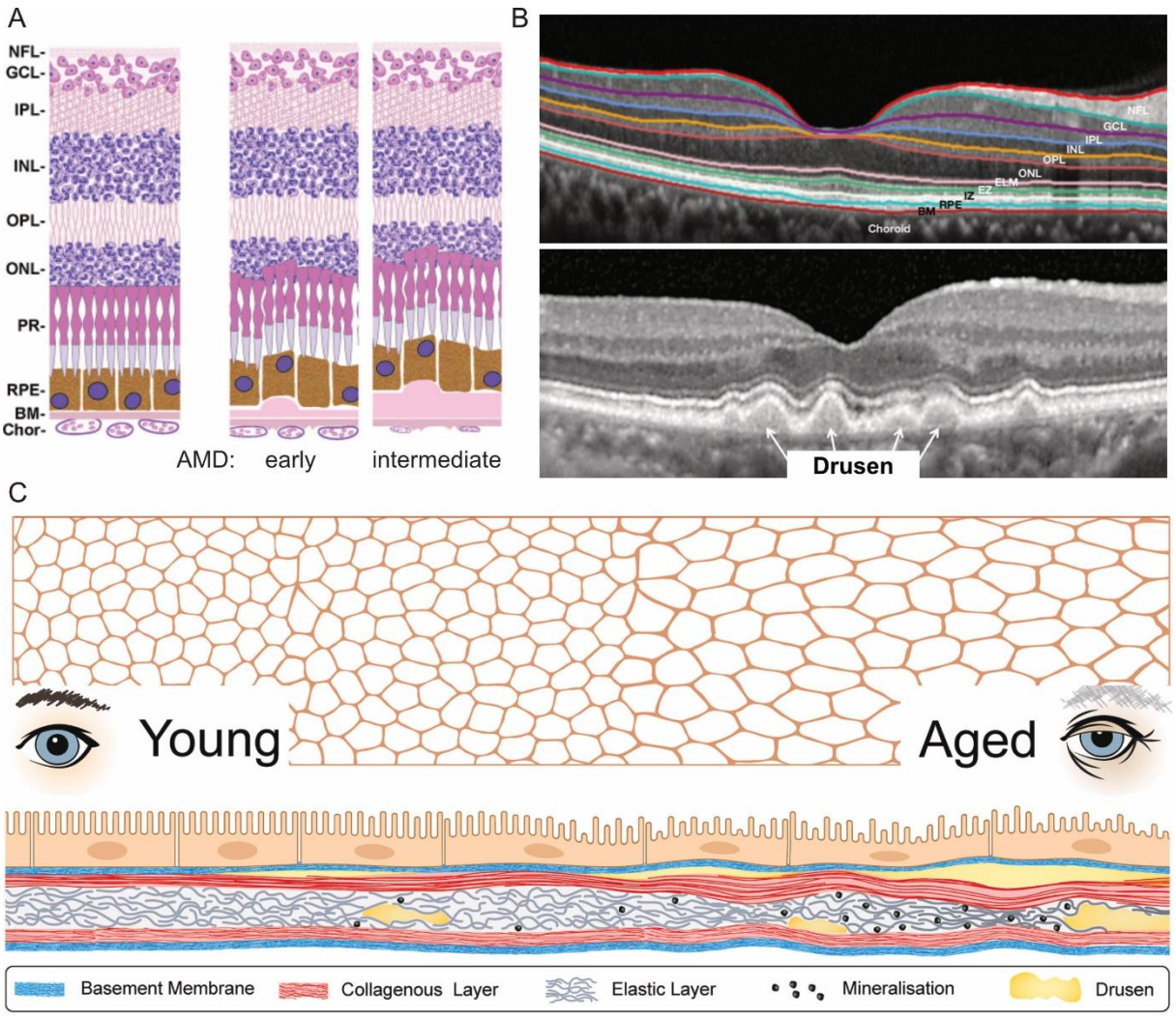


Figure 3: Changes of retinal architecture in ageing. *A) Illustration of retinal architecture with the layers: nerve fiber layer (NFL), ganglion cell layer (GCL), inner plexiform layer (IPL), inner nuclear layer (INL), outer plexiform layer (OPL), outer nuclear layer (ONL), photo receptors (PR), retinal pigment epithelium (RPE), Bruch's membrane (BM), choroid (Chor). In physiological state and during early and intermediate age-related macular degeneration (AMD) adapted from Malek et al.[122]. B) Image of Optical Coherence Tomography (OCT) scan of a healthy retina highlighting the different layers adapted from Ong et al.[123] (Top) and OCT scan of a retina with drusen development adapted from Istanbul Retina Institute[124] (Bottom). C) Schematic representation of the change in organization of the retinal pigment epithelium (RPE) and the underlying Bruch's membrane (BM), adapted from Piskova et al.[105]*

3. Dynamic hydrogel systems for tissue engineering

Hydrogels as substrate mimics

Cells in vivo do not reside on a fixed, inert surface but instead experience a continuously evolving mechanical and biochemical environment shaped by the dynamic ECM. ECM is not merely a passive scaffold; it is remodeled, stiffened, and softened over time through developmental transitions, wound healing, and tissue homeostasis, and these changes are tightly coupled to cell proliferation, differentiation, and function[26,125]. Conventional static cell culture systems have underscored that substrate stiffness, topography, and adhesion ligand density profoundly influence cell morphology, cytoskeletal organization, migration, and differentiation, a phenomenon now often framed as mechanosensing or mechanotransduction[26,126,127]. These realizations have driven the development of dynamically tunable cell culture platforms that allow the mechanical properties, ligand presentation, or topography to be changed in situ, thereby recapitulating key aspects of the native microenvironment more faithfully than static materials such as polystyrene or fixed-stiffness gels[128–130]. Early work by Engler et al. demonstrated that the elastic modulus of a synthetic substrate can directly steer stem cell lineage specification, with softer substrates promoting neurogenic outcomes, moderate stiffness guiding adipogenic differentiation, and stiffer ones favoring myogenic and osteogenic fates, highlighting that matrix elasticity alone can act as a potent regulator of cell fate rather than merely a passive support[26]. Beyond stiffness, the biochemical composition of the matrix, such as type of adhesion motive, density, and presentation also plays a decisive role in cell fate and function[131]. Lutolf et al. introduced the concept of synthetic biomaterials engineered to mimic instructive extracellular microenvironments, where the controlled presentation of integrin-binding motifs, growth-factor binding domains, and degradable crosslinks can be used to orchestrate cell attachment, migration, and tissue-like morphogenesis[132]. These studies showed that when biochemical cues are integrated with specific mechanical properties, cells can be steered toward desired lineages more effectively than by either cue alone. Dingal et al. later expanded this idea by demonstrating that insoluble mechanical cues, such as tailored stiffness and ligand presentation in combination with soluble growth factors allows synergistic control of stem cell fate, enabling more precise and robust lineage specification in vitro[133]. These results highlight that conventional cell culture is increasingly viewed not simply as a static biochemical environment but as a tunable mechanical–biochemical interface whose stiffness and ligand landscape can be rationally designed to mimic the in vivo niche. The ability to decouple and then recombine elasticity and biochemical signaling has provided a powerful framework for building more physiologically relevant in vitro systems, from two-dimensional culture substrates to three-dimensional synthetic matrices, in which specific combinations of mechanical and molecular cues are used to recapitulate developmental, homeostatic, or disease-related microenvironments[99,134].

However, these platforms are typically static, whereas the native ECM undergoes time-dependent changes in composition, stiffness, topography and elasticity during morphogenesis, regeneration, and disease progression. This mismatch has motivated the design of materials whose mechanical properties or biochemical cues can be altered during cell culture through external stimuli, enabling the experimental exploration of how sequential or oscillating change of mechanical environments shape cell fate and tissue organization[128,135]. Tibbitt et al. articulated this shift by framing dynamic microenvironments as the "fourth dimension" of biomaterials, emphasizing that the temporal control of stiffness and ligand presentation is as critical as their spatial and compositional design for recapitulating physiologically relevant niches[136,137]. To advance cell culture substrates into the fourth-dimension various dynamic polymer-based platforms for in vitro application were developed[138,139]. By exploiting the ability of synthetic materials to respond to external or internal stimuli through some form of triggering energetic input[136,140] like heat, light[141,142], electrical fields, magnetic fields, mechanical force[143], enzymatic[144] or pH regulation the physiochemical properties of the system can be changed. Although a major restriction on the possible external stimuli is cell viability and non-invasiveness. Application of stimuli responsive material in cell culture can be in form of surface functionalization, thin films, and 2D or 3D hydrogels[140]. Common polymers for dynamic cell culture application are for example the natural ECM component hyaluronic acid[145–147], or the synthetic elastomer poly (dimethyl siloxane) (PDMS), which excels through its transparency and mechanical stability in uniaxial[148] and multiaxial[149] stretching devices as well as topographical deformation platform[30,150]. Furthermore, synthetic hydrogels built from monomer units like poly (*N*-isopropylacrylamide) (PNIPAAm)[151–153], polyacrylamide (PAA)[26,154], or poly (ethylene glycol) (PEG)[155–160] derivates have received a lot of attention due to their high degree of flexibility as bulk properties can be easily controlled through copolymerization of reactive groups or stimuli responsive crosslinkers. Polymerization of synthetic hydrogels depends on the cell compatibility of the monomer, the reaction environment and kinetics. While step growth reactions like Michael-type or Click reactions have lower chain growth kinetics the necessary polymerization conditions are milder[161,162]. On the other hand, free radical polymerization initiated by either photo initiator or redox pair exhibits a harsher reaction environment but quicker chain growth[163,164].

Photo-responsive hydrogels

Among the most widely used dynamic platforms are photodegradable and photo-responsive hydrogels, in which crosslinks or tethered bioactive ligands are engineered to be cleaved or rearranged upon illumination, allowing precise spatiotemporal control over stiffness, porosity, and integrin-binding site availability[128,135,135]. Such systems can be used to mimic processes such as matrix softening during development or the progressive stiffening associated with fibrosis, and to probe how cells respond to acute or gradual changes in mechanical cues rather than to a single, constant stiffness[26,127,165,166] (**Figure 4**).

Photo-responsiveness can be incorporated into hydrogel platforms through the incorporation of a photolabile crosslinker, which can be triggered by exposure to a light source or laser with a certain wavelength to undergo a conformation change. The most common light responsive crosslinkers in cell-culture application are based on one of three chemical moieties[167–169], azobenzene, spiropyrane and ortho-nitro benzyl (oNB). Azobenzene-based compounds can undergo a photo triggered cis-trans conformation changing, allowing fast control over adhesion sites or substrate stiffness or topography[170–173]. The application of this system is limited by incomplete photoconversion[174] and low thermal stability of the cis isomer[175,176] (**Figure 4** A). The spiropyran moiety undergoes a reversible ring opening reaction when illuminated, cleaving the C-O bond and entering a zwitterionic open confirmation[177,178]. When incorporated in a hydrogel the dynamic nature enables precise and large-scale control over substrate topography. However, the reversibility is sensitive to environment conditions and limited by cycle number, as the reversibility is prone to degrade over time[179] (**Figure 4** B). The third option, ortho-nitro benzyl-based compounds differ from the previous examples as it undergoes an irreversible degradation upon excitation. While losing the ability of oscillatory probing the advantage in hydrogel application lies in that no continuous illumination is needed to induce lasting material change[135,168,169] (**Figure 4** C). The mechanism of the UV induced photocleavage of the oNB moiety is not fully elucidated but proposed and investigated mechanisms follow a multi-step process with extensive research done by Wirz et al. and in short follows five steps. Initially the nitro group gets photoactivated and enters and reactive triplet state[180]. In the second step the free radicals undergo hydrogen transfer. The third step the compound either undergoes a proposed rearrangement with the compound losing the diradical character and aromatic ring[181] or according to Fink et al. enters a transition state exhibiting an O-centered radical at the nitro group and a C-centered radical at the benzyl position[182]. The product of the fourth step matches again with both reaction pathways resulting in a five membered ring structure, resulting from a nucleophilic attack or radical recombination reaction respectively. In the final fifth step the isoxazole decomposes, eliminating the ether[183–185], ester[181,186,187], amide[188], or amine[187] group and leaving a nitroso group and carbonyl group on the aromatic ring.[182,189]

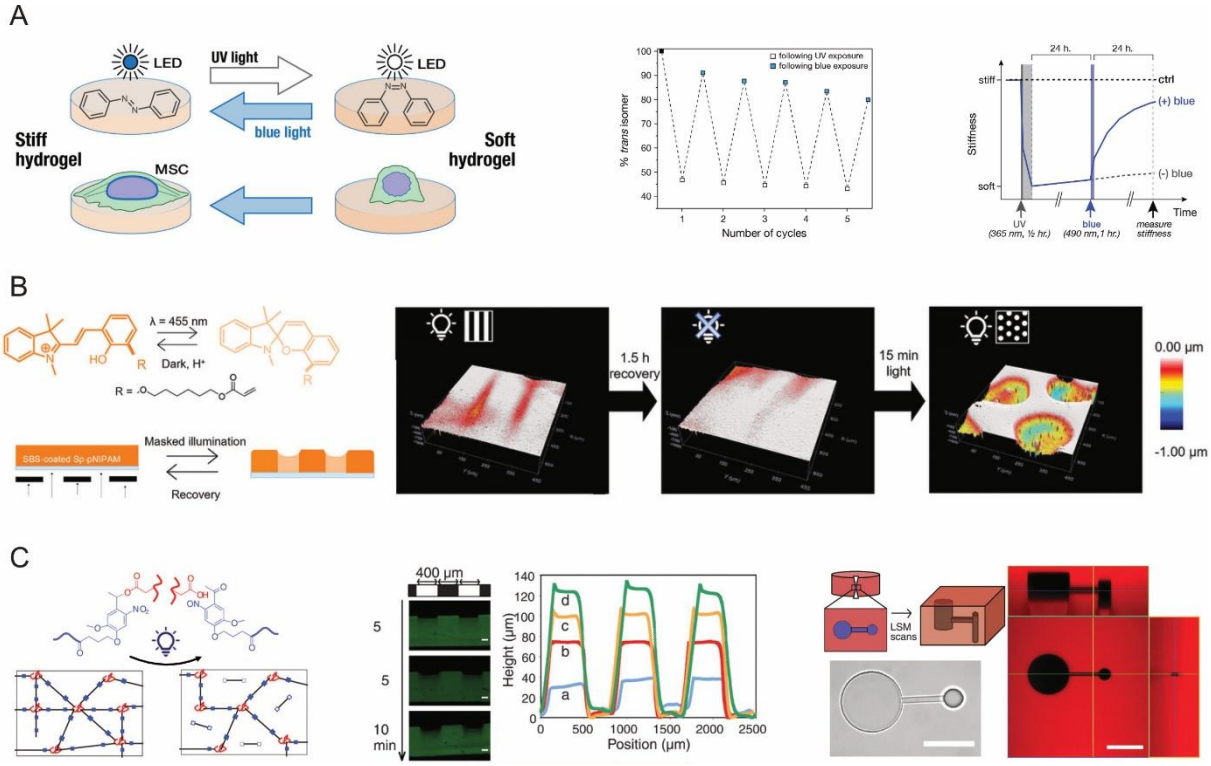


Figure 4: Overview of common photo-responsive molecules and their application in hydrogel systems to facilitate dynamic cell culture environments. *A) Azo benzene based crosslinker undergoes conformational change from trans to cis when illuminated with UV light and reverses the change when illuminated with blue light, enabling a repeatable on-demand change of substrate stiffness. Adapted from Lee et al.[190] B) Spiropyrane-based crosslinker undergoes ring closing reaction when illuminated and recovers over time back into the open confirmation, allowing for the topographical patterning through localized hydrogel collapse. Adapted from Bril et al.[177] C) Degradation of an ortho nitro-benzyl based crosslinker by illumination with UV light facilitating the localized breakdown of the hydrogel and enabling topographical patterning or internal hollowing. Adapted from Kloxin et al.[191]*

Protein functionalization of synthetic polymer-based hydrogels

Attaching protein coatings to the surface of synthetic polymer-based hydrogels is essential to overcome their inherent protein repellent nature and facilitate cell adhesion. The process requires consideration of the polymerization chemistry as this dictates which bio-functionalization strategy is both feasible and practical[192–194]. Step-growth polymerized hydrogels hold an inherent advantage in this regard, as after the formation of the hydrogel unreacted functional groups at the surface of the hydrogel can act as attachment sites in a direct post-functionalization step circumventing the need for additional surface modification[195]. On the other hand, free radical polymerization-based hydrogels are generally regarded as inert, protein repellent materials which require post-functionalization to add protein reactive groups[196,197].

A strategy to circumvent possibly complex post-functionalization entirely is the direct incorporation of peptide motives or full-length protein into the synthetic hydrogel. By covalently coupling cell adhesion motive to reactive polymer precursors, they are directly and evenly incorporated into the hydrogel network. However, for 2D applications where only a surface coating is necessary a large percentage of adhesion motives are not accessible for cell attachment[198–203].

A widely used method employs the hetero-functional crosslinker sulfo-SANPAH[204–207] which, when illuminated UV light, forms a highly reactive nitrene or a seven ring didehydroazepine species[208–210] driven by the elimination of nitrogen. The activated crosslinker readily reacts with double bonds, inserts into C-H or N-H bonds and reacts with nucleophiles establishing a covalent bond with the hydrogel polymer chain. However, the crosslinker has an intrinsic drawback due to the hydrolytic sensitivity of the NHS ester, leading to a rapid degradation under protein attachment conditions requiring precise timing between surface activation and protein incubation. Furthermore, the amine reactive group freely reacts with available amine groups on the protein resulting in non-specific reactions leading to an unoriented attachment and possible blocking of the adhesion site.

In contrast to the uncontrolled whole sample functionalization of the previous method, spatially controlled surface activation can be achieved through the incorporation of a photolabile moiety into the hydrogel. Defined illumination uncages functional group from photolabile protection group, which subsequently can be accessed by hetero-functional crosslinkers in a post-functionalization step allowing a variety of adhesion chemistry. Missirlis et al. established the co-polymerization of caged 2-aminoethylmethacrylamide and demonstrated the spatial control over the uncaging by illumination with a digital micromirror device. Furthermore, they highlighted the compatibility with an assortment of hetero-functional crosslinkers e.g. NHS-PEG-Biotin, NHS-PEG-alkyne, NHS-PEG-azide, and NHS-PEG-Maleimide[211], enabling patterning of peptides and full ECM proteins. In a complementary approach Yamamoto et al. passivated a cell compatible hydrogel with photocleavable PEG chains, such that spatially controlled UV illumination creates a defined area viable for cellular adhesion[212]. Critically, both strategies confine cell accessible area on the hydrogel surface enabling confinement or migration studies of single cells or clusters.

A strategy requiring no copolymer utilizes the generation of a secondary amine-reactive network at the surface of the bulk hydrogel. By swelling the reactive monomer into the established gel and subsequent polymerization of a thin layer at the surface the interpenetrating secondary network facilitates protein adhesion without altering the bulk properties of the primary network. Commonly acrylic acid N-hyroxysuccinimide ester (NHS-AA) is used as the amine reactive monomer and while the method is aimed to be more reliable than sulfo-SANPAH-based approach it suffers from a similar hydrolytic degradation under protein attachment conditions and non-specific binding[205,213–215].

A popular strategy to circumvent the need for post-functionalization is the direct co-polymerization of small hetero-functional molecules which exhibit an amine reactive and a polymerization accessible group. The copolymerization of oxidation of N-hydroxyethyl acrylamide into bulk hydrogels provides aldehyde groups throughout the gel which can be incubated with protein and form covalent Schiff base conjugates[216–218]. Epoxy groups can be incorporated by copolymerization of glycidyl methacrylate (GMA) which reacts through

a ring -opening reaction with thiol, amine and hydroxy groups, offering a broad scope of possible protein binding reactions[219–221]. Lastly, carboxylic acids are a common rest group in synthetic polymer-based hydrogels and can be easily accessed through a well-established activation route. Furthermore, as the activation of the substrate is facilitated by a water soluble carbodiimide derivate a major drawback of hydrolytic degradation of the amine reactive group can be circumvented[222–225].

Microgels in tissue engineering and mechanobiology

A central question in mechanobiology is how to measure and exert forces within a tissue in a non-invasive manner. A prominent approach is the embedment of oil droplets into the tissue, measuring the deformation of the microdroplets and inferring the internal forces in this way[226,227]. The method can be expanded with oil droplets loaded with ferromagnetic particles to enable active and directed force balance disruption from within the tissue[228–230]. However, the approach is limited in size control of the embedded droplets, and the liquid incompressible nature prevents isotropic deformation and the covalent binding of adhesion molecules resulting in mechanical limitations.

Microgels are defined as micrometer scale hydrogels and have emerged as a key building block for mechanobiological and tissue-engineering application as their ability to recapitulate essential aspects of in vivo environments while maintaining precise control over structural and mechanical cues[231–235]. The bottom-up fabrication of microgels can be broadly divided into extrusion[236], emulsion[163,232,237,238] and micro molding[239,240] and photolithography[241,242]-based strategies[241,243,244]. Especially, emulsion based microfluidic approach has emerged as a powerful manufacturing tool in the generation of monodisperse microgels with precise control over size, shape and composition in a high throughput necessary for tissue engineering applications[233,245] (**Figure 5** A). Recapitulating in vivo environments of different tissues requires fabricated materials to mimic a wide range of mechanical stiffnesses, ranging from soft tissues such as brain and adipose tissue (<1 kPa) to stiffer tissues such as cartilage and bone (>100 kPa). Among the building blocks most commonly employed in microfluidic microgel fabrication, natural-derived polymers, such as alginate[246–248] and HA[249,250], hybrid materials, like gelatine methacrylate[251,252] (GelMa), and synthetic polymers including PAA[253,254] and PEG[255–257] cover a broad mechanical range (**Figure 5** B).

Cell mimicking microgels as a tool for tissue engineering

As previously described, tissue cohesion is largely governed by active cell-cell and cell-ECM adhesion and force exchange. External stimuli are transmitted as mechanical inputs through mechanotransduction complexes to the cytoskeleton and subsequently to the nucleus, where they are interpreted and translated into cellular mechanical responses. On a collective level, the balance between these mechanical input and outputs gives rise to tissue homeostasis as an emergent phenomenon. Cell-mimicking microgels have emerged as a promising tool to measure this dynamic environment, enabling the passive and non-invasive readout of tissue-generated internal forces during mechanical

homeostasis[234,236,253,258–260]. In three-dimensional tissue models such force sensors have been established to investigate developmental processes[254], general tissue mechanics[236,253,258,261], and highly specific processes like phagocytosis[262] (**Figure 5** C).

For cell-mimicking microgels to actively participate in the dynamic tissue environment an intrinsic stimuli-responsiveness is essential. Furthermore, to transmit the generated forces a connection to the surrounding cells required. The applicable stimuli for microgel-based cell-mimics mirror those established for their bulk hydrogel counterparts, including thermal[263–266], photo[267,268]-, magnetic field[269,270], enzymatic, and pH-based triggers. Compared to other stimuli, photo-responsiveness offers unique advantages in terms of spatial and temporal precision, enabling localized actuation without direct contact and can be achieved through the incorporation of molecular switches such as spiropyran[271], azobenzene[272], or oNB[267] moieties into the polymer network. In contrast to the former examples the oNB group undergoes UV light induced degradation, so that no oscillatory experiments can be facilitated. However, the irreversible bond cleavage can be an advantage, as a singular illumination is sufficient to induce mechanical change and effectively disrupt the local force balance.

Bio-functionalization of microgels

For stimuli-responsive microgels to function as phantom cells, matching the respective tissue stiffness and force generation is insufficient, as the change in mechanical state needs to be transmitted into the surrounding tissue. This requires the bio-functionalization of the inert synthetic polymer-based microgels to enable cellular adhesion. A common approach involves the incorporation of short peptide sequences, such as Histidine-Alanine-Valine (HAV)[273,274], Isoleucine-Valine-Phenylalanine-Lysine (IVFK)[275] and Arginine-Glycine-Aspartic acid (RGD)[276–278] into the polymer network, which mimic cadherin or integrin binding domains respectively. To recapitulate more complex adhesion motives, full-length can be coated on the microgel surface. However, bio-functionalization of these high molecular weight proteins is more complex in comparison with short chain peptides. While ECM mimicking bio-functionalization does not require oriented or surface specific attachment to facilitate sufficient cellular adhesion[279], cell-cell adhesion mimicking proteins require additional effort to preserve their orientation relative to the in vivo state.

Undirected functionalization couples ECM proteins to the microgel surface via amine reactive moieties co-polymerized into the hydrogel network[280,281], such as GMA[282], activated carboxylic acids[283,284], or aldehyde[283,284] groups. Directed functionalization ensures the correct orientation of the cell-cell adherens protein through the specific binding of the histidine tagging motive[38,285,286]. The tag originates from the need for recombinant proteins to be separated and purified[287,288] but for mechanobiological application the reversibility of the common transition metal nickel complex was substituted by cobalt, as the complex could be oxidized in situ[289,290]. (**Figure 5** D)

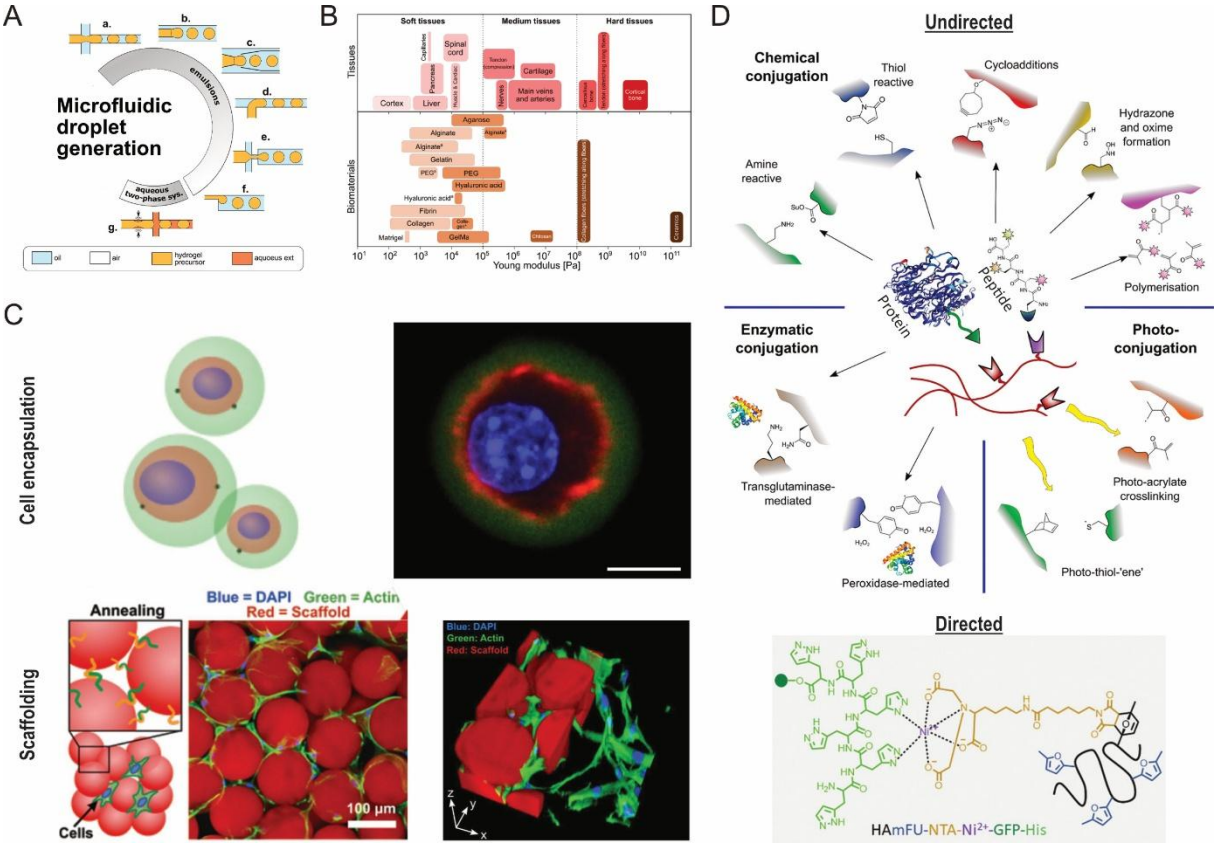


Figure 5: Microfluidic microgel production, functionalization and application in cellular environments. *A) Overview of microgel production via microfluidic droplet generation. B) Tissue stiffness versus mechanical stiffness of polymer materials (* indicates crosslinking under non-physiological conditions and [a] indicates microgels). A) and B) are adapted from Rojek et al.[234] C) Highlighting two common applications for microgels in cellular environments as either cell encapsulation (Top) or scaffolding (Bottom). Adapted from Mao et al.[291] and Rutte et al. [292] respectively. D) Overview of undirected (Top) and directed (Bottom) bio-functionalization pathways. Adapted from Spicer et al. [293] and Kaufmann et al.[294] respectively.*

4. Knowledge gap

Substrate-mediated force balance disruption as a model for RPE disease progression

Despite extensive research into stimuli-responsive hydrogels that facilitate mechanical disruption of homeostasis at the cell and tissue level through substrate stiffening, softening or topographical deflection, a critical gap remains in translating these tools into physiologically relevant disease models. Furthermore, the mechanobiological concept of shape-function relation has been increasingly central to the understanding of tissue homeostasis in ageing and disease. Moreover, in vivo characterization of pathological topographical changes, such as drusen formation in the ageing retina and the associated decline in RPE function, has underscored the importance of substrate-mediated cues in driving disease progression. While epithelial cell lines have yielded important insights into collective cell behavior, monolayer integrity and mechanotransduction, in vitro model systems that recapitulate RPE disease progression in a physiologically relevant model, matching substrate stiffness, topographical disruption and temporal dynamics of disease progression have not yet been established.

Cytoskeleton-specific in monolayer force balance disruption

Despite considerable progress in ECM-mimicking scaffolds, force sensing, and differentiation control, the design of stimuli-responsive microgels capable of engaging lateral intercellular junctions has received little attention. Consequently, due to the lack of fitting tools, the downstream mechanotransduction cascade elicited by such lateral interactions are not being investigated at the mesoscale. This gap is particularly relevant in the context of RPE ageing, where the characteristic hexagonal cell geometry becomes progressively disrupted and cells with irregularly enlarged morphology can be observed. These changes are closely linked to the cytoskeletal reorganization and remodeling, which ultimately disrupts mechanical hemostasis. Furthermore, the collective compensatory response of an epithelial monolayer to such force balance disruption is closely connected to the intercellular junction and associated cytoskeletal network which is mechanically stimulated.

II. Aim

It is well known that in ageing or pathology tissue structure is disrupted and subsequently function declines. Furthermore, current in vitro systems fail to recapitulate fundamental cues such as substrate stiffness, protein environment or spatiotemporal progression, which limits the translatability of the results of these studies. In the context of an RPE model system, this work aims to establish a photodegradable hydrogel platform functional to elucidate how localized mechanical changes influence the force equilibrium present in the monolayer model system.

This thesis aims to establish two complementary experimental models to challenge epithelial mechanics from distinct perspectives. First, a substrate mimicking the dynamic deformations of the ECM will be developed to challenge epithelial monolayers from the basal side and assess their morphological responses. Second, bio-functionalized, cell-sized photodegradable microgels will serve as phantom cells to probe intercellular junction-mediated force dissipation and its contribution to epithelial mechanical equilibrium (Figure 5).

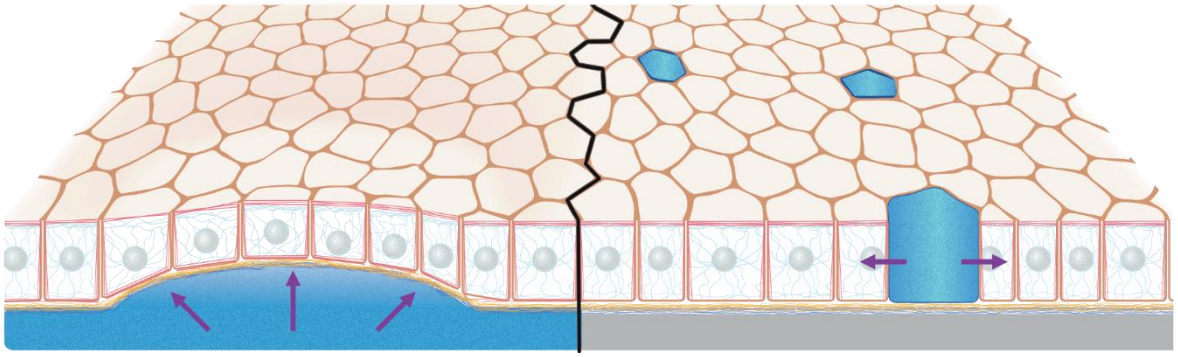


Figure 6: Conceptual overview of the on-demand topographical defect approach on the left and phantom cell approach on the right. *Highlighting with purple arrows the intended directionality of the force balance disruption.*

III. Results

In vivo systems are inherently complex and rarely dedicated to a single function; to maintain tissue homeostasis during ageing or acute insults, cellular collectives rely on multiple compensatory mechanisms. While this ensures that the organism keeps "running", understanding causality in this framework is a difficult challenge. With the long-term aim of reconstituting this complexity in vitro, this thesis contributes to the challenge by developing photodegradable hydrogels that enable on-demand tuning of the mechanical microenvironment, providing a bottom-up platform to dissect epithelial tissue behavior.

1. Synthesis of the photodegradable crosslinker

As the main component of light-controllable hydrogels, the first step in the work was to synthesize a photodegradable crosslinker to include in both ECM-mimicking hydrogels and cell-mimicking microgels. The ortho-nitro benzyl (oNB) moiety is in literature well known for its photolability and synthesis of an oNB-based photodegradable crosslinker (PDC) is published in literature[187,191]. The final synthesis pathway presented in this work combines synthesis steps from both protocols, depending on the results from practical testing, but also incorporates original methodology. The complete synthesis of the photodegradable crosslinker followed both references and started with Williamson ether synthesis where acetovanillone was reacted with ethyl 4-bromobutyrate through a S_N2 nucleophilic substitution mechanism (**Figure 7** Step I). The deprotonation of the starting material **1** was performed in a dimethylformamide potassium carbonate suspension under inert nitrogen atmosphere at room temperature overnight resulting in a deep green colored reaction mixture, which was purified by precipitating the desired product **2** in cold water. After drying compound **2** on pleated filter paper at room temperature, an aromatic nitration was performed (**Figure 7** Step II). The setup of the second reaction step did not follow either protocol. Molecule **2** was dissolved in glacial acetic acid, and the reaction vessel was flushed with nitrogen. Afterwards the solution was cooled with an ice bath as the temperature of the reaction mixture required a temperature range of 6 to 8°C to obtain a mono and ortho functionalized product. Special attention had to be paid to the state of the solution as acetic acid has a freezing point of 16.6°C which could result in the reaction mixture freezing solid. An excess of concentrated nitric acid was added via a dropping funnel under rigorous stirring to ensure even concentration and heat distribution as the nitration reaction is exothermic and has a risk of becoming uncontrollable. After completion of the nitric acid addition the ice bath was removed, and the reaction mixture was stirred for 4 more hours to complete the reaction. The reaction was stopped by precipitating the reaction mixture into cold water and the crude product was extensively washed with water. The crude product was further purified by recrystallization in ethanol to obtain intermediate product **3** as yellow crystalline powder. In reaction step 3 the ketone group was reduced to an alcohol group by sodium borohydride and the process matched both references (**Figure 7** Step III). The reduction agent was specifically chosen

to avoid reducing the nitro group. Compound **3** was dissolved in an ethanol THF mixture, and the reaction vessel was flushed with nitrogen. Under nitrogen counter flow the reducing agent sodium borohydride was added in small quantities. After three days the reaction was stopped by careful addition of water. The solution was periodically acidified to break borate complex with the product and the desired product **4** precipitated as a yellow powder. Both references did not differ in their procedure to cleave the ester group under acidic conditions (**Figure 7** Step IV). The dried intermediate product **4** was suspended in water and excess of trifluoro acetic acid was added to the reaction flask. The reaction mixture was refluxed at 90°C for three hours. In this step, a side reaction occasionally produced a black tar-like substance that could not be separated from the desired product. However, as it occurred only occasionally, and did not significantly affect the outcome, it was not investigated further. In the end step for yielded compound **5** as a fine fellow powder. In step 5 the oNB compound was functionalized with a carbon-carbon double bond to be accessible by free radical polymerization during the formation of the photodegradable hydrogel (PDH) (**Figure 7** Step V). As an interjection, molecule **5** could be obtained commercially, skipping a substantial part of the synthesis pathway. In either case molecule **5** was dissolved in dry dichloromethane (DCM), cooled with an ice bath and the reaction vessel was flushed with nitrogen. To the solution excess amounts of triethylamine were added to deprotonate the hydroxyl group and acryloyl chloride was added slowly via dropping funnel. The reaction was brought to room temperature and proceeded overnight. Afterwards, the reaction was stopped by pouring the reaction mixture into cold water and the crude product was extracted by liquid-liquid extraction with chloroform. As the high reactivity of the acryloyl chloride would result in the functionalization of the carboxylic acid group, the resulting anhydride moiety was broken by dissolving the crude product in an acetone-water solution and stirring it overnight. After removing the acetone and liquid-liquid extraction with DCM, product **6** was obtained as a yellow powder.

The acrylate oNB was attached to a linear PEG linker by activation of carboxylic acid groups and subsequent nucleophilic attack from the amine functionalities of the PEG linker following the procedure by Kloxin et al (**Figure 7** Step VI)[191]. The carboxylic acid activation agent 2-(1H-benzotriazole-1-yl)-1,1,3,3-tetramethyluronium hexafluorophosphate (HBTU) was used to activate the carboxylic acid of intermediate product **6**. After overnight reaction, the reaction mixture was purified in a multi-step process to eliminate, reagents, base and solvent. Furthermore, the crude product was dialyzed to remove unreacted PEG diamine and starting material **6**. The finished acrylate oNB PEG-based PDC was obtained after lyophilization as a brown malleable solid, matching the calculated and published ^{1}H NMR spectrum. The overall molar yield in relation to starting material **1** was only around 1% highlighting the necessity for quantitative reactions with minimal workup requirements.

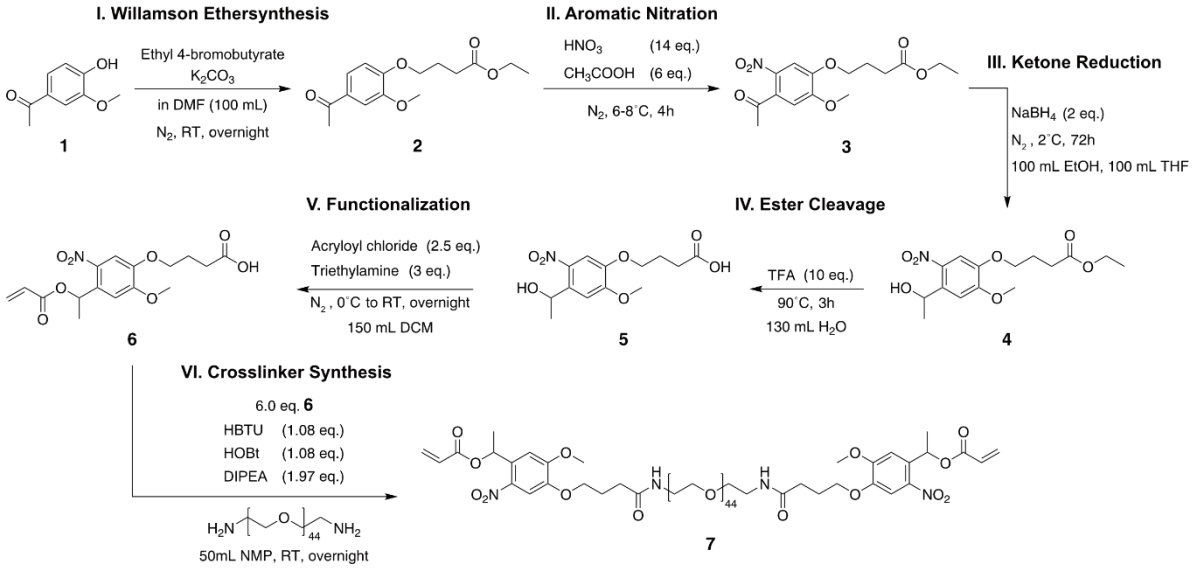


Figure 7: Overview of the complete reaction pathway to synthesize the photodegradable crosslinker (PDC).

Carbamate-based photodegradable crosslinker

The hydrolytic sensitivity of the ester groups in PDC has been reported in the literature and could potentially compromise the long-term feasibility of PDH under cell culture conditions[187]. Structural modifications are possible, but replacement groups are constrained by the need to balance hydrolytic stability, molar absorptivity, and leaving group character while preserving photodegradability. Overall, an optimal replacement to the esters is a carbamate-based connection, as the functional group exhibits a high hydrolytic resilience in acidic and basic environments. This is possible while keeping favorable degradation kinetics as it exhibits a comparable molar absorptivity to the ester-based crosslinker and release of CO_2 during the photocleavage mechanism[187]. To the best of my knowledge no synthesis conditions for an allyl carbamate capped oNB-based photodegradable crosslinker are reported in literature leading to the adaptation of two synthetic conditions of similar functionalities: a one-step reaction of the hydroxy group with an allyl isocyanate was adapted from Kim et al.[295] and Steiger et al.[296], and a synthesis pathway via hydroxy activation reported by LaValley et al[187].

The one-step reaction pathways deprotonated the hydroxyl group of the starting compound and had it attack the carbonyl carbon of the allyl isocyanate. Initial reaction conditions reported by Kim et al.[295] performed the reaction in dichloromethane and at room temperature which yielded a product mixture. The analysis of the crude product by electrospray ionization mass spectrometry (ESI-MS) indicating that the mixture consisted primarily of unreacted starting material **5** and only traces of the desired compound **6a** as well as byproducts **6a'** and **6a''** were present (**Figure 8** and **Table 1**). The reaction conditions were adapted to follow the work of Steiger et al. where the polar solvent tetrahydrofuran (THF) was used to improve the stabilization of the transition state[296]. Finally, a mixture of compounds was obtained and the characterization by ESI-MS showed that the desired product **6a** was only appearing in trace amounts. Notably, the reaction of

the carboxylic acid group of the starting compound with isocyanate derivative **6a'** was observed as a major side reaction. This initial study demonstrated the principal viability of the reaction; however, significant drawbacks, including incomplete conversion and competing side reactions, ultimately made the approach unfeasible.

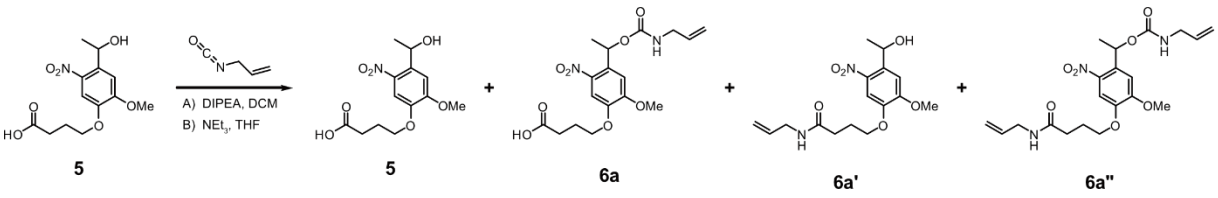


Figure 8: Reaction overview for the two reaction conditions of the isocyanate-based pathway. *Presenting the desired product **6a** and potential byproducts **6a'** and **6a"**. Synthesis was performed by Daniel Gutmann in his role as research intern.*

Table 1: Electrospray ionization mass spectrometry (ESI-MS) table. *Calculated and found masses of the starting material **5**, desired product **6a** and potential byproducts **6a'** and **6a"**.*

molecule	adduct	calculated *M/z*	found *M/z*
5	$[C_{13}H_{17}N_1O_7Na_1]^+$, $[M+Na]^+$	322.0897	322.0908
6a	$[C_{17}H_{22}N_2O_8Na_1]^+$, $[M+Na]^+$	405.1268	405.1276
6a'	$[C_{16}H_{22}N_2O_6Na_1]^+$, $[M+Na]^+$	361.1307	361.1380
6a"	$[C_{20}H_{27}N_3O_7Na_1]^+$, $[M+Na]^+$	444.1741	444.1805

From the prevalence of side reactions, it became apparent that the weak nucleophilicity of the hydroxyl group had to be improved. Thus, in a second approach the hydroxyl group was activated, creating a carbonyl and provided an excellent reaction site for a nucleophilic attack. LaValley et al.[187] facilitated the reaction of the deprotonated hydroxy functional group with 4-nitrophenyl chloroformate compound, yielding an activated carbonate intermediate product, which reacted immediately without purification through the addition of allyl amine. The electron-rich amine would subsequently perform a nucleophilic attack onto the carbonyl carbon of the carbonate-intermediate, resulting in the desired carbamate functional group (**Figure 9**). Analysis of the final product by ESI-MS showed a mixture of products, as the activation agent exhibited reactivity towards the carboxylic acid group of the starting material. Ultimately, the reaction produced **6a'** and **6a"** as main products, while the desired product could not be observed. No further work-up was performed on the reaction mixture, as the low reaction yield, combined with the extensive processing required, was not feasible for PDC preparation.

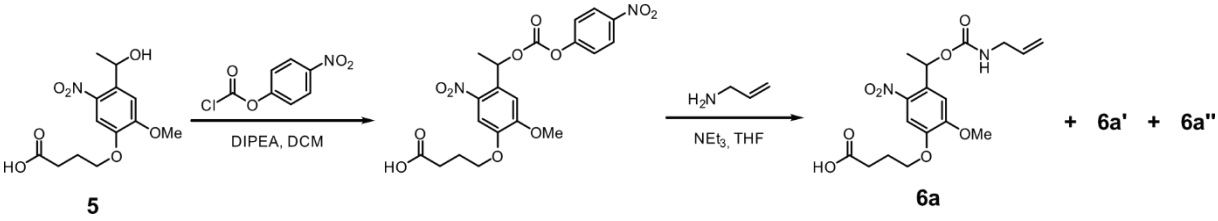


Figure 9: Reaction pathway of hydroxy functional group activation with 4-nitrophenyl chloroformate. *Subsequent reaction with allyl amine, highlighting the desired product **6a** besides byproducts **6a'** and **6a"**. Synthesis was performed by Daniel Gutmann in his role as research intern.*

Due to the recurrence of the side reactions through the acid group, the synthesis pathway was adjusted to use a protected starting material and perform the ester cleavage reaction after the functionalization of the hydroxyl group. Additionally, the hydroxyl group activation compound was exchanged to *N,N'*-carbonyl diimidazole (CDI). The deprotonated hydroxy group would react with the CDI to yield an imidazole carbamate intermediate product, which subsequently reacted with allyl amine. By nucleophilic attack of the amine group, the imidazole was replaced due to its excellent leaving group properties. Lastly, the carboxylic acid group was deprotected by lithium hydroxide cleavage, as the carbamate group is stable in basic conditions (**Figure 10**). The desired allyl carbamate oNB product **6a** was isolated after the two reaction steps with an 84% overall yield, and the purity of the product was determined by ^{1}H NMR. Furthermore, the degradability of the compound was investigated by UV illumination (385 nm, 20 mW/cm^2, 5 min) of 0.5 mg/mL solution in methanol and the degradation product **6b** was identified by ESI-MS ensuring the photodegradability.

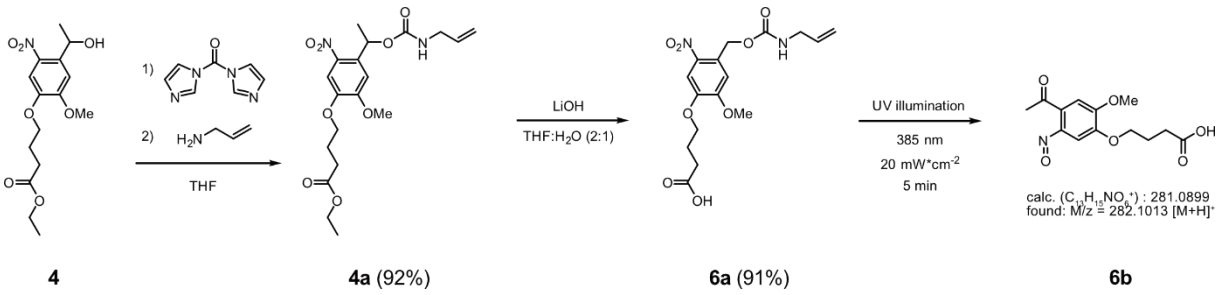
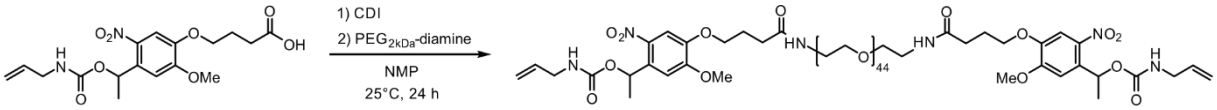


Figure 10: Reaction pathway of the hydroxyl group activation with N,N'-carbonyl diimidazole (CDI). *Subsequent reaction with allyl amine. Subsequent deprotection of the ester to obtain the desired allyl carbamate oNB compound* ***6a****. UV illumination to determine degradability of the carbamate group. Synthesis was performed by Daniel Gutmann in his role as research intern.*

After a synthesis pathway with gram yield of a carbamate-based photodegradable compound was established, the product was used in the final step in the crosslinker synthesis: the bis-functionalization of the linear PEG linker. With the previously observed success of the CDI based coupling reaction an effort was made to improve the original method reported by Kloxin et al. which uses 2-(1H-benzotriazole-1-yl)-1,1,3,3-tetramethyluronium hexafluorophosphate (HBTU) and 1-Hydroxybenzotriazole (HOBt) as coupling reagents to activate the carboxylic acid group and form an amide bond with the amine of the PEG-linker[191]. However, these reagents are difficult to remove during work-up and can influence the application in hydrogel formation and cell culture. The carboxylic acid group of the allyl carbamate oNB compound 6a was activated with CDI forming a reactive acylimidazole intermediate through an intramolecular reaction which eliminated CO_2 and one equivalent imidazole. To ensure a bis-functionalization of the PEG-diamine linker it was added in 0.15 equivalent (0.3 eq. amino groups) stoichiometric deficit resulting in an allyl carbamate-based photodegradable crosslinker (AC-PDC) (**Figure 11**). Overall, the reaction showed a low yield and by ^{1}H-NMR and matrix-assisted laser desorption/ionization time of flight (MALDI-TOF) mass spectroscopy identified a product mixture of unreacted starting material and mono-functionalized PEG linker. In

conclusion, while the feasibility of the approach was demonstrated, further optimization of the reaction protocol would be required to achieve a reliable degree of bis-functionalization, which fell outside the scope of this work.



6a **7a**

Figure 11: Reaction pathway of the allyl carbamate-based photodegradable crosslinker. *Synthesis was performed by Daniel Gutmann in his role as research intern.*

2. A photodegradable hydrogel to mimic ECM ageing of the outer retina

To mimic the topographical changes of the ECM underlying RPE adhesion that characterizes retinal ageing (i.e., drusen formation), I established an RPE model system defined by three parameters: on-demand localized substrate swelling, defined stiffness, and ECM coating. These parameters would ensure a relevant in vitro model which could be exposed to localized ECM deformations and read out the size-dependent effects on tissue morphology mimicking the in vivo appearance of drusen.

Synthesis and characterization of the photodegradable hydrogel

To obtain an on-demand localized swelling of a hydrogel substrate, the acrylate oNB-based PDC was incorporated into a PEG-based hydrogel. When illuminated with UV light the PDC underwent photolytic degradation resulting in a mesh density reduction of the partially degraded hydrogel network and the subsequent influx of water resulted in a topographical deformation (**Figure 12** A). To reliably achieve the partial degradation the degradable aspects of the PDH were balanced by incorporating non-degradable network components during the free radical polymerization. Ultimately, the monomer mixture was composed of predominantly monofunctional PEG-acrylate, which fulfilled the role of a chain-building component and to a lesser extent, the non-degradable crosslinker 8 arm PEG-acrylate. The Aminoethyl methacrylate (AEMA) will be introduced in detail in a later chapter but played an essential role in the bio-functionalization of the PDH. Lastly, in non-degradable hydrogels (NDH), which were employed as control hydrogels, with the PDC substituted by PEG-diacrylate (**Figure 12** B). Once on-demand topographical changes of the desired magnitude could be reliably induced, the hydrogel bulk stiffness was tuned to a physiologically relevant value of 4 kPa[99]. This required balancing degradable and non-degradable crosslinks to preserve network integrity in the partially degraded state while maintaining the target stiffness.

The applicability of the PDH can be qualitatively showcased by ease of use, an inverted microscope with a connected UV-capable LED module can pattern the system in size, location and dose (Figure 12 C-D). Furthermore, the light dosage can be subdivided, showing that repeated illumination steps separated by long breaks maintain an increase in swelling height. For this work the illumination diameter were varied between 100 and 300 µm, relating to medium-sized (63-125 µm) and large (>125 µm) drusen observed in the human retina, representing physiological and pathological ECM ageing respectively[119,121]. By keeping the illumination time and intensity constant at 60 seconds and at 100% (3.83 mW/cm^2) a dose of 230 mJ/cm^2 was set (Figure 12 E). The resulting absolute swelling heights were measured by tracking the vertical displacement of fluorescent beads embedded inside the hydrogel and for the 100 and 300 µm conditions were around 22.5 and 20 µm respectively, showing no significant difference between the conditions (Figure 12 F). Furthermore, the measured stiffness at the top of the swellings showed no significant differences when compared to the average bulk stiffness of the PDH (Figure 12 G).

Lastly, before the PDH could be advanced further towards cell compatibility, the hydrolytic behavior of the hydrogel network under cell culture conditions was investigated. PDHs were exposed for prolonged times to cell culture conditions with the major influences being additives of the cell culture medium, increased temperature during incubation and CO_2 buffering shifting the pH of the solution towards a slightly basic environment. The progress of the passive degradation of PDH was checked by measuring bulk stiffness over time. Initially, the average bulk stiffness of the reference sample was around 4.5 kPa, which did not change after three days under cell culture conditions. Within six days of cell culture conditions the average bulk stiffness of the PDH stabilized at around 4 kPa and after 12 days a decrease to 3.5 kPa could be observed (**Figure 12** H). The progression of bulk stiffness was deemed stable within the first week to support the cell culture and only exit the desired bulk stiffness range after more than 12 days, possibly allowing culture times up to 14 days.

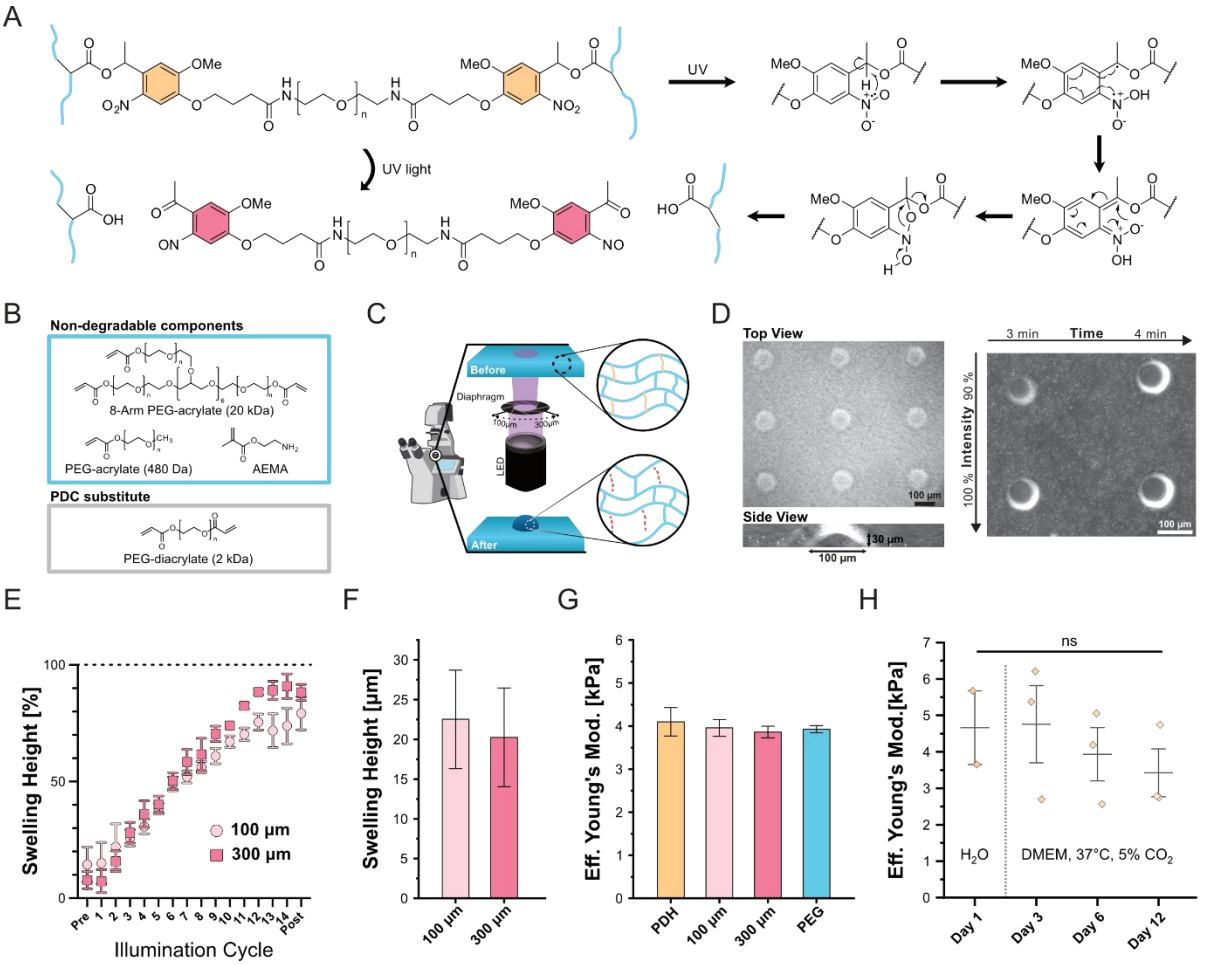


Figure 12: Photodegradable hydrogel synthesis and characteristics *A) Schematic degradation of the photodegradable crosslinker (PDC) when copolymerized into a hydrogel. Additionally, photolytic breakdown mechanism shown in detail, following Wirz et al[181]. B) Non-degradable hydrogel network components are 8-Arm PEG-acrylate, PEG-acrylate and 2-Aminoethyl methacrylate. The PDC substitute for the completely non-degradable control gels is PEG-diacrylate. C) Illustration of the experiment setup to illuminate the samples and induce photolysis consisting of an inverted microscope equipped with 385 nm LED and an adjustable diaphragm. D) Matrix of localized swelling patterned on a photodegradable hydrogel (PDH) and representative overview of the hydrogel behavior to varying illumination duration and UV intensity. E) Additive illumination with each illumination cycle being four seconds of UV at 3.83 mW*cm² followed by one hour break. The post-experiment reference image was taken nine hours after the last illumination cycle. Swelling height is given as a percentage of the maximum height with a standard error mean (SEM)*

and three independent repetitions (N) for both conditions. F) Averaged absolute swelling height ± SEM (N=3) of PDH illuminated with 100 or 300 µm patterns. G) Effective Young's modulus ± SEM (N=3) of all conditions. Statistical significance in E) and F) was assessed using one-way ANOVA. H) PDH bulk stiffness under cell culture conditions over an extended period. Statistical significance in was assessed using one-way ANOVA. Hydrogel images were taken by Iulia Scarlet in her role as master student. Illustrations are partially published in Reul et al.[166]

Bio-functionalization of photodegradable hydrogels with ECM proteins

With the bulk properties set to the desired range and degradation behavior characterized, the hydrogels required protein coating to support monolayer formation and tissue mimicking. The most common approach used to covalently attach full scale ECM proteins to a hydrogel surface is through Sulfo-SANPAH (**Figure 13** A)[197]. This approach is not compatible with the PDH as an intensive UV activation step is required, which would potentially degrade it to an unusable extent. This meant that alternative methods, relying on different cross-linking chemistry, had to be explored.

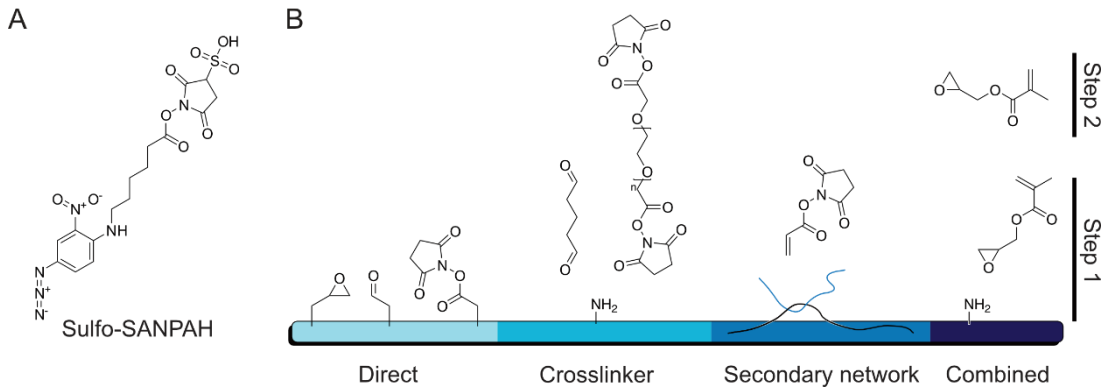


Figure 13: Overview of hydrogel bio-functionalization pathways. *A) Conventional UV-based hydrogel functionalization compound. Azido-nitrobenzene at the bottom can be activated by UV light to release a nitrogen molecule and become reactive. The ester group at the top is amine reactive due to the good leaving group properties of the Sulfo-NHS moiety. B) Overview of the different bio-functionalization pathways, with the following subdivision into direct functionalization, crosslinker based functionalization, secondary network-based functionalization, and the combined approach.*

Direct functionalization strategy

Incorporation of amine reactive moieties into the polymer network enables direct attachment of proteins to the hydrogel surface. To incorporate these moieties into the polymer network, the rest of the molecules required a free radical polymerization accessible group, mainly acrylate or methacrylate groups. With prime examples being GMA and N-hyroxysuccinimide-ester acrylate (NHS) (**Figure 14** A).

The GMA-based approach utilizes epoxy-amine ring opening reaction to covalently link proteins to the hydrogel surface. Different molar concentrations of GMA were incorporated into the hydrogel. With lower concentrations showing better polymerization behavior, as higher concentrations would result in a white precipitate within the hydrogel. To quantify coating efficiency the samples were incubated with fluorescently tagged fibronectin and after imaging the surface of the hydrogel, the efficiency could be derived from the mean grey value of the fluorescent channel (**Figure 14** B). The intensity of the signal increased with the concentration of GMA present in the hydrogel and was significantly higher than the uncoated controls (**Figure 14** C). While no saturation could

be observed, different signal intensities indicated the presence of a varying surface coating, which could be exploited for cell adhesion. As a test, hiPSC-RPE were seeded on hydrogels which were incubated with unlabeled protein, as fluorescent tagging potentially alters cellular adhesion domains. Nevertheless, no cellular attachment could be observed, as cells did not spread on the hydrogel surface and quickly died. To improve the reaction kinetics of the epoxy-amine Click reaction, the incubation temperature was increased from the initial 4°C. Even with this adjustment the protein adhesion efficiency was not high enough to support cell adhesion (**Figure 14** D).

The NHS-ester provides an amine reactive carbonyl as the reaction equilibrium favors the amid formation due to the good leaving group nature of the NHS group. A built-in drawback is the hydrolytic sensitivity of the NHS-ester which becomes very apparent as the PDH pre-polymer mixture is not pH controlled. While the exact pH in the mixture and during the reaction was not investigated, no cell attachment could be observed with this approach. As an alternative pathway, incorporation of acid groups into the polymer backbone was assessed. This approach would circumvent the hydrolytic weakness of the NHS-ester as the acid group would be activated with a carbodiimide during the bio-functionalization. During the trial the optimal ratio of acrylic or meth acrylic acid could not be found as the addition of these compounds would impede the APS/TEMED driven polymerization reaction and prevent the formation of the PDH[297].

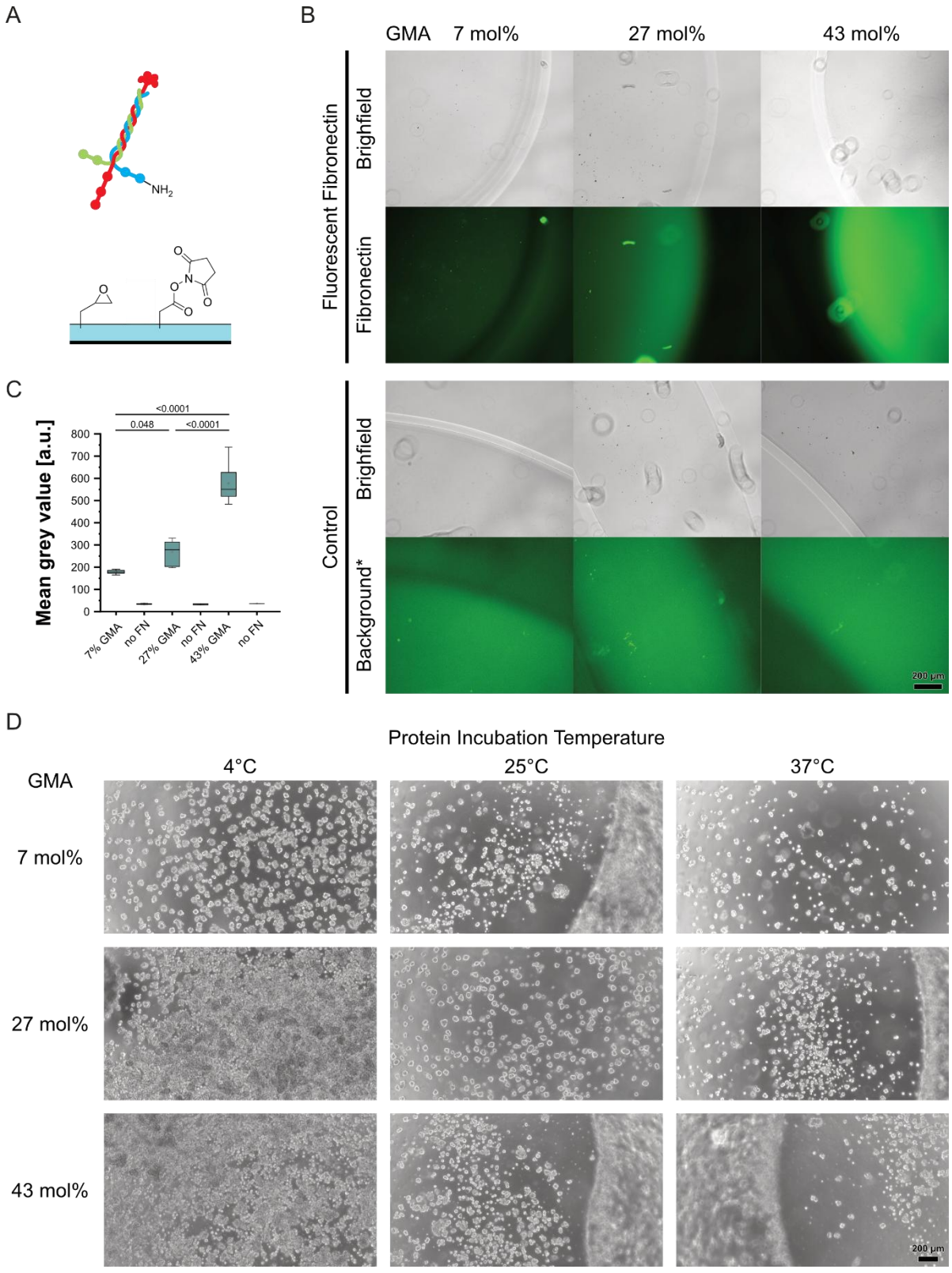


Figure 14: Direct bio-functionalization implementation and preliminary results. *A) Schematic representation of exemplary reaction of amine functionality with the amine reactive moieties on the hydrogel surface. B) Fluorescent fibronectin adhesion assay. Representative images in brightfield and fluorescent channel corresponding to the emission of the HiLyte 488 tag showing surface bound fibronectin in green. The limits of the brightness contrast of the control-background were adjusted to show the residual autofluorescence. C) Quantification of the immunofluorescent intensity by mean grey value measurement. Statistical significance in was assessed using one-way ANOVA. D) hiPSC-RPE seeding overview of the different GMA compositions and protein incubation temperatures.*

Crosslinker-based functionalization strategy

With the direct functionalization pathways not yielding any usable samples, a possible explanation for the insufficient protein attachment was sterically hinderance between the two reaction entities. As the amine reactive moiety is integrated into the polymer backbone, it may have a low degree of freedom to reorient. On the other hand, amine residues in proteins are equally restricted in their movement and orientation by the folded structure of the protein, which is especially restrictive in full scale ECM protein (laminin: ~700kDa). Thus, crosslinker based functionalization pathways aimed to bridge between the two sterically restricted reaction partners.

The easiest reaction design saw a homo-bifunctional crosslinker reacting with an amine from the hydrogel and one from the ECM protein. So, amine functionalities were incorporated into the PDH by co-polymerization with AEMA. Unfortunately, early trials showed that the addition of AEMA drastically changed the polymerization kinetics either inhibiting hydrogel formation completely or resulting in much softer bulk stiffnesses. With the mol/percentage adjusted to preserve the desired bulk stiffness, various linear crosslinking compounds were screened. First, glutaraldehyde was tried as it is a short chained bis-functional aldehyde commonly used in fixation of cells. Unfortunately, although different incubation times and temperatures were tried, no cell attachment could be observed. Lastly, NHS-ester based crosslinker bis functionalized PEG succinimidyl carboxymethyl ester was tried. The crosslinker had two different variants with different molecular weights of the PEG linker of 1 and 3.4 kDa. Also in this case, after tests with different concentrations and incubation times, no cell attachment could be observed.

Secondary network strategy

The formation of a secondary amine reactive network was reported by Przybyla et al.[298] as a reliable post-functionalization method of poly-acrylamide hydrogel. The original procedure was altered to replace the UV initiator with the APS/TEMED redox pair, and the approach showed some promising results as a low percentage of bio-functionalized PDH supported cell attachment and monolayer formation. The monolayer could be maintained for a week, and artificial topographical defects could be induced as demonstrated by the immunofluorescent staining of F-actin and tight junction protein ZO-1 (**Figure 15**). Nevertheless, the method was ultimately deemed too unreliable as the reproducibility was extremely low (25% for PDH, 0% for NDH).

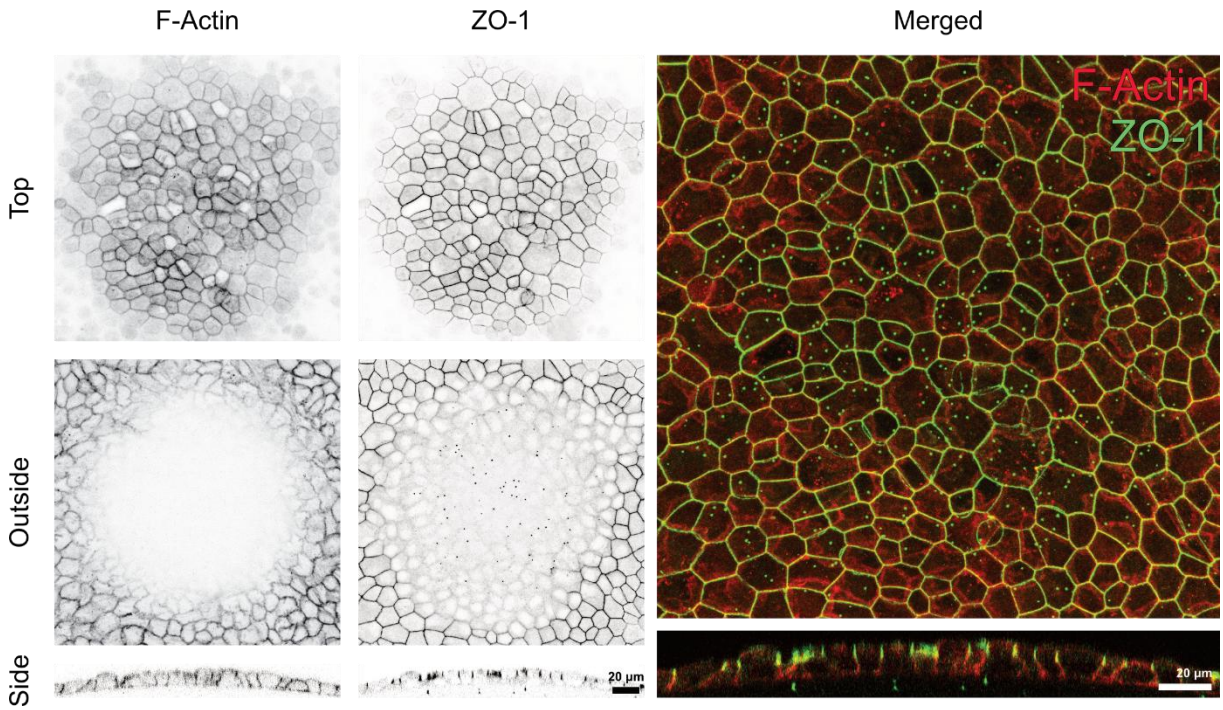


Figure 15: Secondary network bio-functionalization results. *On the left immunofluorescent staining of the F-actin and tight junction protein ZO-1 are shown for the top and outside regions of topographical defect. With the respective side view built from an orthogonal projection of the image. On the right side the two channels were compressed with a maximum intensity projection and merged into a composite. Actin in red and ZO-1 in green. At the bottom the side view of the merged image. Data was generated by Stacy Lok Sze Yam in her role as master student.*

Combined approach strategy

Based on failed strategies using direct biofunctionalization and trials involving secondary network formation, it was postulated that the free acrylate groups of the hydrogel crosslinkers were consumed during the extended polymerization time, either by incorporation into the hydrogel network or by oxidation. The remaining fraction was negligible and could not support cohesive surface functionalization. With this assumption, a replenishment of acrylate groups after the polymerization of the hydrogel would enable a secondary network to connect to the substrate surface, thus combining the crosslinker and secondary network-based approaches.

Utilizing the orthogonal functional group of the established AEMA containing PDH, meth acrylic groups were reintroduced by incubating the hydrogel with a GMA solution. In a second step an amine reactive secondary network could be generated by free radical polymerization. The activated hydrogel surface was incubated with the desired mixture of in vivo relevant ECM proteins (Laminin 332, laminin 511, collagen IV) in a standard cell culture incubator for 24 hours at 37°C. This method reliably produced gels which supported cell adhesion and cohesive monolayer formation across the whole sample (**Figure 16**). While this pathway required multiple steps over two days it was reliable to be chosen as the primary method for bio-functionalization.

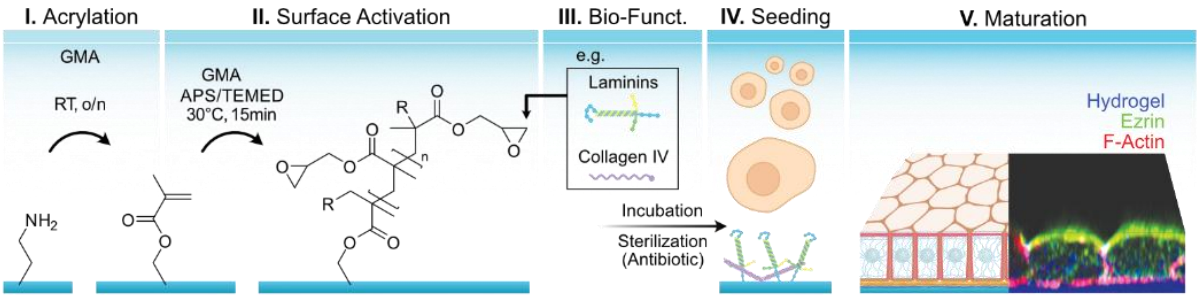


Figure 16: Overview of the combined approach. *Step I) Post-functionalization of the hydrogel to reintroduce free acrylate groups after the free radical polymerization. Step II) Grafting an amine reactive oligomer onto the hydrogel surface by APS/TEMED initiated free radical polymerization. Step III) Bio-functionalization by protein incubation with ECM proteins at 37°C for 16 hours. Step IV) Cell seeding with hiPSC-RPE on bio-functionalized hydrogels. Step IV) Maintaining the monolayer for a week to achieve a degree of maturation. Illustration was published in Reul et al.*[166]

hiPSC-RPE monolayer formation on the photodegradable hydrogel

Before bio-functionalized hydrogels could be used for cell seeding their sterility had to be ensured. As the commonly used method of UV irradiation was not possible due to the photosensitivity of the PDC samples were washed two times for 15 minutes with an antibiotic solution. This was enough to prevent contamination during the experiment time as the harsh reaction environment during the hydrogel polymerization and parts of the biofunctionalization protocol kept contamination risk low

Human induced pluripotent stem cell-derived retinal pigment epithelium (hiPSC-RPE) cells were seeded on PDH and NDH to establish a model system to study topography induced monolayer force disruption, especially focusing on a correlation between defect size and a change of phenotype. After one week of maturation on the flat surface of the hydrogels, the substrates were illuminated with defined patterns of 100 and 300 µm diameter imitating medium and large sized drusen apparent in outer retinal ageing[119,121]. To exclude the influence of UV light exposure on cellular behavior NDH acted as non-deforming controls. After illumination the hydrogel and monolayer required adaptation time to reach a new equilibrium state. So, to avoid capturing an intermediate state, cells were only fixed after 24 hours.

Now that the cell model was established, the screening on the structural impact could begin. First, a qualitative assessment of the topographical defects was performed through immunofluorescent staining of makers for mechanical activity connected to the actin cytoskeleton. An overview image was created by stitching multiple adjacent projections of the actin signal together (**Figure 17** A). Surprisingly the illuminated regions were indistinguishable from the surrounding tissue. While the vinculin staining for RPE on the illuminated regions showed the signal localizing at the cell border, hinting at an increased recruitment of actin to the adherens junctions, RPE on unilluminated controls

showed an even distribution of vinculin signal (**Figure 17** B).

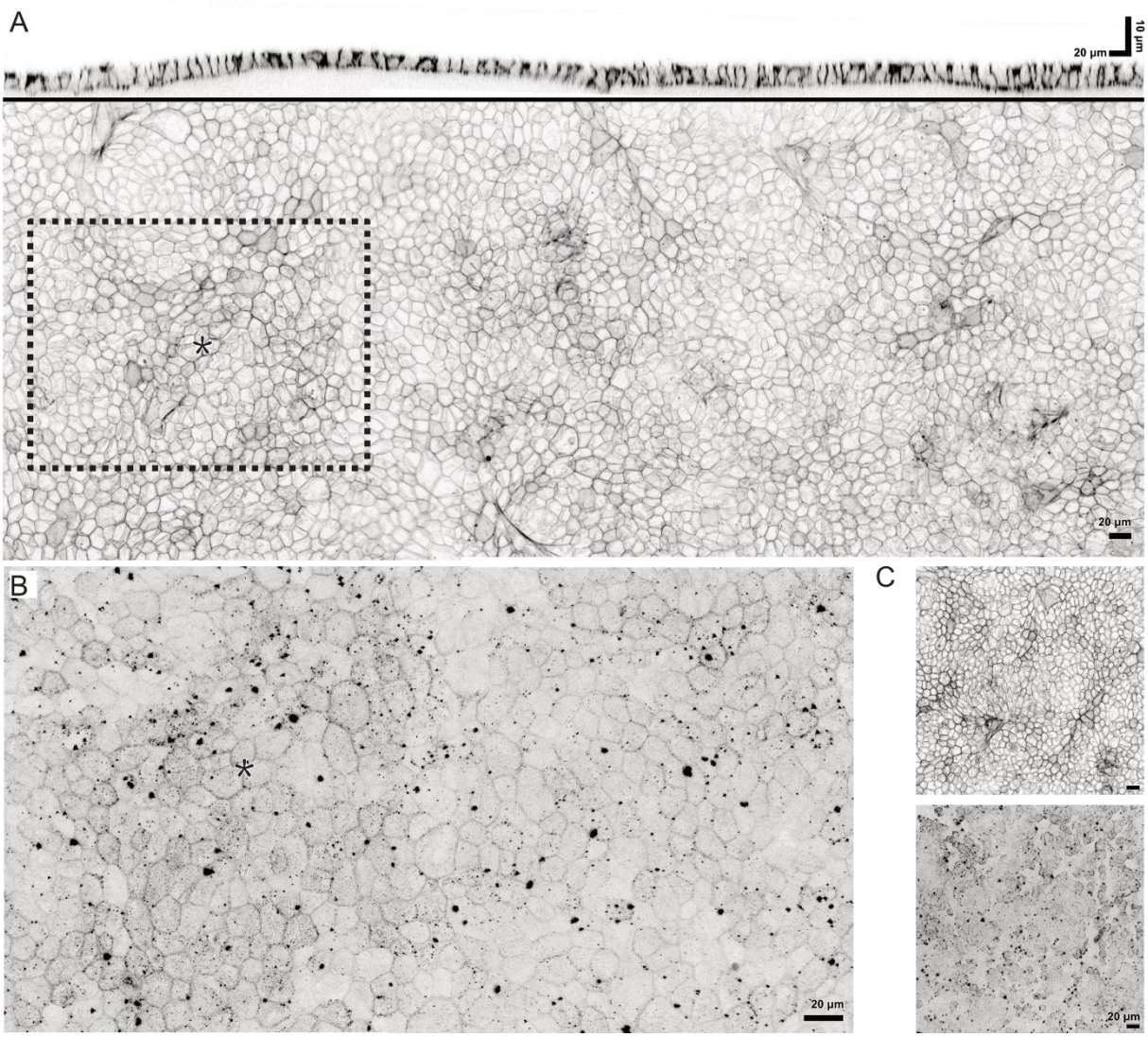


Figure 17: Multi-frame overview of the actin cytoskeleton and vinculin. *A) Orthogonal view of the F-actin signal of the monolayer at the center of the topographical defect (Top). Maximum intensity projection of the F-actin signal with the center of the topographical defect marked by an asterisk and zoom-in indicated by the dashed line (Bottom). B) Stitched high resolution image of the vinculin signal with the center of the topographical defect marked by an asterisk. C) Overview image of the unilluminated control, F-actin (Top), vinculin (Bottom).*

Next, the level of actomyosin contractility was investigated with the immunofluorescent staining of phosphorylated myosin light chain (pMLC). As expected, the pMLC signal overlapped with the actin signal (**Figure 18**). Throughout all conditions randomly located cells with a higher intensity can be observed, although only for the illuminated condition the maximum signal of pMLC staining corresponded closely to the illuminated region. Lastly, the nuclei were stained with the common DNA-binding dyes. As the excitation range is commonly located in the UV-blue light range, a certain overlap with the absorbance spectrum of the PDC is present. The effect of the PDC is expressed as a drastically reduced image quality of the nuclei staining of the PDH samples, which is especially pronounced in the illuminated condition.

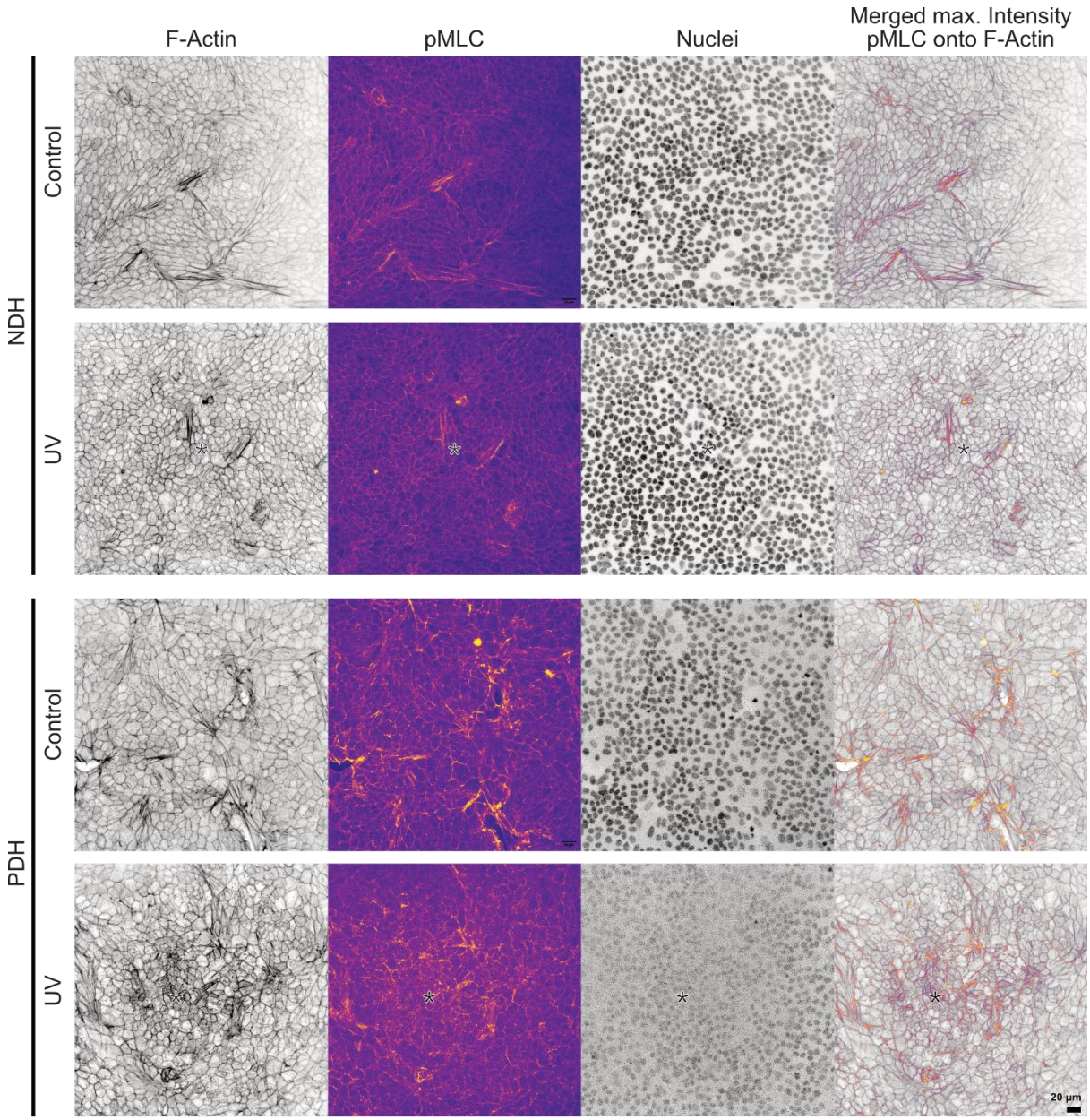


Figure 18: Immunofluorescent staining of F-actin, phospho-myosin light chain (pMLC) and nuclei presented by maximum intensity projection. *Merged maximum intensity of pMLC signal onto the signal of F-actin.*

Moving on from the initial single staining observations, the following images are representative examples of comprehensive immunofluorescent data sets (**Figure 19**). Investigating the actin cytoskeleton, F-actin was stained with phalloidin, and maximum intensity projections of the different conditions showed no peculiar distribution or accumulation of the signal. The expected appearance of intra cellular stress fibers could not be observed, with the F-actin forming regular lateral actin belts, as well as apical and basal cortices.

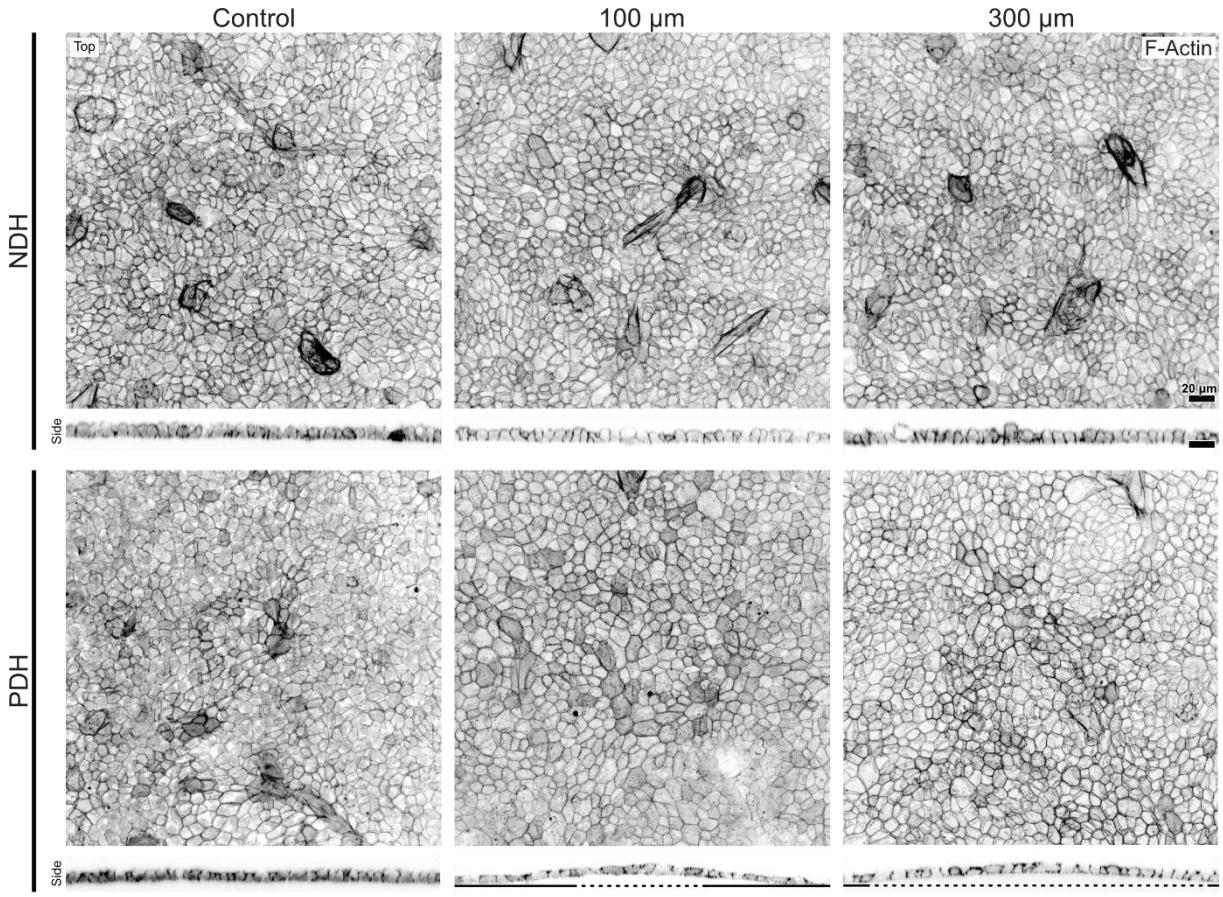


Figure 19: Representative F-actin images by maximum intensity projection, showing lateral distribution. *When relevant, illumination pattern is in the center of the frame. Side shows the orthogonal projection from the center line of the respective image. Images are published in Reul et al.*[166]

Next tight junctions were investigated by immunofluorescent staining of the ZO-1 domain (**Figure 20**). The images show an epithelium characteristic continuous outline at the cell-cell borders. With no qualitative change in organization or signal intensity the barrier function was deemed uncompromised.

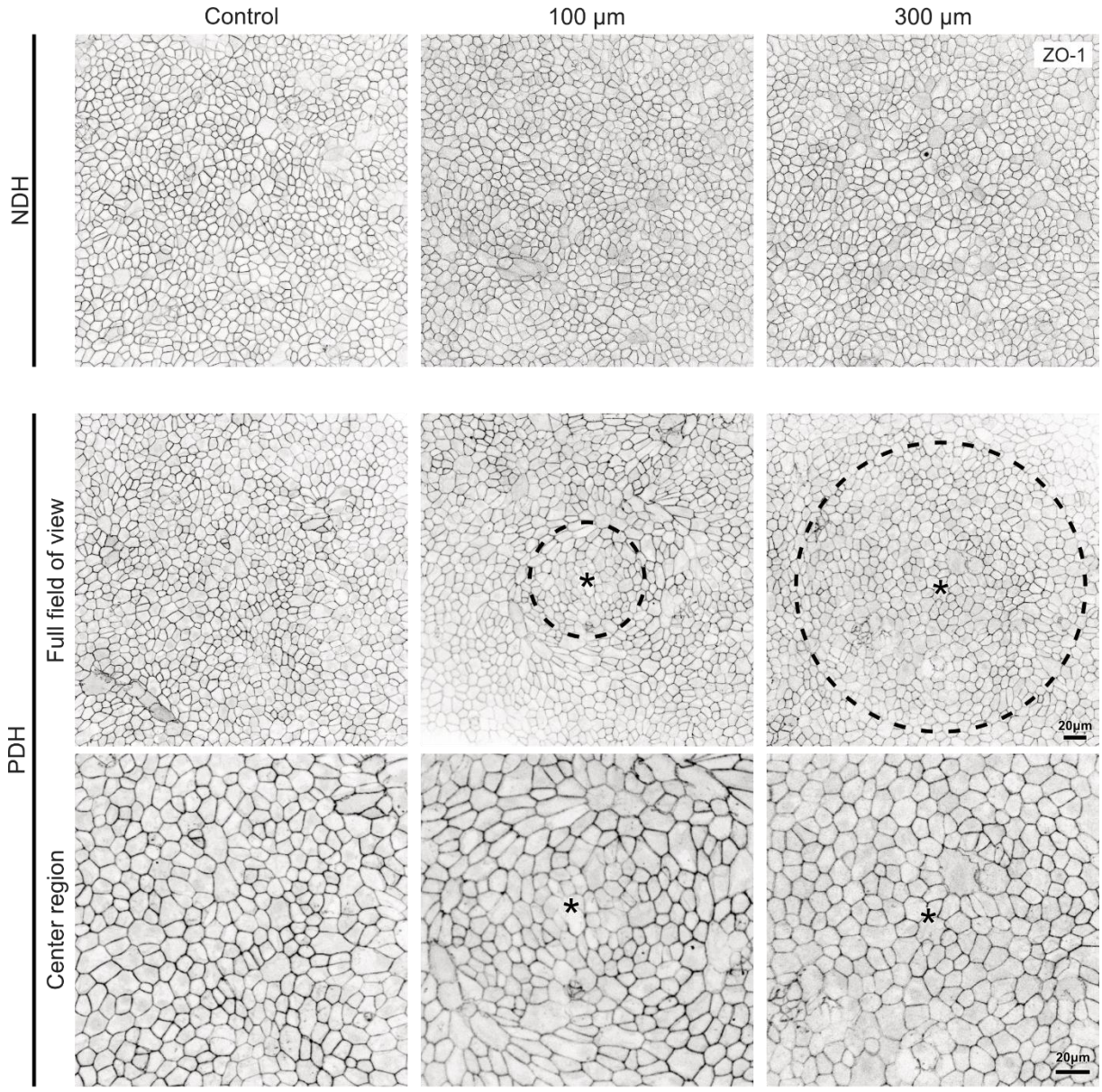


Figure 20: Representative ZO-1 images by maximum intensity projection and condition, showing lateral tight junction distribution. *When relevant, illumination pattern is in the center of the frame and diameter is indicated by a dotted line. Images are published in Reul et al.*[166]

Looking at another functional marker Ezrin, which links the plasma membrane to the actin cytoskeleton and is essential for apical microvilli formation and functionality. It acts as a polarity indicator and can give an overview of the functional state of the tissue. Microvilli structures were imaged with super resolution, and the high-resolution images showed no qualitative differences in distribution or morphology between the different conditions (**Figure 21**).

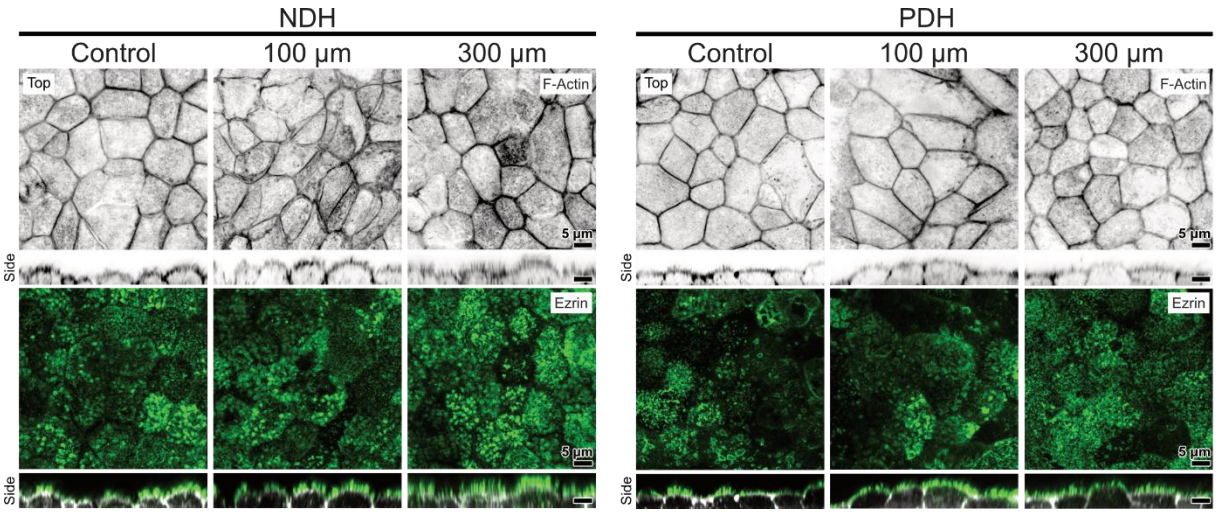


Figure 21: High resolution representative images of F-actin and Ezrin signal by maximum intensity projection and side view from orthogonal projection. *On the left hiPSC-RPE monolayer on non-degradable hydrogels (NDH) and photodegradable hydrogels (PDH) on the right in the three conditions: unilluminated control, 100 µm topographical defects, and 300 µm topographical defects.*

Distance dependent quantification of morphometric parameters

Qualitative assessment of immunofluorescent images suggested that monolayer height varied with distance from the center of the topographical defect, in a manner that depended on the defect diameter. Describing such an observation in detail required tissue level analysis, collecting a multitude of measurements and grouping them into characteristic regions by the distance to the center of the topographical defect. Collecting this volume of data exceeded the capacity of manual approaches and required a comprehensive Fiji script that semi-automatically measured morphological parameters, including monolayer height, cellular area, shape factor, and cellular orientation for each cell individually. From preliminary data the emergence of characteristic regions was observed. With the “Top” region stretching radially from the center of the topographical defect 25 µm outwards, while the “Edge” region extended 25 µm radially inwards. Lastly, an “Outside” region was defined as an annulus with radii of 150 and 175 µm. This subdivision into regions enabled direct comparability between topographical defects of different sizes (**Figure 22**).

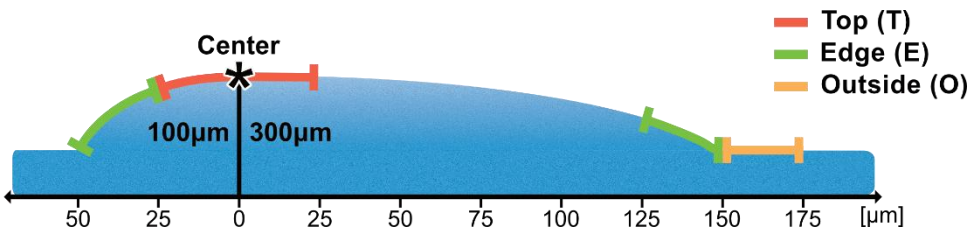


Figure 22: Delineation of regions. Top (T) stretches radially from 0 to 25 µm, Edge (E) goes from the radius of illumination 25 µm inwards radially and the Outside region is in both conditions defined as an annulus from 150 to 175 µm radii. *Illustration is published in Reul et al.*[166]

Epithelial monolayer height

The height of the hiPSC-RPE monolayer was automatically determined from the F-actin signal intensity increases of the apical and basal cortices in the orthogonal projection (**Figure 23** A-B). The absolute values of the monolayer height showed interesting trends for both PDHs, with monolayer heights on 100 µm topographical defects showing increased heights in the Top and Edge region compared to the Outside region. While the monolayer height on 300 µm topographical defects was reduced for the Top region in comparison to the Edge and Outside regions. Although only the regions of the 300 µm topographical defects showed a significant difference compared to the respective controls (**Figure 23** C).

Overall, the monolayer height showed a height heterogeneity between the conditions and to reach a better comparability values were normalized by the mean of the respective technical replicate. The resulting normalized monolayer height of the 100 µm topographical defects increased by roughly 5% in the Top region and 3% in the Edge region, while the Outside region did not increase, even showing a slight decrease. Highlighting a significant difference of the Top and Edge region in comparison to the Outside region but also to the illuminated and unilluminated controls. On the other hand, the normalized height of the Top region of the 300 µm topographical defect showed a 5% decrease, while the Edge region increased by around 2.5% increase and the Outside region stayed mostly unchanged (**Figure 23** D).

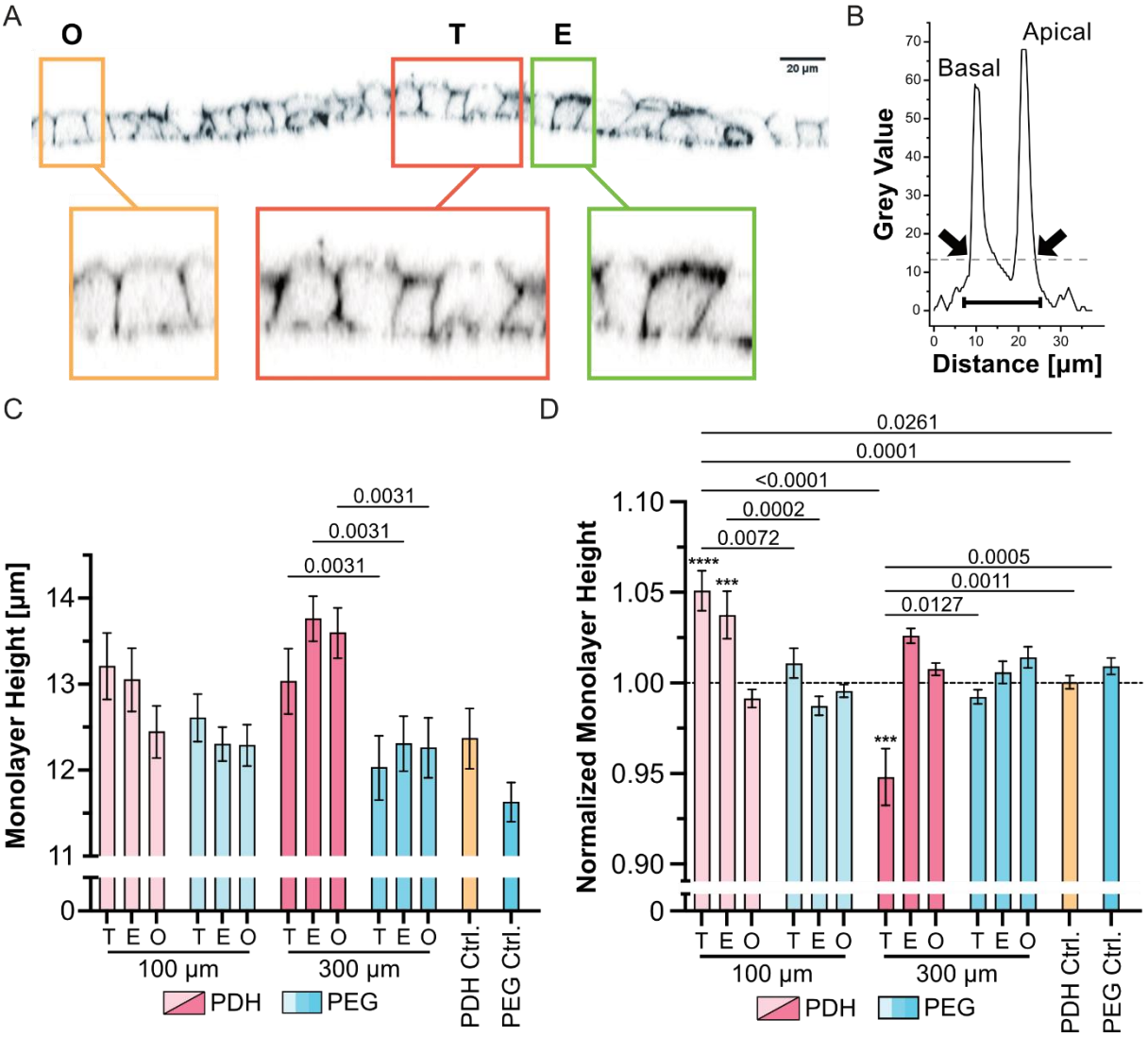


Figure 23: Monolayer height quantification. *A) Representative orthogonal view of the F-actin signal with indications of the regions: Top (T), Edge (E), and Outside (O). B) Grey Value of a perpendicular line plot through the monolayer, with the two intensity peaks indicating apical and basal cortices. The dashed line indicates the measurement specific threshold, while the arrows show the points at which the threshold is exceeded. C) Absolute monolayer height ± SEM. D) Normalized monolayer height ± SEM*. Measurements were normalized by their average. For C-D) Statistical analysis was performed by unpaired two-way *ANOVA* with Tukey's correction for multiple comparisons. The p-values comparisons are indicated in the graph. *** indicate a of p-value = 0.0008 and **** a p-value = <0.0001 when compared to the relative Outside region. Independent repetition (N): 100 µm *PDH* and *PDH* control, N = 5; 100 µm *PEG*, N = 4; 300 µm *PDH*, 300 µm *PEG* and *PEG* Control, N = 3. *Images are published in Reul et al.*[166]

Cell area and shape

The cell area was automatically determined by segmentation of the maximum intensity projection from the F-actin signal. While the absolute cellular area fluctuated around 80 µm² for most conditions, regions of the 300 µm topographical defects exhibited higher values of around 100 µm² (**Figure 24** A). With no trends or significant differences observable the cell area was normalized. While no significant differences emerged two interesting trends were revealed (**Figure 24** B). First, normalized cell area in the Top and Edge regions of the 100 µm topographical defects was almost 10% larger compared to the respective Outside region and showed an extremely high variance. The difference in regard to the respective illuminated control was negligible. Similarly, the second trend showed that the normalized cell area of the Top region of 300 µm topographical defects

was around 10% larger compared to either the Edge or Outside region, exhibiting high variance (**Figure 24** B).

Investigating the high variance observed in the Top regions, the absolute cell area values were binned into relative frequency distributions (**Figure 24** C-E). The extremely high variance of the Top region of the 100 µm topographical defect became apparent as bimodal distribution, with cells splitting into two populations of smaller and larger than average cells. This markedly differed from the normal distribution of the illuminated and unilluminated controls. By the Edge region the frequency distribution had already shifted, and a normal-like curve could be observed (**Figure 24** C).

For the Top region of the 300 µm topographical defects the cell area frequency distribution showed a reduced appearance of cells with a smaller area while a shoulder indicated an increased frequency of cells with a larger area. Compared to the normal frequency distributions of illuminated and unilluminated controls, this explained the average cell area increased. Again, the relative frequency distribution of the Edge region had returned to a normal distribution and matched the controls (**Figure 24** D). Overall, the relative frequency distribution of the Outside region of all the conditions matched relatively closely, generally following a normal distribution (**Figure 24** E).

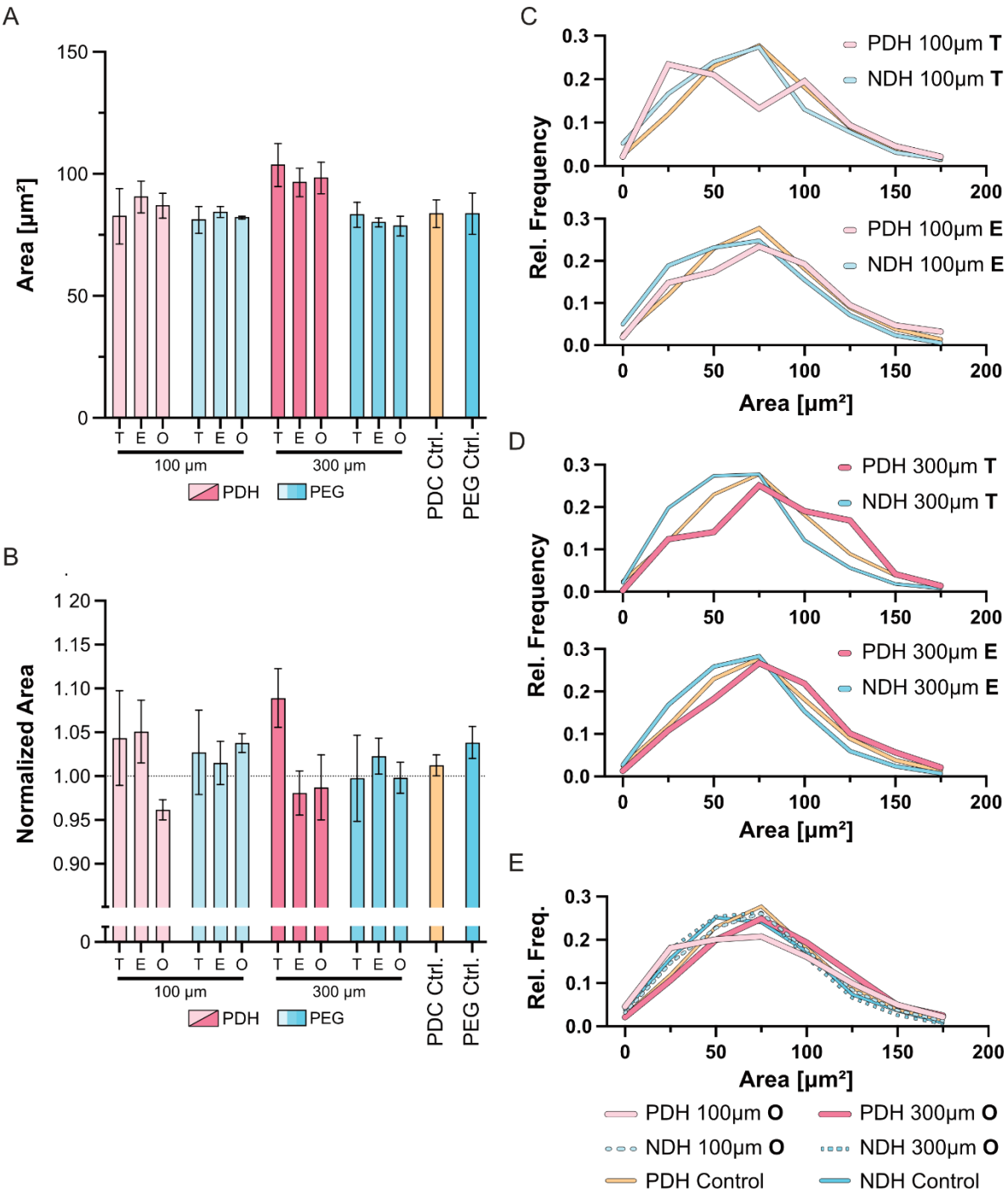


Figure 24: Quantification of cellular area. *A) Absolute cell area ± SEM. B) Normalized cell area ± SEM. Area was normalized by the average cell area of the respective measurement. C) Relative frequency distribution of cellular area for Top (T) and Edge (E) regions of the 100 µm topographical defects. With unilluminated PDH control in yellow. D) Relative frequency distribution of cellular area for Top (T) and Edge (E) regions of the 300 µm topographical defects. With unilluminated PDH control in yellow. E) Relative frequency distribution of cellular area for Outside (O) regions of the two PDHs. With unilluminated PDH and NDH controls in yellow and blue respectively. For A-B) statistical analysis was performed using unpaired two-way ANOVA with Tukey's correction for multiple comparisons. Independent repetition (N): 100 µm PDH, 300 µm PDH and PEG Control, N = 3; 100 µm PEG, N = 6; 300 µm PEG, N = 5; PDH control, N = 4. Images are published in Reul et al.*[166]

To characterize cellular shape, a dimensionless shape factor was calculated as a structural order parameter, which can be indicative of the mechanical state of a two-dimensional tissue. This factor is calculated from the perimeter divided by the square root of the cell area and higher values indicate an increase influence of the lateral cell-cell

junctions and monolayer unjamming, while lower values indicate greater cortical tension with the monolayer being in a jammed state (**Figure 25** A)[42]. The mathematical threshold of 3.81 was exceeded in every region of the different conditions, but no significant difference could be observed (**Figure 25** B). Calculating the difference between the regions of the PDH and the respective illuminated control showed that the Top regions had the highest difference, followed by the Edge regions, while the Outside regions had the lowest difference (**Figure 25** C).

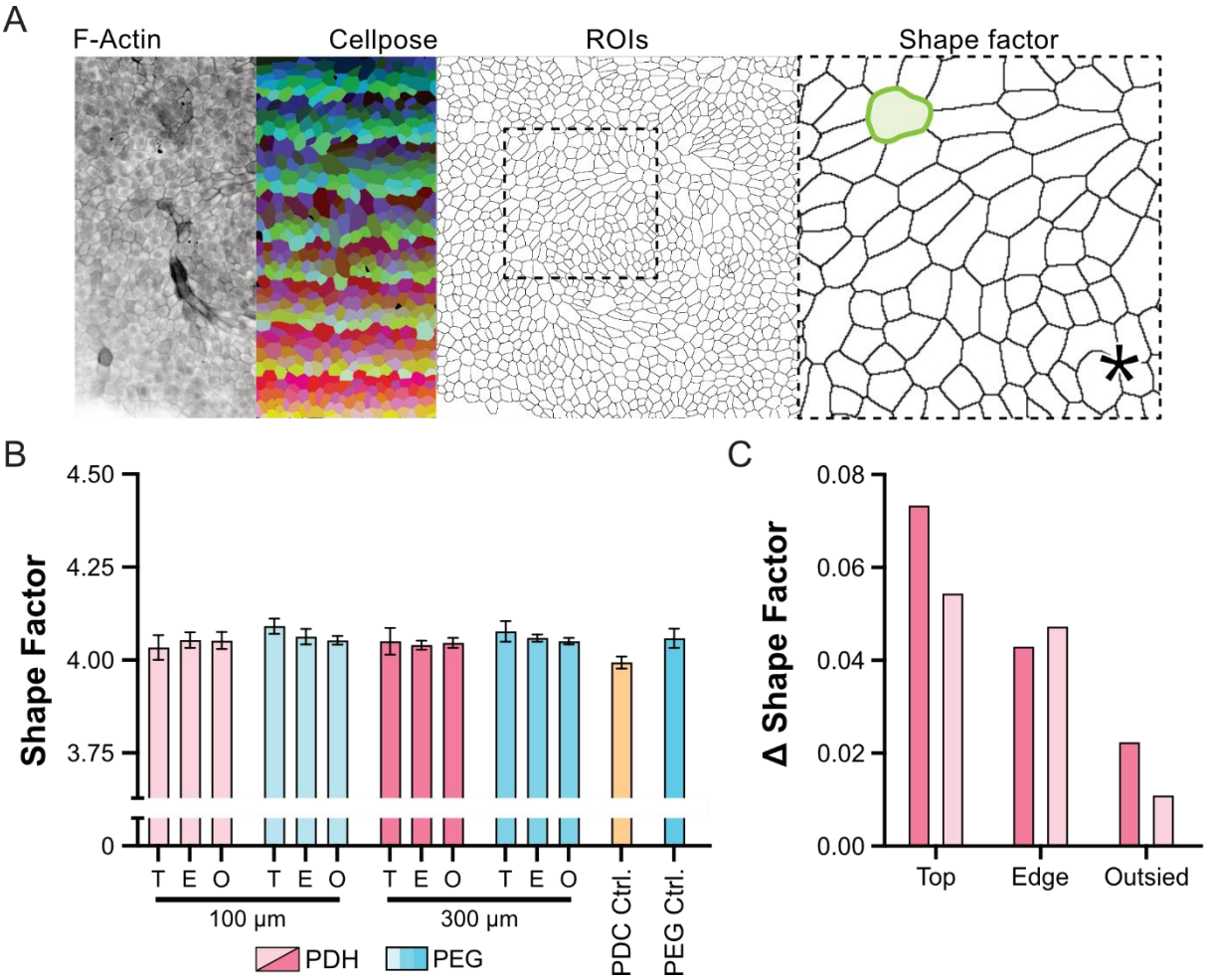


Figure 25: Workflow of the Fiji script highlighting the segmentation and calculation of the shape factor and the binned quantitative results. *A) Workflow of the Fiji script, automatically segmenting the maximum intensity projection of the F-actin signal. The for the ROIs the perimeter and area was determined and the shape factor calculated, while also measuring the distance to the center of the topographical defect. B) Shape factor ± SEM. Statistical analysis was performed using unpaired two-way ANOVA with Tukey's correction for multiple comparisons. Independent repetition (N): 100 µm PDH N = 5, 300 µm PDH N = 4, 100 µm PEG, N = 6; 300 µm PEG, N = 5; PDH control, N = 7, and PEG Control N = 3. C) Difference between the average shape factor of the regions on the illuminated PDH and corresponding illuminated NDH. Images are published in Reul et al.[166]*

Cell orientation

Analyzing cellular orientation in relation to the center of the topographical defect can give an idea about the mechanical continuum as cells in a monolayer align along the axis of maximum average stress[55,299,300]. The relative orientation of each cell was derived by the scalar product between the vectorized absolute angle of the cell and the vector pointing

to the center of the topographical defect, resulting in a scale from 0° to 90° indicating radial or perpendicular alignment respectively (**Figure 26** A).

An average orientation of 45° indicates a random orientation with no preferred alignment of the cells in that region, which is the case for most of the regions. Only the Edge region of the 100 µm topographical defect showed a significant deviation compared to the illuminated control in form of a multicellular response forming a ring around the base of the defect (**Figure 26** B-C). This perpendicular alignment separates the Top region from the Outside region. On the other hand, while not significantly different when compared to the controls, cells of the Top region of the 300 µm topographical defect tend to orient towards the center of the defect (**Figure 26** C).

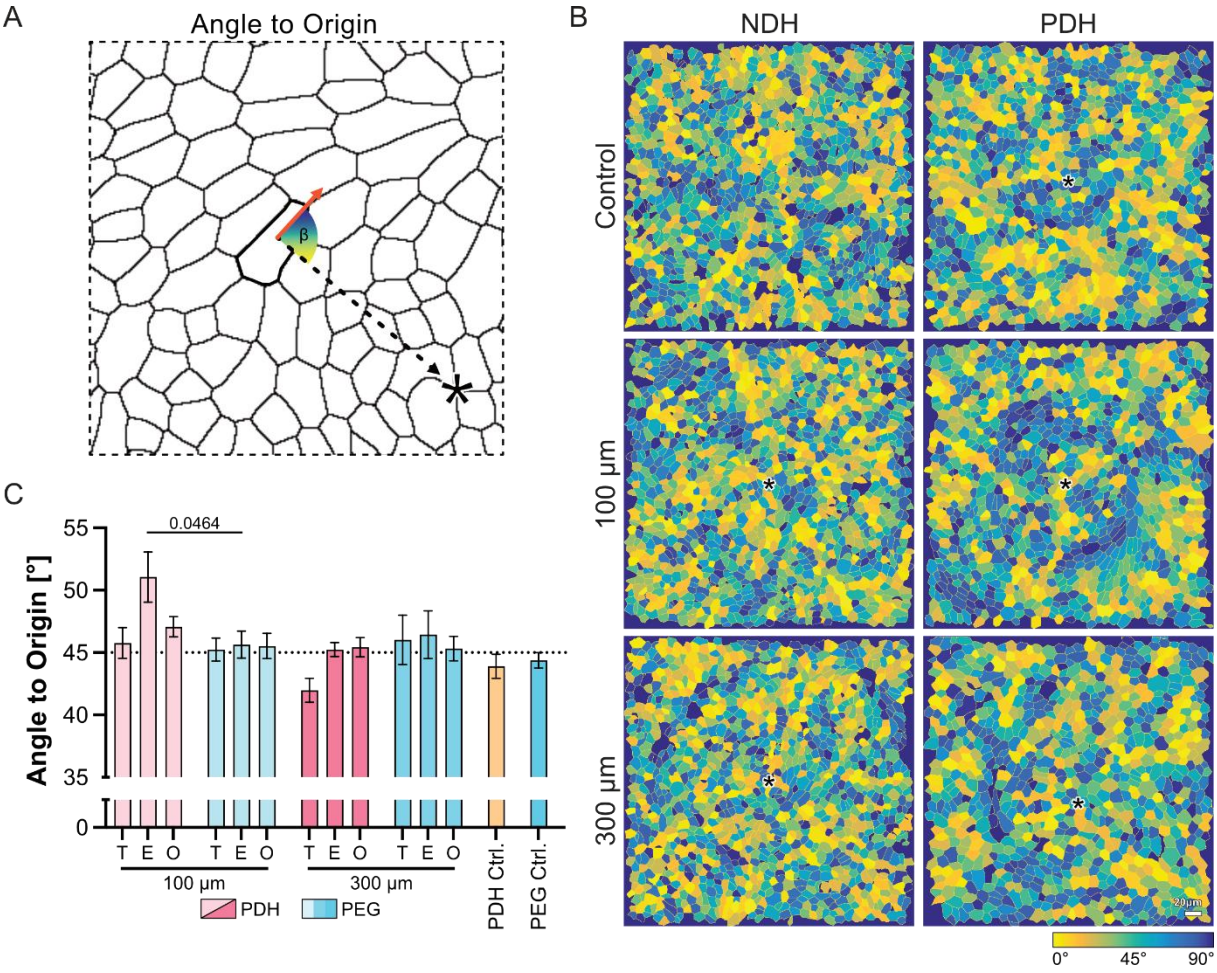


Figure 26: Relating cell orientation to the center of the topographical defect with the Angle to Origin. *A) Schematic of the Angle to Origin calculation, with the red arrow indicating the vector of absolute cellular orientation, the dashed arrow indicating the vector to the center of the topographical defect, and the parula gradient highlighting the scalar product of both giving the Angle to Origin β. B) Representative images with the cells labelled according to their angle to origin, with lower values corresponding to radial alignment in yellow and higher values showing a perpendicular orientation in blue. C) Angle to origin ± SEM. Statistical analysis was performed using unpaired two-way ANOVA with Tukey's correction for multiple comparisons. Independent repetition (N): 100 µm PDH, 300 µm PDH and PEG Control, N = 3; 100 µm PEG, N = 6; 300 µm PEG, N = 5; PDH control, N = 4. Images are published in Reul et al.[166]*

Quantification of substrate adhesion forces

Traction force microscopy was employed to quantify cellular adhesion forces by assessing bead displacement in the hydrogel during cell culture in comparison with a relaxed reference state.

The representative color-coded overview showed regions of higher traction force (yellow) and lower traction force (blue). An interesting qualitative observation was the deeper blue in the Top region of the 300 µm topographical defect, while the Edge region of the same condition showed a higher tendency to feature higher traction spots (**Figure 27** A). These observations were quantified by extracting the mean traction force and putting it into relation to the Outside region of the respective condition. For both conditions the Top region generated lower traction forces than the Outside region, although the 100 µm topographical defect showed a lower mean traction delta. In accordance with the previous observation, the Edge region of the 300 µm topographical defect showed a higher difference in mean traction (**Figure 27** B). The median of the traction force revealed two significant behavior patterns for the illuminated PDHs. Cells in the Edge region of the 100 µm topographical defects expressed significantly higher median traction forces compared to the Top and Edge regions. While in the 300 µm topographical defect condition the Top region exhibited significantly lower median traction forces in comparison to the Edge and Outside regions (**Figure 27** C).

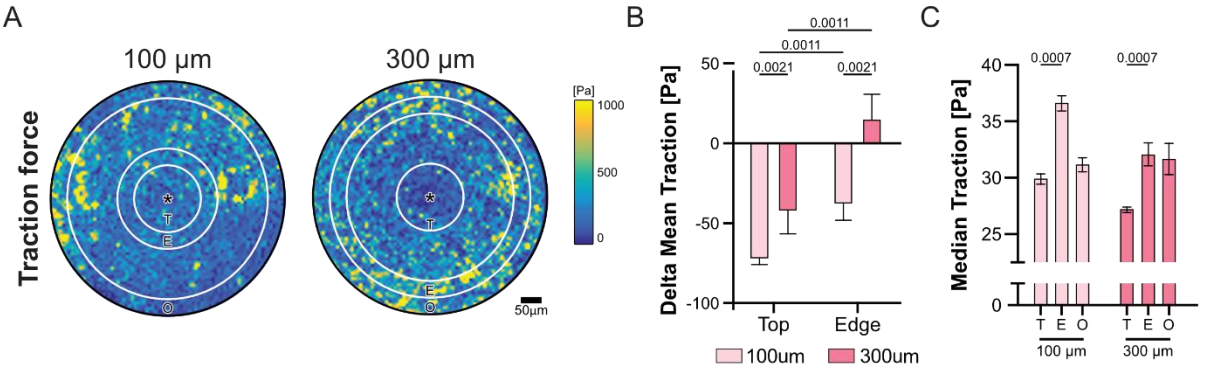


Figure 27: Traction force microscopy (TFM) representative images and quantification. *A) Representative TFM images of the two topographical defects, blue indicating regions of lower traction force and yellow showing higher traction forces. Rings indicate the different regions, Top (T), Edge (E), and Outside (O). B) Mean traction force represented in relation to the Outside region ± SEM. C) Median traction force ± SEM. For B-C) statistical analysis was performed using unpaired two-way ANOVA with Tukey's correction for multiple comparisons. Independent repetition (N): 100 and 300 µm PDH, N = 3. Images are published in Reul et al.*[166]

3. Photodegradable microgels as phantom cells

The second pillar of this work focuses on establishing a photodegradable microgels to perturb lateral force in epithelial monolayers. The minimal set of parameters to establish such a force balance disruption in vitro model was defined as on-demand stiffness change, cell sized, and relevant adherens protein coating.

Microgel synthesis

The requirement of stiffness change was met by employing the PDC to crosslink the microgels, although this places a mayor restriction on the microfluidic setup. The UV sensitivity of the PDC excluded the most common microfluidic approach of UV initiated free radical polymerization. To circumvent this challenge, the redox pair ammonium persulfate (APS) and tetramethyl ethylenediamine (TEMED) was employed to generate radicals and start the free radical polymerization reaction. As the pair reacts upon contact, it must be separated into two separate aqueous phases. The design of the microfluidic chip had to be optimized, mainly the introducing a short mixing channel, where the two aqueous phases are merged before being extruded at the flow focusing junction (FFJ) into the continuous oil phase. Moreover, the elongation of the nozzle after the FFJ was increased to reduce turbulence and improve flow stability (**Figure 28** A). Finally, the degradable aspects of the PDC had to be balanced with non-degradable PEG-based hydrogel network components to improved reactivity and ensured complete gelation (**Figure 28** B).

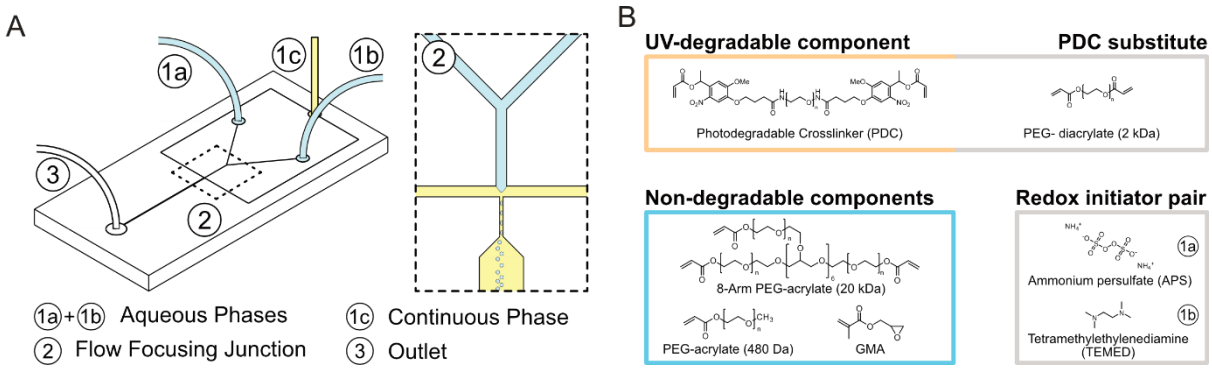


Figure 28: Microfluidic setup and compounds of photodegradable and non-degradable microgels. *A) Schematic of the microfluidic chip highlighting the essential features: 1a Aqueous phase 1, 1b Aqueous phase 2, 1c Continuous phase, 2 Flow focusing junction, 3 Outlet, 4 Collection reservoir. B) Compounds of the photodegradable and non-degradable microgel network. Redox initiator pair with indication in which aqueous phases the respective compound is dissolved. Illustration was prepared by me during pursuit of M. Sc. at RWTH Aachen.*

As little literature is available on PEG-acrylate based APS/TEMED initiated microfluidic the working parameters were established with the completely non-degradable microgels (NDM), which would act as the control microgels. Initial microgel synthesis struggled to form stable microgels, suffering emulsion breakdown and low yields. The problems with the system were attributed to the surfactant. Although Krytox is the gold standard in fluorinated oil-based microfluidics the inhibition of the free radical polymerization reaction suggested a compatibility issue with the APS/TEMED initiator pair. Switching from the carboxyl containing Krytox to the non-ionic block-copolymer based RAN

biotechnologies surfactant showed drastic improvements in emulsion stability and synthesis yield. Furthermore, a general improvement in the work up process was achieved by replacing the harsh isopropanol washing step, which lead to rapid water removal, microgel collapse and agglomeration with a milder detergent solution wash of 0.1 wt% Triton-X 100 in water. With the optimization of the microfluidic system and work up the production of photodegradable microgels (PDM) could begin. The linear PEG-diacrylate non-degradable crosslinker was replaced with the photodegradable crosslinker (PDC), which was a PEG-based, ortho nitro benzyl containing diacrylate.

Expectedly the polymerization characteristics of the PDM differed from the NDM and small adjustments to the protocol had to be made. As the PDC seemed to inhibit the free radical polymerization reaction higher molar ratios of the initiator pair, as well as longer polymerization times were required to achieve microgel formation. Furthermore, the introduction of an orthogonal reaction moiety was necessary as the harsher polymerization conditions drastically reduced the number of free acrylate groups available for post-functionalization. An epoxy functionality was introduced by copolymerization of GMA into the microgel network as preliminary result had shown that GMA localized at the emulsion interface and was available to react with nucleophilic reaction partners.

Diameter and Stiffness characterization

The diameter of the microemulsions and subsequently the microgels were mostly determined by the design of the nozzle size in the microfluidic chip. The nozzle width of 20 µm resulted in NDM with diameters between 35 to 45 µm (**Figure 29** A). In the pursuit of cell-comparable stiffness, the weight percentage of the monofunctional monomer PEG-acrylate was varied in the NDM. This increased the amount of polymer material in the same space and thus increased the compressive modulus without changing the crosslinking density[301]. This assumption was nicely confirmed in the continuous decrease of the effective Young's Modulus over the reduction in PEG acrylate weight percentage in the NDM from 40 to 2 kPa (**Figure 29** B). With the composition of the PDM the average diameter was around 32 µm and effective Young's modulus of 2 kPa (**Figure 29** C-D).

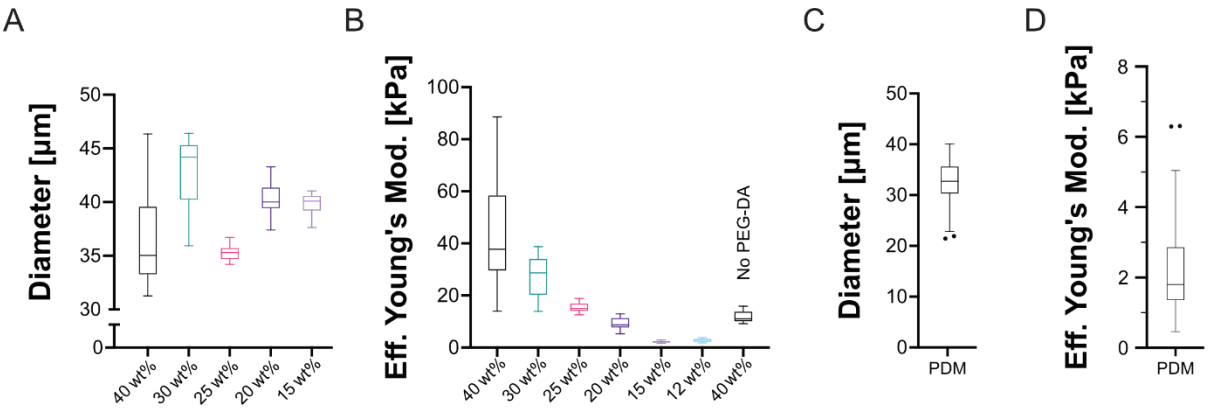


Figure 29: Diameter and stiffness of the NDM and PDM. *A) Diameter of the different compositions of the NDM ± SD. B) Effective Young's Modulus of the different compositions of the NDM ± SD. C) Diameter of the PDM composition ± SD. D) Effective Young's Modulus of the PDM composition ± SD. Data was generated by Alexandra Raab and Yuxin Ji in their role as master students.*

Characterization of photodegradable microgel degradation

As UV illumination of the PDM leads to a mesh density reduction in the hydrogel network a subsequent swelling and softening was expected. Characterization began by onetime illuminating the PDM for different durations and measuring the microgel diameter over the next hour, with the swelling percentage calculated as percentage change in relation to the initial diameter following equation, with d being the measured diameter and d_0 the initial diameter:

$$Rel.Diameter = \frac{d - d_0}{d_0} * 100\%$$

The swelling behavior of illumination durations 1 and 60 seconds showed a quick increase in diameter within the first 10 minutes before expansion slowed down, reaching a plateau after one hour. The experiment showed that even short illumination of one second lead to an expansion of around 10%, while 60 second illumination had a more substantial effect with a maximum expansion of around 20%. Lastly, UV exposure of four minutes showed minor enlargement of only 5%, potentially indicating overexposure and disrupting the characteristic swelling behavior (**Figure 30** A). Investigating stiffness changes in the effective range of one-time illumination times between one and 60 seconds were chosen. The network degradation behavior was calculated as percentage change in relation to the initial stiffness with the following equation, with Y being the measured stiffness and Y_0 the initial stiffness:

$$\Delta Eff.\ Young's\ Mod. = \frac{Y - Y_0}{Y_0} * 100\%$$

The experiment showed that one second illumination resulted in a small reduction in stiffness, reducing the effective Young's modulus by about 10% of the initial stiffness. While illuminations of 15 to 60 seconds resulted in drastic reductions immediately after illumination, with little change afterwards, the final stiffness reduction was around 50 to 70% of the initial stiffnesses ((**Figure 30** B). The 60 second illumination condition was

further investigated with stiffness measurements under cell culture conditions, replacing the distilled water with cell culture medium and performing the measurement at 37°C. The final stiffness reduction averaged 60% which was comparable to the previous measurements (**Figure 30** C). The data sets were compiled, and an exponential decay curve was fitted to the percentage difference representing the average percentage stiffness reduction over the illumination duration (**Figure 30** D).

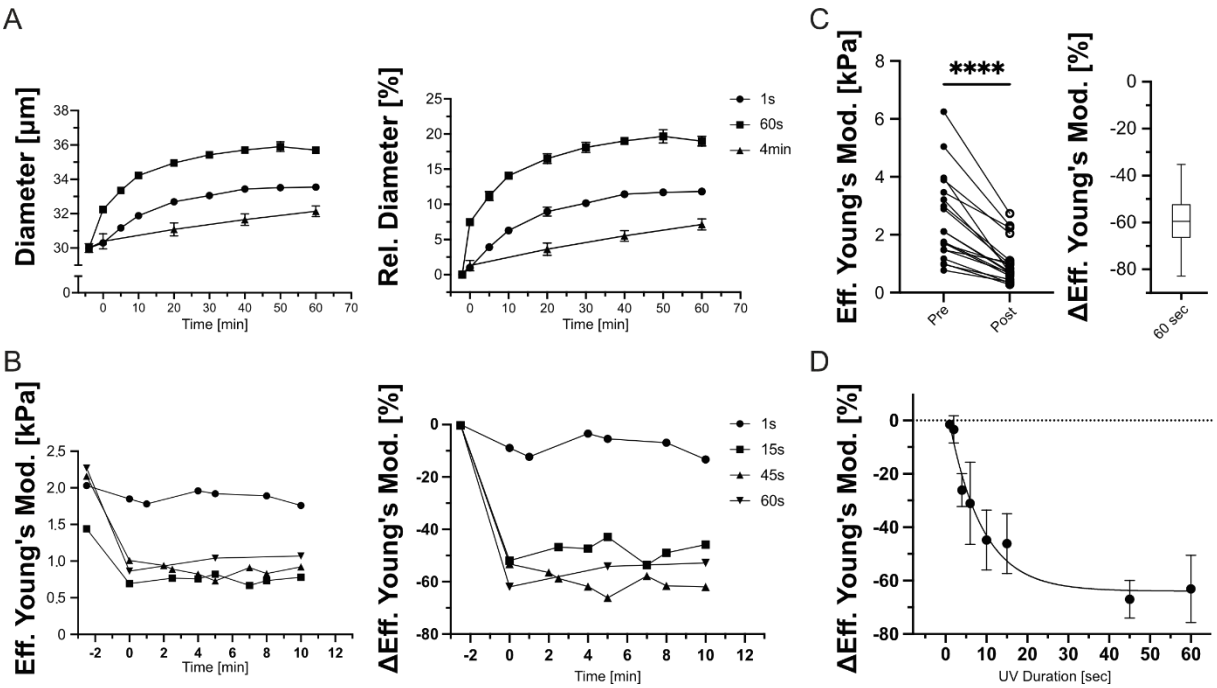


Figure 30: One time illumination diameter and stiffness characterization of the PDM. *A) PDM diameter changes over time and the corresponding relative change of one second, 60 seconds, and four minute illumination durations ± SD. B) PDM Effective Young's Modulus changes after illumination over time and the corresponding percentage decrease from the initial value. C) Stiffnesses before and after 60 second illumination of PDM in cell culture medium at 37°C on the left and average percentage reduction on the right. Statistical analysis was performed using unpaired two-way ANOVA with Tukey's correction for multiple comparisons. **** indicate p value of p < 0.0001. D) Percentage change from initial value over UV illumination duration ± SD. Exponential decay function fitted to the values. Data was generated by Yuxin Ji in her role as master student.*

Next the effect of repeated illumination on the PDM was investigated by additive illumination cycles and repeatedly characterizing the response of the material. An initial short illumination of four seconds was followed by an equilibration time of one hour before the re-measuring the stiffness of the PDM. The cycle was repeated two more times, each time illumination for an additional second, waiting for the microgel to equilibrate for one hour and re-measuring the stiffness. After the first cycle, the effective Young's modulus had decreased from an initial value of 2 kPa down to 1.2 kPa and decreased further to around 1 kPa and ultimately down to 0.8 kPa after the next two cycles (**Figure 31** A). In the end the additive illumination had incrementally and significantly reduced PDM stiffness by 50% of the starting value (**Figure 31** B). To distinguish the effect of subsequent illuminations the percentage change between consecutive measurements was calculated and while the initial difference of 30% did not change the difference between the first and second illumination was significantly lower with around 15%. Furthermore, the difference between the second and third illumination was with around

10% not significantly different to the previous illumination cycle, showing that the two shorter illuminations induced a comparable degradation in the PDM (**Figure 31** C).

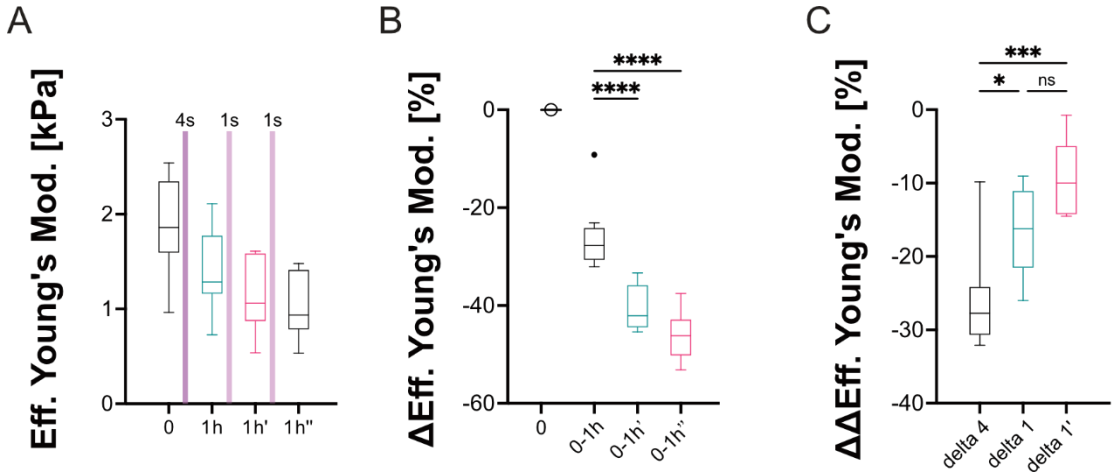


Figure 31: Additive illumination of photodegradable microgels (PDM). *A) Eff. Young's modulus ± SD. Three illuminations are highlighted with purple lines. First illumination was four seconds, followed by an equilibration time of one hour before nanoindentation. Second illumination was one second, followed by an equilibration time of one hour before nanoindentation. Last illumination was one second, followed by an equilibration time of one hour before nanoindentation. B) Percentage change from initial value ± SD. C) Difference between consecutive measurements ± SD. For B-C) statistical analysis was performed using unpaired two-way ANOVA with Tukey's correction for multiple comparisons. * indicate p value of p < 0.05, ** p < 0.01, *** < 0.001, and **** p < 0.0001. Data was generated by Yuxin Ji in her role as master student.*

Bio-functionalization of microgels

As a final step before integrating the microgels into an epithelium, their bio-functionalization with the adherens junction protein cadherin, presented in the correct orientation, was optimized. The functionalization pathway was inspired by the complexation of recombinant proteins by their histidine-tag with nitrilotriacetic acid (NTA) in purification columns. In short, an NTA moiety was covalently attached by ring opening reaction of the epoxy groups on the microgel surface. With the addition of a transition metal ion an intermediate octahedral complex is formed. To reach the desired structure two histidine of the histidine tagged recombinant cadherin complete the coordination sphere by replacing the transient water ligands.

In this work the heterobifunctional crosslinker HS-PEG-NTA was the primary NTA containing molecule as the PEG spacer allows a higher degree of flexibility and circumvents sterical hinderance issues with the complexation of the large recombinant cadherin. Furthermore, the commonly used transition metal for protein purification Ni^{2+} had to be replaced due to the reversibility of the complex, as such a liability could rapidly reduce the cadherin coating on the microgel surface during experiments. To circumvent this challenge, an established protocol was used which employed Co^{2+} as the initial complexing transition metal ion, taking advantage of the favorable complex formation constant and once the NTA-Co^{2+}His-Tag complex was established can be "locked" by oxidation of the of the transition metal ion with hydrogen peroxide. The resulting Co^{3+} complex has a significantly slower ligand exchange constant and is overall more resilient against chelating agents. Thus, the in-situ formation of the Co^{3+} complex nicely

circumvents the slow complex formation rate and yields a connection which can transmit the cell-generate forces into the hydrogel network of the microgel (**Figure 32** A).

As proof-of-concept histidine-tagged green fluorescent protein (HisTag-GFP) was attached to the surface of the microgel with the aforementioned protocol. Along with this, the optimal functionalization parameters in regard to the maximum surface concentration of the NTA moiety and protein were established. As insufficient concentration of the heterobifunctional crosslinker would leave unreacted epoxy groups on the surface of the microgel, which could undergo amine-epoxy ring opening reaction and covalently bind proteins unoriented to the surface. Although lower concentrations of HS-PEG-NTA exhibited a higher GFP signal from the respective controls, a higher signal as well indicated substantial unoriented attachment (**Figure 32** B). Overall, with the functionalization parameters established, the protocol could easily facilitate the attachment of recombinant cadherins, mainly E-cadherin and N-cadherin to the microgel surface. The successful attachment was validated by immunofluorescent staining (**Figure 32** C).

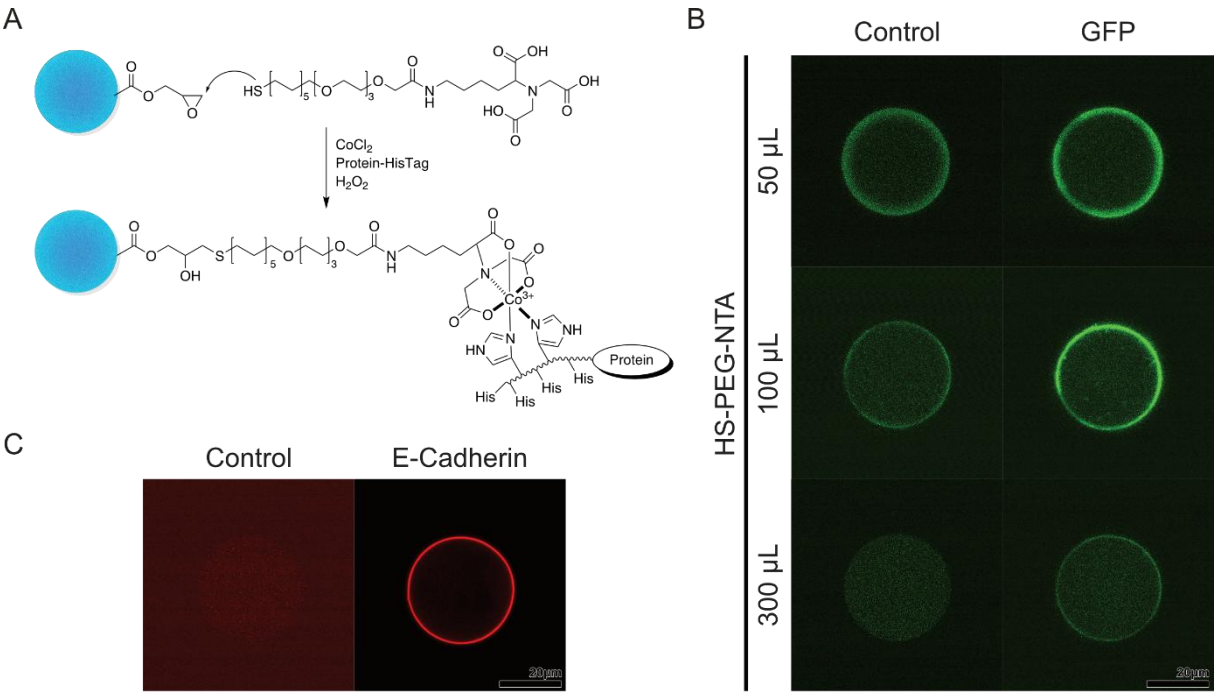


Figure 32: Oriented bio-functionalization of recombinant adherens junction proteins on the microgel surface. *A) Overview of the surface functionalization of Microgels with a heterobifunctional complexing crosslinker, subsequent complex formation by addition of transition metal ion Co^{2+} and HisTag-Protein with NTA moiety of the crosslinker and oxidation of the complexing ion into Co^{3+} for increase complex stability. B) Bio-functionalization of the microgel surface with green fluorescent protein (GFP) to distinguish between oriented adhesion and unspecific surface binding (Control). C) Bio-Functionalization of microgels with adherens junction protein E-cadherin and visualization by immunofluorescent staining. Images were generated by Yuxin Ji in her role as master student.*

Integration of photodegradable microgels within epithelial monolayers

Once the desired parameters had been achieved, namely degradability, size, and bio-functionalization, the cell-mimicking microgel could be integrated into the epithelial monolayer. To ensure effective integration into the epithelial monolayer bio-functionalized and control PDM were immobilized on the activated surface of glass-

bottom dishes prior to cell seeding. This would prevent the extrusion or displacement of the PDM by the surrounding cells during the co-culture experiment. Glass surface activation followed a protocol reported in literature[204,302] and in-short, an amine reactive aldehyde functionalization would react with bio-functionalized and control PDM to covalently attach them to the glass surface. Allowing bio-functionalized PDM to engage laterally with the surrounding monolayer through the formation of hybrid adherens junctions. While the approach works and effectively immobilizes PDM on the sample surface, an apparent drawback is the uncontrolled distribution of the microgels on the surface. Furthermore, spatial heterogeneity could lead to interference of overlapping effects during illumination experiments, which made regions of higher density less representative. Nevertheless, sample preparation was finished with an ECM coating of the remaining substrate surface, and the samples were ready to be used in co-culture experiments (**Figure 33**).

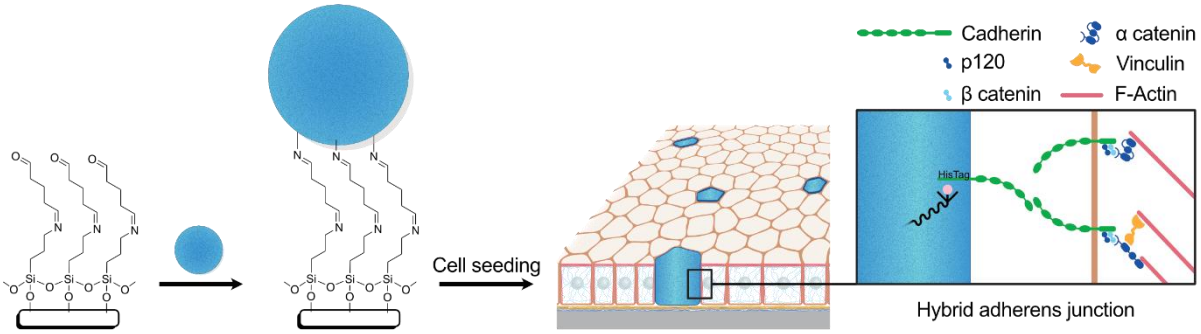


Figure 33: Schematic overview of microgel surface immobilization, cell seeding and co-culture interaction. *Initially the glass surface is activated through oxygen plasma treatment and functionalized with an amine-containing silane compound, which allows subsequent translation into an amine-reactive surface through the addition of glutaraldehyde. Onto this activated glass surface bio-functionalized microgels can be dispersed, resulting in covalent attachment to the substrate surface. After sterilization these samples can be utilized for cell experiments, forming hybrid adherens junctions.*

Integration of photodegradable microgels in Madin-Darby canine kidney epithelium

Madin-Darby canine kidney (MDCK) cells are one of the most common in vitro epithelial cell models as they excel in their ease of handling and quick proliferation. The experimental condition of the co-culture contained E-cadherin coated PDM co-seeded with MDCK cells, with uncoated PDM acting as a control. The effective Young's modulus of the PDM was around 2 kPa, matching cellular values of around 1 kPa[303]. The co-culture was tracked by live-cell imaging using an MDCK cell line expressing Lifeact-GFP, thereby providing fluorescently labelled actin. A significant drawback of the Lifeact-GFP presented itself in the non-specific labeling of the actin, as there was no difference between globular and filamentous actin, which meant that no fibrillar actin structures could be captured as the globular actin signal saturated the cell body. As the MDCK cells showed a high proliferation rate it became evident that the experiment had to be performed one day after seeding, as otherwise samples would become completely overgrown. Before illuminating the PDM to change its mechanical properties, a reference image was taken (t_0). Subsequently, the area of illumination was restricted by closing the

diaphragm of the microscope and singular PDM were illuminated with 60 seconds of UV light (3.83 mW/cm^2, 385nm, 20x objective). Right after illumination another image was taken to capture the quick tissue response (t_1), followed by two hours of equilibration before capturing the monolayer slow response (t_{2h}) (**Figure 34** top). In the control condition, the quick response showed an immediate diameter reduction of the PDM, while there was an increased signal intensity of actin in cells close to the microgel. Transitioning into the slow response domain, the signal intensity of actin reduced, but no further changes could be observed. In contrast, the cell around the unilluminated control PDM showed no significant changes during the observation period. For the bio-functionalized PDM, the quick response was illustrated by the PDM diameter, showing an immediate diameter reduction. However, in the slow response domain, a distinct difference could be observed, as cells started to cover and overgrow the bio-functionalized softened PDM. While the stiffness change induced a cellular response around the unilluminated bio-functionalized PDM showed no significant changes during the observation period. Unfortunately, mitosis and extrusion events were observed around the PDM during the observation period, adding unknown fluctuations and influencing monolayer dynamics. Overall, the motility and proliferation of the epithelium meant that the fluctuations of the monolayer were magnitudes above the induced force balance disruption, essentially making the changes invisible during the live cell imaging and stopping analysis at a qualitative level (**Figure 34** bottom).

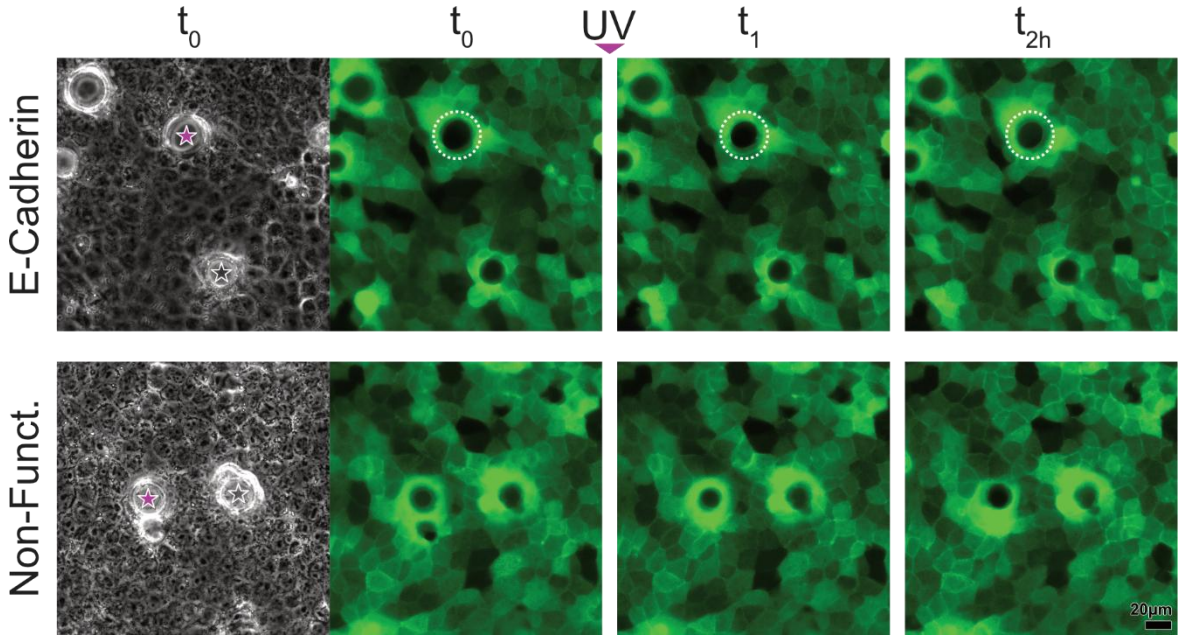


Figure 34: MDCK PDM co-culture live cell imaging of brightfield and Lifeact-GFP (green) signal at different time points. *Reference image before illumination is labelled t_0, UV illumination of 60 seconds (3.83 mW/cm^2, 20x objective) is indicated by UV, image immediately after illumination capturing the quick response is labelled t_1, and image after 2 hours of equilibration time to capture the slow response is labelled t_{2h}. Unilluminated microgels are marked with an unfilled star, while illuminated microgels are marked with a purple star. Images were generated by Yuxin Ji in her role as master student.*

After live cell imaging was completed, samples were fixed and immunofluorescent staining was performed for cytoskeletal markers like F-actin, or force transduction

proteins like α18-catenin. Additionally, tight junction marker ZO-1 and nuclei were stained. Beginning with the nuclei, the controls did not show any qualitative changes in orientation or density. However, the illuminated bio-functionalized PDM showed a noticeable increase in nuclear density near the microgel surface, as well as a preferential perpendicular orientation that follows the microgel's curvature (Figure 35 bottom row). The changes in morphology continued for the F-actin signal with a noticeable restriction of the basal microgel footprint by the surrounding cells in both non-functionalized controls. In contrast, microgels in both bio-functionalized conditions showed a larger basal attachment, independent of the state of degradation (Figure 35 bottom). While the unilluminated microgel showed the F-actin signal following the curvature of the microgel, the UV induced degradation of the PDM triggered an overgrowth by the surrounding cells, as previously observed in the live cell imaging. α-catenin is part of the protein complex connecting the intracellular domain of the E-cadherin to the actin cytoskeleton. Under tension, α-catenin structural conformation changes, and the antibody specifically recognizes its active conformation, highlighting tensile forces[304]. In the controls the signal is mostly concentrated at the lateral cell borders and no interactions with the PDM could be observed. For the illuminated bio-functionalized condition, the signal shows an increased intensity around the microgel. In contrast to the sharp signal from cell-cell junctions, the signal is weaker and spread over a larger area, indicating force generation within the cells connected to E-cadherin junctions. To complete the overview with the ZO-1 staining, the signal only showed cell-cell tight junctions, as the microgels only had E-cadherin on the surface; no tight junctions could be formed between microgels and cells. The main observation was that the monolayer barrier function was not disrupted. Overlaying the α18-catenin and F-actin signal, and generating the orthogonal view, highlights the different responses to the PDMs. Non-functionalized control microgels have a heavily restricted footprint with cells growing in a wedge-like manner underneath the PDM. Especially for the illuminated control, the activation of α18-catenin at the leading edge can be clearly observed, as the change in stiffness allows the surrounding cells to further restrict the microgel. On the other hand, the acceptance of the surrounding cells towards bio-functionalized PDM is evident by their larger footprint, but also from the side view, where the cells follow the curvature of the microgel. Furthermore, the overgrowth of the illuminated PDM becomes more apparent in the side view, where the basal activation of α18-catenin shows the force generation necessary for the enveloping movement (**Figure 35**).

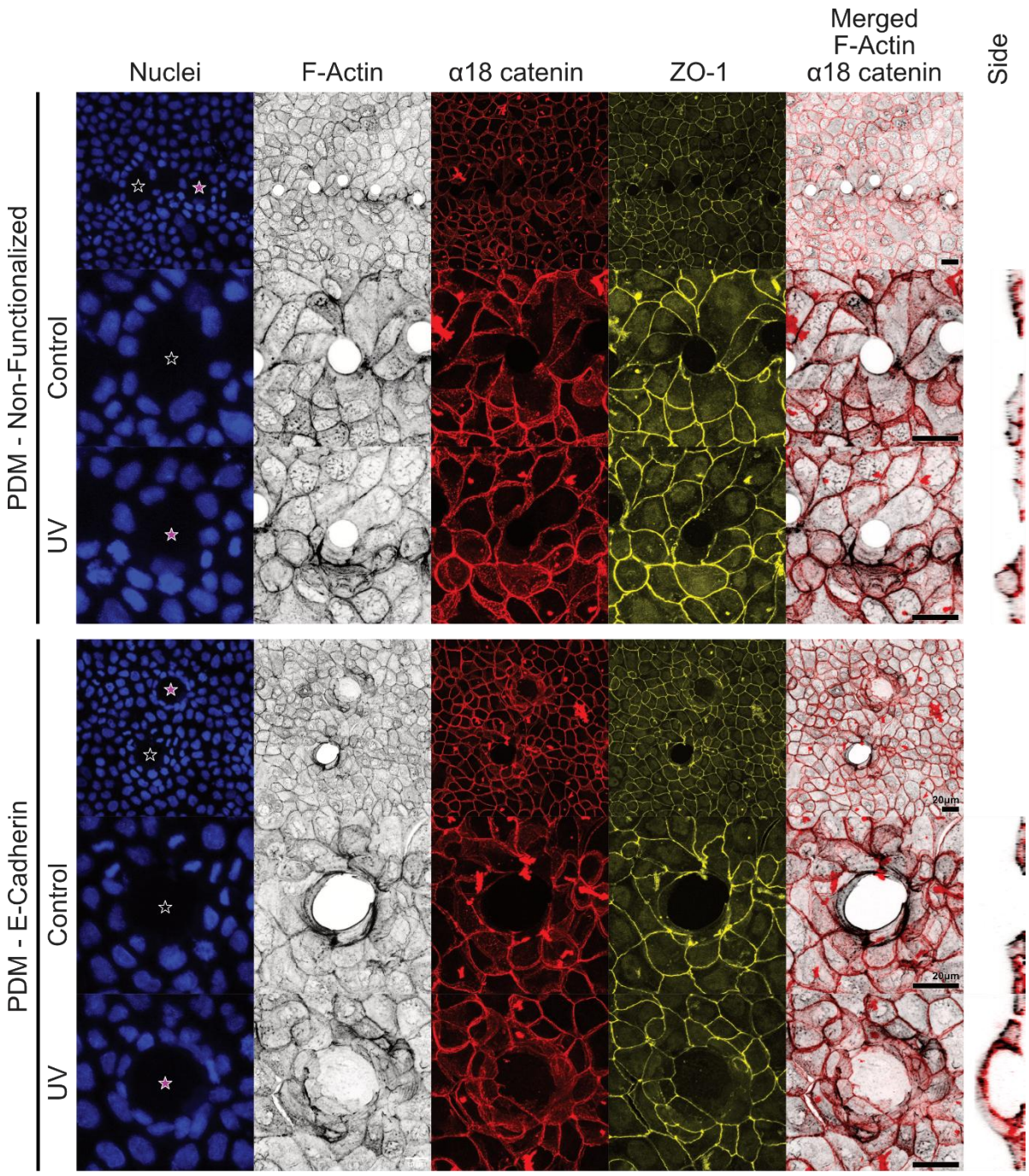


Figure 35:MDCK co-cultured with photodegradable microgels (PDM). *Maximum intensity projections and the relevant zoom-in for Nuclei, F-actin, α18-catenin and ZO-1 immunofluorescent staining. Furthermore, merged images of F-actin and α18-catenin and the respective orthogonal slices. Unilluminated microgels are marked with a black star, while illuminated microgels are marked with a purple star. All scale bars are 20 µm. Images were generated by Yuxin Ji in her role as master student.*

Live imaging and immunofluorescent staining of the MDCK PDM co-culture gave interesting first insights into the interactions between cells and cell-mimicking microgels. Unfortunately, major drawbacks of the system were discovered with MDCK cells exhibiting high motility and proliferation, which masked the tissue-scale force balance disruption induced by the UV degradation of the PDM. Nevertheless, PDM stiffness-dependent changes in cellular behavior could be observed but were not investigated

further. In conclusion, a less motile and proliferative epithelium is required to quantitatively evaluate the effect of the microgel-cell force perturbation.

Integration of photodegradable microgels in a retinal pigment epithelium model

To increase the relevance compared to the in vivo system a human induced pluripotent stem cell-derived retinal pigment epithelium (hiPSC-RPE) was employed as it excels through its intrinsic characteristics as a model system[99,302]. hiPSC-RPE forms a tall, polarized monolayer, and due to its postmitotic nature, once mature, reaches a not proliferative state in vitro[302]. Overall, the increased cell-microgel contact area enables microgels to integrate into the monolayer to a higher degree and the decreased motility as well as the non-proliferative nature minimize interference to the induction of a force balance disruption event.

Non-degradable microgel co-culture

Implementation of the hiPSC-RPE co-culture began with NDM. As NDM were employed as cell mimics the stiffness of the polymer network was set to match cellular values of 1-2 kPa. The synthesis condition employing 12wt% of PEG-A reached an average stiffness of 2 kPa and was used as the standard condition used in co-culture experiments for this chapter. During co-culture the observation was made that surrounding cells reacted differently to the presence of the microgel depending on the bio-functionalization. Microgels that were bio-functionalized with E- or N-cadherin experienced less deformation than non-functionalized control NDM (**Figure 36** A). This qualitatively showed that bio-functionalization was essential for cell-mimicking and integration into the monolayer, and unfunctionalized microgels would be recognized as foreign bodies. Subsequently, NDM induced a “removal reaction” from the surrounding cells, which resulted in a deformation of the microgel. Quantification of the observation was performed by calculating the deformation of the NDM from the major and minor axis after one week in cell culture. Non-functionalized NDM showed a significantly lower circularity in comparison to bio-functionalized NDM (**Figure 36** B).

From this observation it was assumed that cell-microgel interactions in cell culture influenced the stiffness of the NDM through the frequency and pressure of their actuation. The stiffness of the NDM was measured in culture and compared to pre-integration values. The non-functionalized NDM showed a reduction in effective Young's modulus from an average of 2 kPa to around 900 Pa after seven days embedded within the epithelial monolayer, with similar values measured at 14 days (**Figure 36** C). The stiffness of the bio-functionalized NDM was significantly higher, with the average only dropping to 1.5 kPa after seven days under co-culture conditions. The difference to the control became smaller, although still significant, after 14 days in co-culture as the average stiffness had reduced further to around 1 kPa (**Figure 36** C). This stark contrast in NDM stiffness, together with the previously observed change in circularity, was interpreted as a mechanically induced loss of polymer network cohesion in the non-functionalized NDM, as the polymer network itself had no degradable components.

As this change in material properties required force generation by the surrounding cells, the stiffness of the monolayer in relation to the distance of the microgel was investigated. Measurements of cells around non-functionalized NDM showed an average cellular stiffness of approximately 1.6 kPa across most measurement points, with a high standard deviation. In contrast, both bio-functionalized conditions consistently showed higher average stiffnesses of slightly below 2 kPa with similar high standard deviation over the measured distance (**Figure 36** D). Ultimately, for neither condition a distance dependent trend could be observed and the difference in average monolayer stiffness was surprising, as an opposite behavior was expected based on the previous observations.

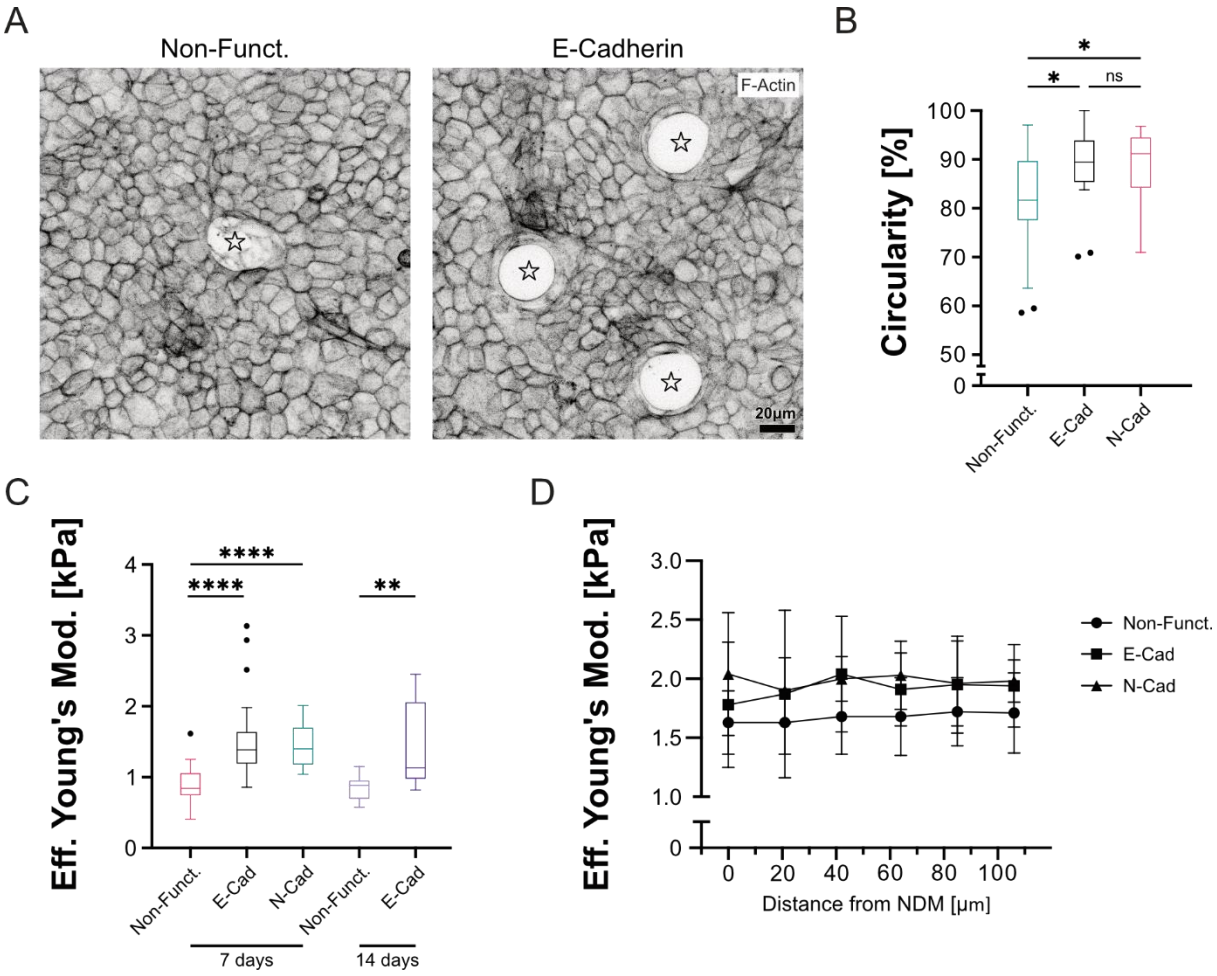


Figure 36: Morphometrical and mechanical parameters of the hiPSC-RPE non-degradable microgels (NDM) co-culture. *A) Representative F-actin staining of NDM. Microgels are marked by transparent stars. Scale bar is 20 µm. B) NDM circularity ± SD. p(E-cadherin vs non-biofunctionalized) = 0.0457; *p(N-cadherin vs non-bio-functionalized) = 0.0306. C) NDM effective Young's modulus ± SD. D) hiPSC-RPE effective Young's modulus in relation to the distance of the NDM ± SD. For B-C) statistical analysis was performed using unpaired two-way ANOVA with Tukey's correction for multiple comparisons. * indicate p value of p < 0.05, ** p < 0.01, *** < 0.001, and **** p < 0.0001. Data was generated by Alexandra Raab in her role as master student.*

The mechanical activity at the cell-microgel interface was investigated by immunofluorescent staining. Initial investigation, was focused on the mechanotransduction proteins vinculin and α18-catenin, which connect the cadherins to the actin cytoskeleton and highlight a potential force transduction between the protein coating of the NDM and the surrounding cells. Investigating the distribution and intensity

of vinculin (**Figure 37** top) and α18-catenin (**Figure 37** bottom) separately, two different samples were prepared keeping the other immunofluorescent staining targets constant. Beginning with the shared staining target the maximum intensity projections of the nuclei signal of both samples showed an even distribution with no preferential orientation visible. Furthermore, the F-actin signal of either sample showed a regular distribution with sharp signals at the cell-cell boarders and cell-microgel interfaces. Lastly, the N-cadherin immunofluorescent staining localized at the cell-cell boarders but did not show a signal for the N-cadherin coated microgels. Moving to the separate mechanotransduction proteins, the immunofluorescent staining of vinculin showed a diffuse distribution in the cytoplasm for most of the cells, with some cell-cell borders showing a higher intensity. Especially at the cell-microgel interface high intensity regions could be observed, indicating increased force generation on the cell side. Combining the vinculin signal with the adherens junction signal in a composite image highlighted the proximity of the high intensity regions with the N-cadherin of the cells (Figure 37 Top, marked with arrows). Furthermore, the same region in the composite orthogonal view shows an overlapping signal mixing at a lateral location, indicating an increased recruitment of vinculin to the cadherin-mediated microgel-cell interface.

On the other hand, the immunofluorescence staining of α18-catenin showed a defined signal at cell-cell junctions, with no increased affinity to localize at the cell-microgel interface. By overlaying the α18-catenin signal with the adherens junction signal the resulting composite image highlighted the co-localization with a combined signal in yellow, producing a non-continuous delimitation line at the apical microgel-cell contact. Furthermore, the composite of the orthogonal view showed both signals overlapping at the lateral and apical cell cortex, indicating the presence of the open α18-catenin conformation at the cadherin mediated microgel-cell interface (Figure 37 bottom, marked with arrows). Overall, these observations suggested a force-active hybrid adherens junctions between NDM and surrounding cells.

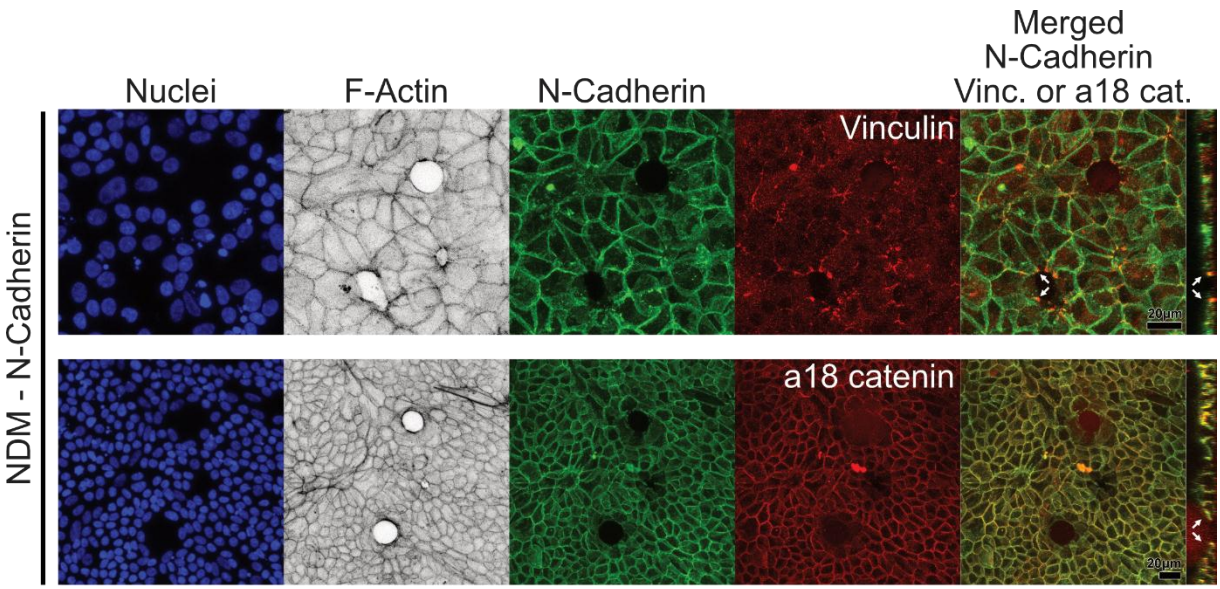


Figure 37: Nuclei, cytoskeleton (F-actin), adherens junction (N-cadherin) and mechanotransduction protein immunofluorescent staining of a seven day hiPSC-RPE co-culture with N-cadherin bio-functionalized non-degradable microgels (NDM). *Composite image shows the respective mechanotransduction protein signal merged with the adherens junction signal in top-down and orthogonal view. All scale bars are 20 µm. Images were generated by Alexandra Raab in her role as master student.*

The culturing time of the NDM hiPSC-RPE co-culture was prolonged to 14 days to investigate the maturity of the epithelial monolayer, focusing on two essential functionalities. First, the polarity and potential ability to perform phagocytosis of the photoreceptor outer segments were investigated by elucidating the microvilli development through immunofluorescent staining of Ezrin. Ezrin acts as a linker protein that connects the cell membrane with the actin cytoskeleton and it's enriched in RPE at the apical microvilli, functioning as a marker. The second area of interest focused on the barrier function of the epithelial monolayer by staining the tight junction protein ZO-1 (**Figure 38**).

Investigation of the baseline parameters shows that the nuclei and F-actin signal is present with expected patterns in distribution, localization and intensity. The top-down view showed an even distribution of Ezrin signal, indicating microvilli formation throughout the monolayer. The slanted sides of the cells, which grew underneath the curvature of the microgel, did not show an Ezrin signal, enforcing the lateral binding character of the microgel surface protein coating. The ZO-1 signal showed the characteristic localization at cell-cell boarders, with sharp lines at the apical cortex of the cells (**Figure 38**). As the NDM did not possess tight junction proteins, no demarcation line at the cell-microgel interface could be observed. Furthermore, microgel-adjacent cells extended the tight junctions at the interface towards the basal cortex, which could weaken the integration of the NDM into the epithelial monolayer. Composite images of the Ezrin and ZO-1 signal suggested that embedded NDM generated an Ezrin exclusion zone with adjacent cells not expressing any signal. As stated previously, and evident from the orthogonal view, the decreased intensity of Ezrin signal follows an artificial curvature which, together with the shrunken NDM (regular diameter around 40 µm, observed

diameter in the sample 30 µm), suggested a reduction in NDM diameter induced by the fixation protocol, resulting in the observed artefact.

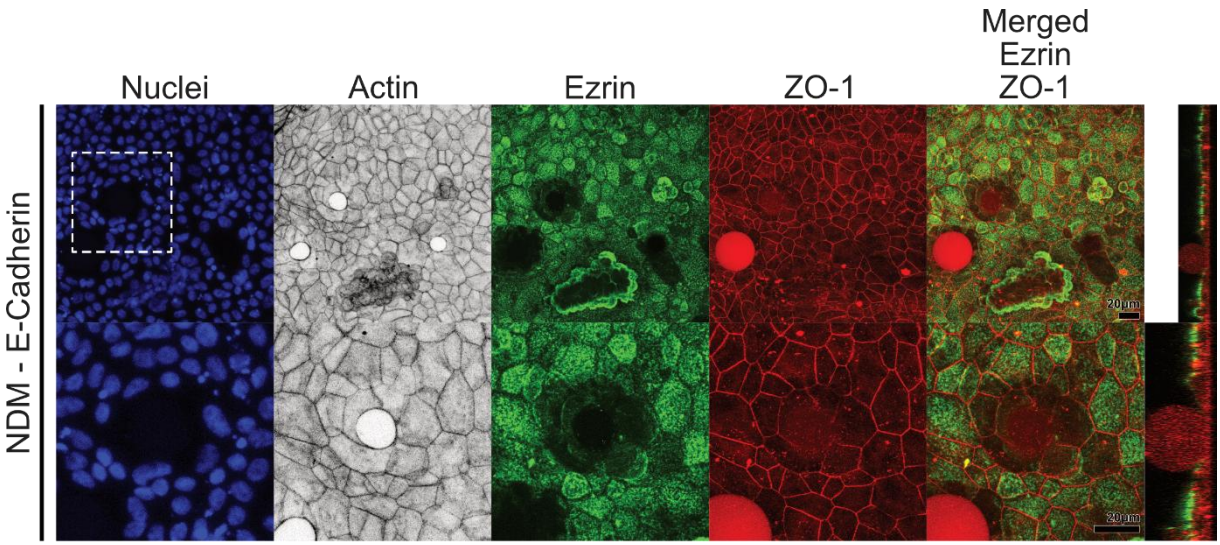


Figure 38: Nuclei, cytoskeleton (F-actin), polarization (Ezrin) and tight junction (ZO-1) immunofluorescent staining of 14 days hiPSC-RPE co-culture with E-cadherin bio-functionalized non-degradable microgels (NDM). *Composite image of polarization and tight junction marker in top-down and orthogonal view. Zoom-in is indicated by dashed square and all scale bars are 20 µm. Images were generated by Alexandra Raab in her role as master student.*

Photodegradable microgel co-culture

With the incorporation of photodegradable crosslinker in the microgel network, the stiffness of the polymer network could be reduced by on-demand UV illumination. Through specific bio-functionalization, this mechanical perturbation would be transmitted to the surrounding epithelium, thereby challenging its homeostatic equilibrium. To assess the effects of induced force balance disruption on a mature epithelium, one-week-old PDM-hiPSC-RPE co-cultures were incubated with the live dye SiR-Actin to track the cellular changes in the cytoskeleton. In short, the force disruption experiment had three distinct stages. In the first stage, a reference image was taken before illuminating the PDM (385 nm, 60 seconds, 3.83 mW/cm^2, 20x magnification). Directly transitioning into the second stage, where an image was taken to capture the fast response of the surrounding monolayer. In the last stage, after one hour of equilibration time for the monolayer to adjust to the changed force balance, another image was taken to capture the slow response. Beginning with the non-functionalized unilluminated control, the PDM-adjacent cells exhibited a strong F-actin signal at the apical cell-microgel contact, forming a discontinuous ring that remained unchanged during the observation time. The unchanged intensity and shape of the signal indicated a force balance between the cells exerting a compressive force on the microgel (**Figure 39** Top left). A similar state is observable for the illuminated non-functionalized control PDM, in which the surrounding tissue expressed a discontinuous F-actin signal at the apical cell-microgel contact. Upon UV illumination, no change in the cellular F-actin signal is observed in the quick response domain. Furthermore, the circumference of the microgel stayed unchanged. Even in the slow response domain, the changed mechanical state of

the PDM hydrogel network does not induce a tissue response, with the F-actin signal showing an unchanged intensity and distribution (**Figure 39** Top right).

Non-illuminated cadherin bio-functionalized PDM proved to be well integrated into the tissue, as evidenced by an even F-actin distribution at the apical cell-microgel interface. In fact, the bio-functionalization of the PDM engaged cellular adherens proteins and supported the formation of a lateral actin cortex facing the microgel. Over the observation period, no change in F-actin structure in the control was noticed. The reduction in intensity is due to an unfortunate shift in focus, occurring because of thermal expansion of either the microscope stage or the glass bottom dish. The even F-actin signal at the apical cell-microgel contact could be observed in the unilluminated reference image of the bio-functionalized PDM (**Figure 39** bottom left). Upon UV illumination, a collapse of the microgel diameter in the quick-response domain could be observed with the cellular F-actin signal moving radially inward. This homogenous response to the softening of the PDM hydrogel network indicated a connection between the microgel and the surrounding tissue, allowing the change of mechanical state to exert a force on the adjacent cells. Furthermore, the mechanical actuation is highlighted by surrounding cells being pulled inwards and expanding in area (**Figure 39** bottom right, highlighted by arrows). After one hour of equilibration time, the force balance had shifted again with a slight expansion of the microgel diameter and the cellular F-actin signal increasing in intensity and diffusing into the cell body, which suggested a force-activated reorganization of the cytoskeleton of the adjacent cells (**Figure 39** bottom right). Overall, the experiment showed a distinct difference in cellular response to stiffness changes of the PDM depending on the presence of protein coating and duration since the UV-induced softening.

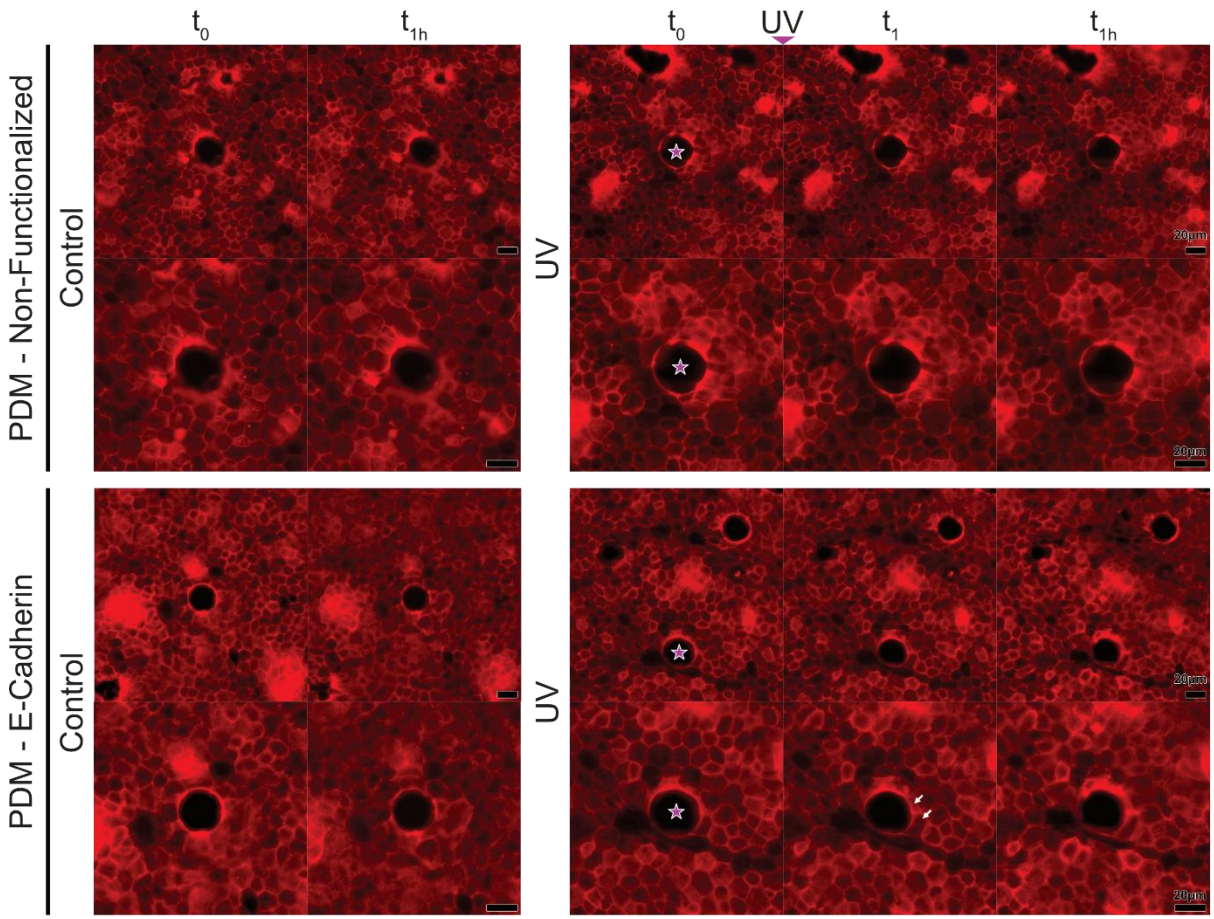


***Figure 39: Live cell imaging of photodegradable microgels (PDM) hiPSC-RPE co-culture by fluorescent SiR-Actin live cell actin probe**. Before (t_0) and directly after (t_1) UV illumination (60 seconds, 3.83 mW/cm^2, 20x magnification) of the PDM, as well as after an equilibration time of one hour (t_{1h}). All scale bars are 20 µm. Images were generated by Yuxin Ji in her role as master student.*

Mechanical adaptation analysis

Building on the qualitative assessment of the live cell imaging, the effects of PDM degradation on the surrounding tissue were quantified. The analysis was divided into two levels of abstraction: first, cellular parameters and calculating the shape factor were quantified as a morphometric descriptor, and second, the monolayer displacement through particle image velocimetry (PIV) was analyzed.

Morphometric changes in the tissue induced by photodegradable microgel degradation

Cell segmentation within the monolayer was performed using Cellpose, and individual cell tracking was attempted throughout the experiment; however, both segmentation and tracking lacked sufficient reliability. Simplifying the analysis, only reference images from the quick and slow response domains were considered, and to analyze spatial differences in cell behavior, cells were grouped into three concentric layers based on their distance from the microgel center: an inner layer (0–25 µm), an intermediate layer (25–35 µm), and an outer layer (35–45 µm) (**Figure 40** A). This grouping would allow for a more comparative analysis of the average cell response in relation to the distance of the microgel and consequently the defect point. From the measured perimeter and area, the shape factor

was calculated, which is a dimensionless parameter reflecting the morphology and mechanical state of the cells in the different layers, with higher values indicating a more fluid state and lower values reflecting a more rigid state.

The unilluminated non-functionalized PDM showed the lowest shape factor over the observation period indicating a rigid arrangement of cells around the PDM, suggesting the microgels to be recognized as a foreign object. Cellular behavior is consistent throughout the two outer layers, while showing slight elevation of the values, while no fluctuations could be observed (**Figure 40** B). On the other hand, the illumination of non-functionalized PDM elicited a pronounced response by the cells of the first layer, with the shape factor increasing from 3.95 to 4.15 during the quick response domain and reaching an extreme value of around 4.4 in the slow response domain. This cellular response, although much less pronounced, was also present in the second layer, with the shape factor increasing from 3.9 to 4.0 during the quick response domain and increasing slightly more in the slow response domain. Surprisingly, the third layer is not influenced by the change in stiffness of the PDM. The transition into a highly fluid state of the cells in the first and second layer after the degradation of the non-functionalized PDM hydrogel network and its subsequent softening showed a coordinated response which aligned with cells reattempting to remove a foreign body, which had undergone degradation (**Figure 40** B). Next, the unilluminated bio-functionalized PDM showed a higher shape factor than the non-functionalized control PDM in all the layers with only minor fluctuations during the period of observation. Indicating a more fluid like state of the cells surrounding the bio-functionalized PDM (**Figure 40** B). Upon illumination of the bio-functionalized PDM the shape factor of the surrounding cells showed the adaptation to the induced force balance disruption generated by the degradation of the PDM. With the average shape factor of 4.05 for cells in the first layer declining below 3.95 in the quick response domain as cells “tensed up” and adapted a more ridged state. In the slow response domain cells in the first layer “relaxed” and readapted a more fluid tissue state. Cells in the second layer showed an increase in shape factor over the observation period from 3.9 to around 4.1. This increased motility in the second layer stands in contrast to the solidification of the first layer in the quick response domain, while the behavior in the slow response aligns with both layers adapting a fluid state. Cells in the third layer showed no fluctuation in shape factor. Overall, the response of the cells in the first layer to the force disruption from the PDM showed a temporal rigidification of the first layer, which suggested an attempt in dampening of the mechanotransduction into the surrounding tissue. Nevertheless, an increase in shape factor in the second layer indicates that the protective response was overcome and the two inner rings had to adapt a fluid state to reorganize into a new mechanical homeostasis. To overcome the limitations of cell segmentation, a complementary approach based on image velocimetry was employed to capture the propagation of force transduction waves independently of cellular morphology (**Figure 40** B).

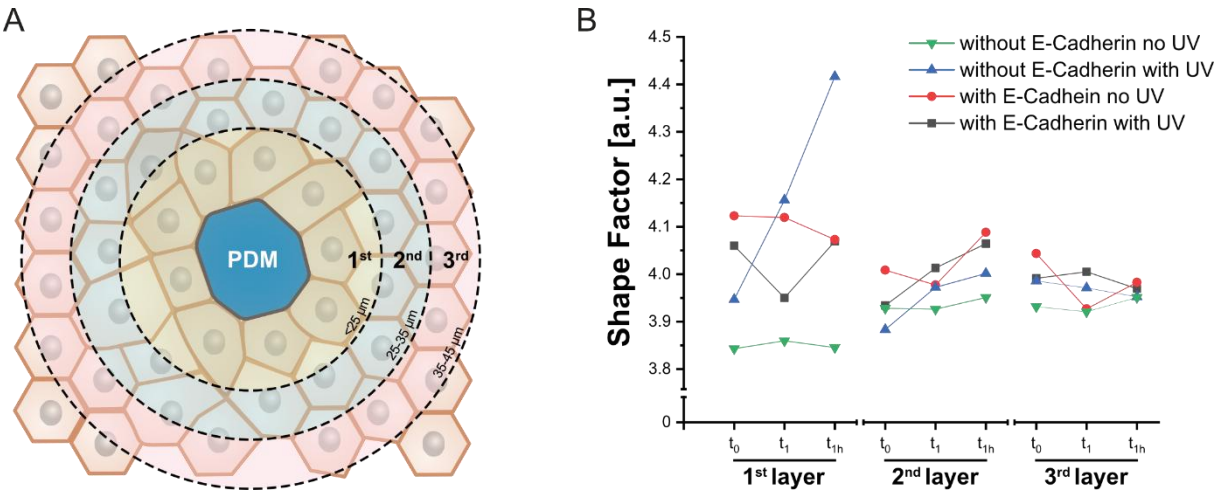


Figure 40: Shape factor quantification in relation to the distance to the photodegradable microgel (PDM) in the PDM hiPSC-RPE co-culture over time. *A) Schematic representation of cell segmentation and grouping into regions depending on the distance to the PDM. B) Line graph of shape factor for the different layers over time. With t_0 being the reference image, the quick response domain at time point t_1 directly after UV illumination and the slow response domain at time point t_{1h} after one hour of equilibration time. Data was generated by Yuxin Ji in her role as master student.*

Particle image velocimetry

The particle image velocimetry followed the basic technique of velocity field measurement between two images and was used to visualize and quantify the microgel-induced force balance disruption in the quick and slow response domains. Beginning with the unilluminated non-functionalized PDM condition, the surrounding monolayer showed an even distribution of background activity during the quick response, with no preferential orientation of the vectors in the velocity field or regions of higher magnitude. Similarly, in the slow response domain neither the vectors of the velocity field nor the magnitude exhibited significant orientation or intensity. Furthermore, the area of the microgel is characteristically empty due to the microgels having no markers which could be captured during epifluorescence imaging and surrounding cells not engaging with the non-functionalized PDM (**Figure 41** A). For the illuminated non-functionalized control PDM no preferential orientation can observed. Although, an increase in vector magnitude in the tissue surrounding the PDM was present during the quick response. While the orientation stays unorganized in the slow response domain the magnitude map showed that larger areas of activity had moved closer to the boarder of the PDM. This suggested that the surrounding tissue sensed the change in PDM stiffness and coordinated a coherent response but without an active force balance disruption permeating from the degraded PDM. This is supported by the observation that the PDM and especially the surrounding cells did not show any movement, underlining the missing force transduction due to the absence of bio-functionalization (**Figure 41** A). In the quick response domain non-illuminated bio-functionalized PDM exhibited vectors much closer to the microgel, indicating integration of the PDM through active forces at the cell-microgel interface mediated by adherens-like junctions. Furthermore, the magnitude of the vectors showed an even distribution, highlighting the homogenic force balance state of the tissue. In the slow response domain, the vector field exhibited an even distribution with no preferential orientation. Unfortunately, the magnitude field was dominated by a local inhomogeneity

reducing the interpretability. Nevertheless, activity around the microgel is evenly distributed, although much further spaced from the center of the PDM (**Figure 41** A). Illuminated bio-functionalized PDM had the ability to transduce the stiffness changes into the surrounding monolayer, which was nicely captured by the vector field of the quick response showing a preferential inwards-directed radial orientation at the cell-microgel interface. While the vector field further from the interface did not show an oriented response, with a mostly random orientation. Only for a limited region at the bottom of the frame a preferential orientation towards the force balance disruption site could be observed. This highlighted a distance-dependent response with a stronger impact to cells at the interface of the PDM than cells further away. Transitioning into the slow response domain a coherent reorientation of the vector field could be observed with larger clusters showing outwards-directed radial orientation from the force disruption site. Although the magnitude map was affected by local inhomogeneity an outward moving wave front could be observed (**Figure 41** A, highlighted by arrows). The PIV analysis highlighted a distinct cellular response in the vector field and its magnitude mapping for illuminated bio-functionalized PDM in comparison to the control conditions.

Preliminary quantification of the vector magnitude field was performed for the available samples, while not enough technical repetitions for statistical significance were available, the analysis revealed an interesting trend. In the quick response domain, a continuous increase in median vector magnitude from the non-functionalized controls towards the bio-functionalized samples was observed. Furthermore, UV induced degradation of the bio-functionalized PDM resulted in an additional increase, although the variance increased substantially. In the slow response domain, a similar difference between non-functionalized and bio-functionalized samples was evident, although the UV illumination of non-functionalized PDM resulted in an increase of median vector magnitude leading to a similar distribution as the non-illuminated bio-functionalized samples (**Figure 41** B). Nevertheless, a substantial increase in the median vector magnitude distribution of the illuminated bio-functionalized PDM was evident in comparison to the slow response of the other samples. Thus, quantification highlighted the importance of biofunctionalization in combination with the UV illumination on effective force transmission of the PDM degradation into the surrounding tissue (**Figure 41** C).

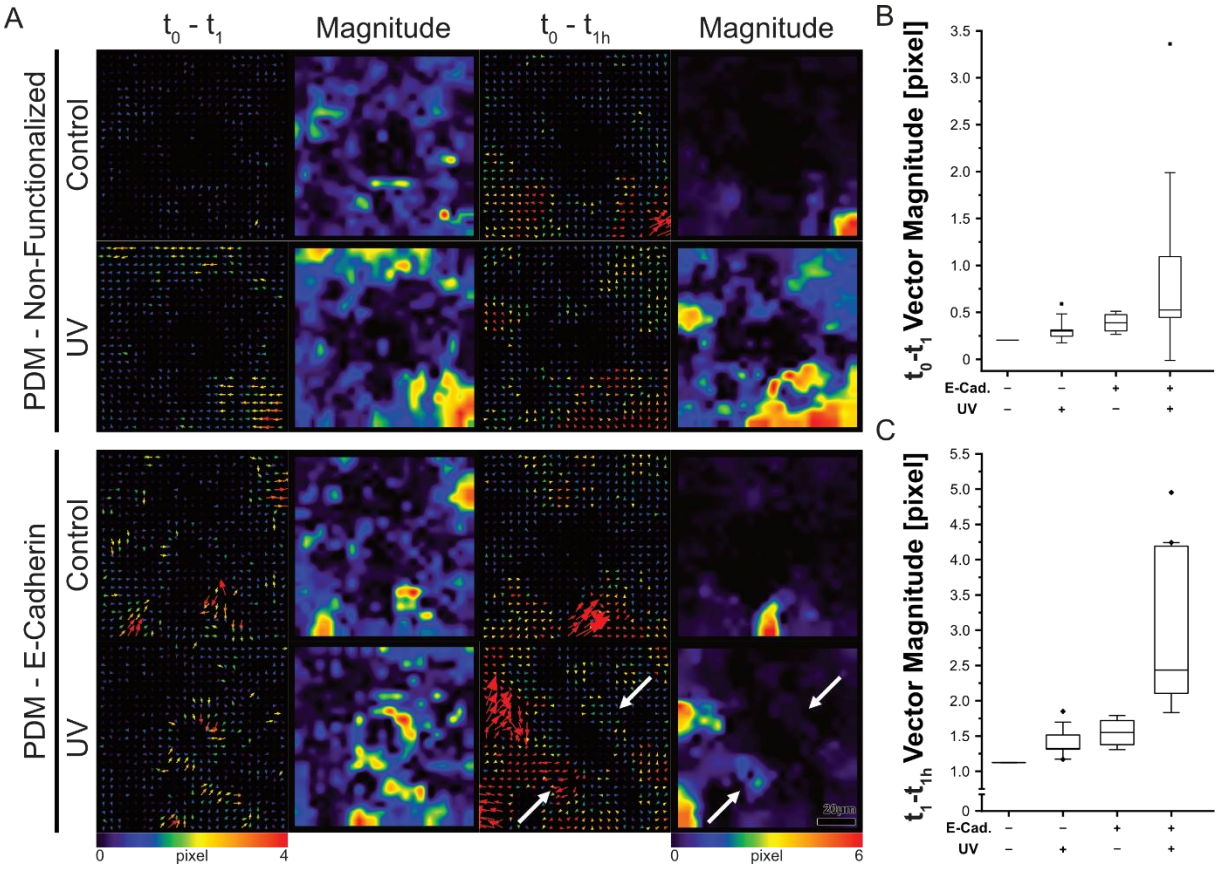


Figure 41: Particle image velocimetry (PIV) of photodegradable microgel (PDM) hiPSC-RPE co-culture. *A) Vector field and magnitude map. B) Quantification of the median vector magnitude in the quick response domain from t_0-t_1. C) Quantification of the median vector magnitude in the quick response domain from t_1-t_{1h}. Images were generated by Yuxin Ji in her role as master student.*

Overall, the qualitative and quantitative investigations highlighted substantial differences in depending on the state of functionalization and UV illumination in the PDM hiPSC-RPE co-culture. This distinct behavior motivated further investigation of the difference in expression and arrangement of cytoskeletal, as well as mechanotransduction and adherens junction proteins in the PDM hiPSC-RPE co-culture by immunofluorescent staining.

Immunofluorescent staining of mechanotransduction relevant proteins

To highlight the difference in expression and arrangement of cytoskeletal and adherens junction proteins in the PDM-hiPSC-RPE co-culture, immunofluorescent staining of samples fixed one hour after UV illumination was performed, to capture the monolayer behavior during the slow response domain. Bio-functionalization of the PDM with E-cadherin produced a surface coating that engaged the adherens junction complex of adjacent cells. This activated a force transmission cascade involving the mechanosensitive protein α18-catenin, which connects to the actin cytoskeleton and drives contractility via myosin motors, making all three targets essential for dissecting the disruption of force balance and the ensuing cellular responses (**Figure 42**).

For the unilluminated non-functionalized control PDM the analyses of nuclear orientation did not show any preferential directionality, although a longer distance to the cell-

microgel interface was noticeable. While investigating the force transmission cascade, the immunofluorescent staining of the α18-catenin protein highlighted the deformation of the microgel, with especially high signal intensity at the cell-cell junctions bordering the interface. The increased presence of the force dependent open conformation of alpha catenin (i.e., α18 catenin) highlights the necessity of additional recruitment of cytoskeletal components to stabilize the compressive force balance developed by the surrounding cells. Furthermore, this observation is supported by the immunofluorescent staining of pMLC, which generally highlights actomyosin contraction and is present in the samples at an elevated intensity as a diffuse signal around the microgel. The F-actin signal matched the pMLC signal around the microgel closely, although throughout the monolayer it showed a higher intensity at the cell-cell boarders.

Moving to the next condition, the illuminated non-functionalized PDM induced no preferential orientation of the nuclei, while the noticeable distance to the cell-microgel interface was maintained. Furthermore, in the α18-catenin it could be observed that the microgel partially regained its circularity after UV induced degradation. Nevertheless, the signal of the immunofluorescent staining of the cell-cell junctions facing the cell-microgel interface still showed an increased intensity. A substantial change in signal expression in the immunofluorescent staining of the pMLC could be observed. The signal had become sharper and precisely localized at the cell-microgel interface, suggesting an intercellular contraction to constrict the degraded non-functionalized PDM further. The F-actin signal on the other hand, had not changed completely, with a diffuse signal on one side of the microgel while the other showed a shape demarcation line. In the orthogonal view of the composite between α18-catenin and F-actin the observation was made that cells formed a wedge like protrusion towards the microgel, which correlated with high intensity signal from the F-actin channel and supported the previous observation of actin network reorganization to constrict the softer PDM (**Figure 42** second column).

For the unilluminated bio-functionalized PDM the nuclei were noticeable closer to the center of the microgel, occasionally showing slight elongation and a perpendicular orientation towards the curvature of the microgel. While the α18-catenin signal had a strong presence at the cell-cell junctions facing the cell-microgel interface, similar to the controls, it also showed a pronounced delineating signal at the apical cell-microgel contact, indicating active force generation through the cell-microgel E-cadherin protein adherens junctions (**Figure 42** highlighted by arrows). Furthermore, immunofluorescent staining of the pMLC showed a strong expression at the basal and apical cell-microgel contacts and in general microgel adjacent cells exhibited elevated pMLC signal intensity compared to the monolayer further out. The F-actin signal followed this trend, showing a reinforced actin cytoskeleton at the cell-microgel interface. In the orthogonal view of a composite image from the F-actin and α18-catenin signal showed a tall monolayer, with cells following the curvature of the embedded microgel. The previously observed increased actin cytoskeleton recruitment to the interface could be observed with co-localized signal from the α18-catenin, which highlighted force generation over the

complete contact area. The overexpression of the F-actin at the cell-microgel interface suggested a compensatory reaction to the relative low concentration of E-cadherin on the microgel. As the typical cadherin bundling cannot happen with the covalently anchored microgel proteins, the few cellular E-cadherin which are engaged with microgel bound E-cadherin must recruit additional cytoskeletal components to support the concentrated force generation (**Figure 42** third column).

Lastly, the UV illumination induced degradation of bio-functionalized PDM resulted in an increased distance of the nuclei to the center of the microgel, while maintaining their slightly elongated morphology and perpendicular orientation. The expansion of the microgel diameter could be observed in the α18-catenin immunofluorescent staining, with the delineating line still present at the basal and apical cell-microgel contact (**Figure 42** highlighted by arrows). Similarly, in the pMLC staining both basal and apical circular signals around the microgel, although the intensity of the apical contraction had reduced in comparison to the basal signal. The F-actin signal showed the same signal distribution, with a pronounced ring at the basal and a less pronounced and discontinuous ring at the apical cell-microgel contact. In the orthogonal composite view of the F-actin and α18-catenin signal, it was observed that the monolayer around the embedded microgel had greatly reduced in height. Nevertheless, co-localization of the F-actin and α18-catenin signal supported the presence of a E-cadherin-based force generation between the cells and microgel. The contact plane angle decreased upon microgel softening, consistent with a disruption of the pre-tensed network's force balance. This can be interpreted as the removal of a central connection node, causing the surrounding tension to collapse and propagate through the monolayer, ultimately resulting in morphometric changes such as a reduction in monolayer height (**Figure 42** fourth column).

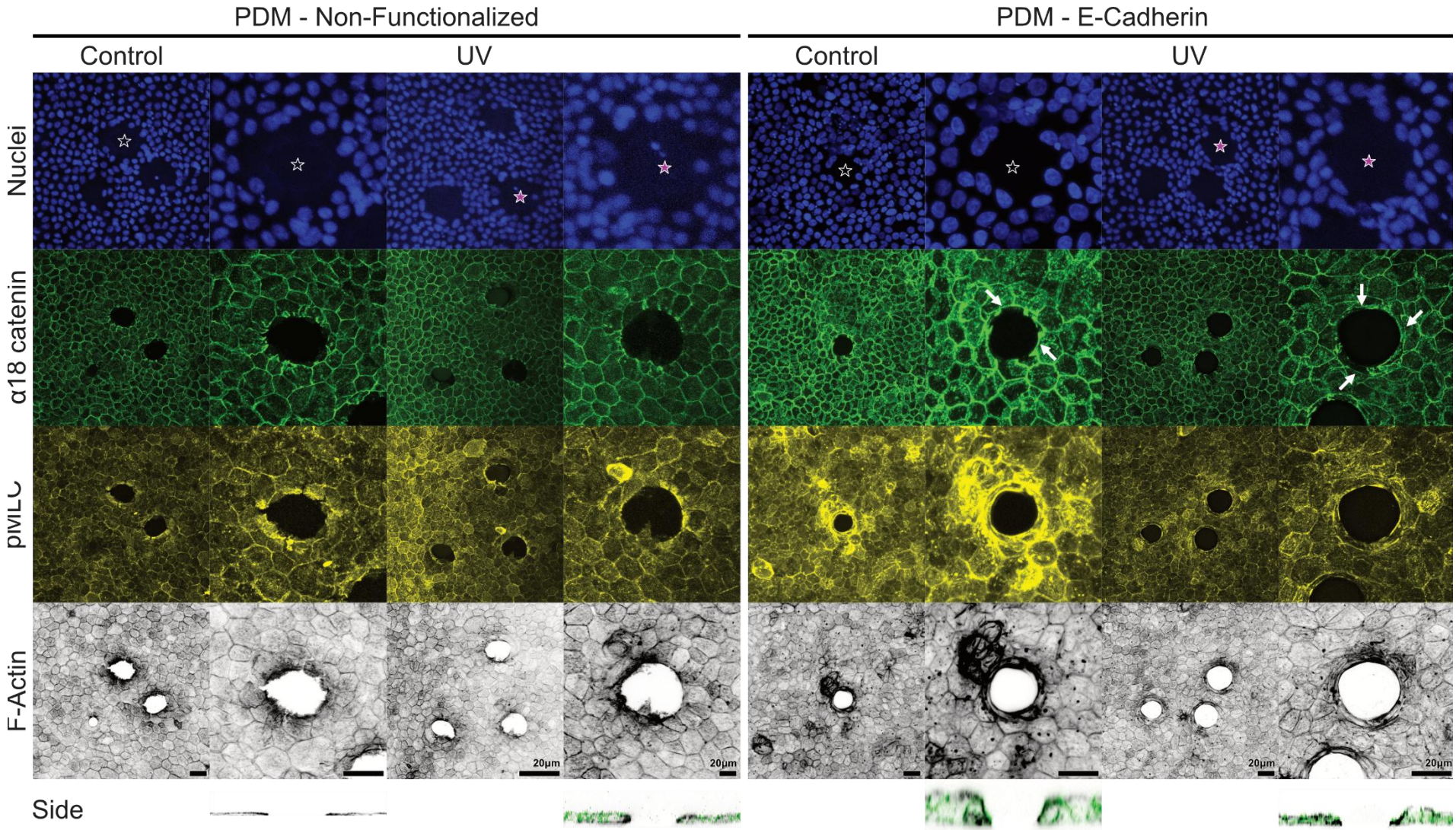


Figure 42: Immunofluorescent staining of Nuclei and mechanotransduction relevant proteins in photodegradable microgel (PDM) hiPSC-RPE co-culture. *Images are maximum intensity projections of complete imaging stack. Unilluminated microgels are highlighted with a transparent star, illuminated microgels are highlighted with a purple star and all scale bars are 20 µm. Images were generated by Yuxin Ji in her role as master student.*

IV. Discussion

1. Photodegradable hydrogel as artificial drusen mimic

In this work, a hydrogel substrate for epithelial cell culture was successfully established and used to investigate tissue level response to dynamic ECM perturbations. The PDH achieved on-demand localized topographical changes, overall stable substrate stiffness and a relevant ECM coating as a simplified in vitro model. Overall, the RPE monolayers adapt to ECM building in a way that more closely resembles in vivo progression of early formation of drusen, without the immediate and severe loss of polarity or cohesion associated with acute or non-physiological deformations[143,305].

Artificial drusen characterization

The bulk stiffness of the PDH was tuned to an in vitro-relevant range without affecting its photodegradable characteristics, and topographical defects introduced, surprisingly, did not produce a significant change in stiffness. While the network degradation mechanism was not investigated in detail, two explanations were formulated which explained the unchanged stiffness of the swollen topographical defects in comparison to the pre-degraded state. In the first possible explanation, the UV light induced reduction of the crosslinking density and the influx of water into the localized topographical defect leads to an increased tension on the polymer chains, which are anchored to the surrounding un-degraded hydrogel. The osmotic pressure induced partial stretching of the polymer network alters the mechanical response to the compressive modulus measurements of the nanoindenter and results in stiffness values comparable to the pre-degraded network.

An alternative explanation takes the absorbance of the photodegradable crosslinker into account. From the immunofluorescent staining experiments, a relatively high absorbance in the UV-blue light range could be observed which is also reported in literature[187]. As the light source illuminates the sample from bottom, the intensity is reduced towards the surface of the substrate. While the average dose exceeds the threshold necessary for topographical defect formation the surface of the substrate is intrinsically protected so that the employed dosage does not lead to a measurable change in stiffness as the topographical defect formation is driven by degradation and swelling of a volume in the hydrogel. Overall, this stable substrate stiffness allowed to connect the observed changes in the epithelial monolayer exclusively to the size of the induced topographical changes.

Bio-functionalization strategies of the photodegradable hydrogel

In this work, a method was established which facilitated even ECM coating on the PDH and allowed for the formation of cohesive epithelial monolayers. While initially three separate reaction pathways in form of direct protein binding through co-polymerization of amine reactive groups, crosslinker-based protein attachment, or formation of an amine reactive secondary network were investigated, only limited results with unreliable

reproducibility could be obtained. A combination of the three approaches resulted in the working protocol of the combined approach. The major advantage of the combined approach is the two-step process to first re-establish reactive groups on the substrate surface before formation of secondary network in a secondary reaction step which allows for even protein coating. At the same time the multi-step process is a significant drawback as the complex process extends the sample preparation time to three days and significantly limits sample throughput. Furthermore, the method employs a volatile and cancerogenic chemical in the form of GMA and requires special equipment to limit exposure, which limits the widespread use as simple benchtop use leads to exposure and major health risk. Overall, the combined approach was the first method that reliably facilitated ECM protein coating on PDH and subsequent monolayer formation of epithelial cells.

Impact of topographical defects on the epithelial monolayer

After establishing the PDH and the ECM protein coating, hiPSC-RPE monolayer were cultured for one week before localized disruption of the substrate-tissue force balance by induction of topographical defects. The defects were induced in two distinct diameters intended to mimic the sizes of medium (63-125 µm) and large (>125 µm) drusen[119,121] which is the threshold in vivo corresponding to the development of a pathological phenotype. Characterization started with qualitative assessments of polarization marker ezrin, as well as mechanotransduction relevant proteins like vinculin and pMLC. With ezrin staining not showing a disruption of the signal inferring, no change in polarity or subsequently microvilli expression, no further efforts were made to assess the functionality of the monolayer through photoreceptor outer segment feeding essays[99,302]. Furthermore, the qualitative assessment of vinculin and pMLC staining showed a slight trend to reorganize in the monolayers confronted with localized topographical defect induced force disruption. Giving an initial hint on monolayer disruption, due to the limited signal quality, no further efforts for repeat experiments or quantification were undertaken. Immunofluorescent staining of F-actin showed no reorganization or stress fiber formation, and ZO-1 displayed a uniform distribution, findings that did not corroborate the mechanical data. Overall, immunofluorescent staining of the disrupted epithelial monolayers did not show a clear effect of the topographical defects on the distribution of the investigated markers. Possibly larger defects or additional stress factors such as reactive oxygen species (ROS)[306,307] or on-demand density reduction[302] are required to induce a visible pathological state of the hiPSC-RPE monolayer.

Despite these mild phenotypes, from the images it was observed that morphometric parameters like cell height, cell area and shape factor as well as cellular orientation showed a defect size and distance dependent behavior. The 100 µm diameter sized topographical defect mimicking a non-symptomatic medium sized drusen. The absence of functional disruption of the in vivo defect indicates that the disruptive event experienced by the RPE monolayer can be isolated and compensated by the collective

through reorganization not crossing the threshold into a pathological phenotype. The corresponding in vitro system showed a distance dependency of the morphological parameters with an increase in monolayer height and reorganization at the center of the topographical deformation and a perpendicular orientation of cells at the edge of the defect. This indicates that sell behavior in the center of the 100 µm topographical defect is similar to reported cell height increase of a stress relaxation response of a monolayer release from pretension[308–310] in combination with the reorganization of monolayer packing during stress relaxation[311–314]. The stress relaxation response requires a mechanical decoupling from the rest of the monolayer which is facilitated though the reorientation of the cells in the Edge region of the topographical defect, which had shown a significant perpendicular orientation. Furthermore, the induced orientation changes by a topographical defect is reported in literature as an epithelium intrinsic compensatory response[30,315,316]. Additionally, traction force microscopy quantification showed a significantly increased median traction in the edge region compared to the other two regions required to induce the preferential perpendicular orientation and mechanically decouple the Top region from the surrounding tissue. Overall, the morphometric parameters show an isolation and reorganization of the Top region facilitated by a protective response of the Edge region. The observed monolayer response to the localized medium sized topographical deformation aligns with the in vivo observation of a non-pathological defect site[120,317].

The larger 300 µm topographical defects exceeded the in vivo threshold for pathological drusen. With the disruptive event exceeding the compensatory capabilities of the epithelial monolayer in vivo the tissue becomes prone to develop a pathological phenotype. The corresponding in vitro system showed a distance dependency of the morphological parameters with a decrease in monolayer height coupled to an increase in cell area as well as a slight reorientation at the center of the topographical defect. The changes in cell morphology are indicative of a tissue scale stretching response in the most deflected region of the topographical defect comparable to observations made in cell stretching experiments[148,310,313,318] and especially radial stretching[30,149], where a radial orientation can be observed. Furthermore, through the quantification of the traction forces it was shown that the Top region generated significantly lower median traction forces aligning with observation from literature where central areas of dome stretching generate lower traction while experiencing higher tension[319]. Overall, the morphometric parameters of the large topographical defect showed stretched monolayers in the Top region with the Edge region showing no compensatory response. This indicates that the 300 µm topographical defect is beyond the compensatory threshold and registers as a tissue scale disruptive event. While the amplitude of the disruptive event is below the threshold of rupture induction the change in local force balance and monolayer tension could influence the functionality of the epithelial monolayer to perform phagocytosis, as is shown for a hiPSC-RPE monolayer which has undergone density reduction[302] and represent a relevant in vitro model for pathological drusen.

2. Photodegradable microgels as phantom cells

In this work, a novel microgel-based phantom cell was successfully established and used to investigate tissue level response to in-monolayer force balance disruptions. The PDM achieved on demand localized morphological changes as a simplified in vitro model mimicking retinal ageing. In comparison to other phantom cell models, the unique lateral directionality enables new possibilities to study epithelial to organoid mechanical homeostasis. Overall, elevating phantom cell models from passive tools of recording mechanics to an active participant in tissue dynamics[236].

Microgel synthesis optimization

A novel PEG-based PDM was established in this work. Reported acryl amide photodegradable microgel[267] it was found that the APS/TEMED redox initiated polymerization of microgels was sensitive to the surfactant and showed a prevalent instability in the presence of the ionic surfactant Krytox. Hence, it was necessary to implement a drastic adjustment of the initiator concentration in the presence of the PDC in comparison to the reported literature[163] to facilitate the polymerization reaction. As the polymerization reaction was initiated upon contact of the two aqueous phases, the timing of the reaction start could not be freely controlled, and a fine balance of quenching and reactivity had to be established. While degassing and nitrogen bubbling generally improves the reactivity of the aqueous solutions, a certain delay in reaction onset improved the mixing of the phases as well as the extrusion, generally preventing clogging of the mixing channel.

UV degradation and bio-functionalization characterization

PDM stiffness and degradation characteristics were tuned to the desired value as it was essential that the UV dosage was within a cell-compatible range, and the resulting changes were on a scale which could be detected by the surrounding monolayer. While the diameter expansion of around 20% was relatively minute the stiffness reduction of 60% of the initial value ensured that the force balance disruption had the magnitude to affect the surrounding monolayer. Oriented immobilization of full-length adherents proteins via a NTA crosslinker was inspired by a protocol of a 2D surface functionalization[38] and successfully established in 3D in the PDM system with E-cadherin as the initial adherens protein enabling a connection to the actin cytoskeleton. Alternative NTA crosslinker with shorter chain length are reported in literature this can lead to steric hindrance of the spacious adherens proteins and reduce the surface functionalization efficiency[285].

During the multi-step bio-functionalization protocol a substantial loss of microgels was observed, which affects sample reproducibility but primarily the universal feasibility as the low final concentration restricts large scale application. The drastic reduction was attributed to the challenge of handling of low concentrations of highly charged microgels either in tubes or on membranes. The repeated exchange of functionalization and

washing solutions could be circumvented by performing the bio-functionalization in a secondary microfluidic chip. Trapping the microgels in an anisotropic structure would allow a continuous flow of functionalization solution and wash out the bio-functionalized PDM with an inverted flow. Furthermore, the method could be fine-tuned to induce an unfunctionalized region at the top and bottom of the microgel which could be used for substrate attachment as well as prevent cells from climbing onto the microgels.

Embedded phantom cells in Madin-Darby canine kidney epithelium

The bio-functionalized PDM were integrated into a MDCK monolayer as an initial proof-of-concept and the induced force balance disruption was followed through live cell imaging. Quickly it was realized that the motile cell environment made observation difficult as the reaction to the change in stiffness to force balance disruption was not clearly attributable to the triggering event. Ultimately, the high intrinsic movement of the MDCK monolayer meant a high level of background noise which overshadowed the change in material properties. Live cell imaging revealed that the force imbalances generated by the PDM are insufficient to overcome the background noise introduced by random cell motility, suggesting that a less motile model system is required. Furthermore, it is possible that the observed time frame misses the curtail moment of force transmission which could give important information about the mechanotransduction cascade in the affected cells and reorganization for a collective response. Nevertheless, immunofluorescent staining revealed an impact on a protein coating and degradation state depending on monolayer response which was not observed during the live cell imaging. In the non-functionalized control conditions, the PDM are not recognized by the surrounding monolayer, and the UV induced degradation leads to a further constriction of the microgel-substrate connection site. This “squeezing-out” is comparable to classical apoptotic cell extrusions in epithelia and the only reason the microgel is not fully removed is the covalent connection to the substrate[277,320–323]. The degradation of E-cadherin bio-functionalized PDM showed an enveloping of the microgel by the surrounding monolayer with substantial basal α18-catenin activation. While the degradation and subsequent softening of the microgel could transmit a mechanical signal similar to a cell undergoing apoptosis the bio-functionalization of the microgel is maintained, which is unlike an apoptotic cell[310,324–328].

Embedded phantom cells in hiPSC-RPE monolayer

Moving to a less motile, non-proliferative and more in vivo relevant cells, the hiPSC-RPE microgel co-culture was established with non-degradable microgels. The importance of the bio-functionalization to integrate into the surrounding monolayer was highlighted immediately as non-functionalized microgels showed a higher degree of deformation and significant reduction in stiffness in cell culture. The change in circularity likely reflects persistent force exertion by the surrounding monolayer, which acts to expel the foreign body. Repeated deformation may additionally promote active liquid exchange, accelerating passive degradation in standard cell culture medium and thereby reducing the compressive modulus. In contrast, bio-functionalized microgels did not exhibit a

decrease in circularity or reduction in stiffness showing good integration into the monolayer. With the comparatively higher stiffness of the bio-functionalized microgels being a direct consequence of the inclusion into the force balance network as the tensile forces exerted by the monolayer could pretense the polymer network. This assumption is supported by a higher average apical stiffness of the surrounding monolayer in the presence of bio-functionalized microgels indicating a closed force balance network. Immunofluorescent staining of the bio-functionalized NDM showed lateral vinculin and apical α18-catenin engagement at the cell-microgel interface highlighting that proteins involved in the mechanotransduction cascade are active at the cell-microgel interface, which indicates force generation between the microgel and surrounding monolayer. Furthermore, the ezrin signal showed maturity of the monolayer in proximity to the microgel although the composite staining reveals a possible reduction in microgel diameter during the fixation process resulting in a delamination of the microgel-cell contact and leaving the fixated wedge-shaped cell in the original deformation behind.

In monolayer force balance disruption through PDM degradation

After the feasibility of microgel embedding into a hiPSC-RPE monolayer was established with NDM the system was expanded to PDM. Initial live cell imaging showed distinct passive versus active force transmission responses to the induced force balance disruption for the non-functionalized and bio-functionalized PDM respectively. The surrounding monolayer around the non-functionalize PDM showed a discontinuous F-actin signal with no visible response to the UV induced degradation of the embedded microgel as the change in mechanical state is not actively transmitted into the surrounding tissue due to the lack of adhesion protein coating. However, quantification of the monolayer response over time revealed an immediate and long-lasting increase of the shape factor in the adjacent cells. Furthermore, by PIV analysis it is revealed that the immediate response follows an outward motion which reverses into an inwards motion during the observation period. In combination, the passive mechanosensing of the adjacent cells transmitted the changed mechanical state of the embedded microgel and initiated a collective response aimed to remove the foreign body. The observations were further supported through immunofluorescent staining where the nuclei of the adjacent cells showed a round morphology and positioned far from the microgel-cell interface[329]. Particularly, in orthogonal view the lateral wedge of the adjacent cells showed extrusion response, driven by the F-actin cytoskeleton. Overall, with no active mechanotransduction the responses were indicative of a passively transmitted change of the mechanical state of the PDM with especially the adjacent cells initiating a foreign body removal response[330,331].

In contrast the bio-functionalized PDM elicited a thin even circumferential F-actin distribution at the apical microgel-cell contact and the microgel adjacent cells showed a substantial reaction to the UV induced degradation of the embedded PDM. Initially the force balance disruption resulted in a collapse of the circumference suggesting a compressive force balance between the microgel and the surrounding cells[332], which

increase their apical area at the same time. Cellular forces in the monolayer are a balance between tensile and compressive interactions governing the homeostasis of the monolayer. As the photodegradable microgels cannot actively generate forces without the UV initiated degradation the initial homeostasis is limited to a passive state determined by microgel stiffness. Only after the force balance disruption tensile interactions come into play, which are ultimately determined by the adhesion protein coating. Furthermore, quantification of the shape factor showed the microgel adjacent cells undergoing a short rigidification followed by a slow return to the initial state. This absorption of the change in mechanical state was transmitted into the surrounding monolayer through adherens junction protein coating and compensated in the quick response domain through adaptation of the surrounding cells. The observation of a biphasic response is supported by the PIV analysis where the initial inward movement was limited to the microgel-cell interface followed by a collective outward movement throughout the surrounding monolayer. Additionally, the immunofluorescent staining of the samples revealed that the nuclei located close to the microgel-cell interface and exhibited an elongated and perpendicular oriented morphology as the adherens protein coating the microgels facilitates active curvature sensing, which is reported on wavy substrates to lead to a similar phenotype[41]. Furthermore, the mechano-active adherens junction complex protein α18-catenin showed a clear delimitation line at the microgel-cell interface after the induction of the mechanical change in the microgel. This supports a tensile force generation of the surrounding cells onto the microgel long after the initial mechanical trigger. The change in mechanical state became very visible after assessing the F-actin orthogonal view where initially the cells followed the microgel curvature closely and formed a tall monolayer. After the change in mechanical state of the microgel the surrounding monolayer flattened and moved outwards while keeping the connection to the microgel[308,333].

V. Conclusion and Outlook

Overall, this work has shown that oNB-based photo-responsive hydrogels are a versatile platform for mechanobiological application. Through spatiotemporally controlled illumination PDH and PDM facilitate on-demand substrate or cell-directed force balance disruptions respectively elucidating the mechanical influence of tissue remodeling by mimicking the dynamic nature of ageing tissues.

1. What is next for the artificial drusen model?

In conclusion, the in vitro model built to recapitulate retinal mechanical ageing enabled the observation and quantification of a size and distance dependent tissue level response to on-demand topographical deformation on an ECM protein coated photodegradable hydrogel substrate. Ultimately, two distinct monolayer responses were observed with small topographical defects compensated and isolated by the surrounding cells collectively forming a separation, while large topographical defects overwhelmed the monolayer leading to a pathological-like stretched state at the center of the defect. However, a multitude of open questions remain regarding experimental design, additional readouts or combination with different in vitro ageing models.

Beginning with the most direct questions regarding experimental settings or how the change of size, density, or growth rate of the topographical defects would affect the RPE monolayer cohesion and improve in vivo relevancy. As this work was limited to two characteristic drusen diameters investigating smaller or larger topographical defects could give a better overview over phenotype progression as well as highlighting the threshold at which monolayer cohesion breaks down and the tissue ruptures. Furthermore, topographical defects were assessed only in isolation, so that the induction of multiple topographical defects in close proximity could mimic the pathological in vivo progression to a more relevant extent. Lastly, a reduction in growth rate by reducing the illumination dose and increasing the break time between illumination cycles could simulate a slower ageing-like progression of the defect formation. To give the in vitro model additional depth the readout could be expanded to include established functionality readouts like photoreceptor outer segment feeding essay[99,302] or ELISA assay of retinal metabolites[334]. As the topographical defects are highly localized structures spatial transcriptomics of the in vitro system could enable a better comparability to in vivo systems[335].

The current model system could be expanded upon by combination with complementary systems challenging the monolayer through orthogonal perturbation. Recently, Piskova et al. reported on an in vitro model facilitating on-demand cell density reduction of an RPE monolayer[302]. On the other hand, Garcia et al. developed an in vitro model focusing on the chronic oxidative stress, a known driver in AMD development[336]. Lastly, there are possible adjustments to the hydrogel itself. Primarily the protein coating procedure, while novel, could be improved through the investigation of an aldehyde-based attachment

method[216]. This adjustment could reduce sample preparation time and complexity and ultimately make the method more accessible.

2. What is next for the photo-responsive phantom cell?

Photodegradable microgels were produced in a tissue comparable stiffness range which could be tuned to 50% of the initial value by short illumination. Furthermore, an oriented adhesion junction protein coating was achieved facilitating the force active embedment of the microgel within an epithelial monolayer. In imagining of live cells as well as immunofluorescent stainings a force balance disruption had a substantial effect on the organization of the surrounding cells. Overall, this work has shown that bio-functionalized photodegradable microgels could be embedded into an epithelial monolayer and act as mechanical phantom cells. However, a catalog of open questions and possible improvements remains, especially regarding experimental settings, model readouts, as well as microgel adjustments.

Expanding the experimental settings by extending the observation time in combination with slower degradation rates could model age-related hypertrophy on more relevant time scales. On the other hand, adjustments to the experimental setup are required to capture the monolayer response to the phantom cell degradation induced force balance disruption in live cell imaging during the illumination to capture the immediate monolayer reaction and response. Furthermore, a higher resolution of the cell-phantom cell interface could give valuable information about the hybrid adhesion junction and cellular response. However, as the current experimental setup does not support capture during illumination, so that the UV light source would have to be decoupled from the imaging microscope in future experiments, trading control over the illuminated area for more detailed imaging.

The only model readout that was qualitatively assessed was the nuclear deformation in response to microgel bio-functionalization and force balance disruption. However, quantifying and relating the phenomenon to in vivo data could strengthen the model significantly. Furthermore, a useful addition to the model system is the implementation of a thin hydrogel layer underneath the epithelial monolayer enabling traction force microscopy while allowing spatial control over phantom cell patterning. Additionally, the height of the hydrogel layer could reduce the height difference between the phantom cells and the surrounding monolayer, reducing the influence of curvature. Moreover, the scope of the phantom cell adherens motives could be expanded through the introduction of different adherens junction proteins. A logical progression is the investigation of the keratin cytoskeleton force balance disruption response by coating the phantom cell with desmoglein, i.e., engaging desmosome junctions.

Lastly, various adjustments to the microgels could be made to improve their feasibility as phantom cells further, ranging from changing the material properties to surface functionalization, or shape adjustments. The major material properties that require

further optimization are material stiffness and viscoelasticity, as well as microgel diameter. Starting with the reduction of the initial stiffness to a lower, more cell relevant stiffness of around 1 kPa, while introducing viscoelasticity to the hydrogel network. Lastly, reducing the microgel diameter further, matching cell heights of around 15-20 µm.

A major point of improvement is the localization and density of the adherens junction proteins on the surface of the microgels. With the current method the protein coating is evenly distributed and at a relatively low concentration. Although reproducing cellular concentrations is inherently not feasible it was shown that the delayed introduction of a tertiary aqueous phase during microfluidic production leads to an enrichment of the co-monomer on the surface of the microgel[164]. Combined with a NTA containing monomer shown by Sommerfeld et al.[286] the functional group needed for complexation of the adherens junction protein could be directly incorporated into the hydrogel network during production. Alternatively, the selective covalent binding of the histidine tag was reported by Jivan et al. circumventing the extensive post-functionalization procedure entirely [337].

VI. Methods

1. Photodegradable crosslinker synthesis

The synthesis pathway followed the reports of Kloxin et al. and Griffin et al. and consisted of 6 steps. In the first 5 steps the photodegradable ortho nitro-benzyl (oNB) acrylate group was built and subsequently attached in the last synthesis step to a PEG-diamine linker completing the photodegradable crosslinker (PDC) synthesis.

The first step followed the Williamson ether synthesis by deprotonating the phenol group of the starting material facilitating a S_N2 nucleophilic substitution with an alkyl-halide compound. 10g of acetovanillone **1** (60mmol, 1 eq.) and 10mL of Ethyl 4-bromobutyrate (70mmol, 1,16 eq.) were dissolved in 100mL of Dimethylformamide (DMF) in a Schlenk flask. The reaction solution was degassed by N_2 for 15 min and the whole reaction flask was purged with N_2. Then under N_2 flow 25g potassium carbonate (180mmol, 3 eq.) were added to the reaction vessel. The inert atmosphere was reestablished, and the suspension was stirred at room temperature overnight. The reaction mixture turned dark green, and the reaction was deemed complete. To stop the reaction and remove solvent and reagents the reaction mixture was added to a 5 L beaker filled with 3 L of cooled DI water under rigorous stirring. The desired product **2** precipitated as a white solid and the suspension was stirred for an additional two hours. After stopping the stirring the solid settled and was separated by filtration with a Buchner funnel over qualitative filter paper and dried under air flow for two hours while continuously crushing aggregates. The collected white solid product **2** was spread on a pleated filter and air dried overnight.

Product: Ethyl 4-(4-acetyl-2-methoxyphenoxy)butanoate **2** (15.38 g, 54.87 mmol, 89%)

^{1}H NMR (400 MHz; $(CD_3)_2SO$, RT): δ[ppm] = 7.60 (dd, 1H), 7.44 (d, 1H), 7.05 (d, 1H), 4.10 – 4.03 (m, 4H), 3.81 (s, 3H), 2.52 (s, 3H), 2.46 (t, 2H), 1.99 (q, 2H), 1.18 (t, 3H).

In the second step the ortho position of the benzyl moiety was nitrated. 15.4 g of **2** (54.87 mmol, 1 eq.) were dissolved in 100 mL glacial acetic acid in a 500 mL three neck flask, cooled to 8°C and the reaction vessel was purged with N_2. The state of the solution needed to be closely monitored at this point as the reaction temperature was below the freezing point of pure acetic acid (16.6°C) and the reaction mixture could freeze and inhibit the reaction. Under N_2 flow a dropping funnel was attached and filled with 32 mL concentrated nitric acid (768 mmol, 14 eq.) which was added dropwise to the reaction mixture over a period of one hour and under rigorous stirring to ensure even dissolving and heat transfer. After the addition was completed, the reaction mixture was brought to room temperature and stirred for an additional 4 hours. The reaction was deemed completed and solution was added dropwise into two liters of cold DI water via a metal canular. The desired product formed a yellow suspension and precipitated when the stirring was stopped. The solid product could be separated with a Buchner funnel and was extensively

washed with cold DI water and air dried on the filter. The crude product was spread out on a pleated filter and dried overnight. To purify the product further it was recrystallized in 70-80 mL of ethanol yielding **3** as a crystalline solid.

Product: Ethyl 4-(4-acetyl-2-methoxy-5-nitrophenoxy)butanoate **3** (10.31 g, 31.69 mmol, 58%)

^{1}H NMR (400 MHz; $(CD_3)_2SO$, RT): δ[ppm] = 7.63 (s, 1H), 7.22 (s, 1H), 4.13 (t, 2H), 4.06 (q, 2H), 3.93 (s, 3H), 2.51 (s, 3H), 2.45 (t, 2H), 2.00 (q, 2H), 1.18 (t, 3H).

In the third step the ketone group was reduced to an alcohol group without reduction of the nitro group. 10.31 g of **3** (31.69 mmol, 1 eq.) were dissolved in an ethanol:THF mixture (100 mL:100mL). The reaction flask was purged with N_2 for 15 minutes and cooled with an ice bath. Under constant stirring and nitrogen counterflow 2.40 g borohydride (63.37 mmol, 2 eq.) were added in small portions and in the beginning bubble formation could be observed. After complete addition the ice bath was removed, and the reaction mixture was stirred at room temperature for three days. The reaction mixture had turned a deep red, and the reaction was terminated by cooling the reaction flask with an ice bath and excess sodium borate was quenched by dropwise addition of 40mL cold DI water. Subsequently, the mixture was precipitated in 1.5 L cold DI water through a metal cannula, and the resulting suspension was occasionally acidified with concentrated hydrochloric acid to protonate the break the borate coordination product and protonate the alcohol group, in the end turning yellow. Crude product was precipitated at the bottom of the beaker and filtered through a Buchner funnel and extensively washed with cold DI water. After air drying the solid on the funnel it was spread on a pleated filter and dried overnight. The product **4** was obtained as a yellow solid.

Product: Ethyl 4-(4-(1-hydroxyethyl)-2-methoxy-5-nitrophenoxy)butanoate **4** (6.51 g, 19.89 mmol, 63%)

^{1}H NMR (400 MHz; $(CD_3)_2SO$, RT): δ[ppm] = 7.52 (s, 1H), 7.35 (s, 1H), 5.49 (d, 1H), 5.25 (qd, 1H), 4.09 – 4.02 (m, 4H), 3.90 (s, 3H), 2.45 (t, 2H), 1.98 (q, 2H), 1.36 (d, 3H), 1.18 (t, 3H).

In the fourth step the ester group was cleaved und acidic conditions. 4.80 g of **4** (14.66 mmol, 1eq) were suspended in 80 mL of DI water in a 250 mL round bottom flask and 9.65 mL trifluoro acetic acid (TFA) (14.37 g, 146.64 mmol, 10 eq.). A reflux condenser was attached, and the reaction mixture was heated to 90°C and refluxed overnight. An additional 5 mL was added, and the reaction was continued for another four hours. After the reaction was completed, the heating was removed and the reaction mixture was brought to room temperature. Subsequently, the crude product precipitated from the solution and could be filtered on a pleated filter by gravitation funnel and washed with

small amounts of cooled DI water. The final product was dried under high vacuum yielding a pale-yellow powder.

Product: 4-(4-(1-hydroxyethyl)-2-methoxy-5-nitrophenoxy)butanoic acid **5** (2.35 g, 7,85 mmol, 54%)

^{1}H NMR (400 MHz; $(CD_3)_2SO$, RT): δ[ppm] = 12.18 (s, 1H), 7.53 (s, 1H), 7.35 (s, 1H,), 5.48 (s, 1H), 5.25 (q, 1H), 4.05 (t, 2H), 3.90 (s, 3H), 2.38 (t, 2H), 1.95 (q , 2H), 1.36 (d, 3H).

The oNB-based photodegradable group was functionalized in step five yielding a free double bond which could be accessed in the free radical polymerization reaction of hydrogels. 2.35 g of **5** (7.85 mmol, 1 eq.) were dissolved in 50 mL anhydrous DCM in a 250 mL two neck Schlenk flask, cooled with an ice bath and the flask was flushed with nitrogen. To the solution 2.35 mL triethylamine (3.18 g, 31.41 mmol, 4 eq.) were added with a syringe. An addition funnel was connected to the central neck; 20 mL anhydrous DCM were added via cannular to the funnel and 1.91 mL acryloyl chloride were added through a syringe and dissolved. The acryloyl chloride solution was added dropwise to the reaction mixture over one hour and after complete addition the reaction mixture was brought to room temperature and stirred overnight. Upon completion the reaction mixture was poured into 1.2 L cold DI water and stirred for two hours. The product was extracted by liquid-liquid extraction and after removing the solvent on a rotary evaporator (keeping the temperature below 35°C) the crude product was dissolved in an acetone:water mixture (100 mL:100 mL) and stirred overnight to break any anhydride side product. The organic solvent was removed by rotary evaporation again (temperature below 35°C) and the orange-brown crude product was extracted with 100 mL DCM. The organic phase was dried over anhydrous magnesium sulfate, and the solvent was removed (temperature below 35°C) yielding an orange-brown sticky solid as product.

Product: 4-(4-(1-(acryloyloxy)ethyl)-2-methoxy-5-nitrophenoxy)butanoic acid **6** (2.29 g, 6.49 mmol, 83%)

^{1}H NMR (400 MHz; $(CD_3)_2SO$, RT): δ[ppm] = 12.18 (s, 1H), 7.53 (s, 1H), 7.35 (s, 1H,), 6.29 (m, 3H), 5.98 (dd, 1H), 4.08 (t, 2H), 3.91 (s , 3H), 2.38 (t, 2H), 1.95 (q, 2H), 1.62 (d, 3H).

In the last step of the synthesis pathway the photodegradable group was connected to a PEG linker. The first reaction solution was prepared by dissolving 3 g of **6** (8.49 mmol, 1 eq.) in 10 mL NMP in a 50 mL round bottom flask and adding 3.54 g HBTU (9.34 mmol, 1.1 eq.) and 1.26 g HOBT (9.34 mmol, 1.1 eq.) via powder funnel, washing the solid residue down with minimal amounts of NMP. At the same time a second solution is prepared in a separate 25 mL round bottom flask by dissolving 1.70 g PEG-diamine (0.85 mmol, 0.1 eq.) in 10 mL NMP with the help of a small stir bar and gentle heating by heat gun. The first reaction mixture was activated by the addition of 3.20 mL DIPEA (16.98 mmol, 2 eq.). The

activation of the carboxylic acid was extended to 5 minutes under continuous stirring before adding the PEG-diamine solution to the flask by cannular, rinsing the second flask with an additional 5 mL NMP to ensure complete transfer. The reaction vessel was flushed with nitrogen, and the reaction was stirred at room temperature overnight. After the reaction was completed, the solution was dropwise precipitated via cannular into eight 50 mL falcon tubes filled with 40 mL ether cooled to -20°C. The falcon tubes were thoroughly vortexed and centrifuged for 5 minutes at 4°C at 1000g. Subsequently the ether was decanted and replaced with fresh -20°C ether repeating the washing cycle two more times. Finally, all the ether was removed, and the crude product was collected as a viscous liquid in a round bottom flask, which was put under high vacuum for four hours. To remove the unreacted photodegradable group as well as reagents the crude product was added to 100 mL DI water and thoroughly vortexed, the resulting suspension was extensively centrifuged at 4°C for 30 minutes at 1400 g. The liquid containing the photodegradable crosslinker was decanted into a fresh falcon tube, discarding the solid and repeating the workup process two more times. The aqueous partitions were combined and transferred into dialysis tubing with a molecular cutoff of 1 kDa and dialyzed against 5 L of DI water for three days, exchanging the water three times a day. Finally, the product solution was transferred into 500 mL round bottom flasks not exceeding 150 mL per flask and frozen solid while continuously rotating the flask resulting in a thin sheet of ice covering spread over the inside of the flask. The water was removed by lyophilization yielding the photodegradable crosslinker as a malleable brown solid.

Product: Photodegradable crosslinker (PDC) (1.5 g, 0.56 mmol, 37%)

^{1}H NMR (400 MHz; $(CD_3)_2SO$, RT): δ[ppm] = 7.55 (s, 1H), 7.14 (s, 1H), 6.29 (m, 3H), 5.99 (dd, 1H), 4.05 (t, 2H), 3.90 (s, 3H), 3.50 (s, 110H), 2.24 (t, 2H), 1.94 (q, 2H), 1.25 (s, 3H).

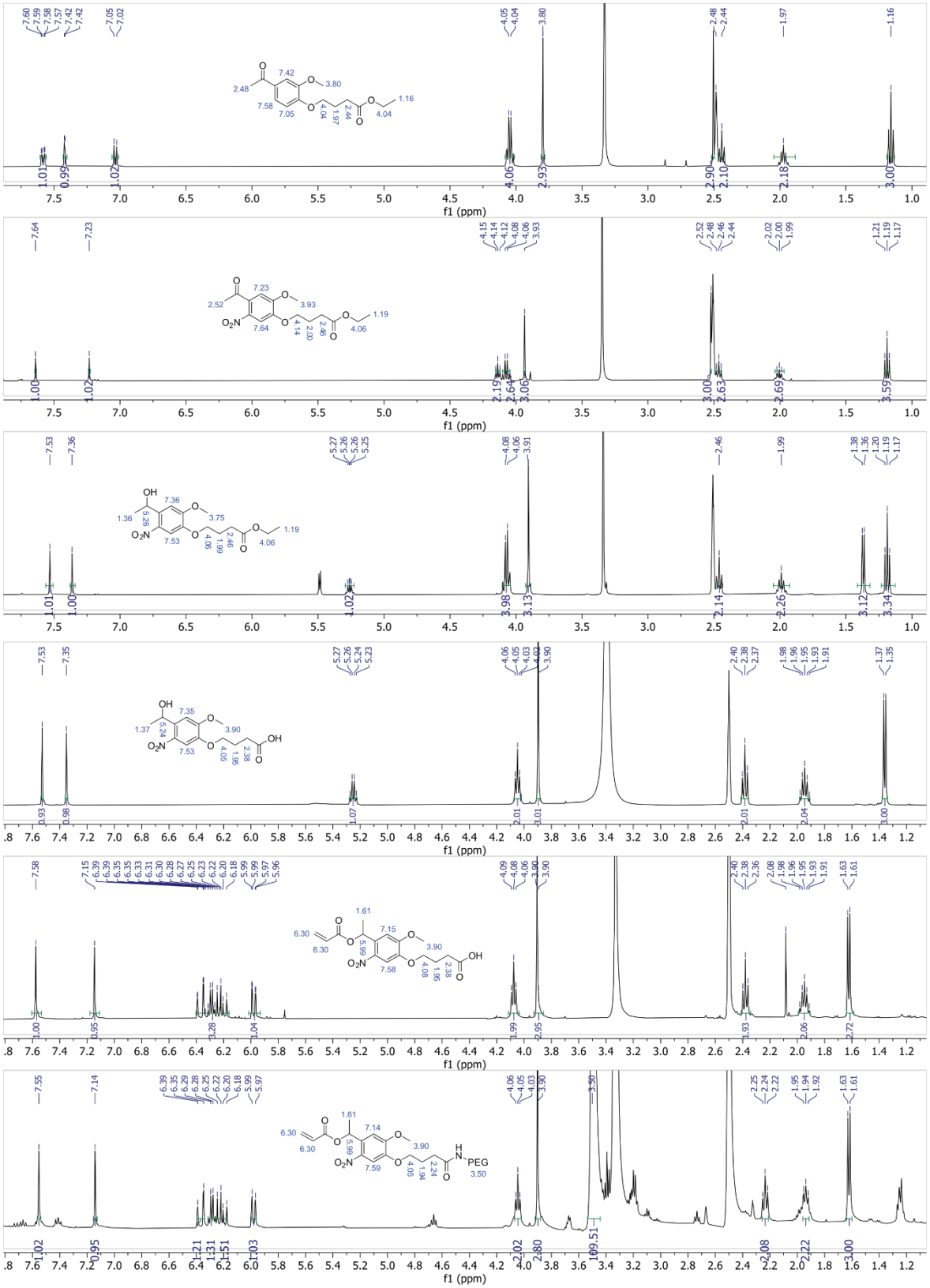


*Figure 43: ^{1}H NMR (400 MHz; $(CD_3)_2SO$, RT) of the complete reaction pathway of the photodegradable crosslinker. From top to bottom: **2**, **3**, **4**, **5**, and **6**.*

2. Carbamate-based photodegradable crosslinker synthesis

1st synthesis strategy adapted from Kim et al.[295]

1 g of 4-(4-(1-hydroxyethyl)-2-methoxy-5-nitrophenoxy)butanoic acid **5** (3.34 mmol, 1 eq.) was suspended in 50 mL of dry dichloromethane (DCM) and the reaction vessel was closed with a septum and flushed with nitrogen. 1.75 mL DIPEA (10.0 mmol, 3 eq.) were added to the round bottom flask via a syringe, and the reaction mixture was cooled to 0°C with an ice bath. In a separate flask 443 µL allyl isocyanate (5.01 mmol, 1.5 eq.) were dissolved in 20 mL dry DCM and added dropwise through a cannular to the first solution over the course of 30 minutes. After the addition was complete the ice bath was removed, and the reaction was stirred for 24 hours at room temperature. To stop the reaction the round bottom flask was put in an ice bath and 50 mL of 0.1 M HCl was added dropwise by syringe. During the quenching the formation of a yellow precipitate and gas generation could be observed. The phases were separate and the organic phase was washed three times with 60 mL 0.1 M HCl solution, dried over anhydrous $MgSO_4$ and the solvent removed under reduced pressure. As the ^1H NMR of the crude product showed a mixture of starting material, desired- and by-products, it was not purified further.

2nd synthesis strategy adapted from Kim et al.[295]

1 g of **5** (3.34 mmol, 1 eq.) was dissolved in 40 mL dry tetrahydrofuran (THF) and the round bottom flask was closed with a septum and flushed with nitrogen. To the solution 1.5 mL triethylamine (10.8 mmol, 3.2 eq) were added by syringe and the resulting yellow solution was cooled to 0°C using an ice bath. In a second round bottom flask 443 µL allyl isocyanate (5.01 mmol, 1.5 eq.) were dissolved in 20 mL dry THF and the solution was added to the reaction mixture by cannular. After the addition was completed the reaction mixture was brought to room temperature and stirred for 48 hours. After the reaction was completed the solvent and volatile reagents were removed under high vacuum with a brown oil remaining. The crude product was dissolved in 30 mL chloroform and washed with 20 mL 0.1 M HCl. The organic phase was separated, dried over anhydrous $MgSO_4$ and the solvent was removed under reduced pressure. As the ^1H NMR and ESI-MS of the crude product showed a mixture of starting material, desired- and by-products, it was not purified further.

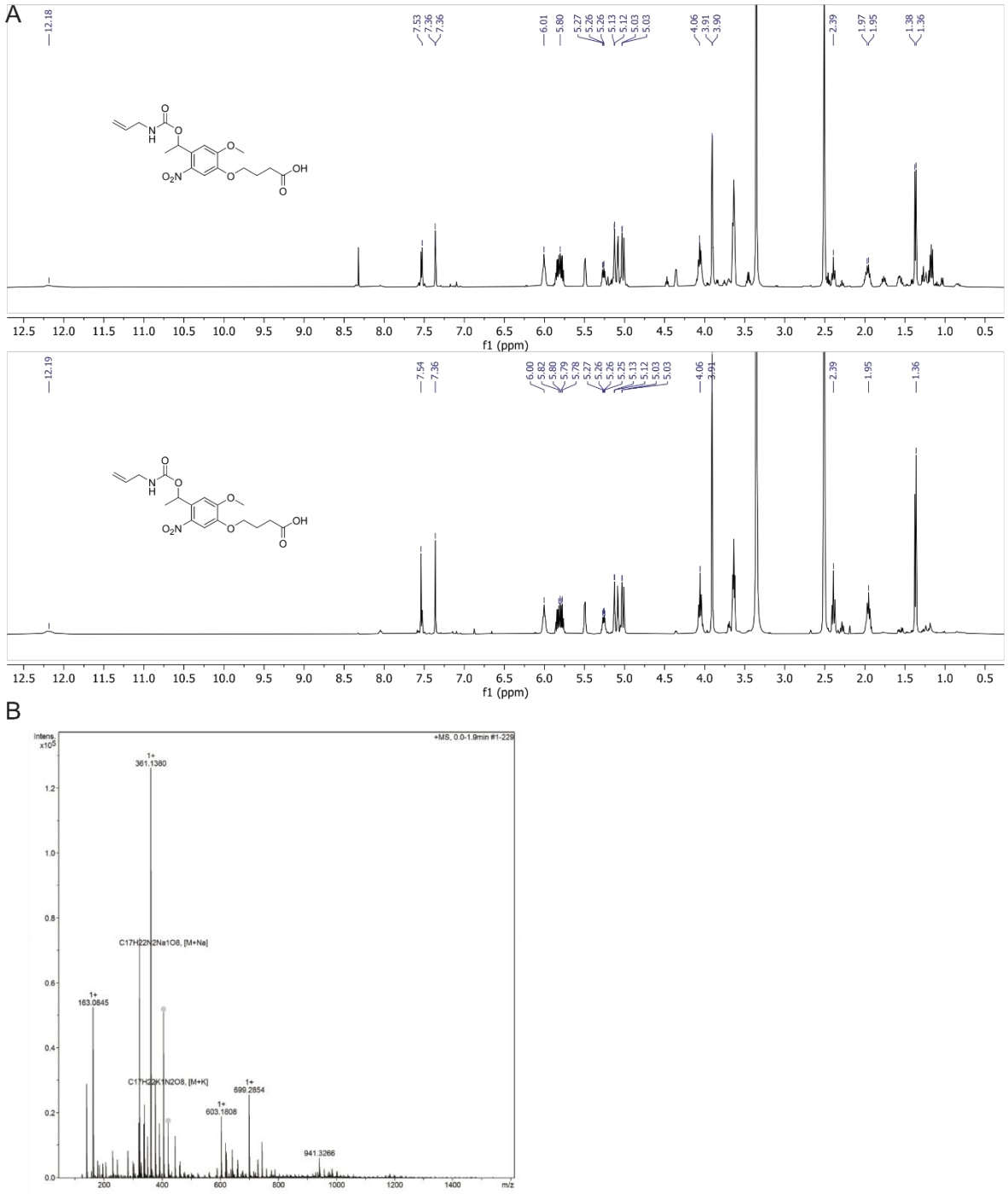


Figure 44: A) ^{1}H NMR (400 MHz; $(CD_3)_2SO$, RT) of both isocyanate-based reaction pathways, top first synthesis using allyl isocyanate and bottom second synthesis using ally isocyanate. B) ESI-MS in methanol of the second synthesis using allyl isocyanate. Data was generated by Daniel Gutmann in his role as research intern.

4-nitrophenyl chloroformate-based hydroxyl activation synthesis adapted from LeValley et al.[187]

2 g of **5** (6.68 mmol, 1 eq.) were dissolved in 50 mL DCM and cooled to 0°C with an ice bath before addition of 3.41 mL DIPEA (20.1 mmol, 3eq.) by syringe. In a separate round bottom flask 1.62 g 4-nitrophenyl chloroformate (8.02 mmol, 1.2 eq.) were dissolved in 50 mL DCM and added dropwise to the reaction mixture via cannular over the course of 20 minutes. After the addition was completed the ice bath was removed and the solution

was stirred for 24 hours. The solution was washed with 50 mL 0.1 M HCl, followed by 50 mL saturated sodium hydrogen carbonate solution three times. The final wash was performed with 50 mL brine, and the organic phase was separated, dried over anhydrous $MgSO_4$and the solvent was removed under reduced pressure. The activated compound was obtained as a yellow solid and was used in the subsequent reaction without further purification. Subsequently, the activated compound was dissolved in 10 mL THF and 766 mg allylamine hydrochloride (8.18 mmol, 2eq.) were added. Under stirring the allylamine was deprotonated by the addition of 1.71 mL triethylamine (12.3 mmol, 3eq.) and the yellow solution was stirred for 24 hours at room temperature. After the reaction was complete the solvent and all volatile reagents were removed under high vacuum. The crude product was dissolved in 40 mL chloroform and washed with 40 mL 0.1 M HCl followed by 40 mL 1.0 NaOH for three times, before a final wash with 40 mL brine solution. The organic phase was separated and dried over anhydrous $MgSO_4$ before removing the solvent under reduced pressure. As the ^1H NMR and ESI-MS of the crude product showed a mixture of starting material, desired- and by-products, it was not purified further.

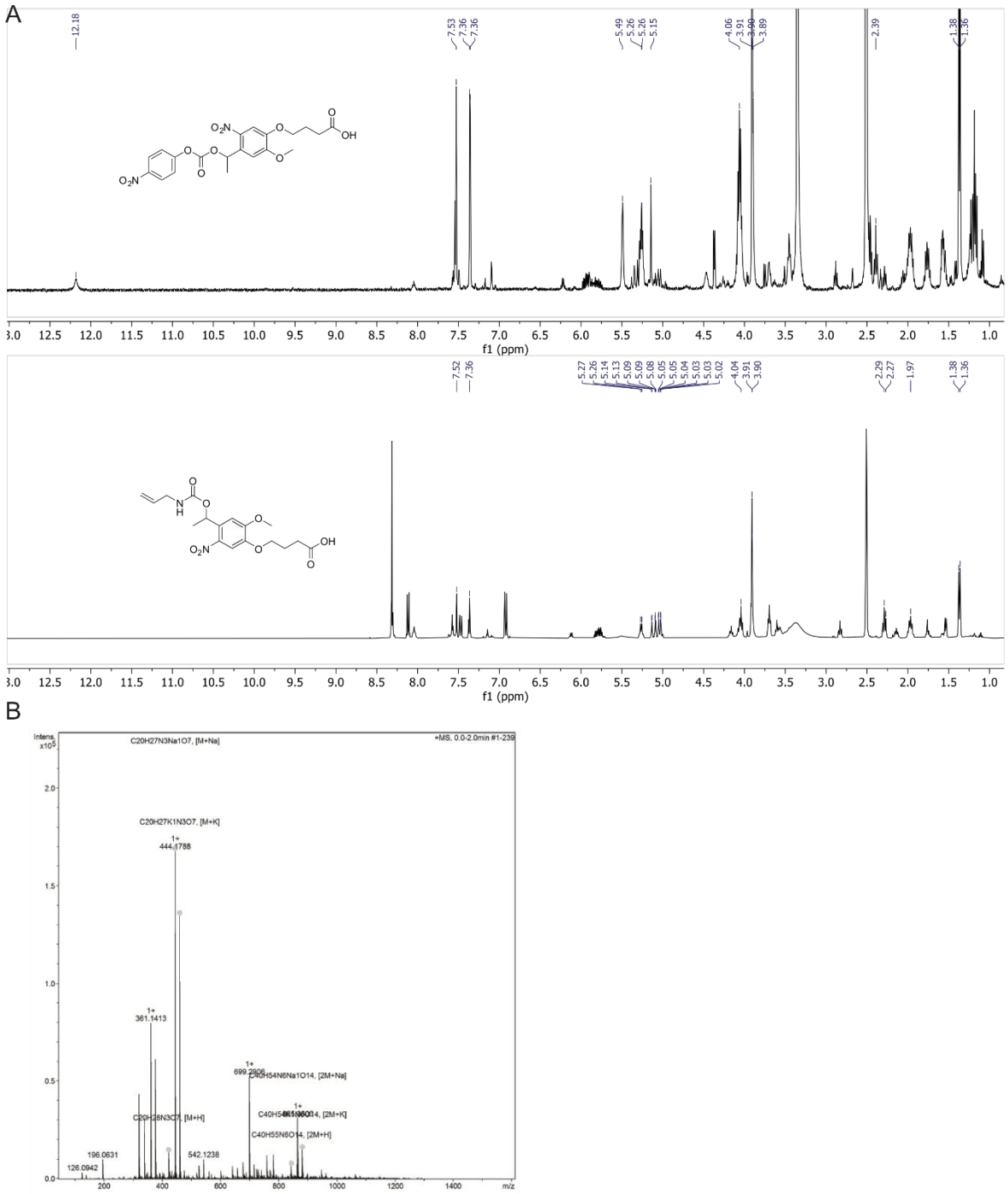


*Figure 45: A) ^{1}H NMR (400 MHz; $(CD_3)_2SO$, RT) of the activated compound after reaction with 4-nitrophenyl chloroformate on top and carbamate product **6a** at the bottom. B) ESI-MS in methanol of the finished product **6a**. Data was generated by Daniel Gutmann in his role as research intern.*

1,1'-carbonyldiimidazole-based hydroxyl activation synthesis[338,339]

4 g of **4** (12.2 mmol, 1 eq.) were dissolved in 40 mL dry THF and 2.18 g 1,1'-carbonyldiimidazole (CDI) (13.44 mmol, 1.2 eq.) were added. The reaction mixture was stirred for 24 hours at room temperature. The activated compound was used directly without isolating the intermediate or purification. To the solution 1.37 g allylamine hydrochloride (14.7 mmol, 1.2 eq.) and added and subsequently deprotonated by addition of 4 mL triethylamine (28.9 mmol, 2.4 eq.). The reaction mixture was stirred for

24 hours at room temperature. After the reaction was completed the solvent and all volatile reagents were removed under high vacuum. The crude product was dissolved in 40 mL chloroform and washed with 40 mL 0.1 M HCl, followed by 40 mL saturated sodium hydrogen carbonate solution three times. After a final 40 mL brine wash the organic phase was separated and dried over anhydrous $MgSO_4$. Subsequently the solvent was removed under reduced pressure and the desired product **4a** was obtained as brown oil.

Product: 4-(4-(1-((allylcarbamoyl)oxy)ethyl)-2-methoxy-5-nitrophenoxy)butanoate **4a** (4.60 g, 11.2 mmol, 92%)

^{1}H NMR (400 MHz; (CD3)2SO, RT): δ[ppm] = 7.60 – 7.56 (m, 1H), 7.57 (s, 1H), 7.14 (s, 1H), 6.11 (q, 1H), 5.74 (ddt,1H), 5.10 – 4.97 (m, 2H), 4.11 – 4.02 (m, 4H), 3.91 (s, 3H), 3.55 (m, 2H), 2.45 (t, 2H), 1.98 (p, 2H), 1.53 (d, 3H), 1.18 (t, 3H).

MS (ESI): calculated for ($C19H26N2O8^+$): 410.1683 found: M/z = 433.1581 $[M+Na]^+$,

449.1353 $[M+K]^+$.

The intermediate product **4a** (4.20 g, 10.2 mmol, 1 eq.) was dissolved in THF:H2O (2:1, 90 mL) and 368 mg LiOH (15.3 mmol, 1.5 eq.) were added to the reaction mixture. The solution was stirred 24 hours at room temperature. After the reaction was complete the reaction mixture was neutralized by the addition of 20 mL 1 M HCl solution and extracted four times with 50 mL chloroform. The organic phase was washed three times with 100 mL 0.1 M HCl solution and dried over anhydrous $MgSO_4$. The desired product was obtained as yellow solid.

Product: 4-(4-(1-((allylcarbamoyl)oxy)ethyl)-2-methoxy-5-nitrophenoxy)butanoic acid **6a** (3.55 g, 9.28 mmol, 91 %)

^{1}H NMR (400 MHz; (CD3)2SO, RT): δ[ppm] = 12.17 (s, 1H), 7.58 (s, 1H), 7.57 – 7.55 (m, 1H), 7.14 (s, 1H), 6.11 (q, 1H), 5.74 (ddt, 1H), 5.16 – 4.95 (m, 2H), 4.07 (t, 2H), 3.91 (s, 3H), 3.55 (m, 2H), 2.38 (t, 2H), 1.95 (p, 2H), 1.53 (d, 3H).

MS (ESI): calculated for (C17H22N2O8+): 382.1370 found: M/z = 405.1272 $[M+Na]^+$,

421.1005 $[M+K]^+$.

Carbamate-based photodegradable crosslinker synthesis

2 g of **6a** (5.23 mmol, 1 eq.) were dissolved in 15 mL NMP and 933 mg 1,1'-carbonyldiimidazole (5.75 mmol, 1.1 eq.) were added to the 50 mL round bottom flask. The flask was capped with a septum and purged with nitrogen. In a separate round bottom flask 1.57 g of PEG_{2000}-diamine (0.78 mmol, 0.15 eq.) in 15 mL NMP under occasional heating by a heat gun. The solution was added to the reaction mixture and stirred for 24 hours at room temperature. After the reaction was completed, the solution was precipitated into falcon tubes filled with ice cold ether, following a ratio of 30 mL of diethyl

ether per 10 mL reaction solution. The tubes were thoroughly vortexed before 5 minutes of centrifugation at 1000 g and 4°C. The ether wash was decanted and replaced by 40 mL fresh ether. Overall, the washing procedure was repeated two more times. The crude product was obtained as a brown viscous liquid and redissolved in 100 mL Di water, transferred into two 50 mL falcon tubes and centrifuged for 30 minutes at 1400 g and 4°C. The solution was decanted into fresh falcon tubes, discarding the sediment and repeating the washing procedure for a total of four times. The aqueous solution was transferred into dialysis tubing with a molecular cutoff of 100 kDa and dialyzed against 5 L of DI water for three days, changing the water every 24 hours. Lastly, the solution was transferred from the dialysis tubing into a 500 mL round bottom flask and frozen under constant rotation with liquid nitrogen, before lyophilization. The product was obtained as a malleable brown solid.

Product: Carbamate-based photodegradable crosslinker **7a** (450 mg, 0.17 mmol, 22%)

^{1}H NMR (600 MHz; (CD3)2SO, RT): δ[ppm] = 7.92 (t, 2H), 7.57 – 7.54 (m, 2H), 7.56 (s, 2H), 7.14 (s, 2H), 6.11 (q, H), 5.74 (ddt, 2H), 5.13 – 4.98 (m, 4H), 4.05 (t, 4H), 3.91 (s, 6H), 3.51 (s, 321H), 3.40 (t, 7H), 3.20 (q, 6H), 2.24 (t, 4H), 1.94 (p, 4H), 1.53 (d, 6H).

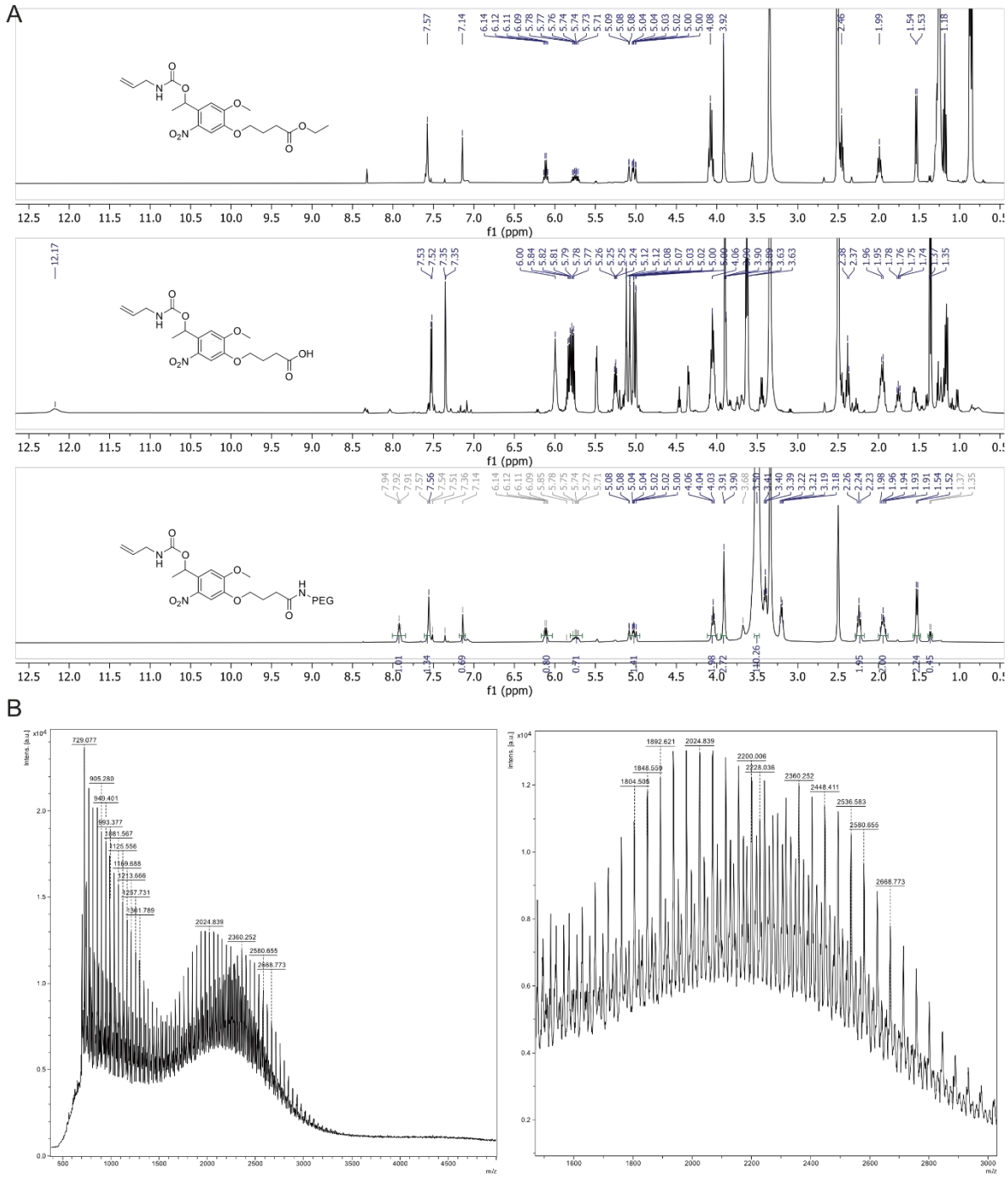


*Figure 46: A) ^{1}H NMR (400 MHz; $(CD_3)_2SO$, RT) from top to bottom **4a**, **6a** and the carbamate based crosslinker. B) MALDI-TOF in DCTB matrix of the carbamate based crosslinker. Data was generated by Daniel Gutmann in his role as research intern.*

3. Photodegradable hydrogel as an artificial drusen mimic

Photodegradable hydrogel preparation

To ensure adhesion of the hydrogels to the glass bottom dishes (Cellvis, D35-20-0-N) the glass surface was chemically activated to support a covalent integration into the polymer backbone. As the glass surface of the glass bottom dishes exhibited a strong dewetting behavior the surface was activated by O_2 plasma (compressed air, 0.41 mL/min, 1 minute, 200 W) in a plasma oven (Zepto, diener electronics). Immediately following the plasma treatment, the activated glass surface was wetted with 200 µL of the functionalization solution. The functionalization solution consisted of a stock solution of 3-(Trimethoxysilyl)propylmethacrylat (TMSPMA) (abcr, AB109006) in ethanol (12.5 µL TMSPMA in 2.5 mL ethanol, 21 mM) mixed with an activation solution of acetic acid (75 µL glacial acetic acid in 750 µL DI water, 1.75 M) to improve methanolate as a leaving group during the silanization reaction. The silanization reaction proceeded for three minutes before the dishes were put in an ethanol bath, quenching the reaction and removing excess reagents. The activated dishes were put in a 60°C oven for 15 minutes to remove ethanol and cure the surface bonding. With acrylate functionalities covalently attached to the surface of the glass bottom dishes the samples were ready to be used in hydrogel casting.

To restrict the hydrogels in height and diameter PDMS rings with a defined height of 200 µm and an inner diameter of 4 mm were stenciled from a PDMS thin film (Darwin Microfluidics, DM-S-PDMS-200) and positioned precisely in the center of the activated glass bottom dishes with the help of a 3D printed guide. To facilitate an easy transfer and sufficient adhesion the PDMS stencils were dipped in ethanol before the transfer, with the ethanol quickly evaporating once positioned. The hydrogel precursor solution was prepared fresh every time by sequentially adding the monomers and resulted in hydrogels with a polymer weight percentage of 17.6 wt/vol% and an effective Young's modulus of 4 kPa.

The photodegradable hydrogel precursor composition in order, beginning with Poly(ethylenglycol)methyletheracrylat (10 µL, 100 mM, 556 eq., Sigma Aldrich, 454990), 2-Aminoethylmethacrylat-hydrochlorid (10 µL, 7.55 mM, 5 eq., Sigma Aldrich, 516155), PDC (22.5 µL, 75 mM, 112 eq.), and 8-Arm PEG-Acrylate (1.5 µL, 10 mM, 1 eq., Biopharma PEG, A88009-20K). The solution was vortexed for three seconds and spun down shortly on a desk centrifuge, then Ammonium persulfate (APS) (4 µL, 1.97 M, Sigma Aldrich, 248614) was added following another repetition of vortexing and short centrifugation. Finally, N,N,N',N'-Tetramethylethylenediamine (TEMED) (2 µL, 1.98 M, Sigma Aldrich, 411019) was added and solution was quickly vortexed, centrifuged and roughly 15 µL of pre-hydrogel solution was transferred into the PDMS stencils and quickly covered with a PTFE lid.

The composition of the non-degradable control gels was adjusted to replace the PDC with a non-degradable PEG-diacrylate crosslinker. The hydrogel reaction mixture was made fresh each time in the following order. To a 500 µL tube 20 µL DI water was added, followed by Poly(ethylenglycol)methyletheracrylat (10 µL, 100 mM, 556 eq.), 2-Aminoethylmethacrylat-hydrochlorid (10 µL, 7.55 mM, 5 eq.), Poly(ethylene glycol) diacrylate (22.5 µL, 100 mM, 150 eq. Sigma Aldrich, 701971), and 8-Arm PEG-Acrylate (1.5 µL, 10 mM, 1 eq., Biopharma PEG, A88009-20K). The solution was vortexed for three seconds and spun down shortly on a desk centrifuge, then Ammonium persulfate (APS) (4 µL, 1.97 M, Sigma Aldrich, 248614) was added following another repetition of vortexing and short centrifugation. Finally, N,N,N',N'-Tetramethylethylenediamine (TEMED) (2 µL, 1.98 M, Sigma Aldrich, 411019) was added and solution was quickly vortexed, centrifuged and roughly 15 µL of pre-hydrogel solution was transferred into the PDMS stencils and quickly covered with a PTFE lid.

The gels were polymerized on a 30°C preheated hot plate for one hour before taking them off the hot plate, flipping them upside down and letting them rest for 20 minutes. This step was implemented to rehydrate the PTFE-hydrogel interface and facilitate an easier removal of the lids. As if this step would be skipped the hydrogels would show large surface ruptures from the edge of the PDMS stencil similar to delamination failures in resin. As manual removal of the lids had the same risk of surface disruptions the dishes were submerged in DI water and sonicated for 3-5 minutes. With the lids removed the PDMS stencil could be removed and cleaned with a Kimtech wipe to be stored in isopropanol for reuse. Furthermore, excess hydrogel formed outside the PDMS stencil and had to be removed by laboratory aspirator, cleaning the residue with an ethanol soaked Kimtech wipe. This step had to be performed diligently as debris free surrounding was crucial for the adhesion of cell seeding boundaries. The gels were stored with 3mL of DI water in the dark under room temperature.

PDH preparation for glycidyl methacrylate-based bio-functionalization protocols

The hydrogel preparation followed the PDH protocol substituting the AEMA for glycidyl methacrylate (GMA). Three different conditions were explored with 0.1, 0.5 and 1.0 µL GMA amounting to 7 mol%, 27 mol%, and 43 mol% respectively. Gels were incubated with 100 µg/mL or 500 µg/mL of fluorescently tagged fibronectin (cytoskeleton, FNR02) at 4°C overnight.

PDH Characterization

Bulk hydrogel stiffness measurements

The compressive modulus of the bulk hydrogels was measured by nanoindentation using the Chiaro Nanoindenter (Optics 11 Life) with a 20 µm spherical glass tip and cantilever stiffness of 0.025 N/m probe. The samples were indented using displacement mode with maximum depth of 3.5 µm. A minimum number of 3 measurements per sample and a maximum of 80-100 in case of matrix scan mode was taken. The raw data was analyzed with the Optics 11 Life software DataViewer V2 (version 2.63) following a Hertz contact

model, single fit mode to 100% of Pmax. In the end the values were filtered depending on the fit by excluding measurements with an R^2 of smaller than 0.95.

Bulk hydrogel stiffness measurements under cell culture conditions

To assess the feasibility of the photodegradable hydrogel as viable cell culture substrate gels was sterilized with a gentamicin solution wash, covered with cell culture medium and stored in the incubator for up to 12 days. The measurement setup and setting were unchanged to the bulk stiffness measurements.

Height and stiffness measurements of topographical defects of one-time illumination experiments

Localized illumination of the photodegradable hydrogels was performed on an Axio Observer 7microscope with a Colibri 5 LED at 385 nm and 3.83 mW/cm^2 for 60 seconds through a 20x objective with the diaphragm opened either at 100 or 300 µm diameters. After illumination an equilibration period of 30 minutes was set before characterizing the induced topographical defect. The stiffness was measured by nanoindentation on the top of the topographical defect with the bulk stiffness measurement settings. The displacement of the nanoindenter probe head was given as a vertical displacement by a piezo motor, which could be related to the surrounding hydrogel surface and the difference was the height. Furthermore, the height of the topographical defect was corroborated by the vertical displacement of fluorescent beads (0.1 µL of 50% solution, Invitrogen FluoSpheres 0.1 µm orange, 540/560) embedded in the hydrogel in relation to the surface of the hydrogel.

Height measurement of topographical defects of additive illumination experiments

Repeated localized illumination of the photodegradable hydrogels containing fluorescent beads (0.1 µL of 50% solution, Invitrogen FluoSpheres 0.1 µm orange, 540/560) was performed on an Axio Observer 7microscope with a Colibri 5 LED. To capture the dynamic deformation of the topographical defect the red fluorescent channel was used to capture images throughout a Z-stack (40 slices, 4 µm step, middle plane at the initial surface of the hydrogel), while the blue channel used for illumination (385 nm, 3.83 mW/cm^2) was restricted to illuminated only the 8th slice, corresponding to a distance of 48 µm from the initial surface of the hydrogel. Furthermore, the imaging was set up to include an equilibration time of one hour between each imaging cycle and a total of 15 cycles were performed, resulting in a total illumination time of 60 seconds for the additive illumination experiment. Lastly, a final reference image was acquired 24 hours after the first imaging cycle.

Hydrogel bio-functionalization

To facilitate cell adhesion on the PEG-based hydrogels adhesion sites need to be introduced to the sample surface. As the free acrylate groups from the crosslinkers within the gel react completely during the polymerization reaction an orthogonal reaction pathway was established. During the hydrogel production AEMA was co-polymerized into

the hydrogel network as its primary amine group could be translated into an amine reactive group after the initial free radical polymerization. In the first functionalization step the hydrogels were incubated with a glycidyl methacrylate (GMA) solution (75 µM, Sigma-Aldrich, 151238), which would react by epoxy-amine click reaction and translate the amines into meth acrylate groups. The gels were washed with DI water to remove the unreacted GMA, and excess solution was removed from the gels before the next functionalization step to allow the hydrogel surface to dry out and the functionalization solution to diffuse in.

The functionalization solution was prepared fresh each time with the following composition. To a 1.5 mL tube 590 µL DI water was added, followed by 3 µL GMA, 10 µL Di(trimethylolpropane) tetraacrylate (TMA, Sigma Aldrich, 408360) solution (0.2 vol/vol% in EtOH). The solution was vortexed for three seconds and centrifuged shortly. Subsequently 10 µL APS (1.97 M) were added and another mixing cycle by vortexing and centrifugation was performed. Finaly 2.5 µL TEMED (1.98 M) was added to the reaction mixture, followed by a quick mixing cycle and 100 µL functionalization solution were quickly pipetted onto the hydrogels. The lids of the glass bottom dishes were closed, and the samples were placed on a 30°C preheated hotplate for 15 minutes for the PDH and 10 minutes for the non-degradable gels. Immediately after the reaction time elapsed two mL of DI water were added onto the samples and excess poly-GMA was washed away for 10 minutes. The wash water was removed at halftime with a laboratory aspirator and replaced with fresh DI water. Special attention had to be given to the surrounding glass surface, where poly-GMA had formed clumps during the free radical polymerization reaction that could impede proper bio-functionalization and cell-seeding later.

As previous iterations had encountered issues with batch processing of samples, the protein solution was added to each sample individually to avoid prolonged drying of the functionalized hydrogel surface. As much DI water as possible was removed from the hydrogel and a hydrophobic barrier with an inner diameter of 6 mm was placed around the gel. A protein solution of 7.5 µL Laminin 332 (100 µg/mL, Biolamina, LN332), 7.5 µL Laminin 511 (100 µg/mL, Biolamina, LN511), 1.5 µL human collagen type IV (30 µg/mL, Sigma-Aldrich, C7521) in 38.5 µL PBS was added into the well, forming a drop inside the barrier. The dishes were placed in a petri dish, covered with a glass lid and placed into a cell culture incubator overnight.

The bio-functionalization of the hydrogel surface was completed, and samples were transferred into a sterile environment. The hydrogels were sterilized by a gentamicin (6.25 mg/L, Gibco, 15750-060) in PBS solution wash for two times 15 minutes. After the sterilization was complete the gentamicin solution was removed and hydrophobic barriers with an inner diameter of 4 mm were placed around the hydrogels, Finally, a bubble of 30 µL cell culture medium was placed into the well, preventing the hydrogel from drying out before the cell seeding procedure.

PDH bio-functionalization with secondary network approach

The protocol was adapted from Przybyla et al.[298] and the functionalization solution had to be prepared fresh each time. The functionalization solution consisted for 2 gels of 433.3 µL DI water, 100 µL 0.5 M HEPES buffered to pH 6, 65 µL ethanol, 50 µL 0.2 wt/vol% bis-acrylamide, 10 µL 0.2 vol/vol% tetramethacrylate in ethanol, 333.3 µL 0.03 wt/vol% N-hydroxysuccinimide ester in 50% ethanol, 8.33 µL 0.1 vol/vol% TEMED in DMSO. Before addition of the functionalization solution excess water was removed from the PDH and the gel was reswollen for 5 minutes with a saturated APS solution. Excess APS solution was aspirated and 500 µL of the functionalization solution was added to each gel. After reacting for 10 minutes the gels were washed with 25 mM HEPES for 5 minutes before adding the protein for incubation at 4°C overnight.

Cell seeding of hiPSC-RPE on PDH

The commercially procured human induced pluripotent stem cell-derived retinal epithelium cells (hiPSC-RPE) (Fujifilm Cellular Dynamics, R1102) were expanded for a week in a vitronectin XF (2.5 µg/mL, 440 µL, StemCell technologies, 07180) coated well of a 24 well culture plate. During the expansion time the medium was changed twice with the medium composition following the manufacturer's composition. In short the medium is composed of MEM-alpha with nucleosides (273.9 mL, Thermo Fisher, 12571063), 100x Glutamax (2.79 mL, Thermo Fisher, 35050061), KnockOut Serum replacement (15 mL, Gibco, 10828028), N2-Supplement (3 mL, Gibco, 17502048), Hydrocortisone (0.33 mL, 50 µM, Sigma Aldrich, H6009), Taurine (1.5 mL, 50 µg/mL, Sigma Aldrich, T8691), Triiodo-L-thyronine (0.21 mL, 20 ng/mL, Sigma Aldrich, T5516) and Gentamicin (0.15 mL, 50 mg/mL, Gibco, 15750060). The quality and density of the cells was checked before seeding, aiming for a culture of densely packed hexagonal cells.

The single cell suspension was generated by pre-treatment of the monolayer with 5 mM PBS/EDTA (Sigma-Aldrich, E6511) for 30 minutes to weaken calcium dependent cell-cell contact. With the cells rounding up and the monolayer losing its cohesion a wash needed to be performed to detach cells in a few spots mechanically so that the following cleaving agent could access basal attachment sites. The final detachment was facilitated by incubation with TrypleE Express (Gibco, 126050) for 5 minutes. Additionally, the well was rinsed with 750 µL warm medium to detach cell clusters at the edge of the well. On average a concentration of 500k cells per milli liter was expected and diluted to a final concentration of 80k per 30 µL. Subsequently, 30 µL of cell suspension were seeded per sample. Furthermore, 500 µL of cell medium were pipetted into the edge of the plastic part of the glass bottom dish to guarantee a humid environment and prevent the medium bubble with the cells from drying out. After the seeding procedure was finished, the dishes were placed for 15 minutes on a non-vibrating surface to allow the cells to sediment and attach evenly to the surface of the hydrogel before the samples were placed into a cell culture incubator. Upon successful attachment the cells formed a monolayer

overnight and 1.5 mL of medium was added to the dish. The cell culture was maintained for a week with two medium changes.

Localized on-demand topographical defect induction on hiPSC-RPE monolayer

The illumination of the samples was performed on a Zeiss Axio observer 7 with a Colibri 5 module, an incubation chamber and CO_2 buffering system. While using the 20x objective in the 385 nm channel at 100% intensity the intensity was measured with a spectrophotometer (Gigahertz-Optik, PT-9610-PD-2T) to be 3.83 mW/cm^2. The area of illumination could be easily controlled by the diaphragm with the minimum opening resulting in a circular illumination with a diameter of 100 µm. To avoid overlapping or interference effects of the topographical defects the illumination positions were set apart from each other at pre-screened positions. Furthermore, the focus plane during illumination was set 50 µm below the monolayer to illuminate primarily the gel and get optimal defect formation characteristics. Finally, the set positions were illuminated in series with each spot being illuminated for 60 seconds resulting in a dose of 230 mJ*cm^2. After illumination, the samples were placed back into the cell culture incubator, and an equilibration time of 24 hours was given for the monolayer to adapt to the localized topographical defect formation.

Immunofluorescent staining and imaging

Fixation of the samples after topographical defect formation was performed after the 24 hours equilibration time elapsed by removing the medium and adding 2 wt/vol% PFA in PBS (Thermo Fisher, J61899.AK) for 8 minutes at room temperature. Subsequently, the samples were washed three times with PBS for 5 minutes and permeabilized with a Triton-X 100 solution (0.3 vol/vol%, Sigma-Aldrich, T8787) for precisely two minutes. Sample preparation was finished three more washing cycles, followed by incubation with a 1% BSA solution (Serva, 11930) for 30 minutes at room temperature to block unspecific binding of the antibodies. The staining started with the addition of the primary antibodies in 1% BSA solution and incubation overnight at 4°C. Afterwards, excess primary antibodies were washed away in three PBS washing cycles before addition of the secondary antibodies or dyes was performed, followed by incubation for two hours at room temperature. Lastly, samples were washed three times with PBS before imaging.

Samples were imaged with a Zeiss LSM710 Confocal microscope with a 40x water immersion objective (Zeiss, 420862-9970-000) in confocal mode (Z-stack 1.1 µm optical slicing) and Airyscan super resolution mode (Z-stack 0.25 µm optical slicing). Captured images were processed and quantification was performed using Fiji software (National Institutes of Health, USA).

Table 2: PDH topographical deformation immunofluorescent staining antibodies and dyes.

Description	Concentration	Antibody Species	Supplier	Cat Number
Primary				
mouse anti-human Ezrin	10 µg/mL	Mouse	ABCAM	ab4069
rabbit anti-human ZO-1	2.5 µg/ml	Rabbit	Thermo Fisher Scientific	61-7300
Secondary				
Alexa Fluor 488 anti-mouse IgG (H+L)	8 µg/ml	Goat	Invitrogen	A11001
Alexa Fluor 594 anti-rabbit IgG (H+L)	4 µg/ml	Goat	Invitrogen	A11012
Dye				
Phalloidin-iFluor 647 dye	1:1000		ABCAM	ab176759

Analysis of cell morphology: monolayer height, cell area, shape factor, and angle to origin

To quantify the effects of localized topographical defect formation on the monolayer in a distance dependent manner and with the necessary number of cells an automatic method was needed. A custom Fiji script was written to measure the following morphological parameters: monolayer height, cell area, shape factor, and the angle to origin.

Beginning with the monolayer height the F-actin channel of the confocal microscopy stack was resliced to obtain a series of orthogonal images. With a 5 percent offset from the edge of the frame intensity line plots were drawn every 10 percent of the frame width to obtain the mean grey value and calculate a dynamic threshold, which was used to determine the two coordinates where the F-actin signal exceeds the limit and from their distance the height of the monolayer. To make the method more robust to false positives a filter was implemented which required the limit to be surpassed for three consecutive measurements before recognizing the apical or basal cortex of the cell. Nevertheless, the values had to be filtered as the thresholding was not robust enough in extreme edge cases, requiring implementation of a static filter with a lower limit of 5 µm and an upper limit of 20 µm, with the filter values originating from manual spot checks throughout the sample set. Furthermore, for each height measurement the respective distance to a predetermined center of the topographical defect was calculated.

The cell area and shape factor required a maximum intensity projection of the F-actin signal of the Z-stack from the confocal imaging and segmentation by the Cellpose plugin in Fiji to determine the cell outlines and subsequently measure cell are and perimeter. From these values the shape factor was calculated by dividing the perimeter through the square root of the area. Furthermore, for each height measurement the respective distance to a predetermined center of the topographical defect was calculated. Additionally, to allow more consistent comparability the values of each technical replicate were normalized by the respective means.

The angle to origin protocol used the previous established segmentation and measured the absolute cellular angle. The angle was vectorized and with the vector from the cell center to the center of the topographical defect a scalar product determined the relative alignment of the cell towards the origin of the defect. As cells in the monolayer had no absolute orientation, the angle to origin could exceed 90° and the inverse was taken.

Traction force microscopy of hiPSC-RPE monolayers on PDH

Traction force microscopy is an established method in literature to measure and quantify cellular forces from a single cell to tissue level. To implement this method for hiPSC-RPE monolayers cultured on PDH substrates fluorescent beads (0.1 µL of 50% solution, Invitrogen FluoSpheres™ 0.1 µm orange, 540/560) were incorporated into the hydrogel composition. The protocol inducing topographical defects was not altered and after the induction the defect formation was followed by the Axio Observer 7 microscope at 20x magnification in bright field and red fluorescent channel, taking a complete Z-stack (40 slices, 4 µm step size, central focus plane at the surface of the monolayer) every hour. After 24 hours the monolayer was destroyed by addition of 3 mL 10wt/vol% SDS solution (ThermoFisher, 28365) and the hydrogel was equilibrated for 30 minutes before taking a reference Z-stack. To reduce the complexity of the three-dimensional Z-stack the fluorescent channel was projected into a single plane by maximum intensity projection, and all the time points were aligned with the reference by the Template Matching plugin in Fiji. From the aligned images the Top, Edge, and Outside regions were cropped and analyzed with Particle Image Velocimetry (PIV) plugin in Fiji to determine the absolute displacement of the beads. Subsequently, from displacement vectors the traction forces were calculated by Fourier Transform Traction Cytometry (FTTC) plugin which took the stiffness of the substrate into account. Finally, the mean and median normal stress magnitudes were calculated by a MatLab script.

4. Photodegradable microgels

Microfluidic chip production

Photodegradable microgels (PDM) were produced in a custom designed microfluidic device with one continuous oil phase and two aqueous phases. The flow focusing junction had a 20 µm width and 200 µm length. The chip was produced by soft lithography from a two-photon (Nanoscribe Professional GT, Nanoscribe GmbH) resin printed master (printing was done by Matthias Mork, M. Sc. and Tom Schneider M. Sc.). In short, a 10:1 mixture of PDMS and activator (Dow chemicals, Sylgard 184) was degassed and poured onto the master, degassed again and cured at 60°C overnight. The PDMS chip was cut out from the surrounding PDMS and inlet and outlet holes were punched with a Rapid-Core Punch (0.75 mm). Afterwards, the PDMS chip was washed with isopropanol, followed by DI water for three times and corresponding glass slides (CarlRoth, XT62.1) with acetone, followed by isopropanol and then water for three times. Both were dried with pressured air to remove moisture and solvents and stored in a low dust environment. The PDMS chip and microscopy slides were placed in a plasma oven (Zepto, Electronic Diener) and treated with an oxygen plasma for one minute (compressed air, flow rate 0.41 mL/min, 1.27 A, 158 V, 200 W). After the plasma treatment was finished the PDMS blank and microscopy slide were brought into contact quickly and pressed together, exploiting the surface activation of both and bonding them together yielding a microfluidic chip. Before use, the channel surface was hydrophobically treated. In the beginning of this work the silanization was performed with Trichloro(1H,1H,2H,2H-perfluorooctyl)silane (Sigma-Aldrich, 448931) by putting the microfluidic chip and 50 µL of the reagent in a desiccator and applying negative pressure. The volatile silanization reagent became gaseous and coated the surface of the microfluidic chip and subsequently reacted with the PDMS surface. After overnight reaction the excess reagent was washed away by n-hexane and HFE 7500 (3M, Novec 7500) wash. As the previously described passivation is messy an alternative protocol was developed, utilizing the silanization solution Sigmacote (Sigma-Aldrich, SL2-25ML). The silanization reaction was directly injected into the channels of the microfluidic chip and all the channels were flushed. After a reaction time of one hour the passivation reaction was completed, and the channels were washed with n-hexane.

Microfluidic microgel production

Non-degradable microgels

During initial microfluidic experiments 1.5 vol/vol% Krytox surfactant (DuPont 157 FSH) in HFE 7500 (3M Novec, Ionic liquids Technologies) was trialed but showed an incompatibility with the free radical reaction initiator pair. Replacing the surfactant with 2 wt/wt% 008-Fluorosurfactant in HFE 7500 (Ran Biotechnologies, 008-Fluorosurfactant) showed better microemulsion stability during production and higher yield and size homogeneity of the microgels. The improved continuous phase was used in all subsequent microfluidic reactions and was filled in 5 mL Micolitre syringe (Hamilton, gastight series 1000, 5.0 mL, 1005 TLL).

The stock solutions for the reactants were as followed: PEG-diacrylate (0.2 g, 0.1 mmol, $1.0*10^{-4}$ mmol/µL, Biophrama PEG, HO009009-2K), 8 arm star-PEG-acrylate solution (0.40 g, 0.02 mmol, 1 mL, $2.00*10^{-5}$ mmol/µL, Biophrama PEG, A88009-20K), APS solution (0.24 g, 1.04 mmol, 1 mL water, $1.04*10^{-3}$ mmol/µL, Sigma-Aldrich, 454990), and TEMED solution (0.03 g, 0.26 mmol, 1 mL water, $2.6*10^{-4}$ mmol, Sigma-Aldrich, 151238). The first aqueous phase was composed of PEG-acrylate (200 µL, 0.45 mmol, Sigma-Aldrich, 454990), PEG-diacrylate solution (120 µL, 0.012 mmol), 8 arm star-PEG-acrylate solution (45 µL, 0.0009 mmol), TEMED solution (39 µL, 0.26 mmol), Saturated Rhodamine B solution (35 µL), and 100 µL MiliQ water. The second aqueous phase consisted of 8 arm star-PEG-acrylate solution (50 µL, 0.001 mmol), APS solution (120 µL, 1.04 mmol), and 464 µL of MiliQ water.

The aqueous solutions were mixed on a roller for 20 minutes and filled into separate 1 mL Micolitre syringe (Hamilton, gastight series 1000, 1.0 mL, 1001 TLL). To three hypodermic needles (26G, 25 mm length, B. Braun) lengths of Teflon tubing (BOLA S, 0.4 inner and 0.9 mm outer diameter, Bohlender) were attached and the needles were fastened onto the Luer-Lock connector of the syringes. The three syringes were locked into separate syringe pumps (Havard apparatus, Standard Infusion Only Pump 11 Elite Syringe Pump) and the following flow rates were established: 100 µL/h for the aqueous phases and 500 µL/h for the continuous phase until the system showed a stable extrusion of microgels. In the steady state the flow rates of the dispersed phases were gradually adjusted to 75 µL/h for the first aqueous phase and 60 µL/h for the second aqueous phase. During production the flow focusing junction was periodically monitored and when a stable flow was established the microemulsions were collected in a 5 mL Protein LoBind Eppendorf tube (Eppendorf, 0030108302) with around 300 µL of fluorinated oil. The product was collected as white foam on top of the fluorinated oil. As the microgels only partially gelated on-chip or in the collection reservoir after the batch production was done, the collection tube was closed, wrapped in parafilm and aluminum foil and placed on a roller for 24 hours to finish the polymerization. First, excess fluorinated oil was carefully removed with a syringe and needle leaving only microgel foam in the tube. In the next step the microgels were washed four times with a 1 wt/vol% Span-80 (Sigma-Aldrich, S67760) in n-hexane solution. Followed by four washing cycles with pure n-hexane. These washing steps were performed in quick succession as the microgels sedimented quickly as white precipitates in the organic phase as the fluorinated oil and surfactant was removed. In the third step excess n-hexane was removed by syringe and a 0.1 vol/vol% Triton-X 100 (Sigma-Aldrich, T8787) in water solution was added to the microgels to ensure complete removal of the surfactants and residual n-hexane. The washing cycle was repeated only one more time as the microgels sedimented slower in the aqueous environment. Finally, the microgels were suspended in MiliQ water and stored in a 5 mL Protein LoBind Eppendorf tube at room temperature until functionalization or measurement.

PEG acrylate weight percentage variation

The microgel stiffness was adjusted by reduction of the monomer content of PEG-acrylate in the first aqueous phase. All other components were constant, and the loss of volume was compensated by addition of MiliQ water so that only the weight percentage of PEG-acrylate and the co-polymerization ratio was affected.

Table 3: Composition adjustment of PEG-acrylate in the first aqueous phase. All other components were kept constat.

PEG-acrylate[a]		***H_2O***	***Co-polymerization ratio***			***Weight%***
[µL]	[mmol]	[µL]	PEG-acrylate	PEG-diacrylate	8 arm star-PEG-acrylate	wt/vol%
200	0.454	100	504	13	1	40
150	0.341	150	379	13	1	30
125	0.284	175	316	13	1	25
100	0.227	200	252	13	1	20
75	0.170	225	189	13	1	15
62.5	0.142	237.5	158	13	1	13

a) Liquid PEG-acrylate was used directly without purification.

Photodegradable microgels

The continuous phase to encapsulate the microemulsions was a commercially available solution of a fluorinated oil with a surfactant at 2 wt/vol% (RAN Biotechnologies, 008-FluoroSurfactant in HFE 7500) and 3 mL were filled in a 5 mL Micolitre syringe (Hamilton, gastight series 1000, 5.0 mL, 1005 TLL). As the photodegradable microgels could not be crosslinked via UV initiated free radical polymerization without inducing undefined photolysis during the initiation and alternative polymerization initiation reaction was established. The redox initiator pair of ammonium persulfate (APS) and tetramethylethylendiamine (TEMED) is an established method in literature but finds little application in a microfluidic environment with PEG-acrylate based monomers. To separate the initiator pair two aqueous phases were established and mixed from stock solutions before production.

Stock solution concentrations of the respective compounds were: APS solution (0.46 g, 2.02 mmol, 1 mL water, $2.02*10^{-3}$ mmol/µL, Sigma-Aldrich, 454990), 8 arm star-PEG-acrylate solution (0.40 g, 0.02 mmol, 1 mL, $2.00*10^{-5}$ mmol/µL, Biophrama PEG, A88009-20K), PDC solution (0.20 g, 0.07 mmol, 1 mL, $7.41*10^{-5}$ mmol/µL). TEMED (Sigma-Aldrich, 151238), PEG-acrylate (Sigma-Aldrich, 454990) and Glycidly methacrylate (Sigma-Aldrich, 151238) were used pure without dissolving beforehand. The first aqueous phase was composed of PEG-acrylate (50 µL, $113.5*10^{-3}$ mmol, Sigma-Aldrich, 454990), PDC solution (60 µL, $4.44*10^{-3}$ mmol), 8 arm star-PEG-acrylate solution (22.5 µL, $0.45*10^{-3}$ mmol), TEMED (19.5 µL, $130*10^{-3}$ mmol) and 117.5 µL MiliQ water. And the second aqueous phase was composed of 8 arm star-PEG-acrylate solution (25 µL, $0.50*10^{-3}$ mmol), APS solution (60 µL, $121*10^{-3}$ mmol, Sigma-Aldrich, 248614), Glycidly methacrylate (0.50 µL, $3.77*10^{-3}$ mmol) and 231.5 µL MiliQ water.

The aqueous solutions were mixed on a roller for 20 minutes and filled into separate 1 mL Micolitre syringe (Hamilton, gastight series 1000, 1.0 mL, 1001 TLL). To three hypodermic needles (26G, 25 mm length, B. Braun) lengths of Teflon tubing (BOLA S, 0.4 inner and 0.9 mm outer diameter, Bohlender) were attached and the needles were fastened onto the Luer-Lock connector of the syringes. The three syringes were locked into separate syringe pumps (Havard apparatus, Standard Infusion Only Pump 11 Elite Syringe Pump) and the following flow rates were established: Aqueous phases 40 µL/h and continuous phase 500 µL/h. An important precaution to minimize the risk of on chip gelation was to establish the continuous phase first and flood the chip and bot aqueous phase channels with fluorinated oil to create a buffer which kept the phases separated until stable flow was established. During production the flow focusing junction was periodically monitored and when a stable flow was established the microemulsions were collected in a 5 mL Protein LoBind Eppendorf tube (Eppendorf, 0030108302) with around 300 µL of fluorinated oil. The product was collected as white foam on top of the fluorinated oil. As the microgels only partially gelated on-chip or in the collection reservoir after the batch production was done, the collection tube was closed, wrapped in parafilm and aluminum foil and placed on a roller for two days to finish the polymerization. Once the hydrogel network of the microgels had formed completely the workup of the suspension was initiated. First, excess fluorinated oil was carefully removed with a syringe and needle leaving only microgel foam in the tube. In the next step the microgels were washed four times with a 1 wt/vol% Span-80 (Sigma-Aldrich, S67760) in n-hexane solution. Followed by four washing cycles with pure n-hexane. These washing steps were performed in quick succession as the microgels sedimented quickly as white precipitates in the organic phase as the fluorinated oil and surfactant was removed. In the third step excess n-hexane was removed by syringe and a 0.3 vol/vol% Triton-X 100 (Sigma-Aldrich, T8787) in water solution was added to the microgels to ensure complete removal of the surfactants and residual n-hexane. The washing cycle was repeated only one more time as the microgels sedimented slower in the aqueous environment. Finally, the microgels were rinsed thoroughly with MiliQ water in a 5 µm cell strainer (pluriSelect, 43-50005-13) and resuspended in MiliQ water. The microgels were stored in a 5 mL Protein LoBind Eppendorf tube wrapped in aluminum foil at room temperature until functionalization or measurement.

Microgel characterization

Size and stiffness measurements via nanoindentation

Non-degradable microgels

Glass bottom dishes (Cellvis, D35-20-0-N) were spincoated (1000 rpm, 1 minute, Laurell Technologies Corporation, 650 Series) with a 40:1 PDMS:Initiator mixture (Sylgard 184). The thin film was partially cured at 60°C overnight resulting in a sticky surface. Microgel solution was added onto the sample and the microgels sank to the surface and bonded overnight. Before characterization the dishes were warmed up in a cell culture incubator for two hours and after a consistent temperature of 37°C was reached the stiffness

characterization was performed with a nanoindenter (Chiaro, Optics 11 Life) on an Axio Observer 7 microscope (Zeiss) with the temperature set at 37°C. The probe calibrated to a geofactor of 2.68, with a cantilever stiffness of 0.49 N/m and a tip radius of 10 µm and the indentation depth was set to 2 µm. The indentation curves were analyzed with the DataViewerV2 software (Optics 11 Life). The microgel size was measured from the microscope images in Fiji.

Photodegradable microgels

Glass bottom dishes (Cellvis, D35-20-0-N) were coated with 100 µL poly-L-lysine (PLL) solution (Sigma-Aldrich, P2707) and incubated for one hour at room temperature. The glass surface was rinsed three times with water and photodegradable microgel suspension was pipetted onto the activated surface and incubated for 30 minutes. In this time the microgels sedimented and the epoxy moieties in the microgel surface reacted with the amines of the PLL. The compressive stiffness of the photodegradable microgels was determined via nanoindentation (Chiaro, Optics 11 Life) with a probe with a 3 µm radius tip and cantilever stiffness of 0.024 N/m yielding the effective Young's modulus. To determine the stiffness changes resulting from UV illumination induced degradation microgels were illuminated (385 nm, 3.83 mW/cm^2) with different time intervals and after an equilibration time of 30 minutes the new stiffness was measured. The recorded indentation curves were processed with the DataViewerV2 software (Optics 11 Life). The initial diameter of the photodegradable microgels and swelling induced diameter changes were tracked through images and measured in Fiji.

Microgel functionalization

Oriented attachment of recombinant adhesion proteins on the microgel surface was adapted from Di Russo et al.[38] A 30 µL suspension of roughly 12k microgels was mixed with 300 µL 2 mM HS-PEG-NTA (ProChimia, TH 007) in ethanol solution in a 1.5 mL DNA LoBind Eppendorf tube (Eppendorf, 0030108051) and the reaction between the thiol group of the linker and epoxy or acrylate groups on the surface of the microgel proceeded at room temperature overnight. Additionally, the ethanol-based solution disinfected the microgels and the following steps were performed under sterile conditions. Excess crosslinker was removed by washing the microgels on a 5 µm cell strainer (pluriSelect, 43-50005-1) with 5 mL MiliQ water. The microgels were reconstituted in 500 µL MiliQ water and the suspension was split and half of the volume being separated to be used as control microgels. To functionalize the microgels further 250 µL $CoCl_2$ (10 mM) was added and one hour on a heated shaker (400 r/min, 37°C) the NTA-Co^{2+} complex formed. Afterwards excess Co+2 was washed away with 3 mL MiliQ on a 5 µm cell strainer and 60 µL histidine-tagged human recombinant E-cadherin (50 µg/mL, R&D Systems, 8505-EC) were added and incubated at37°C for one hour on a shaker. The histidine formed a stable NTA-Co^{2+}His2 complex, excess E-cadherin was washed away with PBS, and the complexing bivalent cobalt ion was oxidized by the addition of 500 µL H_2O_2 solution (10 mM, Thermo Fisher Scientific) for 30 minutes at room temperature. The hydrogen peroxide solution was

washed away with PBS and the bio-functionalized microgels were stored sterile at 4°C and protected from light until used in immunofluorescent staining or cell culture experiments.

Microgel-cell co-culture

To facilitate microgel and cell adhesion the substrate surface had to be activated. Glass bottom dishes (Cellvis, D35-20-0-N) were plasma treated with oxygen plasma (pressured air, flow rate 0.41 mL/h, Zepto, Diener Electronic) for one minute at 200 W, Followed by an incubation with a 3-Aminopropyl triethoxysilane (APTS) solution (4 vol/vol% in isopropanol) for 5 minutes. After the reaction was complete the surface was washed with ethanol and the substrates were incubated with a glutaraldehyde solution (1 vol/vol% in water, Sigma-Aldrich, 354400) to convert the surface bound amine groups into amine reactive aldehyde groups. Finally, the dishes were washed with water and dried in the oven at 60°C for 15 minutes. The activated substrates were stored in dry condition and in the dark to preserve the reactivity for up to one month.

Before further use the dishes were sterilized by 40 minutes of UV exposure. To restrict the seeding area of the microgels a sterile hydrophobic barrier with an inner diameter of 4 mm was placed into the center of the glass bottom dish. 50 µL of microgel suspension (20 microgels/µL) were pipetted into the well. The microgels sedimented and attached to the activated surface overnight at 4°C. The samples were rinsed with PBS to remove unattached microgels and the surface was coated with 50 µL vitronectin solution (2.5 µg/mL in CellAdhere buffer, StemCell Technologies, 07183)

Microgel MDCK co-culture

LifeAct transfected Madin-Darby Canine Kidney cells were cultured in a cell culture flask until confluent. Debris was washed away by an PBS/EDTA (0.5 M, 5 mL) rinse and an additional 5 mL of EDTA solution was added to the flask to detach calcium dependent cell-cell adhesions after an incubation time of 30 minutes. The EDTA solution was replaced by a 1.5 mL Trypsin-EDTA solution (Sigma-Aldrich, T4049-500ML) and incubating two minutes. To prevent degradation of the cells the protease was stopped through the addition of 3.5 mL medium, and the suspension was transferred into a 15 mL falcon tube. After centrifugation (1000g, 4 minutes) the medium Trypsine-EDTA mixture was removed, and cells were resuspended in fresh medium at a concentration of 100k per 100 µL. 50 µL cell suspension were added per microgel coated sample and the culture was maintained for one day. Upon formation of a monolayer additional 1.5 mL medium were added and the samples were ready for further experiments.

Microgel hiPSC-RPE co-culture

Cell seeding protocol followed the method described in chapter Cell seeding of hiPSC-RPE on PDH and in short, a cell suspension of the commercially procured human induced pluripotent stem cell-derived retinal epithelium cells (hiPSC-RPE) (Fujifilm Cellular Dynamics, R1102) with a concentration of 100k cells per 100 µL was generated.

Subsequently 50 µL cell suspension was added to each microgel coated sample. After monolayer formation overnight additional 1.5 mL medium was added to each dish and the co-culture was maintained for one week with two medium changes. The samples were ready for further experiments.

Microgel illumination in co-culture

After one day of maturation time the LifeAct MDCK were ready for experiment while microgel hiPSC-RPE co-culture required one week. Furthermore hiPSC-RPE required live dye staining with SiR-actin (500 nM, Spirochrome, SC001) to fluorescently mark fibrillar actin. The samples were placed on an Axio Observer 7 with incubation and CO_2 buffering and positions with embedded microgels were selected. Before illumination reference images were taken and the diaphragm was closed to restrict UV exposure of the surrounding cells. The positions were illuminated (385 nm, 3.83 mW/cm^2, 60 seconds, 20x magnification). For the live cell imaging experiments the diaphragm was reopened and quick response images were taken. Furthermore, after an equilibration time of two hours for the MDCK co-culture and one hour for the hiPSC-RPE co-culture slow response images were taken. After the live cell imaging was complete the hiPSC-RPE co-culture was returned to the incubator and given overnight equilibration time before fixation with 2 wt/vol% paraformaldehyde solution (Thermo Fisher, J61899.AK) for 8 minutes at room temperature followed by three washing cycles with PBS to prevent over fixation.

Immunofluorescent staining and imaging of co-culture

The fixated samples were permeabilized with 0.3 wt/vol% Triton-X 100 solution (Sigma-Aldrich, T8787) for two minutes at room temperature, followed by three PBS washing cycles and incubation with a 1 wt/vol% BSA solution (Serva, 11930) for 30 minutes at room temperature to minimize unspecific binding. The staining started with the addition of the primary antibodies in 1% BSA solution and incubation overnight at 4°C. Afterwards, excess primary antibodies were washed away in three PBS washing cycles before addition of the secondary antibodies or dyes was performed, followed by incubation for two hours at room temperature. Lastly, samples were washed three times with PBS before imaging.

Samples were imaged with a Zeiss LSM710 Confocal microscope with a 40x water immersion objective (Zeiss, 420862-9970-000) in confocal mode and Airyscan super resolution mode. Captured images were processed and quantification was performed using Fiji software (National Institutes of Health, USA).

Table 4: Microgel hiPSC-RPE co-culture immunofluorescent staining antibodies and dyes.

Description	Concentration	Antibody Species	Supplier	Cat Number
Primary				
Polyclonal anti-E-cadherin	0.6 mg mL	Rabbit	Thermo Fisher	PA5-85088
Anti open conformation α-catenin (clone α-18)	1:2000	Rat	Gift from A. Nagafuchi	
ZO-1 Polyclonal antibody	1:100	Rabbit	Thermo Fisher	61-7300
Anti Phospho-Myosin Light Chain 2 (Ser19)	1:50	Rabbit	Cell Signalling	3671
Secondary				
Anti-rabbit- IgG AF647	1.5 mg mL	Goat	Jackson/ Dianova	111-605-144
Anti-rat-IgG AF488	1.5 mg mL	Donkey	Jackson/ Dianova	712-545-153
Anti-rat-IgG AF647	2 mg mL	Goat	Thermo Fisher	A-21247
Dye				
Phalloidin AF488	6.6 µM		Thermo Fisher	A12379
SiR-actin (live)	1 mM		SpiroChrome	SC001
Hoechst	16 mM		Thermo Fisher	H3570

Analysis of cell morphology in microgel cell co-culture

Images were processed and analyzed with Fiji using Stack Contrast Adjustment and Template matching plugins. The reference, quick and slow response images were segmented with Cellpose plugin, and the regions of interest were measured for cell area and perimeter. Furthermore, the shape factor and distance to the microgel were calculated. While not tracking individual cells the distance and time dependent response to the presence and degradation of the microgels was determined. Additionally, the Particle Image Velocimetry plugin was used between the reference image and either the image of the quick or slow response generating a vector map.

VII. References

[1] Yohalie Kalukula, Giuseppe Ciccone, Danahe Mohammed, Anthony Procès, Marie Versaevel, Amandine Deridoux, Lucie Ergot, Zoé Barbier1, Maxime Mansy, Roxane Aucouturier, Rémi Tranzer, Mathieu Surin, Sylvain Gabriele, Marine Luciano, "Unlocking the therapeutic potential of cellular mechanobiology," *Science Advances (*2025). https://doi.org/10.1126/sciadv.aea6817.

[2] P. Roca-Cusachs, V. Conte and X. Trepat, "Quantifying forces in cell biology," *Nature Cell Biology* 19, no. 7 (2017): 742. https://doi.org/10.1038/ncb3564.

[3] Y. Mao and S. A. Wickström, "Mechanical state transitions in the regulation of tissue form and function," *Nature Reviews Molecular Cell Biology* 25, no. 8 (2024): 654. https://doi.org/10.1038/s41580-024-00719-x.

[4] P. M. Gilbert and V. M. Weaver, "Cellular adaptation to biomechanical stress across length scales in tissue homeostasis and disease," *Seminars in cell & developmental biology* 67 (2017): 141. https://doi.org/10.1016/j.semcdb.2016.09.004.

[5] C. C. DuFort, M. J. Paszek and V. M. Weaver, "Balancing forces: architectural control of mechanotransduction," *Nature Reviews Molecular Cell Biology* 12, no. 5 (2011): 308. https://doi.org/10.1038/nrm3112.

[6] X. Trepat and E. Sahai, "Mesoscale physical principles of collective cell organization," *Nature Physics* 14, no. 7 (2018): 671. https://doi.org/10.1038/s41567-018-0194-9.

[7] D. E. Ingber, N. Wang and D. Stamenovic, "Tensegrity, cellular biophysics, and the mechanics of living systems," *Reports on progress in physics. Physical Society (Great Britain)* 77, no. 4 (2014): 46603. https://doi.org/10.1088/0034-4885/77/4/046603.

[8] J. Yan, M. Yao, B. T. Goult and M. P. Sheetz, "Talin Dependent Mechanosensitivity of Cell Focal Adhesions," *Cellular and molecular bioengineering* 8, no. 1 (2015): 151. https://doi.org/10.1007/s12195-014-0364-5.

[9] E. Hannezo and C.-P. Heisenberg, "Mechanochemical Feedback Loops in Development and Disease," *Cell* 178, no. 1 (2019): 12. https://doi.org/10.1016/j.cell.2019.05.052.

[10] J. F. Eichinger, L. J. Haeusel, D. Paukner, R. C. Aydin, J. D. Humphrey and C. J. Cyron, "Mechanical homeostasis in tissue equivalents: a review," *Biomechanics and Modeling in Mechanobiology* 20, no. 3 (2021): 833. https://doi.org/10.1007/s10237-021-01433-9.

[11] J. D. Humphrey, E. R. Dufresne and M. A. Schwartz, "Mechanotransduction and extracellular matrix homeostasis," *Nature Reviews Molecular Cell Biology* 15, no. 12 (2014): 802. https://doi.org/10.1038/nrm3896.

[12] T. Mammoto and D. E. Ingber, "Mechanical control of tissue and organ development," *Development (Cambridge, England)* 137, no. 9 (2010): 1407. https://doi.org/10.1242/dev.024166.

[13] S. Kaliman, M. Hubert and C. Wollnik et al., "Mechanical Regulation of Epithelial Tissue Homeostasis," *Physical Review X* 11, no. 3 (2021). https://doi.org/10.1103/PhysRevX.11.031029.

[14] J. M. Phillip, I. Aifuwa, J. Walston and D. Wirtz, "The Mechanobiology of Aging," *Annual Review of Biomedical Engineering* 17, no. 1 (2015): 113. https://doi.org/10.1146/annurev-bioeng-071114-040829.

[15] S. Ferrari and M. Pesce, "Stiffness and Aging in Cardiovascular Diseases: The Dangerous Relationship between Force and Senescence," *International Journal of Molecular Sciences* 22, no. 7 (2021): 3404. https://doi.org/10.3390/ijms22073404.

[16] C. Statzer, J. Y. C. Park and C. Y. Ewald, "Extracellular Matrix Dynamics as an Emerging yet Understudied Hallmark of Aging and Longevity," *Aging and disease* 14, no. 3 (2023): 670. https://doi.org/10.14336/AD.2022.1116.

[17] T. R. Cox and J. T. Erler, "Remodeling and homeostasis of the extracellular matrix: implications for fibrotic diseases and cancer," *Disease models & mechanisms* 4, no. 2 (2011): 165. https://doi.org/10.1242/dmm.004077.

[18] P. Lu, K. Takai, V. M. Weaver and Z. Werb, "Extracellular Matrix Degradation and Remodeling in Development and Disease," *Cold Spring Harbor perspectives in biology* 3, no. 12 (2011): a005058-a005058. https://doi.org/10.1101/cshperspect.a005058.

[19] C. Bonnans, J. Chou and Z. Werb, "Remodelling the extracellular matrix in development and disease," *Nature Reviews Molecular Cell Biology* 15, no. 12 (2014): 786. https://doi.org/10.1038/nrm3904.

[20] H. Yu and A. Pathak, "Emergent depth-mechanosensing of epithelial collectives regulates cell clustering and dispersal on layered matrices," *Proceedings of the National Academy of Sciences* 122, no. 37 (2025): e2423875122. https://doi.org/10.1073/pnas.2423875122.

[21] D. T. Butcher, T. Alliston and V. M. Weaver, "A tense situation: forcing tumour progression," *Nature Reviews Cancer* 9, no. 2 (2009): 108. https://doi.org/10.1038/nrc2544.

[22] S. Treppo, H. Koepp, E. C. Quan, A. A. Cole, K. E. Kuettner and A. J. Grodzinsky, "Comparison of biomechanical and biochemical properties of cartilage from human knee and ankle pairs," *Journal of orthopaedic research : official publication of the Orthopaedic Research Society* 18, no. 5 (2000): 739. https://doi.org/10.1002/jor.1100180510.

[23] “M. Wang, Z. Peng, J. A. Watson, G. S. Watson, B. N. Morris and B. A. Rayner 2012, Atomic Force Microscopy Investigation on Young’s Modulus of Cartilage for Osteoarthritis Study.” in Engineering Asset Management and Infrastructure Sustainability, edited by J. Mathew, L. Ma, A. Tan, M. Weijnen and J. Lee, London: Springer London. ISBN 978-0-85729-301-5.

[24] M. Weber, M. A. Rothschild and A. Niehoff, "Anisotropic and age-dependent elastic material behavior of the human costal cartilage," *Scientific Reports* 11, no. 1 (2021): 13618. https://doi.org/10.1038/s41598-021-93176-x.

[25] D. Sun, W. Gao, H. Hu and S. Zhou, "Why 90% of clinical drug development fails and how to improve it?," *Acta pharmaceutica Sinica. B* 12, no. 7 (2022): 3049. https://doi.org/10.1016/j.apsb.2022.02.002.

[26] A. J. Engler, S. Sen, H. L. Sweeney and D. E. Discher, "Matrix elasticity directs stem cell lineage specification," *Cell* 126, no. 4 (2006): 677. https://doi.org/10.1016/j.cell.2006.06.044.

[27] S. Qiu, X. Zhao and J. Chen et al., "Characterizing viscoelastic properties of breast cancer tissue in a mouse model using indentation," *Journal of biomechanics* 69 (2018): 81. https://doi.org/10.1016/j.jbiomech.2018.01.007.

[28] O. Chaudhuri, L. Gu and D. Klumpers et al., "Hydrogels with tunable stress relaxation regulate stem cell fate and activity," *Nature Materials* 15, no. 3 (2016): 326. https://doi.org/10.1038/nmat4489.

[29] M. Luciano, C. Tomba, A. Roux and S. Gabriele, "How multiscale curvature couples forces to cellular functions," *Nature Reviews Physics* 6, no. 4 (2024): 246. https://doi.org/10.1038/s42254-024-00700-9.

[30] A. Marín-Llauradó, S. Kale and A. Ouzeri et al., "Mapping mechanical stress in curved epithelia of designed size and shape," *Nature Communications* 14, no. 1 (2023). https://doi.org/10.1038/s41467-023-38879-7.

[31] Nathan D. Bade, Randall D. Kamien, Richard K. Assoian, Kathleen J. Stebe, "Curvature and Rho activation differentially control the alignment of cells and stress fibers," *Bade et al., Sci. Adv. (*2017): e1700150.

[32] T. Chen, A. Callan-Jones and E. Fedorov et al., "Large-scale curvature sensing by directional actin flow drives cellular migration mode switching," *Nature Physics* 15, no. 4 (2019): 393. https://doi.org/10.1038/s41567-018-0383-6.

[33] L. Pieuchot, J. Marteau and A. Guignandon et al., "Curvotaxis directs cell migration through cell-scale curvature landscapes," *Nature Communications* 9, no. 1 (2018). https://doi.org/10.1038/s41467-018-06494-6.

[34] N. Borghi, M. Sorokina and O. G. Shcherbakova et al., "E-cadherin is under constitutive actomyosin-generated tension that is increased at cell-cell contacts upon externally applied stretch," *Proceedings of the National Academy of Sciences* 109, no. 31 (2012): 12568. https://doi.org/10.1073/pnas.1204390109.

[35] B. Ladoux, W. J. Nelson, J. Yan and R. M. Mège, "The mechanotransduction machinery at work at adherens junctions," *Integrative biology : quantitative biosciences from nano to macro* 7, no. 10 (2015): 1109. https://doi.org/10.1039/c5ib00070j.

[36] M. Yao, W. Qiu and R. Liu et al., "Force-dependent conformational switch of α-catenin controls vinculin binding," *Nature Communications* 5 (2014): 4525. https://doi.org/10.1038/ncomms5525.

[37] A. Angulo-Urarte, T. van der Wal and S. Huveneers, "Cell-cell junctions as sensors and transducers of mechanical forces," *Biochimica et biophysica acta. Biomembranes* 1862, no. 9 (2020): 183316. https://doi.org/10.1016/j.bbamem.2020.183316.

[38] J. Di Russo, J. L. Young, A. Balakrishnan, A. S. Benk and J. P. Spatz, "NTA-Co3+-His6 versus NTA-Ni2+-His6 mediated E-Cadherin surface immobilization enhances cellular traction," *Biomaterials* 192 (2019): 171. https://doi.org/10.1016/j.biomaterials.2018.10.042.

[39] Z. Zhang, B. Sha and L. Zhao et al., "Programmable integrin and N-cadherin adhesive interactions modulate mechanosensing of mesenchymal stem cells by cofilin phosphorylation," *Nature Communications* 13, no. 1 (2022): 6854. https://doi.org/10.1038/s41467-022-34424-0.

[40] B. D. Cosgrove, K. L. Mui and T. P. Driscoll et al., "N-cadherin adhesive interactions modulate matrix mechanosensing and fate commitment of mesenchymal stem cells," *Nature Materials* 15, no. 12 (2016): 1297. https://doi.org/10.1038/nmat4725.

[41] M. Luciano, S.-L. Xue and W. H. de Vos et al., "Cell monolayers sense curvature by exploiting active mechanics and nuclear mechanoadaptation," *Nature Physics* 17, no. 12 (2021): 1382. https://doi.org/10.1038/s41567-021-01374-1.

[42] J.-A. Park, J. H. Kim and D. Bi et al., "Unjamming and cell shape in the asthmatic airway epithelium," *Nature materials* 14, no. 10 (2015): 1040. https://doi.org/10.1038/nmat4357.

[43] M. Vishwakarma, J. P. Spatz and T. Das, "Mechanobiology of leader-follower dynamics in epithelial cell migration," *Current opinion in cell biology* 66 (2020): 97. https://doi.org/10.1016/j.ceb.2020.05.007.

[44] T. B. Saw, A. Doostmohammadi and V. Nier et al., "Topological defects in epithelia govern cell death and extrusion," *Nature* 544, no. 7649 (2017): 212. https://doi.org/10.1038/nature21718.

[45] B. Ladoux and R.-M. Mège, "Mechanobiology of collective cell behaviours," *Nature reviews. Molecular cell biology* 18, no. 12 (2017): 743. https://doi.org/10.1038/nrm.2017.98.

[46] M. Luciano, M. Versaevel and E. Vercruysse et al., "Appreciating the role of cell shape changes in the mechanobiology of epithelial tissues," *Biophysics reviews* 3, no. 1 (2022): 11305. https://doi.org/10.1063/5.0074317.

[47] A. S. Yap, K. Duszyc and V. Viasnoff, "Mechanosensing and Mechanotransduction at Cell-Cell Junctions," *Cold Spring Harbor Perspectives in Biology* 10, no. 8 (2018). https://doi.org/10.1101/cshperspect.a028761.

[48] C. Guillot and T. Lecuit, "Mechanics of epithelial tissue homeostasis and morphogenesis," *Science* 340, no. 6137 (2013): 1185. https://doi.org/10.1126/science.1235249.

[49] M. J. Paszek, N. Zahir and K. R. Johnson et al., "Tensional homeostasis and the malignant phenotype," *Cancer cell* 8, no. 3 (2005): 241. https://doi.org/10.1016/j.ccr.2005.08.010.

[50] C. Grashoff, B. D. Hoffman and M. D. Brenner et al., "Measuring mechanical tension across vinculin reveals regulation of focal adhesion dynamics," *Nature* 466, no. 7303 (2010): 263. https://doi.org/10.1038/nature09198.

[51] W. Kong, O. Loison and P. Chavadimane Shivakumar et al., "Experimental validation of force inference in epithelia from cell to tissue scale," *Scientific Reports* 9, no. 1 (2019): 14647. https://doi.org/10.1038/s41598-019-50690-3.

[52] M. Rauzi, P. Verant, T. Lecuit and P.-F. Lenne, "Nature and anisotropy of cortical forces orienting Drosophila tissue morphogenesis," *Nature Cell Biology* 10, no. 12 (2008): 1401. https://doi.org/10.1038/ncb1798.

[53] D. K. Vig, A. E. Hamby and C. W. Wolgemuth, "On the Quantification of Cellular Velocity Fields," *Biophysical journal* 110, no. 7 (2016): 1469. https://doi.org/10.1016/j.bpj.2016.02.032.

[54] X. Trepat, M. R. Wasserman and T. E. Angelini et al., "Physical forces during collective cell migration," *Nature Physics* 5, no. 6 (2009): 426. https://doi.org/10.1038/nphys1269.

[55] D. T. Tambe, C. Corey Hardin and T. E. Angelini et al., "Collective cell guidance by cooperative intercellular forces," *Nature Materials* 10, no. 6 (2011): 469. https://doi.org/10.1038/nmat3025.

[56] C. Hagios, A. Lochter and M. J. Bissell, "Tissue architecture: the ultimate regulator of epithelial function?," *Philosophical Transactions of the Royal Society of London. Series B: Biological Sciences* 353, no. 1370 (1998): 857. https://doi.org/10.1098/rstb.1998.0250.

[57] D. Hanahan and R. A. Weinberg, "Hallmarks of cancer: the next generation," *Cell* 144, no. 5 (2011): 646. https://doi.org/10.1016/j.cell.2011.02.013.

[58] D. C. Stewart, D. Berrie and J. Li et al., "Quantitative assessment of intestinal stiffness and associations with fibrosis in human inflammatory bowel disease," *PloS one* 13, no. 7 (2018): e0200377. https://doi.org/10.1371/journal.pone.0200377.

[59] S. Saha, D. Müller and A. G. Clark, "Mechanosensory feedback loops during chronic inflammation," *Frontiers in Cell and Developmental Biology* 11 (2023): 1225677. https://doi.org/10.3389/fcell.2023.1225677.

[60] B. Alberts, *Molecular biology of the cell*, Garland Science Taylor and Francis Group, New York NY, 2015.

[61] V. Swaminathan, J. M. Kalappurakkal and S. B. Mehta et al., "Actin retrograde flow actively aligns and orients ligand-engaged integrins in focal adhesions," *Proceedings of the National Academy of Sciences* 114, no. 40 (2017): 10648. https://doi.org/10.1073/pnas.1701136114.

[62] S. Yamashiro, D. M. Rutkowski, K. A. Lynch, Y. Liu, D. Vavylonis and N. Watanabe, "Force transmission by retrograde actin flow-induced dynamic molecular stretching of Talin," *Nature Communications* 14, no. 1 (2023). https://doi.org/10.1038/s41467-023-44018-z.

[63] M. L. Gardel, B. Sabass, L. Ji, G. Danuser, U. S. Schwarz and C. M. Waterman, "Traction stress in focal adhesions correlates biphasically with actin retrograde flow speed," *The Journal of Cell Biology* 183, no. 6 (2008): 999. https://doi.org/10.1083/jcb.200810060.

[64] A. Pora, S. Yoon and G. Dreissen et al., "Regulation of keratin network dynamics by the mechanical properties of the environment in migrating cells," *Scientific Reports* 10, no. 1 (2020). https://doi.org/10.1038/s41598-020-61242-5.

[65] A. Kölsch, R. Windoffer, T. Würflinger, T. Aach and R. E. Leube, "The keratin-filament cycle of assembly and disassembly," *Journal of cell science* 123, no. 13 (2010): 2266. https://doi.org/10.1242/jcs.068080.

[66] C. Sauvanet, J. Wayt, T. Pelaseyed and A. Bretscher, "Structure, Regulation, and Functional Diversity of Microvilli on the Apical Domain of Epithelial Cells," *Annual Review of Cell and Developmental Biology* 31, no. 1 (2015): 593. https://doi.org/10.1146/annurev-cellbio-100814-125234.

[67] T. Pelaseyed and A. Bretscher, "Regulation of actin-based apical structures on epithelial cells," *Journal of cell science* 131, no. 20 (2018): jcs221853. https://doi.org/10.1242/jcs.221853.

[68] A. Barai, M. Soleilhac and W. Xi et al., "A multicellular star-shaped actin network underpins epithelial organization and connectivity," *Nature Communications* 16, no. 1 (2025). https://doi.org/10.1038/s41467-025-61438-1.

[69] Viola Vogel, "Mechanotransduction Involving Multimodular Proteins: Converting Force into Biochemical Signals," *Annu. Rev. Biophys. Biomol. Struct. (*2006).

[70] B. Alberts, *Molecular biology of the cell*, Garland Science Taylor and Francis Group, New York NY, 2015.

[71] S. Antoku, R. Zhu, S. Kutscheidt, O. T. Fackler and G. G. Gundersen, "Reinforcing the LINC complex connection to actin filaments: the role of FHOD1 in TAN line formation and nuclear movement," *Cell Cycle* 14, no. 14 (2015): 2200. https://doi.org/10.1080/15384101.2015.1053665.

[72] S. Wang, E. Stoops and U. CP et al., "Mechanotransduction via the LINC complex regulates DNA replication in myonuclei," *Journal of Cell Biology* 217, no. 6 (2018): 2005. https://doi.org/10.1083/jcb.201708137.

[73] A. A. Khilan, N. A. Al-Maslamani and H. F. Horn, "Cell stretchers and the LINC complex in mechanotransduction," *Archives of biochemistry and biophysics* 702 (2021): 108829. https://doi.org/10.1016/j.abb.2021.108829.

[74] R. Windoffer, N. Schwarz and S. Yoon et al., "Quantitative mapping of keratin networks in 3D," *eLife* 11 (2022). https://doi.org/10.7554/eLife.75894.

[75] C. Lorenz and S. Köster, "Multiscale architecture: Mechanics of composite cytoskeletal networks," *Biophysics reviews* 3, no. 3 (2022): 31304. https://doi.org/10.1063/5.0099405.

[76] P. A. Janmey, U. Euteneuer, P. Traub and M. Schliwa, "Viscoelastic properties of vimentin compared with other filamentous biopolymer networks," *Journal of Cell Biology* 113, no. 1 (1991): 155. https://doi.org/10.1083/jcb.113.1.155.

[77] B. Ranscht, "Cadherins and catenins: interactions and functions in embryonic development," *Current opinion in cell biology* 6, no. 5 (1994): 740. https://doi.org/10.1016/0955-0674(94)90102-3.

[78] R. Kemler, "From cadherins to catenins: cytoplasmic protein interactions and regulation of cell adhesion," *Trends in genetics : TIG* 9, no. 9 (1993): 317. https://doi.org/10.1016/0168-9525(93)90250-l.

[79] R. M. Mège and N. Ishiyama, "Integration of Cadherin Adhesion and Cytoskeleton at Adherens Junctions," *Cold Spring Harbor Perspectives in Biology* 9, no. 5 (2017): a028738. https://doi.org/10.1101/cshperspect.a028738.

[80] O. Campàs, I. Noordstra and A. S. Yap, "Adherens junctions as molecular regulators of emergent tissue mechanics," *Nature Reviews Molecular Cell Biology* 25, no. 4 (2024): 252. https://doi.org/10.1038/s41580-023-00688-7.

[81] C. Collinet and T. Lecuit, "Stability and dynamics of cell-cell junctions," *Progress in molecular biology and translational science* 116 (2013): 25. https://doi.org/10.1016/B978-0-12-394311-8.00002-9.

[82] P.-O. Strale, L. Duchesne and G. Peyret et al., "The formation of ordered nanoclusters controls cadherin anchoring to actin and cell–cell contact fluidity," *Journal of Cell Biology* 210, no. 2 (2015): 333. https://doi.org/10.1083/jcb.201410111.

[83] A. J. Price, A.-L. Cost, H. Ungewiß, J. Waschke, A. R. Dunn and C. Grashoff, "Mechanical loading of desmosomes depends on the magnitude and orientation of external stress," *Nature Communications* 9, no. 1 (2018): 5284. https://doi.org/10.1038/s41467-018-07523-0.

[84] M. Klingeborn and E. D. Reese, "Desmosome and Hemidesmosome Disassembly in Retinal Pigmented Epithelium: Intersection with the Exosome Pathway," *Advances in experimental medicine and biology* 1468 (2025): 339. https://doi.org/10.1007/978-3-031-76550-6_56.

[85] I. Delon and N. H. Brown, "Integrins and the actin cytoskeleton," *Current opinion in cell biology* 19, no. 1 (2007): 43. https://doi.org/10.1016/j.ceb.2006.12.013.

[86] M. L. Gardel, J. H. Shin, F. C. MacKintosh, L. Mahadevan, P. Matsudaira and D. A. Weitz, "Elastic behavior of cross-linked and bundled actin networks," *Science* 304, no. 5675 (2004): 1301. https://doi.org/10.1126/science.1095087.

[87] J. Chang and O. Chaudhuri, "Beyond proteases: Basement membrane mechanics and cancer invasion," *Journal of Cell Biology* 218, no. 8 (2019): 2456. https://doi.org/10.1083/jcb.201903066.

[88] “ 2005, Morphology and Ultrastructure of Basement Membranes.” in Basement Membranes: Cell and Molecular Biology: Elsevier. ISBN 9780121533564.

[89] W. Halfter, J. Candiello, H. Hu, P. Zhang, E. Schreiber and M. Balasubramani, "Protein composition and biomechanical properties of in vivo-derived basement membranes," *Cell adhesion & migration* 7, no. 1 (2013): 64. https://doi.org/10.4161/cam.22479.

[90] A. N. Kozyrina, T. Piskova and J. Di Russo, "Mechanobiology of Epithelia From the Perspective of Extracellular Matrix Heterogeneity," *Frontiers in Bioengineering and Biotechnology* 8 (2020): 596599. https://doi.org/10.3389/fbioe.2020.596599.

[91] R. Zaidel-Bar, C. Ballestrem, Z. Kam and B. Geiger, "Early molecular events in the assembly of matrix adhesions at the leading edge of migrating cells," *Journal of cell science* 116, no. Pt 22 (2003): 4605. https://doi.org/10.1242/jcs.00792.

[92] P. Kanchanawong and D. A. Calderwood, "Organization, dynamics and mechanoregulation of integrin-mediated cell–ECM adhesions," *Nature Reviews Molecular Cell Biology* 24, no. 2 (2023): 142. https://doi.org/10.1038/s41580-022-00531-5.

[93] Z. Sun, S. S. Guo and R. Fässler, "Integrin-mediated mechanotransduction," *Journal of Cell Biology* 215, no. 4 (2016): 445. https://doi.org/10.1083/jcb.201609037.

[94] T. Mitchison and M. Kirschner, "Cytoskeletal dynamics and nerve growth," *Neuron* 1, no. 9 (1988): 761. https://doi.org/10.1016/0896-6273(88)90124-9.

[95] W. Thomas, "Catch bonds in adhesion," *Annual Review of Biomedical Engineering* 10 (2008): 39. https://doi.org/10.1146/annurev.bioeng.10.061807.160427.

[96] J. C. Friedland, M. H. Lee and D. Boettiger, "Mechanically activated integrin switch controls alpha5beta1 function," *Science* 323, no. 5914 (2009): 642. https://doi.org/10.1126/science.1168441.

[97] F. Kong, Z. Li and W. M. Parks et al., "Cyclic mechanical reinforcement of integrin-ligand interactions," *Molecular cell* 49, no. 6 (2013): 1060. https://doi.org/10.1016/j.molcel.2013.01.015.

[98] J. M. de Pereda, E. Ortega, N. Alonso-García, M. Gómez-Hernández and A. Sonnenberg, "Advances and perspectives of the architecture of hemidesmosomes: Lessons from structural biology," *Cell adhesion & migration* 3, no. 4 (2009): 361. https://doi.org/10.4161/cam.3.4.9525.

[99] A. N. Kozyrina, T. Piskova and F. Semeraro et al., "Laminin-defined mechanical status modulates retinal pigment epithelium phagocytosis," *EMBO Reports* 26, no. 13 (2025): 3357. https://doi.org/10.1038/s44319-025-00475-9.

[100] B. J. Hernandez, N. P. Skiba and K. Plössl et al., "Polarized Desmosome and Hemidesmosome Shedding via Small Extracellular Vesicles is an Early Indicator of Outer Blood-Retina Barrier Dysfunction," *Journal of extracellular biology* 2, no. 10 (2023). https://doi.org/10.1002/jex2.116.

[101] P. Rousselle, C. Laigle and G. Rousselet, "The basement membrane in epidermal polarity, stemness, and regeneration," *American journal of physiology. Cell physiology* 323, no. 6 (2022): C1807-C1822. https://doi.org/10.1152/ajpcell.00069.2022.

[102] S. Yang, J. Zhou and D. Li, "Functions and Diseases of the Retinal Pigment Epithelium," *Frontiers in Pharmacology* 12 (2021): 727870. https://doi.org/10.3389/fphar.2021.727870.

[103] J. R. Sparrow, D. Hicks and C. P. Hamel, "The retinal pigment epithelium in health and disease," *Current molecular medicine* 10, no. 9 (2010): 802. https://doi.org/10.2174/156652410793937813.

[104] O. Strauss, "The Retinal Pigment Epithelium in Visual Function," *Physiological reviews* 85, no. 3 (2005): 845. https://doi.org/10.1152/physrev.00021.2004.

[105] T. Piskova, A. N. Kozyrina and J. Di Russo, "Mechanobiological implications of age-related remodelling in the outer retina," *Biomaterials advances* 147 (2023): 213343. https://doi.org/10.1016/j.bioadv.2023.213343.

[106] J. C. Booij, D. C. Baas, J. Beisekeeva, T. G. M. F. Gorgels and A. A. B. Bergen, "The dynamic nature of Bruch's membrane," *Progress in retinal and eye research* 29, no. 1 (2010): 1. https://doi.org/10.1016/j.preteyeres.2009.08.003.

[107] J.-D. Huang, J. B. Presley, M. F. Chimento, C. A. Curcio and M. Johnson, "Age-related changes in human macular Bruch's membrane as seen by quick-freeze/deep-etch," *Experimental eye research* 85, no. 2 (2007): 202. https://doi.org/10.1016/j.exer.2007.03.011.

[108] Moore DJ, Hussain AA, Marshall J, "Age-related variation in the hydraulic conductivity of Bruch's membrane," *Invest Ophthalmol Vis Sci.* 36 (1995).

[109] S. Panda-Jonas, J. B. Jonas and M. Jakobczyk-Zmija, "Retinal pigment epithelial cell count, distribution, and correlations in normal human eyes," *American journal of ophthalmology* 121, no. 2 (1996): 181. https://doi.org/10.1016/S0002-9394(14)70583-5.

[110] Bhatia, S. K., Rashid, A., Chrenek, M. A., Zhang, Q., Bruce, B. B., Klein, M., Boatright, J. H., Jiang, Y., Grossniklaus, H. E. & Nickerson, J. M, "Analysis of RPE morphometry in human eyes," *Mol Vis* 22 (2016): 898.

[111] V. K. Gupta, S. Nam and D. Yim et al., "The nature of cell division forces in epithelial monolayers," *Journal of Cell Biology* 220, no. 8 (2021): e202011106. https://doi.org/10.1083/jcb.202011106.

[112] Del Priore LV, Kuo YH, Tezel TH, "Age-related changes in human RPE cell density and apoptosis proportion in situ," *Invest Ophthalmol Vis Sci.* 43 (2002): 3312.

[113] I.-S. Tarau, A. Berlin, C. A. Curcio and T. Ach, "The Cytoskeleton of the Retinal Pigment Epithelium: from Normal Aging to Age-Related Macular Degeneration," *International Journal of Molecular Sciences* 20, no. 14 (2019): 3578. https://doi.org/10.3390/ijms20143578.

[114] Vera L Bonilha, "Age and disease-related structural changes in the retinal pigment epithelium," *Clinical Ophthalmology (*2008).

[115] G. Inana, C. Murat, W. An, X. Yao, I. R. Harris and J. Cao, "RPE phagocytic function declines in age-related macular degeneration and is rescued by human umbilical tissue derived cells," *Journal of translational medicine* 16, no. 1 (2018): 63. https://doi.org/10.1186/s12967-018-1434-6.

[116] J. Y. W. Ma, U. Greferath and J. H. C. Wong et al., "Aging induces cell loss and a decline in phagosome processing in the mouse retinal pigment epithelium," *Neurobiology of aging* 128 (2023): 1. https://doi.org/10.1016/j.neurobiolaging.2023.03.003.

[117] Q. Ke, L. Gong and X. Zhu et al., "Multinucleated Retinal Pigment Epithelial Cells Adapt to Vision and Exhibit Increased DNA Damage Response," *Cells* 11, no. 9 (2022). https://doi.org/10.3390/cells11091552.

[118] R. Guymer, P. Luthert and A. Bird, "Changes in Bruch's membrane and related structures with age," *Progress in retinal and eye research* 18, no. 1 (1999): 59. https://doi.org/10.1016/S1350-9462(98)00012-3.

[119] S. M. Waldstein, W.-D. Vogl, H. Bogunovic, A. Sadeghipour, S. Riedl and U. Schmidt-Erfurth, "Characterization of Drusen and Hyperreflective Foci as Biomarkers for Disease Progression in Age-Related Macular Degeneration Using Artificial Intelligence in Optical Coherence Tomography," *JAMA Ophthalmology* 138, no. 7 (2020): 740. https://doi.org/10.1001/jamaophthalmol.2020.1376.

[120] F. Schlanitz, B. Baumann and S. Sacu et al., "Impact of drusen and drusenoid retinal pigment epithelium elevation size and structure on the integrity of the retinal pigment epithelium layer," *The British journal of ophthalmology* 103, no. 2 (2019): 227. https://doi.org/10.1136/bjophthalmol-2017-311782.

[121] T. J. Heesterbeek, L. Lorés-Motta, C. B. Hoyng, Y. T. E. Lechanteur and A. I. den Hollander, "Risk factors for progression of age-related macular degeneration," *Ophthalmic and Physiological Optics* 40, no. 2 (2020): 140. https://doi.org/10.1111/opo.12675.

[122] G. Malek and E. M. Lad, "Emerging roles for nuclear receptors in the pathogenesis of age-related macular degeneration," *Cellular and molecular life sciences : CMLS* 71, no. 23 (2014): 4617. https://doi.org/10.1007/s00018-014-1709-x.

[123] S. S. Ong, A. D. Proia, H. E. Whitson, S. Farsiu, P. M. Doraiswamy and E. M. Lad, "Ocular amyloid imaging at the crossroad of Alzheimer's disease and age-related macular degeneration: implications for diagnosis and therapy," *Journal of neurology* 266, no. 7 (2019): 1566. https://doi.org/10.1007/s00415-018-9028-z.

[124] "Age-related Macular Degeneration,".

[125] F. M. Watt and W. T. S. Huck, "Role of the extracellular matrix in regulating stem cell fate," *Nature Reviews Molecular Cell Biology* 14, no. 8 (2013): 467. https://doi.org/10.1038/nrm3620.

[126] I. Levental, P. C. Georges and P. A. Janmey, "Soft biological materials and their impact on cell function," *Soft Matter* 3, no. 3 (2007): 299. https://doi.org/10.1039/B610522J.

[127] P. D. Ross, L. Polson and M.-H. Grosbras, "Developmental Changes in Emotion Recognition from Full-Light and Point-Light Displays of Body Movement," *PloS one* 7, no. 9 (2012): e44815. https://doi.org/10.1371/journal.pone.0044815.

[128] K. Uto, J. H. Tsui, C. A. DeForest and D.-H. Kim, "Dynamically tunable cell culture platforms for tissue engineering and mechanobiology," *Progress in Polymer Science* 65 (2017): 53. https://doi.org/10.1016/j.progpolymsci.2016.09.004.

[129] J. A. Burdick and W. L. Murphy, "Moving from static to dynamic complexity in hydrogel design," *Nature Communications* 3, no. 1 (2012). https://doi.org/10.1038/ncomms2271.

[130] M. Tenje, F. Cantoni and A. M. Porras Hernández et al., "A practical guide to microfabrication and patterning of hydrogels for biomimetic cell culture scaffolds," *Organs-on-a-Chip* 2 (2020): 100003. https://doi.org/10.1016/j.ooc.2020.100003.

[131] W. J. Polacheck, R. Li, S. G. M. Uzel and R. D. Kamm, "Microfluidic platforms for mechanobiology," *Lab on a chip* 13, no. 12 (2013): 2252. https://doi.org/10.1039/C3LC41393D.

[132] M. P. Lutolf and J. A. Hubbell, "Synthetic biomaterials as instructive extracellular microenvironments for morphogenesis in tissue engineering," *Nature Biotechnology* 23, no. 1 (2005): 47. https://doi.org/10.1038/nbt1055.

[133] P. C. D. P. Dingal and D. E. Discher, "Combining insoluble and soluble factors to steer stem cell fate," *Nature Materials* 13, no. 6 (2014): 532. https://doi.org/10.1038/nmat3997.

[134] N. P. Desai and J. A. Hubbell, "Surface physical interpenetrating networks of poly(ethylene terephthalate) and poly(ethylene oxide) with biomedical applications," *Macromolecules* 25, no. 1 (1992): 226. https://doi.org/10.1021/ma00027a038.

[135] A. M. Kloxin, M. W. Tibbitt and K. S. Anseth, "Synthesis of photodegradable hydrogels as dynamically tunable cell culture platforms," *Nature protocols* 5, no. 12 (2010): 1867. https://doi.org/10.1038/nprot.2010.139.

[136] F. Liu and M. W. Urban, "Recent advances and challenges in designing stimuli-responsive polymers," *Progress in Polymer Science* 35, no. 1-2 (2010): 3. https://doi.org/10.1016/j.progpolymsci.2009.10.002.

[137] M. W. Tibbitt and K. S. Anseth, "Dynamic Microenvironments: The Fourth Dimension," *Science Translational Medicine* 4, no. 160 (2012). https://doi.org/10.1126/scitranslmed.3004804.

[138] P. Lu, D. Ruan and M. Huang et al., "Harnessing the potential of hydrogels for advanced therapeutic applications: current achievements and future directions," *Signal Transduction and Targeted Therapy* 9, no. 1 (2024). https://doi.org/10.1038/s41392-024-01852-x.

[139] A. M. Kloxin, C. J. Kloxin, C. N. Bowman and K. S. Anseth, "Mechanical Properties of Cellularly Responsive Hydrogels and Their Experimental Determination," *Advanced materials* 22, no. 31 (2010): 3484. https://doi.org/10.1002/adma.200904179.

[140] M. A. C. Stuart, W. T. S. Huck and J. Genzer et al., "Emerging applications of stimuli-responsive polymer materials," *Nature Materials* 9, no. 2 (2010): 101. https://doi.org/10.1038/nmat2614.

[141] C. G. Rolli, H. Nakayama, K. Yamaguchi, J. P. Spatz, R. Kemkemer and J. Nakanishi, "Switchable adhesive substrates: revealing geometry dependence in collective cell behavior," *Biomaterials* 33, no. 8 (2012): 2409. https://doi.org/10.1016/j.biomaterials.2011.12.012.

[142] J. Nakanishi, Y. Kikuchi, T. Takarada, H. Nakayama, K. Yamaguchi and M. Maeda, "Spatiotemporal control of cell adhesion on a self-assembled monolayer having a

photocleavable protecting group," *Analytica chimica acta* 578, no. 1 (2006): 100. https://doi.org/10.1016/j.aca.2006.04.059.

[143] F. Farjood, A. Ahmadpour, S. Ostvar and E. Vargis, "Acute mechanical stress in primary porcine RPE cells induces angiogenic factor expression and in vitro angiogenesis," *Journal of Biological Engineering* 14, no. 1 (2020). https://doi.org/10.1186/s13036-020-00235-4.

[144] S. J. Todd, D. J. Scurr, J. E. Gough, M. R. Alexander and R. V. Ulijn, "Enzyme-activated RGD ligands on functionalized poly(ethylene glycol) monolayers: surface analysis and cellular response," *Langmuir* 25, no. 13 (2009): 7533. https://doi.org/10.1021/la900376h.

[145] J. L. Young and A. J. Engler, "Hydrogels with time-dependent material properties enhance cardiomyocyte differentiation in vitro," *Biomaterials* 32, no. 4 (2011): 1002. https://doi.org/10.1016/j.biomaterials.2010.10.020.

[146] M. Guvendiren and J. A. Burdick, "Stiffening hydrogels to probe short- and long-term cellular responses to dynamic mechanics," *Nature Communications* 3, no. 1 (2012). https://doi.org/10.1038/ncomms1792.

[147] S. Khetan, M. Guvendiren, W. R. Legant, D. M. Cohen, C. S. Chen and J. A. Burdick, "Degradation-mediated cellular traction directs stem cell fate in covalently crosslinked three-dimensional hydrogels," *Nature Materials* 12, no. 5 (2013): 458. https://doi.org/10.1038/nmat3586.

[148] L.-W. Lee, G.-H. Lee and I.-H. Su et al., "Mechanobiological mechanism of cyclic stretch-induced cell columnarization," *Cell reports* 44, no. 5 (2025): 115662. https://doi.org/10.1016/j.celrep.2025.115662.

[149] D. Jaworski, L. Hundsdorfer, E. Bastounis and I. Constantinou, "StretchView – A Multi-Axial Cell-Stretching Device for Long-Term Automated Videomicroscopy of Living Cells," *Advanced science* 12, no. 9 (2025): 2408853. https://doi.org/10.1002/advs.202408853.

[150] N. J. Douville, P. Zamankhan and Y.-C. Tung et al., "Combination of fluid and solid mechanical stresses contribute to cell death and detachment in a microfluidic alveolar model," *Lab on a chip* 11, no. 4 (2011): 609. https://doi.org/10.1039/C0LC00251H.

[151] N. Yamada, T. Okano, H. Sakai, F. Karikusa, Y. Sawasaki and Y. Sakurai, "Thermo-responsive polymeric surfaces; control of attachment and detachment of cultured cells," *Die Makromolekulare Chemie, Rapid Communications* 11, no. 11 (1990): 571. https://doi.org/10.1002/marc.1990.030111109.

[152] N. Matsuda, T. Shimizu, M. Yamato and T. Okano, "Tissue Engineering Based on Cell Sheet Technology," *Advanced materials* 19, no. 20 (2007): 3089. https://doi.org/10.1002/adma.200701978.

[153] H. Takahashi, T. Shimizu, M. Nakayama, M. Yamato and T. Okano, "The use of anisotropic cell sheets to control orientation during the self-organization of 3D muscle tissue," *Biomaterials* 34, no. 30 (2013): 7372. https://doi.org/10.1016/j.biomaterials.2013.06.033.

[154] B. Trappmann, J. E. Gautrot and J. T. Connelly et al., "Extracellular-matrix tethering regulates stem-cell fate," *Nature Materials* 11, no. 7 (2012): 642. https://doi.org/10.1038/nmat3339.

[155] A. Gandin, V. Torresan, T. Panciera and G. Brusatin, "A Scalable Method to Fabricate 2D Hydrogel Substrates for Mechanobiology Studies with Independent Tuning of Adhesiveness and Stiffness," *Methods and Protocols* 7, no. 5 (2024): 75. https://doi.org/10.3390/mps7050075.

[156] C. Yang, M. W. Tibbitt, L. Basta and K. S. Anseth, "Mechanical memory and dosing influence stem cell fate," *Nature Materials* 13, no. 6 (2014): 645. https://doi.org/10.1038/nmat3889.

[157] C. M. Magin and K. S. Anseth, "In Situ Control of Cell Substrate Microtopographies Using Photolabile Hydrogels," *Small* 9, no. 4 (2013): 578. https://doi.org/10.1002/smll.201201841.

[158] C. A. DeForest and K. S. Anseth, "Cytocompatible click-based hydrogels with dynamically tunable properties through orthogonal photoconjugation and photocleavage reactions," *Nature Chemistry* 3, no. 12 (2011): 925. https://doi.org/10.1038/nchem.1174.

[159] T. L. Rapp and C. A. DeForest, "Tricolor visible wavelength-selective photodegradable hydrogel biomaterials," *Nature Communications* 14, no. 1 (2023): 5250. https://doi.org/10.1038/s41467-023-40805-w.

[160] J. Nakanishi, Y. Kikuchi, S. Inoue, K. Yamaguchi, T. Takarada and M. Maeda, "Spatiotemporal control of migration of single cells on a photoactivatable cell microarray," *Journal of the American Chemical Society* 129, no. 21 (2007): 6694. https://doi.org/10.1021/ja070294p.

[161] C. A. DeForest, B. D. Polizzotti and K. S. Anseth, "Sequential click reactions for synthesizing and patterning three-dimensional cell microenvironments," *Nature Materials* 8, no. 8 (2009): 659. https://doi.org/10.1038/nmat2473.

[162] A. Metters and J. Hubbell, "Network Formation and Degradation Behavior of Hydrogels Formed by Michael-Type Addition Reactions," *Biomacromolecules* 6, no. 1 (2005): 290. https://doi.org/10.1021/bm049607o.

[163] S. Kim, J. Park and H.-W. Kim et al., "Low-Loaded Polyethylene Glycol (PEG) Resin for High-Purity Peptide Synthesis and Cell Binding Assays," *BioChip Journal* 17, no. 4 (2023): 447. https://doi.org/10.1007/s13206-023-00120-4.

[164] S. Kim, S.-M. Lee, S. S. Lee and D.-S. Shin, "Microfluidic Generation of Amino-Functionalized Hydrogel Microbeads Capable of On-Bead Bioassay," *Micromachines* 10, no. 8 (2019): 527. https://doi.org/10.3390/mi10080527.

[165] S. V. Murphy and A. Atala, "3D bioprinting of tissues and organs," *Nature Biotechnology* 32, no. 8 (2014): 773. https://doi.org/10.1038/nbt.2958.

[166] F. Reul, C. Bergerbit and I. Scarlat et al., "Photodegradable Hydrogels for On-Demand Modeling of Age-Related Spatiotemporal ECM Deformation," *Small (*2026): e09246. https://doi.org/10.1002/smll.202509246.

[167] M. L. Ohnsorg, E. A. Hushka and K. S. Anseth, "Photoresponsive Chemistries for User-Directed Hydrogel Network Modulation to Investigate Cell–Matrix Interactions," *Accounts of Chemical Research* 58, no. 1 (2025): 47. https://doi.org/10.1021/acs.accounts.4c00548.

[168] B. Sana, A. Finne-Wistrand and D. Pappalardo, "Recent development in near infrared light-responsive polymeric materials for smart drug-delivery systems," *Materials Today Chemistry* 25 (2022): 100963. https://doi.org/10.1016/j.mtchem.2022.100963.

[169] L. Beauté, N. McClenaghan and S. Lecommandoux, "Photo-triggered polymer nanomedicines: From molecular mechanisms to therapeutic applications," *Advanced drug delivery reviews* 138 (2019): 148. https://doi.org/10.1016/j.addr.2018.12.010.

[170] A. Ansari, S. Bhowmik and K. Zhang et al., "A Visible Light-Responsive Hydrogel to Study the Effect of Dynamic Tissue Stiffness on Cellular Mechanosensing," *Advanced Functional Materials* 35, no. 35 (2025): 2501585. https://doi.org/10.1002/adfm.202501585.

[171] F. Mauro, C. F. Natale, V. Panzetta and P. A. Netti, "Development of an Azobenzene-Based Cell Culture Photoresponsive Platform for In Situ Modulation of Surface Topography in Wet Environments," *ACS Applied Materials & Interfaces* 16, no. 23 (2024): 29823. https://doi.org/10.1021/acsami.4c04186.

[172] C. Fedele, P. A. Netti and S. Cavalli, "Azobenzene-based polymers: emerging applications as cell culture platforms," *Biomaterials science* 6, no. 5 (2018): 990. https://doi.org/10.1039/C8BM00019K.

[173] J. Auernheimer, C. Dahmen, U. Hersel, A. Bausch and H. Kessler, "Photoswitched Cell Adhesion on Surfaces with RGD Peptides," *Journal of the American Chemical Society* 127, no. 46 (2005): 16107. https://doi.org/10.1021/ja053648q.

[174] A. M. Rosales, K. M. Mabry, E. M. Nehls and K. S. Anseth, "Photoresponsive Elastic Properties of Azobenzene-Containing Poly(ethylene-glycol)-Based Hydrogels," *Biomacromolecules* 16, no. 3 (2015): 798. https://doi.org/10.1021/bm501710e.

[175] J. Jiang, X. Yuan and L. Hu, "Recent Advances of Azobenzene-Based Photoresponsive Molecular Switches for Protein-Targeted Photopharmacology," *Molecules* 31, no. 7 (2026): 1205. https://doi.org/10.3390/molecules31071205.

[176] J. Volarić, S. Thallmair, B. L. Feringa and W. Szymanski, "Photoswitchable, Water-Soluble Bisazobenzene Cross-Linkers with Enhanced Properties for Biological Applications," *ChemPhotoChem* 6, no. 12 (2022): e202200170. https://doi.org/10.1002/cptc.202200170.

[177] M. Bril, A. Saberi and I. Jorba et al., "Shape-Morphing Photoresponsive Hydrogels Reveal Dynamic Topographical Conditioning of Fibroblasts," *Advanced science* 10, no. 31 (2023): 2303136. https://doi.org/10.1002/advs.202303136.

[178] C. Li, A. Iscen, L. C. Palmer, G. C. Schatz and S. I. Stupp, "Light-Driven Expansion of Spiropyran Hydrogels," *Journal of the American Chemical Society* 142, no. 18 (2020): 8447. https://doi.org/10.1021/jacs.0c02201.

[179] R. Klajn, "Spiropyran-based dynamic materials," *Chemical Society reviews* 43, no. 1 (2014): 148. https://doi.org/10.1039/C3CS60181A.

[180] R. W. Yip/Y. X. Wen/D. Gravel/R. Giasson/D. K. Sharma, "Photochemistry of the o-nitrobenzyl system in solution: identification of the biradical intermediate in the intramolecular rearrangement," (1991).

[181] A. P. Pelliccioli and J. Wirz, "Photoremovable protecting groups: reaction mechanisms and applications," *Photochemical & photobiological sciences : Official journal of the European Photochemistry Association and the European Society for Photobiology* 1, no. 7 (2002): 441. https://doi.org/10.1039/B200777K.

[182] A. L. Fink, A. G. Groß, F. Puch and R. Geitner, "Photolysis of ortho-Nitrobenzyl Esters: Kinetics and Substituent Effects," *ACS omega* 10, no. 47 (2025): 57560. https://doi.org/10.1021/acsomega.5c08422.

[183] P. K. Yong and A. Banerjee, "Photochemistry of 2-Nitrobenzyl Enol Ethers: Oxidative CC Bond Scission," *Organic Letters* 7, no. 12 (2005): 2485. https://doi.org/10.1021/ol0508072.

[184] C. P. Holmes, "Model Studies for New o-Nitrobenzyl Photolabile Linkers: Substituent Effects on the Rates of Photochemical Cleavage," *The Journal of organic chemistry* 62, no. 8 (1997): 2370. https://doi.org/10.1021/jo961602x.

[185] A. Cahill, M. Walko and B. Fenton et al., "Design and characterisation of photoactivatable and lysine reactive o-nitrobenzyl alcohol-based crosslinkers," *Chemical science* 16, no. 33 (2025): 15239. https://doi.org/10.1039/D5SC03211C.

[186] A. Blanc and C. G. Bochet, "Isotope Effects in Photochemistry. 1. o -Nitrobenzyl Alcohol Derivatives," *Journal of the American Chemical Society* 126, no. 23 (2004): 7174. https://doi.org/10.1021/ja049686b.

[187] P. J. LeValley, R. Neelarapu, B. P. Sutherland, S. Dasgupta, C. J. Kloxin and A. M. Kloxin, "Photolabile Linkers: Exploiting Labile Bond Chemistry to Control Mode and Rate of Hydrogel Degradation and Protein Release," *Journal of the American Chemical Society* 142, no. 10 (2020): 4671. https://doi.org/10.1021/jacs.9b11564.

[188] W. Xiong, Y. Wang, X. Yang and W. H. Liu, "Selective Hydrolysis of Primary and Secondary Amides Enabled by Visible Light," *Organic Letters* 25, no. 17 (2023): 2948. https://doi.org/10.1021/acs.orglett.3c00354.

[189] Y. V. Il'ichev, M. A. Schwörer and J. Wirz, "Photochemical Reaction Mechanisms of 2-Nitrobenzyl Compounds: Methyl Ethers and Caged ATP," *Journal of the American Chemical Society* 126, no. 14 (2004): 4581. https://doi.org/10.1021/ja039071z.

[190] I.-N. Lee, O. Dobre and D. Richards et al., "Photoresponsive Hydrogels with Photoswitchable Mechanical Properties Allow Time-Resolved Analysis of Cellular Responses to Matrix Stiffening," *ACS Applied Materials & Interfaces* 10, no. 9 (2018): 7765. https://doi.org/10.1021/acsami.7b18302.

[191] A. M. Kloxin, A. M. Kasko, C. N. Salinas and K. S. Anseth, "Photodegradable hydrogels for dynamic tuning of physical and chemical properties," *Science (New York, N.Y.)* 324, no. 5923 (2009): 59. https://doi.org/10.1126/science.1169494.

[192] J. M. Guisan, J. M. Bolivar, F. López-Gallego and J. Rocha-Martín, "Immobilization of Enzymes and Cells," *Springer New York, NY (*2020): 2100.

[193] W. Sun, W. Liu, Z. Wu and H. Chen, "Chemical Surface Modification of Polymeric Biomaterials for Biomedical Applications," *Macromolecular Rapid Communications* 41, no. 8 (2020): 1900430. https://doi.org/10.1002/marc.201900430.

[194] S. A. Fisher, A. E. Baker and M. S. Shoichet, "Designing Peptide and Protein Modified Hydrogels: Selecting the Optimal Conjugation Strategy," *Journal of the American Chemical Society* 139, no. 22 (2017): 7416. https://doi.org/10.1021/jacs.7b00513.

[195] M. E. Smithmyer, J. B. Spohn and A. M. Kloxin, "Probing Fibroblast Activation in Response to Extracellular Cues with Whole Protein- or Peptide-Functionalized Step-Growth Hydrogels," *ACS Biomaterials Science & Engineering* 4, no. 9 (2018): 3304. https://doi.org/10.1021/acsbiomaterials.8b00491.

[196] V. Gribova, T. Crouzier and C. Picart, "A material's point of view on recent developments of polymeric biomaterials: control of mechanical and biochemical properties," *Journal of materials chemistry* 21, no. 38 (2011): 14354. https://doi.org/10.1039/C1JM11372K.

[197] A. Wolfel, M. Jin and J. I. Paez, "Current strategies for ligand bioconjugation to poly(acrylamide) gels for 2D cell culture: Balancing chemo-selectivity, biofunctionality, and user-friendliness," *Frontiers in Chemistry* 10 (2022): 1012443. https://doi.org/10.3389/fchem.2022.1012443.

[198] J. S. Miller, C. J. Shen, W. R. Legant, J. D. Baranski, B. L. Blakely and C. S. Chen, "Bioactive hydrogels made from step-growth derived PEG-peptide macromers," *Biomaterials* 31, no. 13 (2010): 3736. https://doi.org/10.1016/j.biomaterials.2010.01.058.

[199] J. A. Shadish, G. M. Benuska and C. A. DeForest, "Bioactive site-specifically modified proteins for 4D patterning of gel biomaterials," *Nature Materials* 18, no. 9 (2019): 1005. https://doi.org/10.1038/s41563-019-0367-7.

[200] K. A. Mosiewicz, L. Kolb and A. J. van der Vlies et al., "In situ cell manipulation through enzymatic hydrogel photopatterning," *Nature Materials* 12, no. 11 (2013): 1072. https://doi.org/10.1038/nmat3766.

[201] O. Dobre, M. A. G. Oliva and G. Ciccone et al., "A Hydrogel Platform that Incorporates Laminin Isoforms for Efficient Presentation of Growth Factors – Neural Growth and Osteogenesis," *Advanced Functional Materials* 31, no. 21 (2021): 2010225. https://doi.org/10.1002/adfm.202010225.

[202] D. Barros, I. F. Amaral and A. P. Pêgo, "Laminin-Inspired Cell-Instructive Microenvironments for Neural Stem Cells," *Biomacromolecules* 21, no. 2 (2020): 276. https://doi.org/10.1021/acs.biomac.9b01319.

[203] A. T. Francisco, P. Y. Hwang, C. G. Jeong, L. Jing, J. Chen and L. A. Setton, "Photocrosslinkable laminin-functionalized polyethylene glycol hydrogel for intervertebral disc regeneration," *Acta biomaterialia* 10, no. 3 (2014): 1102. https://doi.org/10.1016/j.actbio.2013.11.013.

[204] J. R. Tse and A. J. Engler, "Preparation of Hydrogel Substrates with Tunable Mechanical Properties," *Current Protocols in Cell Biology* 47, no. 1 (2010). https://doi.org/10.1002/0471143030.cb1016s47.

[205] J. P. Lee, E. Kassianidou, J. I. MacDonald, M. B. Francis and S. Kumar, "N-terminal specific conjugation of extracellular matrix proteins to 2-pyridinecarboxaldehyde functionalized polyacrylamide hydrogels," *Biomaterials* 102 (2016): 268. https://doi.org/10.1016/j.biomaterials.2016.06.022.

[206] N. Wang, E. Ostuni, G. M. Whitesides and D. E. Ingber, "Micropatterning tractional forces in living cells," *Cell Motility* 52, no. 2 (2002): 97. https://doi.org/10.1002/cm.10037.

[207] ROBERT J. PELHAM,JR., AND YU-LI WANG, "Cell locomotion and focal adhesions are regulated by substrate flexibility," *Proceedings of the National Academy of Sciences* 94 (1997): 13661.

[208] M.-L. Tsao and M. S. Platz, "Photochemistry of Ortho, Ortho‘ Dialkyl Phenyl Azides," *Journal of the American Chemical Society* 125, no. 39 (2003): 12014. https://doi.org/10.1021/ja035833e.

[209] Alan K. Schrock/Gary B. Schuster, "Photochemistry of phenyl azide: chemical properties of the transient intermediates," (1984).

[210] Y. Harada, T. Takahashi and K. Mutai, "Photochemical reaction of phenyl azide studied by ultraviolet photoelectron spectroscopy," *The Journal of Chemical Physics* 75, no. 4 (1981): 2014. https://doi.org/10.1063/1.442232.

[211] D. Missirlis, M. Baños, F. Lussier and J. P. Spatz, "Facile and Versatile Method for Micropatterning Poly(acrylamide) Hydrogels Using Photocleavable Comonomers," *ACS Applied Materials & Interfaces* 14, no. 3 (2022): 3643. https://doi.org/10.1021/acsami.1c17901.

[212] S. Yamamoto, K. Okada, N. Sasaki, A. C. Chang, K. Yamaguchi and J. Nakanishi, "Photoactivatable Hydrogel Interfaces for Resolving the Interplay of Chemical, Mechanical, and Geometrical Regulation of Collective Cell Migration," *Langmuir* 35, no. 23 (2019): 7459. https://doi.org/10.1021/acs.langmuir.8b02371.

[213] L. Przybyla, J. N. Lakins, R. Sunyer, X. Trepat and V. M. Weaver, "Monitoring developmental force distributions in reconstituted embryonic epithelia," *Methods (San Diego, Calif.)* 94 (2016): 101. https://doi.org/10.1016/j.ymeth.2015.09.003.

[214] J. Kumai, S. Sasagawa, M. Horie and Y. Yui, "A Novel Method for Polyacrylamide Gel Preparation Using N-hydroxysuccinimide-acrylamide Ester to Study Cell-Extracellular Matrix Mechanical Interactions," *Frontiers in Materials* 8 (2021): 637278. https://doi.org/10.3389/fmats.2021.637278.

[215] E. Uslu, V. K. Rana and Y. Guo et al., "Enhancing Robustness of Adhesive Hydrogels through PEG-NHS Incorporation," *ACS Applied Materials & Interfaces* 15, no. 43 (2023): 50095. https://doi.org/10.1021/acsami.3c13062.

[216] J. Christian, J. W. Blumberg and D. Probst et al., "Control of Cell Adhesion using Hydrogel Patterning Techniques for Applications in Traction Force Microscopy," *Journal of Visualized Experiments,* no. 179 (2022). https://doi.org/10.3791/63121.

[217] B. Sarker, C. Walter and A. Pathak, "Direct Micropatterning of Extracellular Matrix Proteins on Functionalized Polyacrylamide Hydrogels Shows Geometric Regulation of Cell–Cell Junctions," *ACS Biomaterials Science & Engineering* 4, no. 7 (2018): 2340. https://doi.org/10.1021/acsbiomaterials.8b00331.

[218] T. Grevesse, M. Versaevel, G. Circelli, S. Desprez and S. Gabriele, "A simple route to functionalize polyacrylamide hydrogels for the independent tuning of mechanotransduction cues," *Lab on a chip* 13, no. 5 (2013): 777. https://doi.org/10.1039/C2LC41168G.

[219] N. Cengiz, "Glutathione-responsive multifunctionalizable hydrogels via amine-epoxy “click” chemistry," *European Polymer Journal* 123 (2020): 109441. https://doi.org/10.1016/j.eurpolymj.2019.109441.

[220] E. Hassan, P. Deshpande, F. Claeyssens, S. Rimmer and S. MacNeil, "Amine functional hydrogels as selective substrates for corneal epithelialization," *Acta biomaterialia* 10, no. 7 (2014): 3029. https://doi.org/10.1016/j.actbio.2014.02.043.

[221] K. A. McEwan, S. Slavin, E. Tunnah and D. M. Haddleton, "Dual-functional materials via CCTP and selective orthogonal thiol-Michael addition/epoxide ring opening reactions," *Polymer Chemistry* 4, no. 8 (2013): 2608. https://doi.org/10.1039/c3py21104e.

[222] D. D. Pless, Y. C. Lee, S. Roseman and R. L. Schnaar, "Specific cell adhesion to immobilized glycoproteins demonstrated using new reagents for protein and glycoprotein immobilization," *Journal of Biological Chemistry* 258, no. 4 (1983): 2340. https://doi.org/10.1016/S0021-9258(18)32929-6.

[223] M. A. Boerman, E. Roozen and M. J. Sánchez-Fernández et al., "Next Generation Hemostatic Materials Based on NHS-Ester Functionalized Poly(2-oxazoline)s," *Biomacromolecules* 18, no. 8 (2017): 2529. https://doi.org/10.1021/acs.biomac.7b00683.

[224] M. Segel, B. Neumann and M. F. E. Hill et al., "Niche stiffness underlies the ageing of central nervous system progenitor cells," *Nature* 573, no. 7772 (2019): 130. https://doi.org/10.1038/s41586-019-1484-9.

[225] N. Gupta, B. F. Lin and L. M. Campos et al., "A versatile approach to high-throughput microarrays using thiol-ene chemistry," *Nature chemistry* 2, no. 2 (2010): 138. https://doi.org/10.1038/nchem.478.

[226] O. Campàs, T. Mammoto and S. Hasso et al., "Quantifying cell-generated mechanical forces within living embryonic tissues," *Nature Methods* 11, no. 2 (2014): 183. https://doi.org/10.1038/nmeth.2761.

[227] G. Pirnat, M. Marinčič, M. Ravnik and M. Humar, "Quantifying local stiffness and forces in soft biological tissues using droplet optical microcavities," *Proceedings of the National Academy of Sciences* 121, no. 4 (2024): e2314884121. https://doi.org/10.1073/pnas.2314884121.

[228] A. Mongera, P. Rowghanian and H. J. Gustafson et al., "A fluid-to-solid jamming transition underlies vertebrate body axis elongation," *Nature* 561, no. 7723 (2018): 401. https://doi.org/10.1038/s41586-018-0479-2.

[229] X. Wu, R. Streubel and X. Liu et al., "Ferromagnetic liquid droplets with adjustable magnetic properties," *Proceedings of the National Academy of Sciences* 118, no. 8 (2021): e2017355118. https://doi.org/10.1073/pnas.2017355118.

[230] F. Serwane, A. Mongera and P. Rowghanian et al., "In vivo quantification of spatially varying mechanical properties in developing tissues," *Nature Methods* 14, no. 2 (2017): 181. https://doi.org/10.1038/nmeth.4101.

[231] H. Alzanbaki, M. Moretti and C. A. E. Hauser, "Engineered Microgels—Their Manufacturing and Biomedical Applications," *Micromachines* 12, no. 1 (2021): 45. https://doi.org/10.3390/mi12010045.

[232] G. M. Whitesides, "The origins and the future of microfluidics," *Nature* 442, no. 7101 (2006): 368. https://doi.org/10.1038/nature05058.

[233] A. C. Daly, L. Riley, T. Segura and J. A. Burdick, "Hydrogel microparticles for biomedical applications," *Nature reviews. Materials* 5, no. 1 (2020): 20. https://doi.org/10.1038/s41578-019-0148-6.

[234] K. O. Rojek, M. Ćwiklińska, J. Kuczak and J. Guzowski, "Microfluidic Formulation of Topological Hydrogels for Microtissue Engineering," *Chemical Reviews* 122, no. 22 (2022): 16839. https://doi.org/10.1021/acs.chemrev.1c00798.

[235] Y. Ou, Z. Han and S. Cai et al., "Biomaterials with droplet microfluidics," *Nature Reviews Bioengineering* 4, no. 4 (2026): 353. https://doi.org/10.1038/s44222-025-00389-0.

[236] D. Vorselen, Y. Wang and M. M. de Jesus et al., "Microparticle traction force microscopy reveals subcellular force exertion patterns in immune cell–target interactions," *Nature Communications* 11, no. 1 (2020). https://doi.org/10.1038/s41467-019-13804-z.

[237] T. Nisisako, T. Torii and T. Higuchi, "Droplet formation in a microchannel network," *Lab on a chip* 2, no. 1 (2002): 24. https://doi.org/10.1039/B108740C.

[238] M. Joanicot and A. Ajdari, "Droplet control for microfluidics," *Science* 309, no. 5736 (2005): 887. https://doi.org/10.1126/science.1112615.

[239] A. Khademhosseini, G. Eng and J. Yeh et al., "Micromolding of photocrosslinkable hyaluronic acid for cell encapsulation and entrapment," *Journal of Biomedical Materials Research Part A* 79A, no. 3 (2006): 522. https://doi.org/10.1002/jbm.a.30821.

[240] J. Fukuda, A. Khademhosseini and Y. Yeo et al., "Micromolding of photocrosslinkable chitosan hydrogel for spheroid microarray and co-cultures,"

Biomaterials 27, no. 30 (2006): 5259. https://doi.org/10.1016/j.biomaterials.2006.05.044.

[241] Y. Kittel, A. J. C. Kuehne and L. de Laporte, "Translating Therapeutic Microgels into Clinical Applications," *Advanced Healthcare Materials* 11, no. 6 (2022): 2101989. https://doi.org/10.1002/adhm.202101989.

[242] K. T. Tran and T. D. Nguyen, "Lithography-based methods to manufacture biomaterials at small scales," *Journal of Science: Advanced Materials and Devices* 2, no. 1 (2017): 1. https://doi.org/10.1016/j.jsamd.2016.12.001.

[243] T. Farjami and A. Madadlou, "Fabrication methods of biopolymeric microgels and microgel-based hydrogels," *Food Hydrocolloids* 62 (2017): 262. https://doi.org/10.1016/j.foodhyd.2016.08.017.

[244] C. Rivest, D. Morrison and B. Ni et al., "Microscale hydrogels for medicine and biology: synthesis, characteristics and applications," *Journal of Mechanics of Materials and Structures* 2, no. 6 (2007): 1103. https://doi.org/10.2140/jomms.2007.2.1103.

[245] L. Shang, Y. Cheng and Y. Zhao, "Emerging Droplet Microfluidics," *Chemical Reviews* 117, no. 12 (2017): 7964. https://doi.org/10.1021/acs.chemrev.6b00848.

[246] M. Elsayed, A. Kothandaraman, M. Edirisinghe and J. Huang, "Porous Polymeric Films from Microbubbles Generated Using a T-Junction Microfluidic Device," *Langmuir* 32, no. 50 (2016): 13377. https://doi.org/10.1021/acs.langmuir.6b02890.

[247] M. Costantini, J. Jaroszewicz and Ł. Kozoń et al., "3D-Printing of Functionally Graded Porous Materials Using On-Demand Reconfigurable Microfluidics," *Angewandte Chemie International Edition* 58, no. 23 (2019): 7620. https://doi.org/10.1002/anie.201900530.

[248] M. Costantini, C. Colosi and P. Mozetic et al., "Correlation between porous texture and cell seeding efficiency of gas foaming and microfluidic foaming scaffolds," *Materials science & engineering. C, Materials for biological applications* 62 (2016): 668. https://doi.org/10.1016/j.msec.2016.02.010.

[249] Q. Feng, Q. Li and H. Wen et al., "Injection and Self-Assembly of Bioinspired Stem Cell-Laden Gelatin/Hyaluronic Acid Hybrid Microgels Promote Cartilage Repair In Vivo," *Advanced Functional Materials* 29, no. 50 (2019): 1906690. https://doi.org/10.1002/adfm.201906690.

[250] B. V. Slaughter, S. S. Khurshid, O. Z. Fisher, A. Khademhosseini and N. A. Peppas, "Hydrogels in Regenerative Medicine," *Advanced materials* 21, no. 32-33 (2009): 3307. https://doi.org/10.1002/adma.200802106.

[251] S. Ma, N. Mukherjee, E. Mikhailova and H. Bayley, "Gel Microrods for 3D Tissue Printing," *Advanced Biosystems* 1, no. 8 (2017): 1700075. https://doi.org/10.1002/adbi.201700075.

[252] Z. Dong, Q. Yuan, K. Huang, W. Xu, G. Liu and Z. Gu, "Gelatin methacryloyl (GelMA)-based biomaterials for bone regeneration," *RSC advances* 9, no. 31 (2019): 17737. https://doi.org/10.1039/C9RA02695A.

[253] S. Girardo, N. Träber and K. Wagner et al., "Standardized microgel beads as elastic cell mechanical probes," *Journal of materials chemistry B* 6, no. 39 (2018): 6245. https://doi.org/10.1039/c8tb01421c.

[254] N. Träber, K. Uhlmann and S. Girardo et al., "Polyacrylamide Bead Sensors for in vivo Quantification of Cell-Scale Stress in Zebrafish Development," *Scientific Reports* 9, no. 1 (2019). https://doi.org/10.1038/s41598-019-53425-6.

[255] C. Claaßen, M. H. Claaßen, F. Gohl, G. E. M. Tovar, K. Borchers and A. Southan, "Photoinduced Cleavage and Hydrolysis of o-Nitrobenzyl Linker and Covalent Linker Immobilization in Gelatin Methacryloyl Hydrogels," *Macromolecular bioscience* 18, no. 9 (2018): e1800104. https://doi.org/10.1002/mabi.201800104.

[256] C. B. Highley, K. H. Song, A. C. Daly and J. A. Burdick, "Jammed Microgel Inks for 3D Printing Applications," *Advanced science* 6, no. 1 (2019): 1801076. https://doi.org/10.1002/advs.201801076.

[257] D. Rommel, M. Mork and S. Vedaraman et al., "Functionalized Microgel Rods Interlinked into Soft Macroporous Structures for 3D Cell Culture," *Advanced science* 9, no. 10 (2022): 2103554. https://doi.org/10.1002/advs.202103554.

[258] V. Gensbittel, Z. Yesilata and L. Bochler et al., "Cell viscosity influences haematogenous dissemination and metastatic extravasation of tumour cells," *Nature Materials* 25, no. 4 (2026): 675. https://doi.org/10.1038/s41563-025-02462-w.

[259] A. S. Caldwell, B. A. Aguado and K. S. Anseth, "Designing Microgels for Cell Culture and Controlled Assembly of Tissue Microenvironments," *Advanced Functional Materials* 30, no. 37 (2020): 1907670. https://doi.org/10.1002/adfm.201907670.

[260] H. Wang, H. Liu, H. Liu, W. Su, W. Chen and J. Qin, "One-Step Generation of Core–Shell Gelatin Methacrylate (GelMA) Microgels Using a Droplet Microfluidic System," *Advanced Materials Technologies* 4, no. 6 (2019): 1800632. https://doi.org/10.1002/admt.201800632.

[261] K. Duval, H. Grover and L.-H. Han et al., "Modeling Physiological Events in 2D vs. 3D Cell Culture," *Physiology* 32, no. 4 (2017): 266. https://doi.org/10.1152/physiol.00036.2016.

[262] Daan Vorselen, Sarah R Barger , Yifan Wang, Wei Cai, Julie A Theriot, Nils C Gauthier, Mira Krendel, "Phagocytic ‘teeth’ and myosin-- II ‘jaw’ power target constriction during phagocytosis," *eLife* 10 (2021): e68627.

[263] F. G. Downs, D. J. Lunn and M. J. Booth et al., "Multi-responsive hydrogel structures from patterned droplet networks," *Nature Chemistry* 12, no. 4 (2020): 363. https://doi.org/10.1038/s41557-020-0444-1.

[264] M. Karg, Y. Lu and E. Carbó-Argibay et al., "Multiresponsive Hybrid Colloids Based on Gold Nanorods and Poly(NIPAM-co-allylacetic acid) Microgels: Temperature- and pH-Tunable Plasmon Resonance," *Langmuir* 25, no. 5 (2009): 3163. https://doi.org/10.1021/la803458j.

[265] M. Das, N. Sanson, D. Fava and E. Kumacheva, "Microgels Loaded with Gold Nanorods: Photothermally Triggered Volume Transitions under Physiological Conditions," *Langmuir* 23, no. 1 (2007): 196. https://doi.org/10.1021/la061596s.

[266] R. Chen, J. Shi, C. Liu, J. Li and S. Cao, "In situ self-assembly of gold nanorods with thermal-responsive microgel for multi-synergistic remote drug delivery," *Advanced Composites and Hybrid Materials* 5, no. 3 (2022): 2223. https://doi.org/10.1007/s42114-021-00306-0.

[267] D. Klinger and K. Landfester, "Dual Stimuli-Responsive Poly(2-hydroxyethyl methacrylate- co -methacrylic acid) Microgels Based on Photo-Cleavable Cross-Linkers: pH-Dependent Swelling and Light-Induced Degradation," *Macromolecules* 44, no. 24 (2011): 9758. https://doi.org/10.1021/ma201706r.

[268] D. Klinger and K. Landfester, "Photo-sensitive PMMA microgels: light-triggered swelling and degradation," *Soft Matter* 7, no. 4 (2011): 1426. https://doi.org/10.1039/C0SM00638F.

[269] J. C. Rose, M. Cámara-Torres, K. Rahimi, J. Köhler, M. Möller and L. de Laporte, "Nerve Cells Decide to Orient inside an Injectable Hydrogel with Minimal Structural Guidance," *Nano Letters* 17, no. 6 (2017): 3782. https://doi.org/10.1021/acs.nanolett.7b01123.

[270] A. Omidinia-Anarkoli, S. Boesveld, U. Tuvshindorj, J. C. Rose, T. Haraszti and L. de Laporte, "An Injectable Hybrid Hydrogel with Oriented Short Fibers Induces Unidirectional Growth of Functional Nerve Cells," *Small* 13, no. 36 (2017): 1702207. https://doi.org/10.1002/smll.201702207.

[271] C. Hu, W. Xu, C. M. Conrads, J. Wu and A. Pich, "Visible light and temperature dual-responsive microgels by crosslinking of spiropyran modified prepolymers," *Journal of colloid and interface science* 582, no. Pt B (2021): 1075. https://doi.org/10.1016/j.jcis.2020.08.081.

[272] W. Liang, C. G. Lopez, W. Richtering and D. Wöll, "Photo- and thermo-responsive microgels with supramolecular crosslinks for wavelength tunability of the volume phase transition temperature," *Physical chemistry chemical physics : PCCP* 24, no. 23 (2022): 14408. https://doi.org/10.1039/D2CP00532H.

[273] Z. Lin, Q. Li and X. Han et al., "An injectable and degradable heterogeneous microgel assembly capable of forming a "micro-nest group" for cell condensation and cartilage regeneration," *Materials horizons* 11, no. 21 (2024): 5438. https://doi.org/10.1039/D4MH00724G.

[274] J. M. Lowen, E. E. Wheeler and N. K. Shimamoto et al., "Functionalized Annealed Microgels for Spatial Control of Osteogenic and Chondrogenic Differentiation," *Advanced Functional Materials* 34, no. 30 (2024): 2311017. https://doi.org/10.1002/adfm.202311017.

[275] G. Ramirez-Calderon, H. H. Susapto and C. A. E. Hauser, "Delivery of Endothelial Cell-Laden Microgel Elicits Angiogenesis in Self-Assembling Ultrashort Peptide Hydrogels In Vitro," *ACS Applied Materials & Interfaces* 13, no. 25 (2021): 29281. https://doi.org/10.1021/acsami.1c03787.

[276] D. R. Griffin, W. M. Weaver, P. O. Scumpia, D. Di Carlo and T. Segura, "Accelerated wound healing by injectable microporous gel scaffolds assembled from annealed building blocks," *Nature Materials* 14, no. 7 (2015): 737. https://doi.org/10.1038/nmat4294.

[277] E. Mohagheghian, J. Luo and J. Chen et al., "Quantifying compressive forces between living cell layers and within tissues using elastic round microgels," *Nature Communications* 9, no. 1 (2018). https://doi.org/10.1038/s41467-018-04245-1.

[278] T. Kamperman, N. G. A. Willemen and C. Kelder et al., "Steering Stem Cell Fate within 3D Living Composite Tissues Using Stimuli-Responsive Cell-Adhesive Micromaterials," *Advanced science* 10, no. 10 (2023): 2205487. https://doi.org/10.1002/advs.202205487.

[279] H. Ryoo, R. Giovanni, H. Kimmel, I. Jain and G. H. Underhill, "Combinatorial Microgels for 3D ECM Screening and Heterogeneous Microenvironmental Culture of Primary Human Hepatic Stellate Cells," *Advanced science* 11, no. 15 (2024): 2303128. https://doi.org/10.1002/advs.202303128.

[280] W. Li, S. Lee and M. Ma et al., "Microbead-based biomimetic synthetic neighbors enhance survival and function of rat pancreatic β-cells," *Scientific Reports* 3 (2013): 2863. https://doi.org/10.1038/srep02863.

[281] W. Lee, N. Kalashnikov and S. Mok et al., "Dispersible hydrogel force sensors reveal patterns of solid mechanical stress in multicellular spheroid cultures," *Nature Communications* 10, no. 1 (2019). https://doi.org/10.1038/s41467-018-07967-4.

[282] L. Klasen, M. Mork and R. Nasehi et al., *Microgels enable iPSCs to assemble, expand, and differentiate into organoids – from sizable to high throughput*, 2025.

[283] E. Y. Liu, S. Jung and H. Yi, "Improved Protein Conjugation with Uniform, Macroporous Poly(acrylamide- co -acrylic acid) Hydrogel Microspheres via EDC/NHS Chemistry," *Langmuir* 32, no. 42 (2016): 11043. https://doi.org/10.1021/acs.langmuir.6b02591.

[284] A. Harsányi, A. Kardos and I. Varga, "Preparation of Amino-Functionalized Poly(N-isopropylacrylamide)-Based Microgel Particles," *Gels* 9, no. 9 (2023): 692. https://doi.org/10.3390/gels9090692.

[285] C. Castro-Hinojosa, S. Del Sol-Fernández and E. Moreno-Antolín et al., "A Simple and Versatile Strategy for Oriented Immobilization of His-Tagged Proteins on Magnetic Nanoparticles," *Bioconjugate Chemistry* 34, no. 12 (2023): 2275. https://doi.org/10.1021/acs.bioconjchem.3c00417.

[286] I. K. Sommerfeld, E. M. Dälken, L. Elling and A. Pich, "Nitrilotriacetic Acid Functionalized Microgels for Efficient Immobilization of Hyaluronan Synthase," *Macromolecular bioscience* 24, no. 9 (2024): 2400075. https://doi.org/10.1002/mabi.202400075.

[287] E. Hochuli, H. Döbeli and A. Schacher, "New metal chelate adsorbent selective for proteins and peptides containing neighbouring histidine residues," *Journal of chromatography* 411 (1987): 177. https://doi.org/10.1016/S0021-9673(00)93969-4.

[288] E. Hochuli, W. Bannwarth, H. Döbeli, R. Gentz and D. Stüber, "Genetic Approach to Facilitate Purification of Recombinant Proteins with a Novel Metal Chelate Adsorbent," *Nature Biotechnology* 6, no. 11 (1988): 1321. https://doi.org/10.1038/nbt1188-1321.

[289] S. V. Wegner, F. C. Schenk and J. P. Spatz, "Cobalt(III)-Mediated Permanent and Stable Immobilization of Histidine-Tagged Proteins on NTA-Functionalized Surfaces," *Chemistry (Weinheim an der Bergstrasse, Germany)* 22, no. 9 (2016): 3156. https://doi.org/10.1002/chem.201504465.

[290] S. V. Wegner and J. P. Spatz, "Cobalt(III) as a stable and inert mediator ion between NTA and His6-tagged proteins," *Angewandte Chemie (International ed. in English)* 52, no. 29 (2013): 7593. https://doi.org/10.1002/anie.201210317.

[291] A. S. Mao, J.-W. Shin and S. Utech et al., "Deterministic encapsulation of single cells in thin tunable microgels for niche modelling and therapeutic delivery," *Nature Materials* 16, no. 2 (2017): 236. https://doi.org/10.1038/nmat4781.

[292] J. M. de Rutte, J. Koh and D. Di Carlo, "Scalable High-Throughput Production of Modular Microgels for In Situ Assembly of Microporous Tissue Scaffolds," *Advanced Functional Materials* 29, no. 25 (2019): 1900071. https://doi.org/10.1002/adfm.201900071.

[293] C. D. Spicer, E. T. Pashuck and M. M. Stevens, "Achieving Controlled Biomolecule-Biomaterial Conjugation," *Chemical Reviews* 118, no. 16 (2018): 7702. https://doi.org/10.1021/acs.chemrev.8b00253.

[294] A. Kaufmann, K. Ivanova and J. Thiele, "Regulating Protein Immobilization During Cell-Free Protein Synthesis in Hyaluronan Microgels," *Advanced biology* 9, no. 5 (2025): e2400668. https://doi.org/10.1002/adbi.202400668.

[295] H.-K. Kim and A. Lee, "One-pot synthesis of carbamates and thiocarbamates from Boc-protected amines," *Tetrahedron letters* 57, no. 44 (2016): 4890. https://doi.org/10.1016/j.tetlet.2016.09.038.

[296] A. K. Steiger, S. Pardue, C. G. Kevil and M. D. Pluth, "Self-Immolative Thiocarbamates Provide Access to Triggered H2S Donors and Analyte Replacement Fluorescent Probes," *Journal of the American Chemical Society* 138, no. 23 (2016): 7256. https://doi.org/10.1021/jacs.6b03780.

[297] S. Caglio and P. G. Righetti, "On the pH dependence of polymerization efficiency, as investigated by capillary zone electrophoresis," *Electrophoresis* 14, no. 5-6 (1993): 554. https://doi.org/10.1002/elps.1150140184.

[298] L. Przybyla, J. N. Lakins and V. M. Weaver, "Tissue Mechanics Orchestrate Wnt-Dependent Human Embryonic Stem Cell Differentiation," *Cell stem cell* 19, no. 4 (2016): 462. https://doi.org/10.1016/j.stem.2016.06.018.

[299] Dapeng Bi1, J. H. Lopez, J. M. Schwarz, and M. Lisa Manning, "A density-independent rigidity transition in biological tissues," (2015).

[300] A. Nestor-Bergmann, G. Goddard, S. Woolner and O. E. Jensen, "Relating cell shape and mechanical stress in a spatially disordered epithelium using a vertex-

based model," *Mathematical medicine and biology : a journal of the IMA* 35, no. suppl_1 (2018): 1. https://doi.org/10.1093/imammb/dqx008.

[301] G. Ciccone, M. Azevedo Gonzalez-Oliva and M. Versaevel et al., "Epithelial Cell Mechanoresponse to Matrix Viscoelasticity and Confinement Within Micropatterned Viscoelastic Hydrogels," *Advanced science* 12, no. 18 (2025): 2408635. https://doi.org/10.1002/advs.202408635.

[302] T. Piskova, A. N. Kozyrina and G. Astrauskaitė et al., "Cell loss disrupts mechanical homeostasis to drive retinal pigment epithelium ageing-like phenotype in vitro," *Nature Communications* 17, no. 1 (2026). https://doi.org/10.1038/s41467-026-71493-x.

[303] Y.-W. Chiou, H.-K. Lin, M.-J. Tang, H.-H. Lin and M.-L. Yeh, "The influence of physical and physiological cues on atomic force microscopy-based cell stiffness assessment," *PloS one* 8, no. 10 (2013): e77384. https://doi.org/10.1371/journal.pone.0077384.

[304] A. Nagafuchi and S. Tsukita, "The Loss of the Expression of α Catenin, the 102 kD Cadherin Associated Protein, in Central Nervous Tissues during Development: (α catenin/cadherin/cell adhesion/CNS)," *Development, growth & differentiation* 36, no. 1 (1994): 59. https://doi.org/10.1111/j.1440-169X.1994.00059.x.

[305] F. Farjood and E. Vargis, "Novel devices for studying acute and chronic mechanical stress in retinal pigment epithelial cells," *Lab on a chip* 18, no. 22 (2018): 3413. https://doi.org/10.1039/c8lc00659h.

[306] M. Kulbay, K. Y. Wu, G. K. Nirwal, P. Bélanger and S. D. Tran, "The Role of Reactive Oxygen Species in Age-Related Macular Degeneration: A Comprehensive Review of Antioxidant Therapies," *Biomedicines* 12, no. 7 (2024). https://doi.org/10.3390/biomedicines12071579.

[307] M. Nebbioso, F. Franzone and A. Lambiase et al., "Oxidative Stress Implication in Retinal Diseases-A Review," *Antioxidants (Basel, Switzerland)* 11, no. 9 (2022). https://doi.org/10.3390/antiox11091790.

[308] N. Khalilgharibi, J. Fouchard and N. Asadipour et al., "Stress relaxation in epithelial monolayers is controlled by the actomyosin cortex," *Nature Physics* 15, no. 8 (2019): 839. https://doi.org/10.1038/s41567-019-0516-6.

[309] R. Thiagarajan, M. M. Inamdar and D. Riveline, "Interplay between cell height variations and planar pulsations in epithelial monolayers," *The European Physical Journal E* 45, no. 5 (2022). https://doi.org/10.1140/epje/s10189-022-00201-6.

[310] J. F. E. Bodenschatz, K. Ajmail and M. Skamrahl et al., "Epithelial cells sacrifice excess area to preserve fluidity in response to external mechanical stress," *Communications Biology* 5, no. 1 (2022). https://doi.org/10.1038/s42003-022-03809-8.

[311] T. P. J. Wyatt, A. R. Harris and M. Lam et al., "Emergence of homeostatic epithelial packing and stress dissipation through divisions oriented along the long cell axis," *Proceedings of the National Academy of Sciences* 112, no. 18 (2015): 5726. https://doi.org/10.1073/pnas.1420585112.

[312] F. Pérez-Verdugo and S. Banerjee, "Tension Remodeling Regulates Topological Transitions in Epithelial Tissues," *PRX Life* 1, no. 2 (2023). https://doi.org/10.1103/PRXLife.1.023006.

[313] A. Ouzeri, S. Kale and N. Chahare et al., *Theory of multiscale epithelial mechanics under stretch: from active gels to vertex models*, 2025.

[314] E. Latorre, S. Kale and L. Casares et al., "Active superelasticity in three-dimensional epithelia of controlled shape," *Nature* 563, no. 7730 (2018): 203. https://doi.org/10.1038/s41586-018-0671-4.

[315] K. D. Endresen, M. Kim, M. Pittman, Y. Chen and F. Serra, "Topological defects of integer charge in cell monolayers," *Soft Matter* 17, no. 24 (2021): 5878. https://doi.org/10.1039/D1SM00100K.

[316] Z. Zhao, H. Li and Y. Yao et al., "Integer topological defects offer a methodology to quantify and classify active cell monolayers," *Nature Communications* 16, no. 1 (2025). https://doi.org/10.1038/s41467-025-57783-w.

[317] K. I. Mazzitello, Q. Zhang and M. A. Chrenek et al., *Druse-Induced Morphology Evolution in Retinal Pigment Epithelium*, arXiv, 2016.

[318] A. R. Harris, L. Peter, J. Bellis, B. Baum, A. J. Kabla and G. T. Charras, "Characterizing the mechanics of cultured cell monolayers," *Proceedings of the National Academy of Sciences* 109, no. 41 (2012): 16449. https://doi.org/10.1073/pnas.1213301109.

[319] L. Casares, R. Vincent and D. Zalvidea et al., "Hydraulic fracture during epithelial stretching," *Nature Materials* 14, no. 3 (2015): 343. https://doi.org/10.1038/nmat4206.

[320] Y. Mori, N. Shiratsuchi and N. Sato et al., "Extracellular ATP facilitates cell extrusion from epithelial layers mediated by cell competition or apoptosis," *Current biology : CB* 32, no. 10 (2022): 2144-2159.e5. https://doi.org/10.1016/j.cub.2022.03.057.

[321] D. Krueger, W. K. Spoelstra and D. J. Mastebroek et al., "Epithelial tension controls intestinal cell extrusion," *Science* 389, no. 6764 (2025): eadr8753. https://doi.org/10.1126/science.adr8753.

[322] S. Okuda and K. Fujimoto, "A Mechanical Instability in Planar Epithelial Monolayers Leads to Cell Extrusion," *Biophysical journal* 118, no. 10 (2020): 2549. https://doi.org/10.1016/j.bpj.2020.03.028.

[323] Thomas W. Marshall, Isaac E. Lloyd, Jean Marie Delalande, Inke Näthke, and Jody Rosenblatt, "The tumor suppressor adenomatous polyposis coli controls the direction in which a cell extrudes from an epithelium," *Molecular Biology of the Cell (*2011): 3962.

[324] G. M. Slattum and J. Rosenblatt, "Tumour cell invasion: an emerging role for basal epithelial cell extrusion," *Nature Reviews Cancer* 14, no. 7 (2014): 495. https://doi.org/10.1038/nrc3767.

[325] Magali Suzanne and Hermann Steller, "Letting go: modification of cell adhesion during apoptosis," *Journal of Biology (*2009).

[326] J. V. Patankar and C. Becker, "Cell death in the gut epithelium and implications for chronic inflammation," *Nature Reviews Gastroenterology & Hepatology* 17, no. 9 (2020): 543. https://doi.org/10.1038/s41575-020-0326-4.

[327] S. Karsch, D. Kong, J. Großhans and A. Janshoff, "Single-Cell Defects Cause a Long-Range Mechanical Response in a Confluent Epithelial Cell Layer," *Biophysical journal* 113, no. 12 (2017): 2601. https://doi.org/10.1016/j.bpj.2017.10.025.

[328] A. Bonfim-Melo, I. Noordstra and S. Gupta et al., "Rapid lamellipodial responses by neighbor cells drive epithelial sealing in response to pyroptotic cell death," *Cell reports* 38, no. 5 (2022): 110316. https://doi.org/10.1016/j.celrep.2022.110316.

[329] T. Kawaue, I. Yow and Y. Pan et al., "Inhomogeneous mechanotransduction defines the spatial pattern of apoptosis-induced compensatory proliferation," *Developmental cell* 58, no. 4 (2023): 267-277.e5. https://doi.org/10.1016/j.devcel.2023.01.005.

[330] S. A. Gudipaty and J. Rosenblatt, "Epithelial cell extrusion: Pathways and pathologies," *Seminars in cell & developmental biology* 67 (2017): 132. https://doi.org/10.1016/j.semcdb.2016.05.010.

[331] L. Kocgozlu, T. B. Saw and A. P. Le et al., "Epithelial Cell Packing Induces Distinct Modes of Cell Extrusions," *Current biology : CB* 26, no. 21 (2016): 2942. https://doi.org/10.1016/j.cub.2016.08.057.

[332] O. Chaudhuri, J. Cooper-White, P. A. Janmey, D. J. Mooney and V. B. Shenoy, "Effects of extracellular matrix viscoelasticity on cellular behaviour," *Nature* 584, no. 7822 (2020): 535. https://doi.org/10.1038/s41586-020-2612-2.

[333] Z. Liu, J. L. Tan and D. M. Cohen et al., "Mechanical tugging force regulates the size of cell–cell junctions," *Proceedings of the National Academy of Sciences* 107, no. 22 (2010): 9944. https://doi.org/10.1073/pnas.0914547107.

[334] Z. Ablonczy, M. Dahrouj and P. H. Tang et al., "Human retinal pigment epithelium cells as functional models for the RPE in vivo," *Investigative ophthalmology & visual science* 52, no. 12 (2011): 8614. https://doi.org/10.1167/iovs.11-8021.

[335] U. Schumann, L. Liu and R. Aggio-Bruce et al., "Spatial transcriptomics reveals regionally altered gene expression that drives retinal degeneration," *Communications Biology* 8, no. 1 (2025): 629. https://doi.org/10.1038/s42003-025-07887-2.

[336] T. Y. Garcia, M. Gutierrez, J. Reynolds and D. A. Lamba, "Modeling the Dynamic AMD-Associated Chronic Oxidative Stress Changes in Human ESC and iPSC-Derived RPE Cells," *Investigative ophthalmology & visual science* 56, no. 12 (2015): 7480. https://doi.org/10.1167/iovs.15-17251.

[337] F. Jivan and D. L. Alge, "Bio-Orthogonal, Site-Selective Conjugation of Recombinant Proteins to Microporous Annealed Particle Hydrogels for Tissue Engineering," *Advanced Therapeutics* 3, no. 1 (2020): 1900148. https://doi.org/10.1002/adtp.201900148.

[338] H. A. Staab, "New Methods of Preparative Organic Chmistry IV. Syntheses Using Heterocyclic Amides (Azolides)," *Angewandte Chemie International Edition in English* 1, no. 7 (1962): 351. https://doi.org/10.1002/anie.196203511.

[339] J. L. Defreese, S.-J. Hwang, A. N. G. Parra-Vasquez and A. Katz, "Molecular motion of tethered molecules in bulk and surface-functionalized materials: a comparative study of confinement," *Journal of the American Chemical Society* 128, no. 17 (2006): 5687. https://doi.org/10.1021/ja0556474.

VIII. Appendix

1. List of abbreviations

AC-PDC - allyl carbamate-based photodegradable crosslinker

AEMA - Aminoethyl methacrylate

AMD - Age-related macular degeneration

ANOVA - Analysis of variance

APS - Ammonium persulfate

ATP - Adenosine triphosphate

BM - Bruch's membrane

BSA - Bovine serum albumin

CDI - N,N'-carbonyl diimidazole

Chor - Choroid

DCM - Dichloromethane

DCTB - trans-2-[3-(4-tert-Butylphenyl)-2-methyl-2-propenylidene]malononitrile

DIPEA - N,N-Diisopropylethylamine

DMF - Dimethylformamide

DMSO - Dimethyl sulfoxide

DNA - Deoxyribonucleic acid

ECM - Extra cellular matrix

EDTA - Ethylenediaminetetraacetic acid

ELISA - Enzyme-linked immunosorbent assay

ESI-MS - electrospray ionization mass spectrometry

FA - focal adhesion

FFJ - Flow focusing junction

FRET - Förster resonance energy transfer

FTTC - Fourier Transform Traction Cytometry

GCL - Ganglion cell layer

GFP - Green fluorescent protein

GMA - Glycidyl methacrylate

HAV - Histidine-Alanine-Valine

HAVDI - Histidine-Alanine-Valine-Aspartic acid-Isoleucine

HBTU - 2-(1H-benzotriazole-1-yl)-1,1,3,3-tetramethyluronium hexafluorophosphate

HEPES- 4-(2-hydroxyethyl)-1-piperazineethanesulfonic acid

HCl - Hydrochloric acid

hiPSC-RPE - human induced pluripotent stem cells derived retinal pigment epithelium

HOBt - 1-Hydroxybenzotriazole

IgG (H+L) - Immunoglobulin G heavy and light chains

INL - Inner nuclear layer

IPL - Inner plexiform layer

IVFK - Isoleucine-Valine-Phenylalanine-Lysine

LED - Light-emitting diode

LINC - Linker of nucleoskeleton and cytoskeleton

LSM - Laser scanning microscope

MALDI-TOF - matrix-assisted laser desorption/ionization time of flight

MDCK - Madin-Darby canine kidney

$MgSO_{4}$ - Magnesium sulfate

MSM - Monolayer stress microscopy

NDH - Non-degradable hydrogel

NDM - Non-degradable microgel

NFL - Nerve fiber layer

NHS - *N*-Hydroxysuccinimide

NHS-AA - Acrylic acid N-hyroxysuccinimide ester

NMP - N-Methyl-2-pyrrolidone

NMR - Nuclear magnetic resonance

NTA - nitrilotriacetic acid

OCT - Optical coherence tomography

oNB - Ortho nitrobenzol

ONL - Outer nuclear layer

OPL - Outer plexiform layer

PAA - Polyacrylamide

PBS - Phosphate-buffered saline

PDC - Photodegradable crosslinker

PDH - Photodegradable hydrogel

PDM - Photodegradable microgel

PDMS - poly (dimethyl siloxane)

PEG - Poly (ethylene glycol)

PFA - Paraformaldehyde

PIV - Particle image velocimetry

PLL - Poly-L-lysine

pMLC - phosphorylated myosin light chain

PNIPAAm - poly (N-isopropylacrylamide)

PR - Photo receptors

PTFE - Polytetrafluoroethylene

RGD - Arginine-Glycine-Aspartic acid

ROI - Region of interest

ROS - Reactive oxygen species

RPE - retinal pigment epithelium

SDS - Sodium dodecyl sulfate

SEM - Standard error mean

sulfo-SANPAH - Sulfosuccinimidyl-6-(4'-azido-2'-nitrophenylamino) hexanoate

TEMED - Tetramethylethylenediamine

TFA - Trifluoroacetic acid

TFM - Traction force microscopy

THF - Tetrahydrofuran

TMA - Di(trimethylolpropane) tetraacrylate

TMSPMA - 3-(Trimethoxysilyl)propylmethacrylat

UV - Ultraviolet

2. List of figures

Figure 1: Cellular tensegrity and tissue-scale mechanical homeostasis. A) Tensegrity model in a round configuration, anchored to the substrate (grey grid) and under applied force at node D_1. Adapted from Ingber et al.[7] B) Tissue-scale mechanical homeostasis is governed through the balance of intercellular and cell-ECM forces. Adapted from Luciano et al.[41] 3

Figure 2: Cellular cytoskeleton and adhesion motives. A) Simplified rendition of epithelia cytoskeleton, highlighting the actin and keratin networks and their respective cell-cell and cell-ECM junctions. Adapted from Kozyrina et al. [90] B) Adherens junction complex showing the unengaged state and the complex under tension when engaged with cadherin of another cell. B) and C) adapted from Alberts et al.[60] D) Schematic of basal integrin adhesion motives β4 and β1 with their respective ECM laminins and cytoskeletal partners. Adapted from Rousselle et al.[101] 8

Figure 3: Changes of retinal architecture in ageing. A) Illustration of retinal architecture with the layers: nerve fiber layer (NFL), ganglion cell layer (GCL), inner plexiform layer (IPL), inner nuclear layer (INL), outer plexiform layer (OPL), outer nuclear layer (ONL), photo receptors (PR), retinal pigment epithelium (RPE), Bruch's membrane (BM), choroid (Chor). In physiological state and during early and intermediate age-related macular degeneration (AMD) adapted from Malek et al.[122]. B) Image of Optical Coherence Tomography (OCT) scan of a healthy retina highlighting the different layers adapted from Ong et al.[123] (Top) and OCT scan of a retina with drusen development adapted from Istanbul Retina Institute[124] (Bottom). C) Schematic representation of the change in organization of the retinal pigment epithelium (RPE) and the underlying Bruch's membrane (BM), adapted from Piskova et al.[105] 10

Figure 4: Overview of common photo-responsive molecules and their application in hydrogel systems to facilitate dynamic cell culture environments. A) Azo benzene based crosslinker undergoes conformational change from trans to cis when illuminated with UV light and reverses the change when illuminated with blue light, enabling a repeatable on-demand change of substrate stiffness. Adapted from Lee et al.[190] B) Spiropyrane-based crosslinker undergoes ring closing reaction when illuminated and recovers over time back into the open confirmation, allowing for the topographical patterning through localized hydrogel collapse. Adapted from Bril et al.[177] C) Degradation of an ortho nitro-benzyl based crosslinker by illumination with UV light facilitating the localized breakdown of the hydrogel and enabling topographical patterning or internal hollowing. Adapted from Kloxin et al.[191] 14

Figure 5: Microfluidic microgel production, functionalization and application in cellular environments. A) Overview of microgel production via microfluidic droplet generation. B) Tissue stiffness versus mechanical stiffness of polymer materials (* indicates crosslinking under non-physiological conditions and [a] indicates microgels). A) and B) are adapted from Rojek et al.[234] C) Highlighting two common applications for microgels in cellular environments as either cell encapsulation (Top) or scaffolding

(Bottom). Adapted from Mao et al.[291] and Rutte et al. [292] respectively. D) Overview of undirected (Top) and directed (Bottom) bio-functionalization pathways. Adapted from Spicer et al. [293] and Kaufmann et al.[294] respectively. 18
Figure 6: Conceptual overview of the on-demand topographical defect approach on the left and phantom cell approach on the right. Highlighting with purple arrows the intended directionality of the force balance disruption. 20
Figure 7: Overview of the complete reaction pathway to synthesize the photodegradable crosslinker (PDC). 23
Figure 8: Reaction overview for the two reaction conditions of the isocyanate-based pathway. Presenting the desired product **6a** and potential byproducts **6a'** and **6a''**. Synthesis was performed by Daniel Gutmann in his role as research intern. 24
Figure 9: Reaction pathway of hydroxy functional group activation with 4-nitrophenyl chloroformate. Subsequent reaction with allyl amine, highlighting the desired product **6a** besides byproducts **6a'** and **6a''**. Synthesis was performed by Daniel Gutmann in his role as research intern. 24
Figure 10: Reaction pathway of the hydroxyl group activation with N,N'-carbonyl diimidazole (CDI). Subsequent reaction with allyl amine. Subsequent deprotection of the ester to obtain the desired allyl carbamate oNB compound **6a**. UV illumination to determine degradability of the carbamate group. Synthesis was performed by Daniel Gutmann in his role as research intern. 25
Figure 11: Reaction pathway of the allyl carbamate-based photodegradable crosslinker. Synthesis was performed by Daniel Gutmann in his role as research intern. 26
Figure 12: Photodegradable hydrogel synthesis and characteristics A) Schematic degradation of the photodegradable crosslinker (PDC) when copolymerized into a hydrogel. Additionally, photolytic breakdown mechanism shown in detail, following Wirz et al[181]. B) Non-degradable hydrogel network components are 8-Arm PEG-acrylate, PEG-acrylate and 2-Aminoethyl methacrylate. The PDC substitute for the completely non-degradable control gels is PEG-diacrylate. C) Illustration of the experiment setup to illuminate the samples and induce photolysis consisting of an inverted microscope equipped with 385 nm LED and an adjustable diaphragm. D) Matrix of localized swelling patterned on a photodegradable hydrogel (PDH) and representative overview of the hydrogel behavior to varying illumination duration and UV intensity. E) Additive illumination with each illumination cycle being four seconds of UV at 3.83 mW*cm^2 followed by one hour break. The post-experiment reference image was taken nine hours after the last illumination cycle. Swelling height is given as a percentage of the maximum height with a standard error mean (SEM) and three independent repetitions (N) for both conditions. F) Averaged absolute swelling height ± SEM (N=3) of PDH illuminated with 100 or 300 µm patterns. G) Effective Young's modulus ± SEM (N=3) of all conditions. Statistical significance in E) and F) was assessed using one-way ANOVA. H) PDH bult stiffness under cell culture conditions over an extended period. Statistical significance in was assessed

using one-way ANOVA. Hydrogel images were taken by Iulia Scarlet in her role as master student. Illustrations are partially published in Reul et al.[166] 28
Figure 13: Overview of hydrogel bio-functionalization pathways. A) Conventional UV-based hydrogel functionalization compound. Azido-nitrobenzene at the bottom can be activated by UV light to release a nitrogen molecule and become reactive. The ester group at the top is amine reactive due to the good leaving group properties of the Sulfo-NHS moiety. B) Overview of the different bio-functionalization pathways, with the following subdivision into direct functionalization, crosslinker based functionalization, secondary network-based functionalization, and the combined approach..... 29
Figure 14: Direct bio-functionalization implementation and preliminary results. A) Schematic representation of exemplary reaction of amine functionality with the amine reactive moieties on the hydrogel surface. B) Fluorescent fibronectin adhesion assay. Representative images in brightfield and fluorescent channel corresponding to the emission of the HiLyte 488 tag showing surface bound fibronectin in green. The limits of the brightness contrast of the control-background were adjusted to show the residual autofluorescence. C) Quantification of the immunofluorescent intensity by mean grey value measurement. Statistical significance in was assessed using one-way ANOVA. D) hiPSC-RPE seeding overview of the different GMA compositions and protein incubation temperatures. 31
Figure 15: Secondary network bio-functionalization results. On the left immunofluorescent staining of the F-actin and tight junction protein ZO-1 are shown for the top and outside regions of topographical defect. With the respective side view built from an orthogonal projection of the image. On the right side the two channels were compressed with a maximum intensity projection and merged into a composite. Actin in red and ZO-1 in green. At the bottom the side view of the merged image. Data was generated by Stacy Lok Sze Yam in her role as master student. 33
Figure 16: Overview of the combined approach. Step I) Post-functionalization of the hydrogel to reintroduce free acrylate groups after the free radical polymerization. Step II) Grafting an amine reactive oligomer onto the hydrogel surface by APS/TEMED initiated free radical polymerization. Step III) Bio-functionalization by protein incubation with ECM proteins at 37°C for 16 hours. Step IV) Cell seeding with hiPSC-RPE on bio-functionalized hydrogels. Step IV) Maintaining the monolayer for a week to achieve a degree of maturation. Illustration was published in Reul et al.[166]..... 34
Figure 17: Multi-frame overview of the actin cytoskeleton and vinculin. A) Orthogonal view of the F-actin signal of the monolayer at the center of the topographical defect (Top). Maximum intensity projection of the F-actin signal with the center of the topographical defect marked by an asterisk and zoom-in indicated by the dashed line (Bottom). B) Stitched high resolution image of the vinculin signal with the center of the topographical defect marked by an asterisk. C) Overview image of the unilluminated control, F-actin (Top), vinculin (Bottom). 35

Figure 18: Immunofluorescent staining of F-actin, phospho-myosin light chain (pMLC) and nuclei presented by maximum intensity projection. Merged maximum intensity of pMLC signal onto the signal of F-actin..... 36
Figure 19: Representative F-actin images by maximum intensity projection, showing lateral distribution. When relevant, illumination pattern is in the center of the frame. Side shows the orthogonal projection from the center line of the respective image. Images are published in Reul et al.[166] 37
Figure 20: Representative ZO-1 images by maximum intensity projection and condition, showing lateral tight junction distribution. When relevant, illumination pattern is in the center of the frame and diameter is indicated by a dotted line. Images are published in Reul et al.[166] 38
Figure 21: High resolution representative images of F-actin and Ezrin signal by maximum intensity projection and side view from orthogonal projection...... 39
Figure 22: Delineation of regions. Top (T) stretches radially from 0 to 25 µm, Edge (E) goes from the radius of illumination 25 µm inwards radially and the Outside region is in both conditions defined as an annulus from 150 to 175 µm radii. Illustration is published in Reul et al.[166] 39
Figure 23: Monolayer height quantification. A) Representative orthogonal view of the F-actin signal with indications of the regions: Top (T), Edge (E), and Outside (O). B) Grey Value of a perpendicular line plot through the monolayer, with the two intensity peaks indicating apical and basal cortices. The dashed line indicates the measurement specific threshold, while the arrows show the points at which the threshold is exceeded. C) Absolute monolayer height ± SEM. D) Normalized monolayer height ± SEM. Measurements were normalized by their average. For C-D) Statistical analysis was performed by unpaired two-way ANOVA with Tukey's correction for multiple comparisons. The p-values comparisons are indicated in the graph. *** indicate a of p-value = 0.0008 and **** a p-value = <0.0001 when compared to the relative Outside region. Independent repetition (N): 100 µm PDH and PDH control, N = 5; 100 µm PEG, N = 4; 300 µm PDH, 300 µm PEG and PEG Control, N = 3. Images are published in Reul et al.[166] 41
Figure 24: Quantification of cellular area. A) Absolute cell area ± SEM. B) Normalized cell area ± SEM. Area was normalized by the average cell area of the respective measurement. C) Relative frequency distribution of cellular area for Top (T) and Edge (E) regions of the 100 µm topographical defects. With unilluminated PDH control in yellow. D) Relative frequency distribution of cellular area for Top (T) and Edge (E) regions of the 300 µm topographical defects. With unilluminated PDH control in yellow. E) Relative frequency distribution of cellular area for Outside (O) regions of the two PDHs. With unilluminated PDH and NDH controls in yellow and blue respectively. For A-B) statistical analysis was performed using unpaired two-way ANOVA with Tukey's correction for multiple comparisons. Independent repetition (N): 100 µm PDH, 300 µm PDH and PEG Control, N = 3; 100 µm PEG, N = 6; 300 µm PEG, N = 5; PDH control, N = 4. Images are published in Reul et al.[166] 43

Figure 25: Workflow of the Fiji script highlighting the segmentation and calculation of the shape factor and the binned quantitative results. A) Workflow of the Fiji script, automatically segmenting the maximum intensity projection of the F-actin signal. The for the ROIs the perimeter and area was determined and the shape factor calculated, while also measuring the distance to the center of the topographical defect. B) Shape factor ± SEM. Statistical analysis was performed using unpaired two-way ANOVA with Tukey's correction for multiple comparisons. Independent repetition (N): 100 µm PDH N = 5, 300 µm PDH N = 4, 100 µm PEG, N = 6; 300 µm PEG, N = 5; PDH control, N = 7, and PEG Control N = 3. C) Difference between the average shape factor of the regions on the illuminated PDH and corresponding illuminated NDH. Images are published in Reul et al.[166]..... 44
Figure 26: Relating cell orientation to the center of the topographical defect with the Angle to Origin. A) Schematic of the Angle to Origin calculation, with the red arrow indicating the vector of absolute cellular orientation, the dashed arrow indicating the vector to the center of the topographical defect, and the parula gradient highlighting the scalar product of both giving the Angle to Origin β. B) Representative images with the cells labelled according to their angle to origin, with lower values corresponding to radial alignment in yellow and higher values showing a perpendicular orientation in blue. C) Angle to origin ± SEM. Statistical analysis was performed using unpaired two-way ANOVA with Tukey's correction for multiple comparisons. Independent repetition (N): 100 µm PDH, 300 µm PDH and PEG Control, N = 3; 100 µm PEG, N = 6; 300 µm PEG, N = 5; PDH control, N = 4. Images are published in Reul et al.[166]..... 45
Figure 27: Traction force microscopy (TFM) representative images and quantification. A) Representative TFM images of the two topographical defects, blue indicating regions of lower traction force and yellow showing higher traction forces. Rings indicate the different regions, Top (T), Edge (E), and Outside (O). B) Mean traction force represented in relation to the Outside region ± SEM. C) Median traction force ± SEM. For B-C) statistical analysis was performed using unpaired two-way ANOVA with Tukey's correction for multiple comparisons. Independent repetition (N): 100 and 300 µm PDH, N = 3. Images are published in Reul et al.[166] 46
Figure 28: Microfluidic setup and compounds of photodegradable and non-degradable microgels. A) Schematic of the microfluidic chip highlighting the essential features: 1a Aqueous phase 1, 1b Aqueous phase 2, 1c Continuous phase, 2 Flow focusing junction, 3 Outlet, 4 Collection reservoir. B) Compounds of the photodegradable and non-degradable microgel network. Redox initiator pair with indication in which aqueous phases the respective compound is dissolved. Illustration was prepared by me during pursuit of M. Sc. at RWTH Aachen..... 47
Figure 29: Diameter and stiffness of the NDM and PDM. A) Diameter of the different compositions of the NDM ± SD. B) Effective Young's Modulus of the different compositions of the NDM ± SD. C) Diameter of the PDM composition ± SD. D) Effective Young's Modulus of the PDM composition ± SD. Data was generated by Alexandra Raab and Yuxin Ji in their role as master students. 49

Figure 30: One time illumination diameter and stiffness characterization of the PDM. A) PDM diameter changes over time and the corresponding relative change of one second, 60 seconds, and four minute illumination durations ± SD. B) PDM Effective Young's Modulus changes after illumination over time and the corresponding percentage decrease from the initial value. C) Stiffnesses before and after 60 second illumination of PDM in cell culture medium at 37°C on the left and average percentage reduction on the right. Statistical analysis was performed using unpaired two-way ANOVA with Tukey's correction for multiple comparisons. **** indicate p value of $p < 0.0001$. D) Percentage change from initial value over UV illumination duration ± SD. Exponential decay function fitted to the values. Data was generated by Yuxin Ji in her role as master student. 50
Figure 31: Additive illumination of photodegradable microgels (PDM). A) Eff. Young's modulus ± SD. Three illuminations are highlighted with purple lines. First illumination was four seconds, followed by an equilibration time of one hour before nanoindentation. Second illumination was one second, followed by an equilibration time of one hour before nanoindentation. Last illumination was one second, followed by an equilibration time of one hour before nanoindentation. B) Percentage change from initial value ± SD. C) Difference between consecutive measurements ± SD. For B-C) statistical analysis was performed using unpaired two-way ANOVA with Tukey's correction for multiple comparisons. * indicate p value of $p < 0.05$, ** $p < 0.01$, *** < 0.001, and **** $p < 0.0001$. Data was generated by Yuxin Ji in her role as master student..... 51
Figure 32: Oriented bio-functionalization of recombinant adherens junction proteins on the microgel surface. A) Overview of the surface functionalization of Microgels with a heterobifunctional complexing crosslinker, subsequent complex formation by addition of transition metal ion Co^{2+} and HisTag-Protein with NTA moiety of the crosslinker and oxidation of the complexing ion into Co^{3+} for increase complex stability. B) Bio-functionalization of the microgel surface with green fluorescent protein (GFP) to distinguish between oriented adhesion and unspecific surface binding (Control). C) Bio-Functionalization of microgels with adherens junction protein E-cadherin and visualization by immunofluorescent staining. Images were generated by Yuxin Ji in her role as master student. 52
Figure 33: Schematic overview of microgel surface immobilization, cell seeding and co-culture interaction. 53
Figure 34: MDCK PDM co-culture live cell imaging of brightfield and Lifeact-GFP (green) signal at different time points. Reference image before illumination is labelled t_0, UV illumination of 60 seconds (3.83 mW/cm^2, 20x objective) is indicated by UV, image immediately after illumination capturing the quick response is labelled t_1, and image after 2 hours of equilibration time to capture the slow response is labelled t_{2h}. Unilluminated microgels are marked with an unfilled star, while illuminated microgels are marked with a purple star. Images were generated by Yuxin Ji in her role as master student. 54
Figure 35:MDCK co-cultured with photodegradable microgels (PDM). Maximum intensity projections and the relevant zoom-in for Nuclei, F-actin, α18-catenin and ZO-1 immunofluorescent staining. Furthermore, merged images of F-actin and α18-catenin

and the respective orthogonal slices. Unilluminated microgels are marked with a black star, while illuminated microgels are marked with a purple star. All scale bars are 20 µm. Images were generated by Yuxin Ji in her role as master student. 56
Figure 36: Morphometrical and mechanical parameters of the hiPSC-RPE non-degradable microgels (NDM) co-culture. A) Representative F-actin staining of NDM. Microgels are marked by transparent stars. Scale bar is 20 µm. B) NDM circularity ± SD. p(E-cadherin vs non-biofunctionalized) = 0.0457; *p(N-cadherin vs non-bio-functionalized) = 0.0306. C) NDM effective Young's modulus ± SD. D) hiPSC-RPE effective Young's modulus in relation to the distance of the NDM ± SD. For B-C) statistical analysis was performed using unpaired two-way ANOVA with Tukey's correction for multiple comparisons. * indicate p value of $p < 0.05$, ** $p < 0.01$, *** < 0.001, and **** $p < 0.0001$. Data was generated by Alexandra Raab in her role as master student. 58
Figure 37: Nuclei, cytoskeleton (F-actin), adherens junction (N-cadherin) and mechanotransduction protein immunofluorescent staining of a seven day hiPSC-RPE co-culture with N-cadherin bio-functionalized non-degradable microgels (NDM). Composite image shows the respective mechanotransduction protein signal merged with the adherens junction signal in top-down and orthogonal view. All scale bars are 20 µm. Images were generated by Alexandra Raab in her role as master student.... 60
Figure 38: Nuclei, cytoskeleton (F-actin), polarization (Ezrin) and tight junction (ZO-1) immunofluorescent staining of 14 days hiPSC-RPE co-culture with E-cadherin bio-functionalized non-degradable microgels (NDM). Composite image of polarization and tight junction marker in top-down and orthogonal view. Zoom-in is indicated by dashed square and all scale bars are 20 µm. Images were generated by Alexandra Raab in her role as master student. 61
Figure 39: Live cell imaging of photodegradable microgels (PDM) hiPSC-RPE co-culture by fluorescent SiR-Actin live cell actin probe. Before (t_0) and directly after (t_1) UV illumination (60 seconds, 3.83 mW/cm^2, 20x magnification) of the PDM, as well as after an equilibration time of one hour (t_{1h}). All scale bars are 20 µm. Images were generated by Yuxin Ji in her role as master student. 63
Figure 40: Shape factor quantification in relation to the distance to the photodegradable microgel (PDM) in the PDM hiPSC-RPE co-culture over time. A) Schematic representation of cell segmentation and grouping into regions depending on the distance to the PDM. B) Line graph of shape factor for the different layers over time. With t_0 being the reference image, the quick response domain at time point t_1 directly after UV illumination and the slow response domain at time point t_{1h} after one hour of equilibration time. Data was generated by Yuxin Ji in her role as master student. 65
Figure 41: Particle image velocimetry (PIV) of photodegradable microgel (PDM) hiPSC-RPE co-culture. A) Vector field and magnitude map. B) Quantification of the median vector magnitude in the quick response domain from t_0-t_1. C) Quantification of the median vector magnitude in the quick response domain from t_1-t_{1h}. Images were generated by Yuxin Ji in her role as master student. 67

Figure 42: Immunofluorescent staining of Nuclei and mechanotransduction relevant proteins in photodegradable microgel (PDM) hiPSC-RPE co-culture. Images are maximum intensity projections of complete imaging stack. Unilluminated microgels are highlighted with a transparent star, illuminated microgels are highlighted with a purple star and all scale bars are 20 µm. Images were generated by Yuxin Ji in her role as master student. 70
Figure 43: ^{1}H NMR (400 MHz; $(CD_3)_2SO$, RT) of the complete reaction pathway of the photodegradable crosslinker. From top to bottom: **2**, **3**, **4**, **5**, and **6**. 85
Figure 44: A) ^{1}H NMR (400 MHz; $(CD_3)_2SO$, RT) of both isocyanate-based reaction pathways, top first synthesis using allyl isocyanate and bottom second synthesis using ally isocyanate. B) ESI-MS in methanol of the second synthesis using allyl isocyanate. Data was generated by Daniel Gutmann in his role as research intern. 87
Figure 45: A) ^{1}H NMR (400 MHz; $(CD_3)_2SO$, RT) of the activated compound after reaction with 4-nitrophenyl chloroformate on top and carbamate product **6a** at the bottom. B) ESI-MS in methanol of the finished product **6a**. Data was generated by Daniel Gutmann in his role as research intern. 89
Figure 46: A) ^{1}H NMR (400 MHz; $(CD_3)_2SO$, RT) from top to bottom **4a**, **6a** and the carbamate based crosslinker. B) MALDI-TOF in DCTB matrix of the carbamate based crosslinker. Data was generated by Daniel Gutmann in his role as research intern. 92

3. List of tables

Table 1: Electrospray ionization mass spectrometry (ESI-MS) table. Calculated and found masses of the starting material **5**, desired product **6a** and potential byproducts **6a'** and **6a''**. 24
Table 2: PDH topographical deformation immunofluorescent staining antibodies and dyes. 99
Table 3: Composition adjustment of PEG-acrylate in the first aqueous phase. All other components were kept constat. 103
Table 4: Microgel hiPSC-RPE co-culture immunofluorescent staining antibodies and dyes. 108

4. Code for analysis

Fiji macro for batch analysis of Shape Factor/Area, Angle to Origin, Monolayer height

```
//@ File (label = "Input directory", style = "directory") input                // Macro cannot do subfolders and gets confused when there are other folders in the directory
//@ File (label = "Output directory", style = "directory") output
//@ String (label = "File suffix", value = ".czi") suffix
run("Bio-Formats Macro Extensions");

// function to scan folders/subfolders/files to find files with correct suffix ----------
function processFolder(input) {
	list = getFileList(input);
	list = Array.sort(list);
	for (i = 0; i < list.length; i++) {
		if(File.isDirectory(input + File.separator + list[i]))
			CurrentOutput = output  + File.separator + list[i];
			processFolder(input + File.separator + list[i]);
		if(endsWith(list[i], suffix))
			processFile(input, CurrentOutput, list[i]);
	}
}
// Setting up image processing ----------------------------------------------------------
function processFile(input, output, file) {

	print("Processing: " + input + file);
	print("Saving to: " + output);
	showProgress(i, list.length);

	Ext.openImagePlus(input+ "/" +file);
	//open(file);
	rename(file);
	run("Arrange Channels...", "new=2");
	run("Grays");
	run("Z Project...", "projection=[Max Intensity]");
	run("Invert LUT");
//--------[[[Shape Factor / Area]]]-------------------------------------------------------
	getPixelSize(unit, pixelWidth, pixelHeight);
	getDimensions(width, height, channels, slices, frames);
	if (startsWith(file, "PDC_Drusen")) {
		setTool(7);
	//Center of the Drusen for later
		waitForUser("Click center of the Drusen");
		getSelectionCoordinates(xCenter, yCenter);
		xCenter = xCenter[0]*pixelWidth;
		yCenter = yCenter[0]*pixelHeight;
	} else {
```

```
		xCenter = width/2*pixelWidth;
		yCenter = height/2*pixelHeight;
	}
	run("Set Measurements...", "area center fit perimeter redirect=None decimal=3");
	run("Cellpose ...", "env_path=C:\\Users\\f_reu\\anaconda3\\envs\\cellpose
env_type=conda model=cyto3 model_path=path\\to\\own_cellpose_model
diameter=15 ch1=1 ch2=-1 additional_flags=[]"); //Adjust diameter here
	run("Label image to ROIs", "rm=[RoiManager[size=0, visible=true]]");
	roiManager("Measure");
	numROIs = roiManager("count");
	adistance = newArray();
	aArea = newArray();
	aSF = newArray();

	xCoordinate = Table.getColumn("XM");
	yCoordinate = Table.getColumn("YM");
	for (k=0; k<numROIs;k++) {
		xcurrentvalue = xCoordinate[k];
		ycurrentvalue = yCoordinate[k];
		xpredistance = pow(xcurrentvalue-xCenter, 2);
		ypredistance = pow(ycurrentvalue-yCenter, 2);
		distance = sqrt(xpredistance + ypredistance);
		setResult("DistanceSF", k, distance);
		adistance = Array.concat(adistance, distance);
	}
	for (i=0; i<numROIs;i++) {
		Perim = getResult("Perim.", i);
		Area = getResult("Area", i);
		sqrtArea = sqrt(Area);
		ShapeFactor = Perim/sqrtArea ;
		setResult("Cell Area", i, Area);
		setResult("SF", i, ShapeFactor);
		aArea = Array.concat(aArea, Area);
		aSF = Array.concat(aSF, ShapeFactor);
	}
	roiManager("delete");
	close();
//-----------[[ Angle to Origin v2 ]]----------------------------------------------------
function Rad2Deg(angleInRad) {
	return angleInRad * 180 / PI;
}
function Deg2Rad(angleInDeg) {
	return angleInDeg / 180 * PI;
}
aATO = newArray();

for (q = 0; q < numROIs; q++) {
	AngleRad = Deg2Rad(getResult("Angle", q));
```

```
		AngleRad = PI-AngleRad;
		//Transposition needed
		//Alpha Vector
		aX = cos(AngleRad);
		aY = sin(AngleRad);
		//Reference Vector
		rX = xCenter-xCoordinate[q];
		rY = yCenter-yCoordinate[q];
		lengthR = sqrt(rX*rX + rY*rY);
		//Normalize
		rX = rX / lengthR;
		rY = rY / lengthR;
		//Compute both Gammas
		GammaDeg = Rad2Deg(acos(aX*rX + aY*rY));
		GammaDashDeg = Rad2Deg(acos(-aX*rX + -aY*rY));
		//Return smaller Gamma
			if(GammaDeg < GammaDashDeg){
				setResult("Angle to origin v2", q, GammaDeg);
				aATO = Array.concat(aATO, GammaDeg);
			}else {
				setResult("Angle to origin v2", q, GammaDashDeg);
				aATO = Array.concat(aATO, GammaDashDeg);
			}
		}
//--------[[[Monolayer Height]]]-----------------------------------------------------------
		selectImage(file);
		setTool("rectangle");
		run("Select All");
		run("Reslice [/]...", "output=1.117 start=Top flip");
		run("Invert LUT");
		reslice = getImageID();
		ImageName = getTitle();
		selectImage(reslice);
		getPixelSize(unit, pixelWidth, pixelHeight);
		getDimensions(width, height, channels, slices, frames);

		slice =0;
		rowcounter =0;
		anticounterTOP =0;
		anticounterBOT =0;
		a =0;
			//Line spacing
		ArrayDistance = newArray();
		ArrayMLthickness = newArray();

		for (i = 0.1; i < 1; i+=0.1) {
			currentwidth = width*0.05 + width*a;
			makeLine(currentwidth, 0, currentwidth, height);
```

```
		n = nSlices;
		slice =1;
		count =0;

		for (slice=1; slice<n; slice++){
	//Counts in slice direction

			setSlice(slice);
			profile = getProfile();
			Array.getStatistics(profile, min, max, mean, stdDev);
			for (k=0; k<profile.length; k++){
				anticounterTOP++;
				if (profile[k]>mean){
	//profile[k]>mean when...; profile[k]<mean when threshold
					count++;
				}
				if (count>3) {
					break;
				}
			}
			count=0;
			for (k=profile.length-1; k>0; k--){
				anticounterBOT++;
				if (profile[k]>mean){
	//profile[k]>mean when...; profile[k]<mean when threshold
					count++;
				}
				if (count>3) {
					break;
				}
			}
			thickness = (height-
(anticounterTOP+anticounterBOT)+6)*pixelHeight;
			dx = pow((width/2 - currentwidth)*pixelWidth, 2);
			dy = pow((n/2 - slice)*1.17, 2);
			distance = sqrt(dx + dy);

			if (5 < thickness && thickness < 20) {
				//filtering
				setResult("DistanceMLT", rowcounter, distance);
				setResult("MLthickness", rowcounter, thickness);
				rowcounter++;
				ArrayDistance = Array.concat(ArrayDistance, distance);
				ArrayMLthickness = Array.concat(ArrayMLthickness,
thickness);
			}
			count=0;
			thickness=0;
```

```
                    anticounterTOP=0;
                    anticounterBOT=0;
                }
                a+=0.05;
        }

updateResults();
```